CAUSTICS AND FLAGS OF CHAOS IN

QUANTUM MANY-BODY SYSTEMS

CAUSTICS AND FLAGS OF CHAOS IN QUANTUM MANY-BODY SYSTEMS

By

WYATT J. KIRKBY, BSc., MSc.

A Thesis Submitted to the School of Graduate Studies in Partial Fulfilment of the Requirements for the Degree DOCTOR OF PHILOSOPHY

Doctor of Philosophy (2021)   McMaster University
(Physics)   Hamilton, Ontario, Canada

Title: Caustics and Flags of Chaos in Quantum Many-Body Systems
Author: Wyatt J. Kirkby, BSc., MSc.
Supervisor: Professor Duncan H. J. O'Dell
Number of Pages: xii, 179

LAY ABSTRACT

Caustics are signatures of singularities in a classical geometrical ray theory which are best exemplified by bright lines of focused light, like those at the bottom of a swimming pool or the cusp inside a coffee cup. Caustics also appear in the theories of hydrodynamics and gravitational lensing, and are described by the mathematics of catastrophe theory.

In this thesis we focus on the formation of caustics in dynamics of quantum many-body systems out of equilibrium, determine how they are organized by symmetry, and identify their presence as a type of universality in these systems. Attention is also paid to their existence (or lack thereof) when many-body quantum chaos is present. We make use of an object known as the out-of-time-ordered correlator (OTOC), which we show can yield caustics, and address how care must be taken by identifying 'false flags' of chaos.

ABSTRACT

We explore the dynamics of integrable and chaotic quantum many-body systems with a focus on universal structures known as caustics, which are a type of singularity categorized by catastrophe theory.

Papers I and II study light cones in quantum spin chains, which we show are caustics and therefore inherits specific functional forms. For integrable systems, the edge of the cone is a fold catastrophe, making the wavefunction locally of Airy form. We also identify the cusp catastrophe in the XY model, thus the secondary light cone is a Pearcey function. Vortex pairs appear in the dynamics, are sensitive to phase transitions, and permit the extraction of critical scaling exponents. In paper II we use a Gaussian wavefront form to distinguish integrable and chaotic models. Writing the wavefront as $\exp[-m(x)(x - vt)^2 + b(x)t]$, the scaling of coefficients $m(x)$ and $b(x)$ is the diagnostic. The local Airy function description in free models leads to a power-law $\sim x^{-n/3}$ scaling, while for the chaotic case the scaling is exponential $\sim \mathrm{e}^{-cx}$.

In Paper III, we study the function $F_n(t) = \langle (A(t)B)^n \rangle$, a generalization of the four-point out-of-time ordered correlator (OTOC) $F_2(t)$, for an integrable system and show that the function $F_n(t)$ can be recast as the return amplitude of an effective time-dependent chaotic system, exhibiting signals of chaos such as a positive Lyapunov exponent, spectral statistics consistent with random matrix theory, and relaxation.

In Paper IV we perform a comprehensive investigation of caustics in many-body systems in (1+1)- and (2+1)-dimensional Fock space and time. We show how a hierarchy of caustics appear in the dynamics of many-body models, using two- and three-mode Bose-Hubbard models as guiding systems. We show that, in the case of the trimer, high dimensional caustics appear and are organized by the catastrophe X_9.

Acknowledgements

First I'd like to thank Dr. Duncan H. J. O'Dell for being an excellent supervisor, and supporting me through the more than six years and two degrees at McMaster University. To the members of my committee, Erik Søresnen and Sung-Sik Lee, thank you for what you've taught me, both in the classroom and on the blackboards in your respective offices.

This thesis and the papers it contains wouldn't exist without our research group. Thanks to Jesse for being an inexhaustible well of good ideas and bright insights into all kinds of topics. Thanks to Ryan for putting up with my constant questions during our time as office mates. To the other members of the group: Sriram, Matt, Liam, Denise, and Josh, we probably didn't get quite the opportunity to socialize as much as in normal times, but our research conversations were always much appreciated. To the members of the greater condensed matter area: James, Jon, Anton, thanks for all the help and research ideas.

To the fine people with whom I've had the pleasure of sharing a home with: Sean, James, Joey, Alex, Dan, and Hector, thank you all for being great housemates. I like to think the department was made brighter by our friendship and social gatherings; I know my time here certainly was. To Jacqueline, Thanassis, Carmen, Claude, Sarah (D. and M.-P.), J.-C., Flo, Tom, Lili, Ian, Ashley, Ben, James B., Connor, Laszlo, Greg, and all the members of the P&A department who I've met throughout the years, thanks for joining in on all the fun. To Hassan, Alex, Randy, Stone (the dumdums), Blair, Jeff, Robyn, Siobhan, Taylor, Josée, Sophie, Sean, Annica, and Michael, thanks so much for being a big part of my life outside the department, all the way from high school through undergrad, to the end of the PhD. and beyond, you guys are going to make it really hard to leave Canada for any length of time.

To my parents, Bruce and Margaret, my sisters, Lauren and Kristine, Kevin, and my grandparents, Jean and Ken. You've all been with me since before I even took my first steps down this road (or my first literal steps). Thank you for all your support, and although maybe I took the advice "stay in school" a bit literal, I hope I make you proud.

TABLE OF CONTENTS

List of Tables

List of Figures

LIST OF ABBREVIATIONS

AQD – Atomic Quantum Dot

BH – Bose-Hubbard (model, dimer, trimer, etc.)

BEC – Bose-Einstein Condensate

GOE/COE – Gaussian/Circular Orthogonal Ensemble

GUE/CUE – Gaussian/Circular Unitary Ensemble

GSE/CSE – Gaussian/Circular Symplectic Ensemble

IPR – Inverse Participation Ratio

OTOC – Out-of-time-ordered correlator

PDF – Probability Density Function

PR – Participation Ratio

RMT – Random Matrix Theory

TFIM – Transverse-Field Ising Model

WKB – Wigner-Kramers-Brillouin

Declaration of Academic Achievement

Chapter 2 (Paper I)

W. Kirkby, J. Mumford, and D. H. J. O'Dell

Quantum caustics and the hierarchy of light cones in quenched spin chains

Phys. Rev. Research **1**, 033135 (2019).

Jesse Mumford provided the original idea for the project. Nearly all calculations present in the article were performed by Wyatt Kirkby, along with all numerics and figure generation. The main sections in the article were written by Wyatt Kirkby, with input from Jesse Mumford and Duncan O'Dell. The introduction and conclusion were written by Duncan O'Dell with input from Wyatt Kirkby.

Chapter 3 (Paper II)

J. Riddell, W. Kirkby, D. H. J. O'Dell, and E. S. Sørensen

Scaling at the OTOC Wavefront: Integrable versus chaotic models

Submitted to Physical Review Letters, arXiv:2111.01336

This project was originally conceived by Jonathan Riddell and Erik Sørensen. The author is responsible for deriving the analytic scaling forms for the integrable case, as well as the corresponding figures. Key results sections and overall direction of the article is due to both Jonathan Riddell and Wyatt Kirkby, with the exception of the introduction and conclusions which were mostly written by Duncan O'Dell and Erik Sørensen.

Chapter 4 (Paper III)

W. Kirkby, D. H. J. O'Dell, and J. Mumford

False signals of chaos from quantum probes

Phys. Rev. A **104**, 043308 (2021).

Jesse Mumford initiated this project. All numerics and figures appearing in this paper

are generated by Wyatt Kirkby. Analytic calculations were performed by both WK and Jesse Mumford. The introduction and conclusion were largely written by Duncan O'Dell with input from Wyatt Kirkby.

Chapter 5 (Paper IV)
W. Kirkby, Y. Yee, K. Shi, and D. H. J. O'Dell
Caustics in quantum many-body dynamics
Submitted to Physical Review Research, arXiv:2102.00288

Kevin Shi and Yohan Yee performed an initial investigation into caustics appearing in the three-mode model. All figures, equations, and numerics were generated by Wyatt Kirkby, along with the majority of the content of the article, including the experimental diffraction images appearing in Figure 1. Duncan O'Dell is responsible for large sections of the introduction and discussion of the paper.

1

INTRODUCTION

One of the most valued keystones of modern physics is the concept of universality: common signatures of natural phenomena which occur independent of microscopic details. Perhaps the classic and most heavily studied example of universality is the second-order equilibrium phase transition, which gives rise to universal scaling exponents and emergent scaling symmetries. At the heart of each of these universal features is a singularity; correlation lengths, susceptibilities, and relevant time scales diverge as the system is tuned through the transition. In this way, different models, both classical and quantum, can be categorized according to universality classes which obey the same macroscopic behaviour.

Our goal in this thesis is to study universal features in non-equilibrium many-body quantum dynamics. Like in the case of phase transitions, many of the dynamical structures we discuss here also have their origins in a singularity, which in our case will turn out to be an intense focusing of classical trajectories resulting in a *caustic*. As we will discuss later, a caustic is a universal type of singularity which appears in optics, hydrodynamics, and even astrophysics, and which is described by the mathematics of catastrophe theory. Although caustics have been studied in quantum systems to some degree before, our goal is to examine how they appear in a many-body second-quantized context, in which regime we associate them with the name *quantum catastrophes*.

In this thesis, we also pay particular attention to the study of an object known as the out-of-time-ordered correlator (OTOC). A generalization of a dynamical two-point correlation function, the OTOC is a popular tool in systems for studying phase

transitions, but also the onset of scrambling and chaos in many-body quantum systems. In the case of systems with local (in our case, nearest neighbour) interactions, we pay particular attention to the edge of the OTOC, which is itself a caustic. We also demonstrate that generalizations of the OTOC can lead to typical predictors for chaos in completely regular systems, indicating that these types of functions should be treated with some care.

We motivate many of the problems studied in this thesis in the context of experimental trapped ultracold atomic [1] and ionic [2] systems. These types of setups provide a robust testing platform for quantum quenches in many-body quantum systems and quantum simulation, that is, the ability to simulate a model Hamiltonian with another quantum system that is easy to control. Since the first realization of the Bose-Einstein condensate (BEC) in 1995 [3–5], techniques in controlling ultracold atoms have improved dramatically to include the control of multiple condensates trapped in a lattice [1], and spinor condensates [6, 7] with tuneable interactions [8]. For the specific systems we study in this thesis, simulations of dynamics of Bose-Hubbard [9–12] and spin chain [13] models are particularly relevant.

Overview of this Thesis

This first chapter will attempt to introduce the important topics required for each of the papers in Chapters 2-5 (Papers I-IV, respectively). In Section 1.1, we give a rapid overview of quantum many-body dynamics, starting from the foundations of quantum many-body theory, to the introduction of the types of models relevant to this thesis, including both quantum and classical treatments. We finish the section with a discussion of light cones and how perturbations propagate information in quantum systems. In Section 1.2, we attempt to explain the important theorems of catastrophe theory, including Thom's classification theorem, without a formal mathematical treatment. We show analytically and geometrically where many of the elementary catastrophes (and beyond) come from, and their connection to a physical optics context in the form of diffraction integrals. Finally, Section 1.3 will present an overview of some important concepts of classical and quantum chaos. We introduce the necessary details of random matrix theory, followed by a presentation of the out-of-time-ordered correlator and its applications. We end the chapter with a brief overview of a publication where out-of-time-ordered correlators were used to detect phase transitions in a two-mode Bose-Hubbard system.

Chapters 2-5 will consist of four publications, each featuring a summary and statement by the author on contributions to each work. Chapter 2 (Paper I) applies catas-

trophe theory to quenches in spin chains by identifying the light cone-like structures
in theses systems as examples of quantum caustics. A description of these light cones
in terms of special functions with associated scaling laws follows. Chapter 3 (Paper
II) extends the work of the previous chapter by considering how the structure of light
cones is altered by the inclusion of chaos. We verify via a Gaussian wave approx-
imation that the catastrophe nature of the light cone changes in a chaotic system.
Chapter 4 (Paper III), addresses signatures of chaos in quantum many body systems
from the perspective of a generalized two-time correlation function. Signatures which
are typically associated with chaotic systems are shown also appear in integrable
systems under certain conditions. Chapter 5 (Paper IV) provides an investigation of
higher-dimensional caustics which appear in quenched many-body systems. A demon-
stration of the formation of corank-2 catastrophes such as the hyperbolic and elliptic
umbilics, and their organization within a catastrophe known as X_9 is presented. In
this and previous chapters, we argue that caustics form a type of universality in quan-
tum many-body systems. Chapter 6 presents a final summary, conclusions, and an
outlook to future work.

1.1   Many-body Quantum Dynamics

The focus of Chapters 2-5 are either caustics, which we introduce in detail in Section
1.2, or flags of chaos, outlined in Section 1.3. This Section, however, lays the founda-
tions for understanding each of the models and their dynamics. We begin from basic
quantum many-body theory, proceed to introduce each model individually, along with
quantum and mean-field equations of motion and finish with a discussion of quantum
light cones (a quantum speed limit).

1.1.1   Many-body Quantum Theory

A standard formulation of many-body quantum mechanics begins with the many-body
wavefunction $\Psi(\mathbf{x}_1, \mathbf{x}_2, ..., \mathbf{x}_N, t)$ which is governed by the time-dependent Schrödinger
equation [14, 15],

$$\left[-\frac{\hat{\hbar}^2}{2m} \sum_{i=1}^{N} \nabla_i^2 + \sum_{i<j}^{N} U(\mathbf{x}_i, \mathbf{x}_j) + \sum_{i=1}^{N} V(\mathbf{x}_j) \right] \Psi = i\hbar \frac{\partial \Psi}{\partial t} \qquad (1.1)$$

where we assume that the interaction between particles is at most two-body ($\hat{U}$),
and the wavefunction is subject to some external potential $\hat{V}$. There exist very few

exact analytic solutions to this equation. Even for a single electron, the solution of the Hydrogen atom with a stationary proton is considered a triumph, while the only slightly more complicated Helium atom requires approximation methods. Nearly all N-body problems therefore require some form of approximation, for example relying on U to be reduced to contact interactions and localized wavefunctions (the tight-binding approximation), and mean-field theory.

Under so-called first quantization, which involves the study of the many-body wavefunction directly, variables and coordinates are promoted to the status of operators [16]. For example, in the position representation,

$$E \to \hat{H} = i\hbar \frac{\partial}{\partial t} \tag{1.2}$$

$$\mathbf{p} \to \hat{\mathbf{p}} = -i\hbar \nabla \tag{1.3}$$

$$\mathbf{x} \to \hat{\mathbf{x}} = x \ , \tag{1.4}$$

while the Poisson bracket is replaced with a commutator [158],

$$\{x, p\}_P \to \frac{1}{i\hbar} [\hat{x}, \hat{p}] \ . \tag{1.5}$$

where the commutator is defined to be $\left[\hat{A}, \hat{B}\right] \equiv \hat{A}\hat{B} - \hat{B}\hat{A}$.

In order to develop an intuition for the models studied in this thesis, we shall briefly review the idea of *second quantization*. This treats quantum many-body systems in terms of quantum fields and elevates the wavefunction to an operator-valued function, which we call a 'field operator' [16, 17],

$$\Psi(\mathbf{x}) \to \hat{\Psi}(\mathbf{x}) \tag{1.6}$$

The field operator $\hat{\Psi}(\mathbf{x})$ annihilates a particle at the point $\mathbf{x}$ while its Hermitian conjugate $\hat{\Psi}^\dagger(\mathbf{x})$ creates a particle at $\mathbf{x}$. In the case of bosonic particles, the field operators obey,

$$\left[\hat{\Psi}(\mathbf{x}), \hat{\Psi}^\dagger(\mathbf{y})\right] = \delta(\mathbf{x} - \mathbf{y}) \ . \tag{1.7}$$

This formalism was introduced by Jordan and Wigner [18]. For Fermionic particles, the anticommutator is required,

$$\left\{\hat{\Psi}(\mathbf{x}), \hat{\Psi}^\dagger(\mathbf{y})\right\} = \delta(\mathbf{x} - \mathbf{y}) \ , \tag{1.8}$$

where $\left\{\hat{A}, \hat{B}\right\} = \hat{A}\hat{B} + \hat{B}\hat{A}$ (note the lack of subscript to distinguish from the Poisson bracket). In order to understand how to construct a many-body theory, we consider

a the representation,

$$\hat{\Psi}(\mathbf{x}) = \sum_m \hat{a}_m \psi_m(\mathbf{x}) \tag{1.9}$$

$$\hat{\Psi}(\mathbf{x}) = \sum_m \hat{a}_m^\dagger \psi_m^*(\mathbf{x}) \tag{1.10}$$

where $\{\psi_m\}$ is an orthonormal basis of single-particle wavefunctions, or modes. The operators $\hat{a}_m^{(\dagger)}$ destroy (create) a particle in state m with amplitude $\psi_m^{(*)}(x)$. We can also define an occupation number operator $\hat{N}_m \equiv \hat{a}_m^\dagger \hat{a}_m$ which counts the number of particles in mode m.

The next step is to represent one-body operators such as the kinetic energy operator $\hat{T} = \sum_i \hat{p}_i^2/2m$ and the external potential $\hat{U} = \sum_i U(\hat{x}_i)$ and note that these types of operators are simply sums of operators acting on each particle i, so that $\hat{O}_1 = \sum_i \hat{o}_i$. The representation of such operators in a general basis is [17] (see Appendix A for a proof),

$$\hat{O}_1 = \sum_{ij} \langle i|\hat{o}|j\rangle \hat{a}_i^\dagger \hat{a}_j \tag{1.11}$$

where we have dropped the subscript on $\hat{o}$ since each single-particle operator is identical. Similarly, for a two-body operator,

$$\hat{O}_2 = \sum_{ijk\ell} \langle ij|\hat{o}|k\ell\rangle \hat{a}_i^\dagger \hat{a}_j^\dagger \hat{a}_k \hat{a}_\ell \tag{1.12}$$

One can invert the relationships from Eqs. (1.9)-(1.10) to rewrite the Hamiltonian in second-quantized form,

$$\hat{H} = \int \mathrm{d}\mathbf{x}\mathrm{d}\mathbf{y}\, \hat{\Psi}^\dagger(\mathbf{x})\langle \mathbf{x}|\hat{H}|\mathbf{y}\rangle \hat{\Psi}(\mathbf{y}) \tag{1.13}$$

$$= \int \mathrm{d}\mathbf{x}\hat{\Psi}^\dagger(\mathbf{x})\left[-\frac{\nabla^2}{2m} + V(\mathbf{x})\right]\hat{\Psi}(\mathbf{x}) + \int \mathrm{d}\mathbf{x}\mathrm{d}\mathbf{y}\, \hat{\Psi}^\dagger(\mathbf{x})\hat{\Psi}^\dagger(\mathbf{y})U(\mathbf{x},\mathbf{y})\hat{\Psi}(\mathbf{x})\hat{\Psi}(\mathbf{y}) \tag{1.14}$$

Particularly important are potentials of the form $U(\mathbf{x},\mathbf{y}) = U(\mathbf{x}-\mathbf{y})$ (e.g. the Coulomb potential). We can also write the Hamiltonian in its representation using creation/annihilation operators directly,

$$\hat{H} = \sum_{i<j} \langle i|\hat{T}|j\rangle \hat{a}_i^\dagger \hat{a}_j + \sum_i \langle i|\hat{V}|i\rangle \hat{a}_i^\dagger \hat{a}_i + \sum_{ijk\ell} \langle ij|\hat{U}|k\ell\rangle \hat{a}_i^\dagger \hat{a}_j^\dagger \hat{a}_k \hat{a}_\ell \tag{1.15}$$

This form of the Hamiltonian is widely studied as the *tight-binding* representation of an interacting Hamiltonian [17] (we have neglected the spin indices σ, σ' from common definitions of Eq. (1.15) when studying e.g. electrons, as they only serve to

add to the complexity of the model, and we will not be using them in this thesis). The name 'tight binding' arises from when the operators $\hat{a}_i^\dagger$ create Wannier states, which approximate localized wavefunctions and are tightly bound to lattice positions in a condensed matter system.

1.1.2 Two-Mode Bose-Hubbard Model

As it currently stands, Eq. (1.15) is still quite complicated, since each matrix element involves integrals over many wavefunctions in states $i, j, ...$ etc. A particularly common approximation in the tight-binding model assumes that the sites are separated by large enough distances that the wavefunction overlap is small between sites [16, 17] and that the rate of tunnelling is exponentially suppressed as the distance between sites increases, leading to the Hubbard Model,

$$\hat{H} = -T \sum_{\langle ij \rangle} \hat{a}_i^\dagger \hat{a}_j + \sum_i \epsilon_i \hat{N}_i + U \sum_i \hat{N}_i^2 . \tag{1.16}$$

In this definition, we have therefore assumed that $\langle ij|\hat{U}|k\ell\rangle = U\delta_{ijkl}$, $\langle i|\hat{V}|i\rangle = \epsilon_i$, and set $\langle i|\hat{T}|j\rangle = T$ provided i and j are nearest neighbours, denoted $\langle ij \rangle$.

Chapters 4 and 5 study the two- and three-mode Hubbard models, respectively, such that the operators $\hat{a}_i^{(\dagger)}$ correspond to bosonic degrees of freedom. In these papers, the physical systems in mind correspond to trapped Bose-Einstein condensates (BEC) which either have access to different spatially separated modes (like the Wannier states), or internal modes of a single trapped BEC (for example, a spinor condensate). At low temperatures and in dilute systems, we approximate the interatomic potential with a contact interaction of the form [19],

$$U(\mathbf{x}, \mathbf{y}) = g\delta(\mathbf{x} - \mathbf{y}) . \tag{1.17}$$

In doing so, the short-wavelength degrees of freedom have been eliminated in favour of an effective interaction under the assumption that the typical distance between bosons is much larger than the interaction range. The interaction strength is $g = \frac{4\pi\hbar^2 a}{m}$ (in three dimensions), where m is the atomic mass and a is the s-wave scattering length which can sometimes be tuned via Feshbach resonance to give attractive or repulsive interactions.

For the two- and three-mode models, we also truncate the field operator expansions at the appropriate order. In the two-mode model, let us suppose that the modes correspond to BEC modes which occupy left (L) and right (R) wells of a double-well potential, and so we truncate at second-order:

$$\hat{\Psi}_2(\mathbf{x}) = \hat{a}_L \psi_L(\mathbf{x}) + \hat{a}_R \psi_R(\mathbf{x}) . \tag{1.18}$$

The energy eigenstates of the non-interacting double-well system are symmetric $\psi_s(\mathbf{x}) = \frac{1}{\sqrt{2}}[\psi_L(\mathbf{x}) + \psi_R(\mathbf{x})]$ and antisymmetric $\psi_a(\mathbf{x}) = \frac{1}{\sqrt{2}}[\psi_L(\mathbf{x}) - \psi_R(\mathbf{x})]$ combinations [20], however the left/right picture is more useful for the scenario we consider. Inserting this into the Hamiltonian (1.14) using the contact interaction gives,

$$\hat{H} \approx \epsilon_L \hat{a}_L^\dagger \hat{a}_L + \epsilon_R \hat{a}_R^\dagger \hat{a}_R - J\left(\hat{a}_R^\dagger \hat{a}_L + \hat{a}_L^\dagger \hat{a}_R\right) + U\left(\hat{a}_R^\dagger \hat{a}_R^\dagger \hat{a}_R \hat{a}_R + \hat{a}_L^\dagger \hat{a}_L^\dagger \hat{a}_L \hat{a}_L\right) \quad (1.19)$$

where,

$$\epsilon_{L/R} = \int d\mathbf{x}\, \psi_{L/R}^*(\mathbf{x})\left[-\frac{\hbar^2}{2m}\nabla^2 + V(\mathbf{x})\right]\psi_{L/R}(\mathbf{x}) \quad (1.20)$$

$$J = -\int d\mathbf{x}\, \psi_{L/R}^*(\mathbf{x})\left[-\frac{\hbar^2}{2m}\nabla^2 + V(\mathbf{x})\right]\psi_{R/L}(\mathbf{x}) \quad (1.21)$$

$$U = g\int d\mathbf{x}\, |\psi_{L/R}(\mathbf{x})|^4 . \quad (1.22)$$

We have ignored interaction terms in (1.22) which include cross terms of $\psi_{L/R}(\mathbf{x})$, since we expect that the overlap of the wavefunctions in different modes to be very small [20, 21], and have assumed that the interaction energy is well-independent. By making use of the identity $\hat{N} = \hat{a}_L^\dagger \hat{a}_L + \hat{a}_R^\dagger \hat{a}_R$, defining the half-number-difference operator $\hat{n} \equiv (\hat{a}_R^\dagger \hat{a}_R - \hat{a}_L^\dagger \hat{a}_L)/2$, the imbalance or tilt $\Delta\epsilon = \epsilon_R - \epsilon_L$, and neglecting terms which only provide a constant shift in energy,

$$\hat{H}_2 = U\hat{n}^2 - J\left(\hat{a}_R^\dagger \hat{a}_L + \hat{a}_L^\dagger \hat{a}_R\right) + \Delta\epsilon\hat{n} \quad (1.23)$$

A convenient representation of the two-mode Bose-Hubbard Hamiltonian (1.23) involves replacing the bosonic operators with $SU(2)$ spin operators, called the Schwinger boson representation [22, 23],

$$\hat{S}_x = \frac{1}{2}\left(\hat{a}_R^\dagger \hat{a}_L + \hat{a}_L^\dagger \hat{a}_R\right) \quad (1.24)$$

$$\hat{S}_y = \frac{1}{2i}\left(\hat{a}_R^\dagger \hat{a}_L - \hat{a}_L^\dagger \hat{a}_R\right) \quad (1.25)$$

$$\hat{S}_z = \frac{1}{2}\left(\hat{a}_R^\dagger \hat{a}_R - \hat{a}_L^\dagger \hat{a}_L\right) \quad (1.26)$$

noting that the $SU(2)$ relation $\left[\hat{S}_\alpha, \hat{S}_\beta\right] = i\epsilon^{\alpha\beta\gamma}\hat{S}_\gamma$, with $\alpha, \beta, \gamma \in \{x, y, z\}$ and $\epsilon^{\alpha\beta\gamma}$ is the completely antisymmetric tensor, holds. In this representation, the two-mode Bose-Hubbard model becomes a model of spins of total angular momentum $S = N/2$ and quantum number m_s such that spin states can be written as,

$$|S, m_s\rangle = \frac{1}{\sqrt{(S + m_s)(S - m_s)}}\left(\hat{a}_R^\dagger\right)^{S+m_s}\left(\hat{a}_L^\dagger\right)^{S-m_s}|0\rangle \quad (1.27)$$

such that $|S, m_s\rangle$ are the simultaneous eigenstates of $\hat{S}_z$ and $\boldsymbol{S}^2 = \hat{S}_x^2 + \hat{S}_y^2 + \hat{S}_z^2$. We define the critical parameter $\Lambda \equiv UN/2J$, and write the Hamiltonian scaled by the hopping energy,

$$\frac{\hat{H}_2}{J} = \frac{2\Lambda}{N}\hat{S}_z^2 - 2\hat{S}_x + \frac{\Delta\epsilon}{J}\hat{S}_z \ . \tag{1.28}$$

This Hamiltonian takes the form of an infinite-range Ising model with a transverse field via,

$$\hat{S}_\alpha = \frac{1}{2}\sum_i \hat{\sigma}_\alpha^i \ , \tag{1.29}$$

where $\hat{\sigma}_\alpha^i$ are Pauli operators acting only on site i.

The Hamiltonian $\hat{H}_2$ describes a bosonic Josephson junction (BJJ) [21], (so-named since it consists of two weakly-coupled macroscopically quantum states, like a super-conducting Josephson junction), which has been realized experimentally both by using spatially linked BECs [9–11, 24, 25] formed by splitting a single condensate or by internal spin states of a single BEC [26] using ^{87}Rb atoms. The BJJ has also been more recently realized [27] using two spatial modes of an ^{39}K atomic condensate. In addition to analogues of ac and dc Josephson effects [24], the BJJ also displays a phenomenon known as macroscopic quantum self-trapping [20, 28, 29], where a population imbalance between the wells is maintained, provided the initial number difference between the wells is above a critical value.

By tuning Λ, the system described by $\hat{H}_2$ can be brought to different regimes [30]:

(i) Rabi ($\Lambda \ll 1$): Tunnelling term $\hat{a}_R^\dagger \hat{a}_L + \hat{a}_L^\dagger \hat{a}_R$ dominates, atoms display nearly single-particle harmonic oscillations

(ii) Josephson ($1 \ll \Lambda \ll N^2$): Neither term dominates, relatively rich dynamics.

(iii) Fock ($N^2 \ll \Lambda$): Number-difference term $\hat{n}^2$ dominates, eigenstates are approximately Fock states, $\hat{n}|n\rangle = n|n\rangle$

Furthermore, when $\Delta\epsilon = 0$, the system undergoes a $\mathbb{Z}_2$ symmetry-breaking quantum phase transition [32, 33] below $\Lambda_c = -1$ (attractive interactions), where the bosons 'select' a well to occupy macroscopically. It should be noted that self-trapping is different from the symmetry-breaking transition, since it occurs for $\Lambda > 0$ (repulsive interactions).

1.1.3 Bose-Hubbard system coupled to an atomic quantum dot

The system studied in Paper III makes use of the model in Eq. (1.28), coupled to a trapped atomic quantum dot (AQD). In such a system, we require that the AQD be

distinguishable from the BEC atoms, and so we need to introduce a new field operator $\hat{\Phi}$ which we also truncate to two modes,

$$\hat{\Phi} = \hat{d}_u \phi_u(\mathbf{x}) + \hat{d}_d \phi_d(\mathbf{x}) \tag{1.30}$$

where now the two levels are labelled according to the up (u) and down (d) states of the two-level AQD. The AQD operators can be rewritten using an $SU(2)$ Schwinger representation, where since $N = 1$ the operators are simply the Pauli spin operators,

$$\hat{\sigma}_x = \frac{1}{2} \left(\hat{d}_u^\dagger \hat{d}_d + \hat{d}_d^\dagger \hat{d}_u \right) \tag{1.31}$$

$$\hat{\sigma}_y = \frac{1}{2\mathrm{i}} \left(\hat{d}_u^\dagger \hat{d}_d - \hat{d}_d^\dagger \hat{d}_u \right) \tag{1.32}$$

$$\hat{\sigma}_z = \frac{1}{2} \left(\hat{d}_u^\dagger \hat{d}_u - \hat{d}_d^\dagger \hat{d}_d \right) \tag{1.33}$$

In its second-quantized form, the action of the AQD amounts to a coupling of the Hilbert spaces of the condensate and the dot, hence the end result is that operators which couple condensate-dot degrees of freedom therefore take the form $\hat{S}_i \otimes \hat{\sigma}_j$. In the case of an AQD whose states couple only to the hopping energy of the bosons, the Hamiltonian becomes,

$$\hat{H}_D = \frac{2\Lambda J}{N} \hat{S}_z^2 - 2J\hat{S}_x + \Delta\epsilon \hat{S}_z + \beta \hat{S}_x \hat{\sigma}_z - \Delta \frac{(1 + \hat{\sigma}_z)}{2} \tag{1.34}$$

$$= \frac{k_z}{N+1} \hat{S}_z^2 - \alpha_x \hat{S}_x + \alpha_z \hat{S}_z + \beta \hat{S}_x (1 + \hat{\sigma}_z) - \Delta \frac{(1 + \hat{\sigma}_z)}{2} \tag{1.35}$$

where in the second line we have redefined $\alpha_x = 2J - \beta$ and $\alpha_z = \Delta\epsilon$ in order to establish consistency with Paper III. The imbalance between the AQD modes is,

$$\Delta = \int \mathrm{d}\mathbf{x}\, \phi_u^*(\mathbf{x}) \left[-\frac{\hbar^2}{2m} \nabla^2 + V(\mathbf{x}) \right] \phi_u(\mathbf{x}) - \int \mathrm{d}\mathbf{x}\, \phi_d^*(\mathbf{x}) \left[-\frac{\hbar^2}{2m} \nabla^2 + V(\mathbf{x}) \right] \phi_d(\mathbf{x}) , \tag{1.36}$$

while the new coupling parameter is given by,

$$\beta = \int \mathrm{d}\mathbf{x}\, \psi_{R/L}^*(\mathbf{x}) \phi_u^*(\mathbf{x}) \left[-\frac{\hbar^2}{2m} \nabla^2 + V(\mathbf{x}) \right] \phi_u(\mathbf{x}) \psi_{L/R}(\mathbf{x})$$

$$- \int \mathrm{d}\mathbf{x}\, \psi_{R/L}^*(\mathbf{x}) \phi_d^*(\mathbf{x}) \left[-\frac{\hbar^2}{2m} \nabla^2 + V(\mathbf{x}) \right] \phi_d(\mathbf{x}) \psi_{L/R}(\mathbf{x}) \tag{1.37}$$

Similar Hamiltonians have been studied which model an impurity atom or ion [31–35] embedded in the condensate, where interaction terms such as $\hat{S}_z \sigma_z$ and bare σ_z terms exist. By including these terms, the integrability of the system is broken, and the impurity interactions will act as a weak source of chaos in the system [32] (See Section 1.3.4). By only including the terms proportional to $\hat{\sigma}_z$ and $\hat{S}_x \hat{\sigma}_z$ (see Section 1.3.4),

no energy is allowed to exchange between the BEC and the AQD, thus the model remains completely regular.

In the model we consider in Paper III, rather than an impurity embedded in the BEC, a closer picture might be that the AQD sits *between* the wells, such that it has negligible interaction energy between the modes $\psi_{L/R}$, but can affect the tunnelling rate. A similar setup was studied in Ref. [36], where an experiment was proposed such that a single $^+$Yb ion acting as a two-level system can act as a control switch for the tunnelling of the BEC across the junction.

1.1.4 Three-mode Bose-Hubbard model

In Paper IV, we study the Bose-Hubbard model with three modes. The inclusion of the extra mode adds a great deal of complexity to the dynamics, as we shall soon see. In this case, we truncate the field expansion at the third mode,

$$\hat{\Psi}_3(\mathbf{x}) = \hat{a}_1\psi_1(\mathbf{x}) + \hat{a}_2\psi_2(\mathbf{x}) + \hat{a}_3\psi_3(\mathbf{x}) \tag{1.38}$$

which we insert into Eq. (1.14) again using the contact interaction, assuming that the modes $\psi_i(\mathbf{x})$ are each localized in one of three potential wells which can be written as a linear superposition of the hopping eigenmodes of the non-interacting system [37], much like in the double-well. This time, there are far more cross terms, which we again assume are negligible due to small overlap. We have a resulting three-mode Hamiltonian,

$$\hat{H}_3 = -K_L(\hat{a}_1^\dagger\hat{a}_2 + \hat{a}_2^\dagger\hat{a}_1) - K_R(\hat{a}_2^\dagger\hat{a}_3 + \hat{a}_3^\dagger\hat{a}_2) - K_X(\hat{a}_3^\dagger\hat{a}_1 + \hat{a}_1^\dagger\hat{a}_3) \tag{1.39}$$
$$+ \frac{U}{2}\sum_{i=1}^3 \hat{n}_i(\hat{n}_i - 1) + \sum_{i=1}^3 \epsilon_i\hat{n}_i.$$

where now,

$$\epsilon_i = \int d\mathbf{x}\, \psi_i^*(\mathbf{x})\left[-\frac{\hbar^2}{2m}\nabla^2\right]\psi_i(\mathbf{x}) \tag{1.40}$$

$$K_{ij} = -\int d\mathbf{x}\, \psi_i^*(\mathbf{x})\left[-\frac{\hbar^2}{2m}\nabla^2\right]\psi_{j\neq i}(\mathbf{x}) \tag{1.41}$$

$$U = 2g\int d\mathbf{x}\, |\psi_i(\mathbf{x})|^4 . \tag{1.42}$$

where now the hopping amplitudes correspond to $K_L \equiv K_{12} = K_{21}$, $K_R \equiv K_{23} = K_{32}$, and $K_X \equiv K_{13} = K_{31}$. The factor of 2 in the definition of U is simply to fit with existing literature [38–45]. Unlike the dimer, the trimer has the capacity to model different well geometries by adjusting hopping strengths. The two geometries we will

primarily be interested in are the triangular case ($K_L = K_R = K_X$), and the linear trimer ($K_L = K_R$ with $K_X = 0$). Through a Schwinger-type map, there exists an $SU(3)$ representation of the three-mode model [23, 46, 47], which is given by,

$$\hat{Q}_1 = \frac{1}{2} \left(\hat{a}_1^\dagger \hat{a}_1 - \hat{a}_2^\dagger \hat{a}_2 \right) \tag{1.43}$$

$$\hat{Q}_2 = \frac{1}{3} \left(\hat{a}_1^\dagger \hat{a}_1 + \hat{a}_2^\dagger \hat{a}_2 - 2\hat{a}_3^\dagger \hat{a}_3 \right) \tag{1.44}$$

$$\hat{J}_k = \mathrm{i} \left(\hat{a}_k^\dagger \hat{a}_j - \hat{a}_j^\dagger \hat{a}_k \right) \tag{1.45}$$

$$\hat{P}_k = \hat{a}_k^\dagger \hat{a}_j + \hat{a}_j^\dagger \hat{a}_k \tag{1.46}$$

where $k = 1, 2, 3$ and $j = (k + 1)\mathrm{mod}3 + 1$, for which the Hamiltonian (1.39) (for $\epsilon_i = 0$) can be succinctly written,

$$\hat{H}_3 = -K_L \hat{P}_2 - K_R \hat{P}_3 - K_X \hat{P}_1 + \frac{U}{4} \left(4\hat{Q}_1^2 + 3\hat{Q}_2^2 \right) \tag{1.47}$$

however we will only be making use of the boson representation in Paper IV.

The Bose-Hubbard trimer has been studied theoretically in a wide variety of settings, including as a model for adiabatic passage [38, 48–50], where a coherent transfer of particles is achieved between left and right wells (in the system's linear configuration) while the population in the center well remains exponentially suppressed. In the triangular geometry, particles have the ability to 'flow' in a closed loop, and for this reason the trimer has also been studied as a minimal model for a superfluid circuit [44, 51, 52]. The three-mode model is also the shortest chain which exhibits signals of chaos [41, 42, 53, 54], becoming nonintegrable for $U \neq 0$.

1.1.5   Quantum Equations of Motion

The dynamics of the BH dimer and trimer in the basis of Fock states can be calculated via a set of coupled differential equations. We begin with the dimer and write a general state in the Fock basis,

$$|\Psi(t)\rangle = \sum_n C_n(t)|n\rangle \tag{1.48}$$

where $\hat{n}|n\rangle = n|n\rangle$ are the eigenstates of the number difference operator $\hat{n}$, and the time dependent coefficients $C_n(t)$ are generically complex. The Fock basis here only needs a single index n when we assume total particle number is conserved. We insert

this expansion into the time-dependent Schrödinger equation,

$$i\hbar\frac{\partial}{\partial t}\sum_n C_n(t)|n\rangle = \left[U\hat{n}^2 - J\left(\hat{a}_R^\dagger\hat{a}_L + \hat{a}_L^\dagger\hat{a}_R\right) + \Delta\epsilon\hat{n}\right]\sum_n C_n(t)|n\rangle \qquad (1.49)$$

$$= \sum_n C_n(t)\left[Un^2|n\rangle - J\left(\sqrt{\frac{N^2}{4} + \frac{N}{2} - n^2 - n}|n+1\rangle\right.\right. \qquad (1.50)$$

$$\left.\left. + \sqrt{\frac{N^2}{4} + \frac{N}{2} - n^2 + n}|n-1\rangle\right) + \Delta\epsilon n|n\rangle\right].$$

We then assert that the relationship between the right- and left-hand sides must hold true for all members of the sum since the eigenfunction expansion must be unique. Thus, term-by-term,

$$i\hbar\frac{\partial}{\partial t}C_n(t) = (Un^2 + \Delta\epsilon n)C_n(t) - J\left[C_{n-1}(t)\sqrt{\frac{N^2}{4} + \frac{N}{2} - n^2 + n} + C_{n+1}(t)\sqrt{\frac{N^2}{4} + \frac{N}{2} - n^2 - n}\right]$$
$$(1.51)$$

We will be referring to the set of $N + 1$ coupled differential equations, and their three-mode counterparts, as the Raman-Nath equations for the dimer. This is due to their resemblance with the original Raman-Nath equations [55] for the dynamical diffraction of light. In fact, under circumstances when $n \ll N$, we can approximate the square root terms,

$$\sqrt{\frac{N^2}{4} + \frac{N}{2} - n^2 + n} \stackrel{N\gg1}{\approx} \frac{N}{2}, \qquad (1.52)$$

assuming that the dynamics are dominated by states where the wells are macroscopically occupied, set $\Delta\epsilon = 0$, and change variables to $C_n \to (-i)^n C_n$ to recover a set of equations equivalent to Raman and Nath's original set. Unless otherwise noted, we will not be approximating the full Raman-Nath equations given by Eq. (1.51).

In the case of the BH dimer, one can alternatively numerically diagonalize the Hamiltonian and use the eigenstates to find the dynamics. The Raman-Nath equations do, however, allow for a time-dependent Hamiltonian without the need of diagonalization at each time step, so the optimal method is situationally dependent. Exact diagonalization is usually much harder for spin chains with local interactions which has a Hilbert space of size 2^N, whereas for the all-to-all situation represented by the BH dimer the Hilbert space has size $N + 1$. Practically speaking, this means that in the dimer, system sizes can be of the order $N \sim 10^4$ bosons before they are as slow or memory-intensive as an Ising model even with $N = 16$ spins.

For the Bose-Hubbard trimer, we can again derive a set of Raman-Nath equations in the exact same way, however the number of coupled differential equations is

increased. We begin as before by taking a general time-dependent Fock state,

$$|\Psi(t)\rangle = \sum_{n_2, n_X} C_{n_1, n_X}(t) |n_2, n_X\rangle \tag{1.53}$$

where now we have selected $n_X \equiv n_1 - n_3$ to be the number difference between wells 1 and 3. Inserting this into the time-dependent Schrödinger equation,

$$i\hbar \sum_{n_2, n_X} \frac{\partial}{\partial t} C_{n_2, n_X}(t) |n_2, n_X\rangle = \Big[-K_L(\hat{a}_1^\dagger \hat{a}_2 + \hat{a}_2^\dagger \hat{a}_1) - K_R(\hat{a}_2^\dagger \hat{a}_3 + \hat{a}_3^\dagger \hat{a}_2) - K_X(\hat{a}_3^\dagger \hat{a}_1 + \hat{a}_1^\dagger \hat{a}_3) \tag{1.54}$$

$$+ \frac{U}{2} \sum_{i=1}^{3} \hat{n}_i(\hat{n}_i - 1) + \sum_{i=1}^{3} \epsilon_i \hat{n}_i \Big] \sum_{n_2, n_X} C_{n_2, n_X}(t) |n_2, n_X\rangle$$

The diagonal terms are fairly straightforward,

$$\hat{n}_1^2 |n_1, n_3\rangle = \frac{1}{4}(N - n_2 + n_X)^2 |n_1, n_3\rangle \tag{1.55}$$

$$\hat{n}_2^2 |n_1, n_3\rangle = n_2^2 |n_1, n_3\rangle \tag{1.56}$$

$$\hat{n}_3^2 |n_1, n_3\rangle = \frac{1}{4}(N - n_2 - n_X)^2 |n_1, n_3\rangle \ , \tag{1.57}$$

while the hopping terms are slightly more complicated,

$$(\hat{a}_1^\dagger \hat{a}_2 + \hat{a}_2^\dagger \hat{a}_1) |n_2, n_X\rangle = \frac{1}{\sqrt{2}} \sqrt{n_2(N - n_2 + n_X + 2)} |n_2 - 1, n_X + 1\rangle \tag{1.58}$$

$$+ \frac{1}{\sqrt{2}} \sqrt{(N - n_2 + n_X)(n_2 + 1)} |n_2 + 1, n_X - 1\rangle$$

$$(\hat{a}_2^\dagger \hat{a}_3 + \hat{a}_3^\dagger \hat{a}_2) |n_2, n_X\rangle = \frac{1}{\sqrt{2}} \sqrt{(N - n_2 - n_X)(n_2 + 1)} |n_2 + 1, n_X + 1\rangle \tag{1.59}$$

$$+ \frac{1}{\sqrt{2}} \sqrt{n_2(N - n_2 - n_X + 2)} |n_2 - 1, n_X - 1\rangle$$

$$(\hat{a}_3^\dagger \hat{a}_1 + \hat{a}_1^\dagger \hat{a}_3) |n_2, n_X\rangle = \frac{1}{2} \sqrt{(N - n_2 + n_X)(N - n_2 - n_X + 2)} |n_2, n_X - 2\rangle$$

$$+ \frac{1}{2} \sqrt{(N - n_3 - n_X)(N - n_2 + n_X + 2)} |n_2, n_X + 2\rangle \ .$$

Since again we must ensure that the eigenfunction expansion is unique we equate each term in the sum, which amounts to relabelling terms like,

$$C_{n_2, n_X}(t) \sqrt{n_2(N - n_2 + n_X + 2)} |n_2 - 1, n_X + 1\rangle \to C_{n_2+1, n_X-1}(t) \sqrt{(n_2 + 1)(N - n_2 + n_X)} |n_2, n_X\rangle \tag{1.60}$$

etc. Finally, we make a change of variables, $\delta n_2 \equiv n_2 - N/3$ so that our Fock space variables are centred around the origin, $|\delta n_2, n_X\rangle = |0, 0\rangle$. Hence our three-mode

Raman-Nath equations are,

$$
\begin{aligned}
i\hbar\frac{\partial}{\partial t}C_{\delta n_2,n_X}(t) = \; & -\frac{K_L}{\sqrt{2}}\sqrt{\left(\tfrac{N}{3}+\delta n_2+1\right)\left(\tfrac{2N}{3}-\delta n_2+n_X\right)}C_{\delta n_2+1,n_X-1} \\
& -\frac{K_L}{\sqrt{2}}\sqrt{\left(\tfrac{N}{3}+\delta n_2\right)\left(\tfrac{2N}{3}-\delta n_2+n_X+2\right)}C_{\delta n_2-1,n_X+1} \\
& -\frac{K_R}{\sqrt{2}}\sqrt{\left(\tfrac{N}{3}+\delta n_2\right)\left(\tfrac{2N}{3}-\delta n_2-n_X+2\right)}C_{\delta n_2-1,n_X-1} \\
& -\frac{K_R}{\sqrt{2}}\sqrt{\left(\tfrac{N}{3}+\delta n_2+1\right)\left(\tfrac{2N}{3}-\delta n_2-n_X\right)}C_{\delta n_2+1,n_X+1} \\
& -\frac{K_X}{2}\sqrt{\left(\tfrac{2N}{3}-\delta n_2+n_X+2\right)\left(\tfrac{2N}{3}-\delta n_2-n_X\right)}C_{\delta n_2,n_X+2} \\
& -\frac{K_X}{2}\sqrt{\left(\tfrac{2N}{3}-\delta n_2-n_X+2\right)\left(\tfrac{2N}{3}-\delta n_2+n_X\right)}C_{n_2,n_X-2} \\
& +\frac{U}{4}\left[3\delta n_2^2+n_X^2+\frac{\epsilon_1}{2}\left(n_X-\delta n_2\right)+\epsilon_2\delta n_2-\frac{\epsilon_3}{2}\left(n_X+\delta n_2\right)\right]C_{\delta n_2,n_X}\,.
\end{aligned}
\tag{1.61}
$$

The number of coupled differential equations (and thus the size of the Hilbert space) is now $\frac{(N+1)(N+2)}{2}$. The corresponding approximation which assumes that the wells are all macroscopically occupied will approximate each of the square roots as $N/3$ (again, unless otherwise noted, we will not be making use of this approximation). Fock space for the triple-well is triangular due to particle number conservation, and since six hopping terms are possible, it is visually ideal to tile the full two-dimensional Fock space with hexagons representing individual states with well-defined particle numbers as in Fig. 1.1. In Paper IV, we colour the states according to the amplitude $|C_{\delta n_2,n_X}(t)|^2$.

1.1.6   Mean-field theory

The mean-field theory description of each of the models studied above is approached in the same way. Starting from the Hamiltonians written in the original $\hat{a}_i^\dagger$ basis, one can use the 'Heisenberg substitution rules' [28, 29, 57–61] to replace the bosonic operators with complex numbers,

$$
\hat{a}_i \to \sqrt{N_i}e^{i\theta_i} \qquad\qquad \hat{a}_i^\dagger \to \sqrt{N_i}e^{-i\theta_i}\;,
\tag{1.62}
$$

where now N_i is a real number representing the (classical) number of particles in well i, and θ_i is an associated phase.
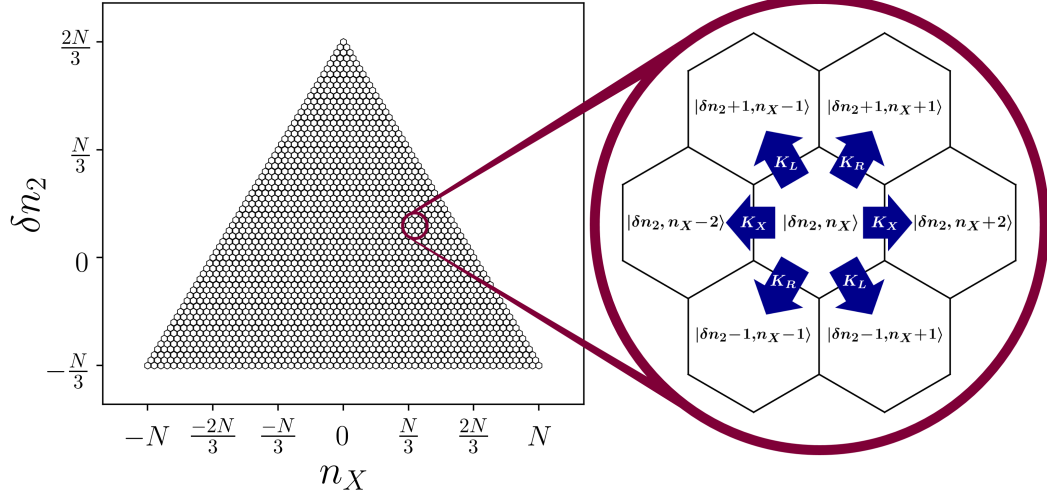
Figure 1.1: Fock space of the triple-well, where the entire Fock space is triangular due to total particle number conservation and the six possible hopping directions allow us to tile the space with hexagons. Zoomed-in portion is from Paper IV (Ref. [56]).

Classical two-mode system

After this substitution, it is relatively straightforward to show that the classical limit of the two-mode model can thus be written (for $\Delta\epsilon = 0$),

$$\frac{H}{NJ} \equiv \mathcal{H}_2 = \frac{\Lambda}{2}z^2 - \sqrt{1 - z^2}\cos\phi \tag{1.63}$$

where, as before $\Lambda = UN/2J$, and we have defined the scaled number-difference $z \equiv (N_R - N_L)/N$ and the phase difference $\phi = \phi_R - \phi_L$. The variables z now lies in the range $[-1, 1]$, such that each extremal value corresponds to all of the particles in the left and right wells, respectively. The Hamiltonian (1.63) corresponds to a nonrigid pendulum [28], where the number difference z plays the role of an angular momentum, the phase difference ϕ becomes the angle of the pendulum, and the length is $\propto \sqrt{1 - z^2}$. Given that z and ϕ are canonically conjugate, one can make use of Hamilton's equations,

$$\dot{z} = -\frac{\partial\mathcal{H}}{\partial\phi} \tag{1.64}$$

$$\dot{\phi} = \frac{\partial\mathcal{H}}{\partial z} \tag{1.65}$$

to therefore find the classical equations of motion for $\mathcal{H}_2$,

$$\dot{z} = -\sqrt{1 - z^2}\sin\phi \tag{1.66}$$

$$\dot{\phi} = \Lambda z + \frac{z\cos\phi}{\sqrt{1 - z^2}} \tag{1.67}$$

The classical solutions of these equations in various regimes of the Bose-Josephson Junction have been studied in Ref. [25, 29]. By making the approximation $z \ll 1$ (i.e. both wells macroscopically occupied), which corresponds to $\sqrt{1 - z^2} \approx 1$, we return to the rigid pendulum Hamiltonian,

$$\mathcal{H}_P = \frac{\Lambda}{2} z^2 - \cos \phi \tag{1.68}$$

This model gives dynamics which are analogous to the Josephson equations [29], and can yield small-amplitude oscillations $\langle \phi \rangle = \langle z \rangle = 0$, called "plasma" oscillations.

There exist modes which oscillate around $\langle z \rangle \neq 0$, indicating the onset of macroscopic quantum self-trapping: bosons tend to clump in one well and only perform small oscillations about the original number difference. These exist above the separatrix: the energy contour separating the states where the pendulum oscillates around the bottom and those for which the pendulum swings completely around. Above a critical Λ, however, there exists motion that is unique to the non-rigid pendulum picture, particularly oscillations about $\langle \phi \rangle = \pi$ but $\langle z \rangle = 0$. These trajectories, called π-oscillations are analogous to a pendulum which is oscillating about its upright position.

Although the rigid pendulum approximation does not allow for π-oscillation trajectories, one can derive an improvement on the 'potential' term in the pendulum case Refs. [29, 58], by first linearizing Eqs. (1.66)-(1.67) in z,

$$\dot{z} = - \sin \phi \tag{1.69}$$

$$\dot{\phi} = \Lambda z + z \cos \phi \tag{1.70}$$

Taking the time derivative of Eq. (1.70) gives $\ddot{\phi} = \Lambda \dot{z} + \dot{z} \cos \phi - z \sin \phi \dot{\phi}$. Inserting $\dot{z}$ and $\dot{\phi}$ and keeping terms of only order less than z^2 gives,

$$\ddot{\phi} = -\Lambda \sin \phi - \sin \phi \cos \phi \tag{1.71}$$

which, integrating over ϕ gives an effective potential term. Combining the above with the fact that the moment of inertia is $2/\Lambda$, the effective Hamiltonian which reproduces the π-oscillations is,

$$\mathcal{H}_\pi = \frac{\Lambda}{2} z^2 - \frac{1}{2\Lambda} \cos^2 \phi - \cos \phi \, . \tag{1.72}$$

Compared to $\mathcal{H}_P$, this new Hamiltonian has an additional local minimum around $\phi = \pi$, effectively "trapping" systems which do not have enough momentum z to escape. This local minimum only exists for $\Lambda < 1$, by tuning to $\Lambda > 1$ there are no possible π-oscillations, however microscopic quantum self trapping is still possible.

Classical two-mode system with an AQD

The AQD modes can be included identically to the boson modes using the substitution rule above. Since a single two-level system is entirely characterized by two real numbers (i.e. two angles on the Bloch sphere), the mean-field theory of the dot becomes quantitatively exact [32]. From (1.35), we have,

$$\mathcal{H}_D = \frac{2}{N}H = \frac{k_z}{2}z^2 - \alpha_x\sqrt{1-z^2}\cos\phi + \alpha_z z - \frac{\Delta}{N}\left(1+\frac{y}{2}\right) + \beta\sqrt{1-z^2}\cos\phi\left(1+\frac{y}{2}\right) \tag{1.73}$$

where now the classical variable y comes from the substitution,

$$\hat{\sigma}_z = \frac{1}{2}\left(\hat{d}_u^\dagger\hat{d}_u - \hat{d}_d^\dagger\hat{d}_d\right) \to \frac{1}{2}(y_u - y_d) \equiv \frac{y}{2}\ , \tag{1.74}$$

and we can simply call the absent conjugate phase variable φ_y. Hamilton's equations of motion follow,

$$\dot{z} = -\frac{\partial\mathcal{H}}{\partial\phi} = -\alpha_x\sqrt{1-z^2}\sin\phi + \beta\sqrt{1-z^2}\sin\phi\left(1+\frac{y}{2}\right) \tag{1.75}$$

$$\dot{\phi} = \frac{\partial\mathcal{H}}{\partial z} = k_z z + \alpha_z + \alpha_x\frac{z\cos\phi}{\sqrt{1-z^2}} - \beta\frac{z\cos\phi}{\sqrt{1-z^2}}\left(1+\frac{y}{2}\right) \tag{1.76}$$

$$\dot{y} = -\frac{\partial\mathcal{H}}{\partial\varphi} = 0 \tag{1.77}$$

$$\dot{\varphi} = \frac{\partial\mathcal{H}}{\partial y} = \frac{\beta}{2}\sqrt{1-z^2}\cos\phi - \frac{\Delta}{2N} \tag{1.78}$$

Classical three-mode system

For the triple-well, we again replace each boson operator with a corresponding complex number $\hat{a}_i \to \sqrt{N_i}e^{i\theta_i}$, the classical Hamiltonian is,

$$N\mathcal{H}_3 = -2K_L\sqrt{n_1 n_2}\cos(\theta_2 - \theta_1) - 2K_R\sqrt{n_2 n_3}\cos(\theta_3 - \theta_2) \tag{1.79}$$

$$- 2K_X\sqrt{n_3 n_1}\cos(\theta_1 - \theta_3) + \frac{U}{2}\sum_{i=1}^{3}n_i(n_i - 1) + \sum_{i=1}^{3}\epsilon_i n_i\ .$$

The process of determining the conjugate coordinates is not as simple as in the double-well case. In Ref. [60], Mossman and Jung use as conjugates $(\phi_L, \phi_R, \varphi_2) \leftrightarrow (n_1, n_3, N)$, where $\phi_L \equiv \theta_1 - \theta_2$ and $\phi_R \equiv \theta_3 - \theta_2$. Therefore, in this coordinate system,

$$\dot{n}_1 = -\frac{\partial H}{\partial\phi_L} \qquad \dot{n}_3 = -\frac{\partial H}{\partial\phi_R} \tag{1.80}$$

(of course $\dot{N} = 0$ due to particle conservation).

However, following our quantum analysis want to use n_X and n_2 as our coordinates, and so we must derive the appropriate conjugate phases, which we shall define to be ϕ_X and ϕ_C, respectively. The remaining classical number coordinate will be $N/3$, which is of course a constant, meaning its conjugate phase Θ does not affect the dynamics at all (in fact it does not even appear in the Hamiltonian).

Begin by taking,

$$\dot{n}_X = \dot{n}_1 - \dot{n}_3 = -\frac{\partial H}{\partial \phi_L} - \left(-\frac{\partial H}{\partial \phi_R}\right) = -\left(\frac{\partial H}{\partial \phi_L} - \frac{\partial H}{\partial \phi_R}\right) \equiv -\frac{\partial H}{\partial \phi_X} \qquad (1.81)$$

By the chain rule, we can replace the derivatives with respect to $\phi_{L/R}$,

$$\frac{\partial H}{\partial \phi_{L/R}} = \frac{\partial H}{\partial \phi_X}\frac{\partial \phi_X}{\partial \phi_{L/R}} + \frac{\partial H}{\partial \phi_C}\frac{\partial \phi_C}{\partial \phi_{L/R}} + \frac{\partial H}{\partial \Theta}\frac{\partial \Theta}{\partial \phi_{L/R}} \ . \qquad (1.82)$$

The derivatives $\left(\frac{\partial H}{\partial \phi_L} - \frac{\partial H}{\partial \phi_R}\right)$ from Eq. (1.81) must, by definition of the conjugate variable Φ_X, not contain any terms with derivatives of the form $\frac{\partial H}{\partial \phi_C}$ or $\frac{\partial H}{\partial \Theta}$, and hence $\frac{\partial H}{\partial \phi_X} = \frac{\partial H}{\partial \phi_X}\left(\frac{\partial \phi_X}{\partial \phi_L} - \frac{\partial \phi_X}{\partial \phi_R}\right)$, for which a possible solution is that $\phi_X \equiv \frac{1}{2}(\phi_L - \phi_R)$. We can double check that this works out via,

$$\dot{\phi}_X = \frac{\dot{\phi}_L - \dot{\phi}_R}{2} = \frac{1}{2}\left(\frac{\partial H}{\partial n_1} - \frac{\partial H}{\partial n_3}\right) = \frac{1}{2}\frac{\partial H}{\partial n_X}\left(\frac{\partial n_X}{\partial n_1} - \frac{\partial n_X}{\partial n_3}\right) = \frac{\partial H}{\partial n_X} \qquad (1.83)$$

Hence $n_X \leftrightarrow \phi_X$ are conjugate.

Next, consider,

$$\dot{n}_2 = -\dot{n}_1 - \dot{n}_3 = \frac{\partial H}{\partial \phi_L} + \frac{\partial H}{\partial \phi_R} \equiv -\frac{\partial H}{\partial \phi_C} \ . \qquad (1.84)$$

Similarly to what we used above, we require that by definition of the conjugate coordinate ϕ_C, all other derivatives of the Hamiltonian with respect to the other angles. Hence $\frac{\partial H}{\partial \phi_C} = \frac{\partial H}{\partial \phi_C}\left(-\frac{\partial \phi_C}{\partial \phi_L} - \frac{\partial \phi_C}{\partial \phi_R}\right)$, for which a solution is $\phi_C \equiv -\frac{1}{2}(\phi_L + \phi_R)$, we then check,

$$\dot{\phi}_C = -\frac{\dot{\theta}_L + \dot{\theta}_R}{2} = -\frac{1}{2}\left(\frac{\partial H}{\partial n_1} + \frac{\partial H}{\partial n_3}\right) = -\frac{1}{2}\frac{\partial H}{\partial n_2}\left(\frac{\partial n_2}{\partial n_1} + \frac{\partial n_2}{\partial n_3}\right) = \frac{\partial H}{\partial n_2} \qquad (1.85)$$

since $n_2 = N - n_1 - n_3$. Hence $\phi_C \leftrightarrow n_2$ are conjugate coordinates. Since particle number is conserved, there is no need to consider the remaining coordinates, however for completeness, we simply state that they are $N/3 \leftrightarrow \Theta$, where the angle $\Theta \equiv \theta_1 + \theta_2 + \theta_3$ does not appear in the Hamiltonian and therefore $\dot{N} = 0$.

We can take the classical Hamiltonian (1.79), replace $n_1 = (N - n_2 + n_X)/2$, $n_3 = (N - n_2 - n_X)/2$ and using our new angle coordinates, $\phi_X = (\theta_1 - \theta_2)/2$

and $\phi_C = -(\theta_1 + 2\theta_2 - \theta_3)/2$. We can define a set of normalized number difference coordinates $z_2 = n_2/N$ and $z_X = n_X/N$ analogous to the double well's z. Finally, we shift to the coordinate $\delta z_2 = z_2 - 1/3$ and define $\tilde{U} \equiv UN$,

$$\mathcal{H}_3 = -\sqrt{2}K_L\sqrt{z_2(1 - z_2 + z_X)}\cos(\phi_X - \phi_C) - \sqrt{2}K_R\sqrt{z_2(1 - z_2 - z_X)}\cos(\phi_X + \phi_C)$$

$$(1.86)$$

$$- K_X\sqrt{(1 - z_2)^2 - z_X^2}\cos(2\phi_X) + \frac{\tilde{U}}{2}\left[3z_2^2 - 2z_2 + z_X^2\right]$$

The classical equations of motion for the trimer are therefore,

$$\dot{z}_X = -K_L\sqrt{2\left(\tfrac{1}{3} + \delta z_2\right)\left(\tfrac{2}{3} - \delta z_2 + z_X\right)}\sin(\phi_X - \phi_C) - K_R\sqrt{2\left(\tfrac{1}{3} + \delta z_2\right)\left(\tfrac{2N}{3} - \delta z_2 - z_X\right)}$$

$$\times \sin(\phi_X + \phi_C) - 2K_X\sqrt{\left(\tfrac{2}{3} - z_2\right)^2 - z_X^2}\cos(2\phi_X) \tag{1.87}$$

$$\dot{\delta z}_2 = K_L\sqrt{2\left(\tfrac{1}{3} + \delta z_2\right)\left(\tfrac{2}{3} - \delta z_2 + z_X\right)}\sin(\phi_X - \phi_C) \tag{1.88}$$

$$- K_R\sqrt{2\left(\tfrac{1}{3} + \delta z_2\right)\left(\tfrac{2}{3} - \delta z_2 - z_X\right)}\sin(\phi_X + \phi_C) \tag{1.89}$$

$$\dot{\phi}_X = \frac{\tilde{U}}{2}z_X - K_L\frac{\left(\tfrac{N}{3} + \delta z_2\right)\cos(\phi_X - \phi_C)}{\sqrt{2\left(\tfrac{1}{3} + \delta z_2\right)\left(\tfrac{2}{3} - \delta z_2 + z_X\right)}} + K_R\frac{\left(\tfrac{1}{3} + \delta z_2\right)\cos(\phi_X + \phi_C)}{\sqrt{2\left(\tfrac{1}{3} + \delta z_2\right)\left(\tfrac{2}{3} - \delta z_2 - z_X\right)}}$$

$$+ K_X\frac{z_X\cos(2\phi_X)}{\sqrt{\left(\tfrac{2}{3} - \delta z_2\right)^2 - z_X^2}} \tag{1.90}$$

$$\dot{\phi}_C = \frac{3\tilde{U}}{2}\delta z_2 - K_L\frac{\left(\tfrac{1}{3} - 2\delta z_2 + z_X\right)\cos(\phi_X - \phi_C)}{\sqrt{2\left(\tfrac{1}{3} + \delta z_2\right)\left(\tfrac{2N}{3} - \delta n_2 + n_X\right)}} - K_R\frac{\left(\tfrac{1}{3} - 2\delta z_2 - z_X\right)\cos(\phi_X + \phi_C)}{\sqrt{2\left(\tfrac{1}{3} + \delta z_2\right)\left(\tfrac{2}{3} - \delta z_2 - z_X\right)}}$$

$$+ K_X\frac{\left(\tfrac{2}{3} - \delta z_2\right)\cos(2\phi_X)}{\sqrt{\left(\tfrac{2}{3} - \delta z_2\right)^2 - z_X^2}}. \tag{1.91}$$

In Paper IV, the classical Hamiltonian and equations are left in terms of n_X and δn_2 in an effort to reduce the confusion of too many changes of variables, however there is also some benefit to making contact with the conventions we used previously in the dimer. If one wanted to make the analogy even more explicit, we could scale the Hamiltonian again by some hopping parameter $K_{L/X/R}$, hence defining a three-mode analogue to Λ.

Between Mean-Field and Many-Body Theory

Next, we can consider a regime in which we wish to extend the classical theory described above to include wave effects, resulting in an intermediate regime which is a continuized version of the full quantum many-body theory, valid as $N \to \infty$ (semiclassical regime). To do so, we promote the number difference $z \to \hat{z}$ and phase difference

$\phi \to \hat{\phi}$ coordinates to operators obeying $[\hat{\phi}, \hat{z}] = 2i/N$, hence in this wave theory N^{-1} becomes a parameter which plays the role of $\hbar$. In the phase representation, this means we can make the correspondence,

$$\hat{\phi} \to \phi \tag{1.92}$$

$$\hat{z} \to -\frac{2i}{N} \frac{\partial}{\partial \phi} \tag{1.93}$$

Let us apply this quantization procedure to Eq. (1.68),

$$\hat{H}_P = -\frac{2\Lambda}{N^2} \frac{\partial^2}{\partial \phi^2} - \cos \phi \ . \tag{1.94}$$

which is sometimes called the *quantum phase model* [58, 59]. We can apply $\hat{H}_P$ to a mean-field wavefunction $\psi(\phi)$, such that the time-independent Schrödinger equation $\hat{H}\psi = E\psi$ can be rearranged to,

$$\psi'' + \left(\frac{N^2}{2\Lambda} E + \frac{N^2}{2\Lambda} \cos \phi \right) \psi = 0 \ . \tag{1.95}$$

Which is the Mathieu equation [63, Eq. 28.2.1],

$$y'' + (a - 2q \cos(2x))y = 0 \tag{1.96}$$

the solutions to which are even $y = \mathcal{C}(a, q, x)$ and odd $y = \mathcal{S}(a, q, x)$ Mathieu functions. Thus, the wavefunction solutions are a superposition of these,

$$\psi = C_1 \mathcal{C} \left(\frac{N^2 E}{2\Lambda}, \frac{N^2}{2\Lambda}, \phi \right) + C_2 \mathcal{S} \left(\frac{N^2 E}{2\Lambda}, \frac{N^2}{2\Lambda}, \phi \right) \tag{1.97}$$

where C_1 and C_2 are constants.

Performing a similar quantization procedure on Eq. (1.72), we have,

$$\hat{H}_\pi = -\frac{2\Lambda}{N^2} \frac{\partial^2}{\partial \phi^2} - \frac{1}{2\Lambda} \cos^2 \phi - \cos \phi \ . \tag{1.98}$$

This has been dubbed the *exact* quantum phase model [58], and can also be derived by making use of an overcomplete set of 'Bargmann' phase states in the limit of large N.

The corresponding Schrödinger equation can be rearranged in the form,

$$\psi''(\theta) + \left[\frac{N^2}{4\Lambda^2} \cos^2 \theta + \frac{N^2}{2\Lambda} \cos \theta + \frac{N^2}{4\Lambda^2} (2\Lambda E - 1) \right] \psi(\theta) = 0 \ , \tag{1.99}$$

In this type of differential equation, the potential $V(\theta)$ is sometimes referred to as the trigonometric Razavy potential [62]. In its current form, Eq. (1.99) is a differential equation known as the Whittaker-Hill equation [63, Eq. 28.31.1],

$$y'' + \left(A + \frac{c^2 k^2}{2} + B \cos 2x - c^2 k^2 \cos^2 2x \right) y = 0 \ , \tag{1.100}$$

which is also related to the Ince equation [64, 65] through a change of variables, and can thus be solved by Ince polynomials.

1.1.7   Spin chains

Models of spin-$\frac{1}{2}$ chains can also be put into a form which mimics a tight-binding model by mapping spin degrees of freedom to fermionic operators using the Jordan-Wigner transformation [16, 18]. The correspondence is relatively simple, an "up" state can be represented by a vacant single-particle state while a "down" state can correspond to a filled state,

$$| \downarrow \rangle \leftrightarrow |1\rangle = \hat{c}^\dagger|0\rangle \qquad\qquad | \uparrow \rangle \leftrightarrow |0\rangle \qquad\qquad (1.101)$$

and since the notion of a doubly-occupied state would make no sense in the spin language, we require that the operators are fermionic: $\{c_i^\dagger, c\} = \delta_{ij}$. Unfortunately, naively replacing spin operators with linear combinations of $\hat{c}_i^\dagger$ and $\hat{c}_i$ will fail to reproduce the fact that angular momentum operators on different sites commute. Thus, the anti-commutative property of fermionic operators must be countered by a string operator $e^{i\pi\sum_{j<i}\hat{c}_j^\dagger\hat{c}_j}$ which counts the fermion occupancy and ensures the system is symmetric under exchange on different sites. Following Sachdev's [66] convention that the down and up states in the $\hat{\sigma}^x$ basis correspond to occupied and empty states, respectively, we can then define,

$$\sigma_i^x = 1 - 2c_i^\dagger c_i. \qquad\qquad (1.102)$$

$$\sigma_i^y = i(c_i - c_i^\dagger)\prod_{j<i}(1 - 2c_j^\dagger c_j) = i(c_i - c_i^\dagger)e^{i\pi\sum_{j<i}c_j^\dagger c_j} \qquad\qquad (1.103)$$

$$\sigma_i^z = -(c_i + c_i^\dagger)\prod_{j<i}(1 - 2c_j^\dagger c_j) = -(c_i + c_i^\dagger)e^{i\pi\sum_{j<i}c_j^\dagger c_j}. \qquad\qquad (1.104)$$

This transformation is particularly useful for mapping spin chains into non-interacting fermion models [67], which we will outline here for the transverse-field Ising model (TFIM) (the XY model is outlined in the appendices of Paper I). The TFIM with neareast-neighbour interactions is,

$$\hat{H}_{\text{TFIM}} = -J\sum_i \sigma_i^z \sigma_{i+1}^z - h\sum_i \sigma_i^x, \qquad\qquad (1.105)$$

where J corresponds to a spin-spin interaction (ferromagnetic for $J > 0$) and h an applied external field. This Hamiltonian was originally considered by de Gennes [68] in 1963 as a low-energy model of proton modes in KH_2SO_4, and was first treated as

a model for magnetism and solved by Pfeuty [69] using the Jordan-Wigner transformation in 1969. By making the replacements (1.102)-(1.104), we get,

$$\hat{H}_{\text{TFIM}} = -J \sum_j \left(c_j^\dagger c_{j+1}^\dagger + c_j^\dagger c_{j+1} + c_{j+1}^\dagger c_j + c_{j+1} c_j - 2g c_j^\dagger c_j \right) \tag{1.106}$$

where $g = h/J$. In transforming from Eq. (1.105) to (1.106), many terms have been simplified using identities of fermionic operators, $(1 - 2c_j^\dagger c_j)^2 = c_j^\dagger c_j^\dagger = c_j c_j = 0$, and dropping constant shifts in energy $\propto N$. Now we have a Hamiltonian which is entirely quadratic in fermion operators, however it includes terms which do not conserve fermion number. Since the original model is translation-invariant, momentum becomes a good quantum number. Hence, it is more convenient to work in momentum space by defining,

$$\tilde{c}_k = \frac{1}{\sqrt{N}} \sum_j c_j e^{-\mathrm{i}kja} , \tag{1.107}$$

where a is the lattice spacing. With this, the Hamiltonian can be written conveniently in matrix form,

$$\hat{H}_{\text{TFIM}} = J \sum_k \begin{pmatrix} \tilde{c}_k^\dagger & \tilde{c}_{-k} \end{pmatrix} \begin{pmatrix} g - \cos(ka) & -\mathrm{i}\sin(ka) \\ \mathrm{i}\sin(ka) & -(g - \cos(ka)) \end{pmatrix} \begin{pmatrix} \tilde{c}_k \\ \tilde{c}_{-k}^\dagger \end{pmatrix} \tag{1.108}$$

The final step is to make use of the Bogoliubov transformation [70] (originally developed for the theory of superfluidity with bosonic operators [71], but extended to fermions via BCS theory [72]),

$$\tilde{b}_k^\dagger = u_k \tilde{c}_k^\dagger + \mathrm{i} v_k \tilde{c}_{-k} \tag{1.109}$$

where the fermionic anticommutation rules $\{\tilde{c}_k^\dagger, \tilde{c}_{k'}\} = \delta_{kk'}$, and $u_k = u_{-k}$, $v_k = -v_{-k}$ require that $u_k^2 + v_k^2 = 1$, allowing us to define $u_k \equiv \cos(\phi_k/2)$ and $v_k \equiv \sin(\phi_k/2)$. Then, by ensuring the off-diagonal elements of the Hamiltonian vanish in the Bogoliubov basis, we require that $\tan \phi_k = \sin(ka)/(\cos(ka) - g)$, and thus,

$$\hat{H}_{\text{TFIM}} = \sum_k \epsilon_k \left(\tilde{b}_k^\dagger \tilde{b}_k - \frac{1}{2} \right) \tag{1.110}$$

with $\epsilon_k = 2J\sqrt{g^2 - 2g\cos(ka) + 1}$, and the sum over k runs from $-\frac{\pi}{a}$ to $\frac{\pi}{a} - \frac{2\pi}{Na}$. The resulting Hamiltonian represents free fermions in a 'rotated' operator basis, meaning the corresponding position-space Bogoliubov fermions $\hat{b}_i$ can only hop lattice sites and do not interact. Because of the rotation, a direct interpretation of the position space fermions in terms of spin operators is not simple, however we can view them as quasiparticle excitations of the system which travel through the chain. Thus,

perturbing a spin chain at some position x_i amounts to the creation of one (or more) quasiparticles $\hat{b}_i$ which propagate at a finite velocity and spread information of the perturbation throughout the system.

Before considering an example of dynamics in the system, we note that the Bogoliubov transformation is model-dependent since u_k and v_k depend implicitly on the interaction and field strengths. The nature of the transformation also requires that the vacuum in the Jordan-Wigner basis also be different from the vacuum in the Bogoliubov basis since,

$$\tilde{c}_k|0\rangle_{\text{JW}} = 0 , \qquad \text{then,} \qquad \tilde{b}_k|0\rangle_{\text{JW}} = \left(u_k\tilde{c}_k^\dagger + iv_k\tilde{c}_{-k} \right)|0\rangle_{\text{JW}} = u_k\tilde{c}_k^\dagger|0\rangle_{\text{JW}} \neq 0 . \tag{1.111}$$

thus one must construct the Bogoliubov vacuum $|0\rangle_{\text{B}}$. In order to do this, choose an ansatz $|0\rangle_{\text{B}} = (\alpha_1 + \alpha_2\tilde{c}_k^\dagger\tilde{c}_{-k}^\dagger)|0\rangle_{\text{JW}}$ (motivated by the vacuum having zero net momentum), then enforcing $0 = \tilde{b}_k|0\rangle_{\text{B}}$ gives $\alpha_2/\alpha_1 = iv_k/u_k$, hence,

$$|0\rangle_{\text{B}} = \prod_{k>0} \left(u_k + iv_k\tilde{c}_k^\dagger\tilde{c}_{-k}^\dagger \right)|0\rangle_{\text{JW}} = \prod_{k>0} u_k \, e^{i\frac{v_k}{u_k}\tilde{c}_k^\dagger\tilde{c}_{-k}^\dagger}|0\rangle_{\text{JW}} . \tag{1.112}$$

One must take care here, since if the momenta had been selected such that they are in pairs $\pm|k|$ over the entire Brillouin zone, there is a double counting problem which leads to

$$\tilde{b}_k|0\rangle_{\text{JW}} = \left(u_k\tilde{c}_k - iv_k\tilde{c}_{-k}^\dagger \right) \prod_{k'} \left(u_{k'} + iv_{k'}\tilde{c}_{k'}^\dagger\tilde{c}_{-k'}^\dagger \right)|0\rangle_{\text{JW}} \tag{1.113}$$

$$= iv_ku_k^2\tilde{c}_{-k}^\dagger \prod_{k'\neq\pm k} \left(u_{k'} + iv_{k'}\tilde{c}_{k'}^\dagger\tilde{c}_{-k'}^\dagger \right)|0\rangle_{\text{JW}} \neq 0 . \tag{1.114}$$

If the product is chosen to run only over half the Brillouin zone, $k' \in [0, \pi/a)$, then the double counting problem is eliminated.

Before we discuss the dynamics of spin-chains, let us first briefly examine how the procedure outlined above affects more general spin systems. The Heisenberg XXZ model is [16, 23],

$$\hat{H}_{\text{H}} = -J\sum_i \left[\hat{\sigma}_i^x\hat{\sigma}_{i+1}^x + \hat{\sigma}_i^y\hat{\sigma}_{i+1}^y \right] - J_z\sum_i \hat{\sigma}_i^z\hat{\sigma}_{i+1}^z , \tag{1.115}$$

In this case, however there is no transformation which eliminates all fermion interactions, and we are left with[1] [16],

$$\hat{H}_{\text{H}} = \sum_k \omega_k\tilde{c}_k^\dagger\tilde{c}_k - \frac{J_z}{N}\sum_{k,k',q} \cos(qa)\tilde{c}_{k-q}^\dagger\tilde{c}_{k'+q}^\dagger\tilde{c}_{k'}\tilde{c}_k \tag{1.116}$$

---

[1]To arrive at this form of the Hamiltonian, it is more convenient to choose a Jordan-Wigner basis such that $\sigma_i^z = 2\hat{c}_i^\dagger\hat{c}_i - 1$, etc. See Coleman [16] Chapter 4. The principle and process remains the same.

where now the second sum now indicates that the quasiparticles are interacting. This model remains integrable, however, but must be solved using the Bethe ansatz [73,74]. In the limit $J_z = 0$ the model reduces to an XY chain (studied in Paper I with an additional transverse field), the quasiparticles no longer interact, and therefore the system can again be solved using the methods above. In the XY limit, no Bogoliubov transformation is required, and thus this additional step is only necessary in the presence of a transverse field.

The addition of a longitudinal (i.e. in the same direction as the spin-spin interaction) magnetic field term,

$$\hat{H}_{\text{LTFIM}} = -J \sum_i \sigma_i^z \sigma_{i+1}^z - h \sum_i \sigma_i^x - b \sum_i \sigma_i^z \ , \tag{1.117}$$

breaks the integrability of the TFIM, and similarly with Heisenberg models. This system cannot be solved with either the Jordan-Wigner transformation nor the Bethe ansatz, and is chaotic [75].

1.1.8 Light-cones and the Lieb-Robinson Bound

In 1972, Elliot Lieb and Derek Robinson demonstrated [77] that operator growth across quantum systems which obey the Schrödinger equation has a speed limit according to,

$$\left|\left|\left[\hat{A}(t), \hat{B}\right]\right|\right| \leq c \exp\left[-q\left(\text{dist}(\mathcal{A}, \mathcal{B}) - v_{LR}|t|\right)\right] \ . \tag{1.118}$$

This limit is called the Lieb-Robinson (LR) bound. $\hat{A}(t)$ and $\hat{B}$ are operators with local support on $\mathcal{A}$ and $\mathcal{B}$, respectively, q and c are model-dependent constants, t is time, and v_{LR} is the Lieb-Robinson velocity. The operator norm $||\hat{O}||$ is defined by,

$$||\hat{O}|| = \sup\left[\sqrt{|\langle v|\hat{O}^\dagger \hat{O}|v\rangle|}\right] \tag{1.119}$$

which, for our purposes, is equal to the square root of the largest eigenvalue of $\hat{O}$. The function $\text{dist}(\mathcal{A}, \mathcal{B})$ measures the shortest distance between sets $\mathcal{A}$ and $\mathcal{B}$. For example, in a spin chain, let's say the set $\mathcal{A}$ contains only site i, and $\mathcal{B}$ contains the sites $i+5$ through $i+10$, $\text{dist}(\mathcal{A}, \mathcal{B}) = 5$. For a relatively lucid proof of the LR bound, see Ref. [76].

The main consequence of Eq. (1.118) is that for systems which have interactions which are sufficiently short range, there is a maximal, non-universal model-dependent, speed at which physical perturbations can propagate, above which they will be exponentially suppressed. The exact nature of what it means to be 'sufficiently' short

ranged was originally an exponential decay of interactions [77], which must result in a linear $t = x/v_{LR}$ bound for this region, or a *quantum light cone*. Recently, extensions of the LR bound to include long-range inverse-power-law interactions, which can either result in a linear light cone [78–81] or a curved light cone with speed between $t \sim \log x$ and $t \sim x^{\xi}$ [78, 82], where $0 < \xi < 1$, which implies that there is an acceleration of the causal boundary.

When we concern ourselves with models which can be mapped to free-particles with dispersion ϵ_k, such as the cases with the Bogoliubov fermions in the TFIM or XY models, then one can straightforwardly calculate v_{LR} by maximizing the group velocity of the quasiparticles [83],

$$v_{LR} = \max_k \left| \frac{\partial \epsilon_k}{\partial k} \right| \tag{1.120}$$

This will provide us with a motivation to connect quantum light cones with caustics in Paper I.

Experiments with ultracold atoms and ions have demonstrated the presence of light cones in quantum systems. In Ref. [12], Cheneau *et al.* demonstrate that a long Bose-Hubbard chain at half-filling can be quenched from the Mott-insulator phase to a superfluid phase, inducing pairwise doublon-holon quasiparticles which propagate through the system as a light cone. Other experiments [13, 84] with ions demonstrate the presence of linear cones, flared non-linear cones, and the absence of cones in as the interactions are tuned to the long-range limit in one-dimensional quantum systems.

1.2 Catastrophe theory and caustics

Chapters 2, 3, and 5 (Papers I, II, and IV, respectively)are concerned with caustics in the dynamics many-body systems. A *caustic* is an envelope of classical rays, which, when considering the geometrical theory of light, corresponds to bright regions of intense focusing. Caustics are everyday events, and can be seen as the cusp at the bottom of a cup, as bright lines at the bottom of swimming pools, and rainbows [85]. Caustics have been studied for centuries, with the earliest surviving drawing of a cusp caustic appearing in a journal by Leonardo da Vinci in c. 1508 [86], and even an early (albeit incorrect) attempt to describe a fourfold-cusped caustic later known as 'Leonardo's cross' [87], but we shall come to understand that is the high-order catastrophe X_9. Non-optical examples include ship's wakes [88], shock waves and sonic booms [89], and more recently the formation of caustics in a BEC through aberrated lenses [90] and in atom optics experiments [91–95].

In contrast to the cases considered above, we are interested in the existence of caustics as a quantum many-body phenomenon. In the systems we study in Papers I, II, and IV, the caustics exist in Fock space, and the overlying diffraction patterns become true many-body fringes in a fundamentally discrete space. We posit that these caustics are a for of universality in quantum dynamics, whose appearance, structure, and stability are governed by catastrophe theory.
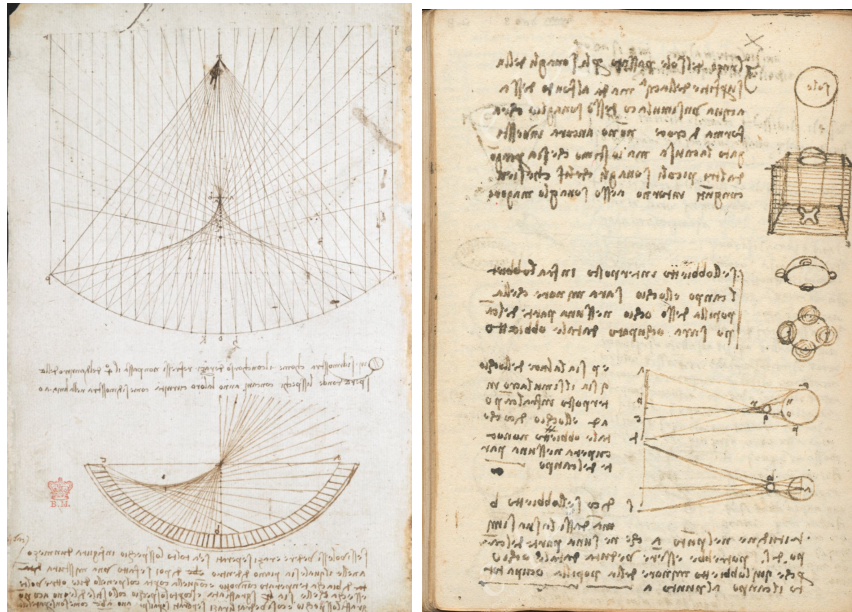

Figure 1.2: da Vinci's caustic drawings [86]. The left drawing corresponds to the earliest known portrayal of a caustic formed by a geometric ray theory of light. The right image features a sketch of a fourfold cusped shape 'Leonardo's cross', formed by light focusing through a bubble.

The mathematical foundations for the categorization of these caustics were laid by René Thom and Vladimir Arnol'd in the late 1960s and early 1970s [97, 98] via catastrophe theory (CT). In general, focusing events can be stable or unstable, and it is the stable ones which are more generic in nature and hence shall be of greater interest to us. Here, we outline the necessary details of CT which we will need to study the systems mentioned in the previous section. The full derivations of many proofs in CT are far beyond the scope of this thesis, however we will present instructive examples while making use of its core results. Most importantly, we will be making use of Thom's theorem, which guarantees universal local forms of functions around a degenerate stationary point. When considering gradient maps, these degenerate stationary points are often sources of singularities, for example, the failure of the WKB approximation around a turning point or at a region of focused classical rays. Finally, building on the work of Thom and Arnol'd, Michael Berry and John

Nye applied CT to physical optics, paving the way for 'catastrophe optics' [85, 99], which ultimately introduces a hierarchy of diffraction patterns which smooth out the catastrophe singularities.

1.2.1 Key theorems

For some function $f : \mathbb{R}^n \to \mathbb{R}$, we say the point $\mathbf{x}^*$ is a *stationary* point of f if,

$$\nabla f|_{\mathbf{x}^*} = \left. \frac{\partial f}{\partial x_1} \right|_{x_1^*} = ... = \left. \frac{\partial f}{\partial x_n} \right|_{x_n^*} = 0 \tag{1.121}$$

The stationary point $\mathbf{x}^*$ is a *degenerate* stationary point if the above is true and,

$$\det \left[Hf|_{\mathbf{x}^*} \right] = 0 \tag{1.122}$$

where the Hessian matrix of f is defined,

$$Hf = \frac{\partial^2 f}{\partial x_i \partial x_j} \ . \tag{1.123}$$

In one dimension ($n = 1$), such a point is typically called a point of inflexion, which occurs when two stationary points (a maximum and a minimum) merge.

The implicit function theorem

Suppose there exists a function $f(\mathbf{x}) : \mathbb{R}^n \times \mathbb{R}^m \to \mathbb{R}$, then [89],

Theorem. *For some smooth function $f(\boldsymbol{x}, \boldsymbol{y}) : \mathbb{R}^n \times \mathbb{R}^m \to \mathbb{R}$, if $f(\boldsymbol{x}_0, \boldsymbol{y}_0) = 0$ and $\nabla f|_{(\boldsymbol{x}_0, \boldsymbol{y}_0)} \neq 0$ (i.e. the Jacobian matrix is invertable), then $f(\boldsymbol{x}_0, \boldsymbol{y}_0)$ is locally the graph of a smooth function $y = \tilde{y}(\boldsymbol{x})$.*

Practically speaking, the implicit function theorem simply gives the conditions under which one can write $y = \tilde{y}$, meaning that under the appropriate smooth change of variables, one can locally write f as a linear function in a neighbourhood of this point [96]. Furthermore, under this appropriate change of variables, there is only one direction that has a nonzero gradient. Since in physics, the function f typically is represented by an action or potential, the condition $f(\mathbf{x}_0, \mathbf{y}_0) = 0$ is achieved by a translation of the origin which does not affect the dynamics.

The Morse lemma

Lemma. *For some non-degenerate stationary point $\boldsymbol{x}^*$ of the smooth function $f : \mathbb{R}^n \to \mathbb{R}$, there exists a local coordinate system in a neighbourhood of $\boldsymbol{x}^*$ such that*

$s_i(\boldsymbol{x}^*) = 0$ *and,*

$$f = f(\boldsymbol{x}^*) - s_1^2 - s_2^2 - \ldots - s_\ell^2 + s_{\ell+1}^2 + \ldots + s_n^2 \ . \tag{1.124}$$

Also implicitly included is the fact that under the smooth change of variables, the coefficients which would naturally arise from the Taylor series around the stationary point are absorbed into the new coordinates s_i such that now each coefficient is simply ± 1. The signs of the coefficients indicates whether the we are in a local maximum ($\ell = n$), minimum ($\ell = 0$), or saddle ($0 < \ell < n$). Again, in physical problems, f typically represents some potential or action, hence a global coordinate change will effectively set $f(\mathbf{x}^*) = 0$.

The splitting lemma and Thom's theorem

If $\mathbf{x}^*$ is a degenerate stationary point, i.e. if $\det\left[Hf|_{\mathbf{x}^*}\right] = 0$, then a generalization of the Morse lemma is required.

Lemma. *For a smooth function $f : \mathbb{R}^n \to \mathbb{R}$ with $Df|_{\boldsymbol{x}^*} = 0$, and with a Hessian of rank r at $\boldsymbol{x}^*$, then under an appropriate smooth change of variables,*

$$f = \pm s_1^2 \pm \ldots \pm s_r^2 + \Phi_{NM}(s_{r+1}, \ldots, s_n) \ . \tag{1.125}$$

Here, Φ_{NM} is a 'non-Morse' function.

Essentially, the lemma states that we can take the r coordinates contributing to the non-degenerate part and write them in a quadratic form (this quadratic form is sometimes called 'Morse' form), while moving the $n - r$ coordinates contributing to degeneracy to some as-of-yet unknown function Φ_{NM}. This allows the important behaviour of the critical point to be studied by only considering $n-r$ variables, rather than all n coordinates.

Finally, Thom's theorem [96, 97] states that at a degenerate critical point, the only structurally stable non-Morse functions are the 'catastrophes' listed in Table 1.1. Each of these contains a catastrophe germ and a perturbation,

$$\Phi_{\mathrm{NM}} = \Phi_Q(\mathbf{s}; \mathbf{C}) = \mathrm{Germ}(\mathbf{s}) + \mathrm{Pert}(\mathbf{s}, \mathbf{C}) \ . \tag{1.126}$$

The catastrophe germ is only a function of the local coordinates $\mathbf{s}$ and contains information about the degree of degeneracy of the stationary point, hence it is the source of the singularity. The perturbation corresponds to terms which together 'stabilize' the catastrophe function, and is a function of both $\mathbf{s}$ and a set of coordinates called 'state

Catastrophe	Symbol	Corank	Q	$\Phi_Q(\mathbf{s}; \mathbf{C})$
Fold	A_2	1	1	$s^3 + Cs$
Cusp	A_3	1	2	$s^4 + C_2 s^2 + C_1 s$
Swallowtail	A_4	1	3	$s^5 + C_3 s^3 + C_2 s^2 + C_1 s$
Butterfly	A_5	1	4	$s^6 + C_4 s^4 + C_3 s^3 + C_2 s^2 + C_1 s$
Hyperbolic Umbilic	D_4^+	2	3	$s_1^3 + s_2^3 + C_3 s_1 s_2 + C_2 s_2 + C_1 s_1$
Elliptic Umbilic	D_4^-	2	3	$3 s_1^2 s_2 - s_2^3 + C_3 (s_1^2 + s_2^2) + C_2 s_2 + C_1 s_1$
Parabolic Umbilic	D_5	2	4	$s_2^4 + s_1^2 s_2 + C_4 s_2^2 + C_3 s_1^2 + C_2 s_2 + C_1 s_1$

Table 1.1: Thom's seven elementary catastrophes, their symbols, and generating functions $\Phi_Q(\mathbf{s}; \mathbf{C})$, organized by corank n, and codimension Q. This table has been adapted from the Paper IV (Ref. [56]).

variables' $\mathbf{C}$. The process of including the perturbation is called the 'unfolding' of the singularity. The number of state variables is called the codimension of the catastrophe, which we indicate by Q, and depends directly on the degree of degeneracy of the non-Morse stationary point. Important note for Papers I and IV: we take a slightly different notation such that the corank is labeled by n, since we're not interested in the r extra coordinates.

Thom's theorem is powerful: it states that local to a degenerate critical point, we can approximate a function entirely by a quadratic piece and a universal non-Morse piece which is uniquely determined by the nature of the singularity. It is, however, qualitative in that it does not tell us the exactly which appropriate coordinates to choose from, and that different functions with the same type of singularity will locally be equivalent under this classification [96] (however again, the coordinate transformations may vary). Each catastrophe is given a group-theoretic symbol according to its connection to reflection-generated groups as introduced by Vladimir Arnol'd [98]. We will simply use these symbols as identifiers for catastrophes which do not have widely-accepted names.

The list of seven elementary catastrophes in Table 1.1 was considered by Thom, however, Arnol'd showed it can be extended for higher codimension $Q > 5$, higher corank $n - r$ and higher dimension of codomain for f (i.e. for $f : \mathbb{R}^n \to \mathbb{R}^m$ with $m > 1$). Arnol'd classified all non-Morse germs for $Q \leq 10$, $(Q + m + 1) \leq 16$ and $m \leq 2$ [96]. We shall only make use of a few of these, however, we list many of them in Table 1.2. For catastrophes beyond $Q = 5$, there begin to exist germs which contain an extra parameter which is not a member of the control space $\mathbf{C}$. This extra parameter, called a 'modulus', cannot be scaled away by any smooth change

Symbol	Corank	$\Phi_Q(\mathbf{s}; \mathbf{C})$
A_{Q+1}	1	$s^{Q+2} + \sum_{i=1}^{Q-1} C_i s^i$
$D_{Q+1}^{\pm}$	2	$s_1^Q \pm s_1 s_2^2 + C_{Q+1}s_2^2 + \sum_{i=2}^{Q-1} C_i s_1^i + C_1 s_2$
E_6	2	$s_1^3 + s_2^4 + C_5 s_1 s_2^2 + C_4 s_2^2 + C_3 s_1 s_2 + C_2 s_2 + C_1 s_1$
E_7	2	$s_1^3 + s_1 s_2^3 + C_6 s_2^4 + C_5 s_2^3 + C_4 s_2^2$ $+C_3 s_1 s_2 + C_2 s_1 + C_1 s_2$
E_8	2	$s_1^3 + s_2^5 + C_7 s_1 s_2^3 + C_6 s_1 s_2^2 + C_5 s_2^3$ $+C_4 s_1 s_2 + C_3 s_2^2 + C_2 s_1 + C_1 s_2$
$X_9^{\pm}$	2	$s_2^4 + K s_1^2 s_2^2 \pm s_1^4 + C_7 s_2^2 s_1 + C_6 s_2 s_1^2$ $+C_5(s_2^2 + s_1^2) + C_4(s_2^2 - s_1^2)$ $+C_3 s_2 s_1 + C_2 s_2 + C_1 s_1$

Table 1.2: Higher-order catastrophes beyond Thom's seven appearing in Table 1.1. General cuspoids and umbilics are listed as A_{Q+1} and $D_{Q+1}^{\pm}$, respectively. This table has also been adapted from the Paper IV (Ref. [56]).

of variables and is first found in the X_9 catastrophe [85, 100] corresponding to the variable K. As we shall see, different values of K can lead to structurally distinct sections of the catastrophes.

We note that precise definition of each catastrophe function varies, up to a smooth change of variables, generally according to the author's taste. For example, sometimes catastrophes are defined with different coefficients,

$$\Phi_1 = \frac{1}{3}s^3 + Cs \tag{1.127}$$

$$\Phi_2 = \frac{1}{4}s^4 + \frac{1}{2}C_2 s^2 + C_1 s \tag{1.128}$$

$$\vdots$$

or by a rotation of coordinates, like the Hyperbolic Umbilic, which can also be written,

$$\Phi_3^{\mathrm{H}} = s_1^2 s_2 + s_2^3 + C_3 s_1^2 + C_2 s_2 + C_1 s_1 \tag{1.129}$$

In this thesis we shall use those listed in the Tables 1.1-1.2, unless otherwise noted.

1.2.2 Geometry of catastrophes

In this section, we will examine the structure of each of Thom's elementary catastrophes, with the exception of the butterfly and parabolic umbilic since (i) the general procedure is unchanged, and (ii) they will not be appear for the remainder of the thesis. We will also introduce and examine the high-order catastrophe X_9. We begin with the cuspoids, which are corank-1 catastrophes whose catastrophe germs are s^{Q+2} with successively higher codimension Q.

Fold

The generating function of the fold is,

$$\Phi_1 = s^3 + Cs \ . \tag{1.130}$$

The first derivative gives,

$$\frac{d\Phi_1}{ds} = 3s^2 + C \tag{1.131}$$

and the second derivative,

$$\frac{d^2\Phi_1}{ds^2} = 6s \tag{1.132}$$

Solving $\frac{d\Phi_1}{ds} = \frac{d^2\Phi_1}{ds^2} = 0$ gives a singular point $x = C = 0$. The equation (1.131) reveals that the bifurcation set is a single point, $C = 0$, which divides the full control space into two regions: a region where two stationary points of the generating function exist $(C < 0)$, and a region where no such points exist $(C > 0)$, see Fig. 1.3.
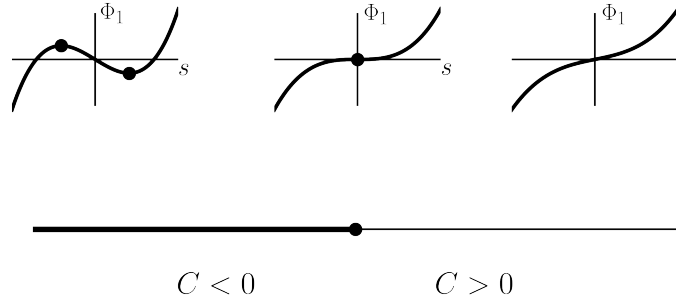

Figure 1.3: Geometry of the fold. Snapshots of generating function Φ_1 are plotted at three different points over the control space. The stationary points of the generating function coalesce and annihilate at $s = 0$ as the point $C = 0$ is crossed.

The fold is the simplest and most common catastrophe. Examples of the fold include rainbows, ships' wakes, and as we will discuss in Papers I and II, quantum light cones. In the case of rainbows, classical light rays exist for an observer looking between roughly $40° - 42°$ (depending on the colour) and the ground, while none exist above, where the no rays exist [85]. The ray which marks the fold is called the 'Descartes ray' and is the brightest point in the rainbow.

Cusp

The cusp generating function is,

$$\Phi_2 = s^4 + C_2 s^2 + C_1 s \ . \tag{1.133}$$

With caustic conditions,

$$\frac{d\Phi_2}{ds} = 4s^3 + 2C_1 s + C_2 = 0 \tag{1.134}$$

and,

$$\frac{d^2\Phi_2}{ds^2} = 12s^2 + 2C_1 = 0 \tag{1.135}$$

Eq. (1.135) yields the condition $s = \pm\sqrt{C_2/6}$, and inputting into Eq. (1) gives,

$$C_1 = \pm\sqrt{\frac{8}{27}}(-C_2)^{3/2} \tag{1.136}$$

which gives a cusped curve in the control space, shown in Fig. 1.4. Away from the origin, the curves described by Eq. (1.136) indicate where a pair of stationary points in the generating function coalesce (and hence describe fold lines), and it is only at the highly singular origin $C_1 = C_2 = 0$ where the fold lines meet and all three stationary points annihilate.
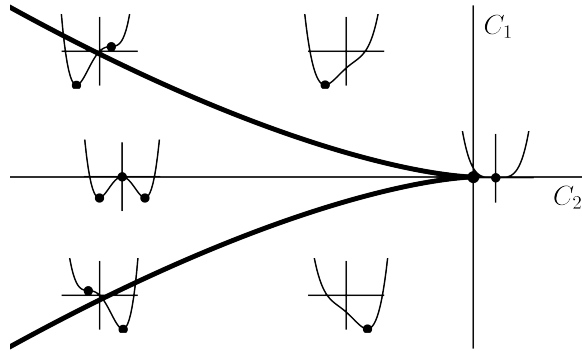

Figure 1.4: Geometry of the cusp. The generating function Φ_2 is plotted as insets over the now two-dimensional control space. As the fold lines are crossed, pairs of stationary points of the generating function coalesce and annihilate, leaving a single stationary point outside the cusp. At the cusp point $C_1 = C_2 = 0$, all three critical points coalesce.

The cusp is readily visible when light is shone onto a semi-cylindrical surface down onto a screen. For example, the reflection off the side of a coffee cup onto the bottom forms a cusp. Inside the cusp, three light rays meet at each point and the region is bright, while the darker outer region only has one light ray hits each point.

Swallowtail

The swallowtail generating function is,

$$\Phi_3 = s^5 + C_3 s^3 + C_2 s^2 + C_1 s \tag{1.137}$$

The process for finding the caustic structure is identical to above, however now we are faced with finding simultaneous solutions to,

$$\frac{\mathrm{d}\Phi_3}{\mathrm{d}s} = 5s^4 + 3C_3 s^2 + 2C_2 s + C_1 = 0 \tag{1.138}$$

and,

$$\frac{\mathrm{d}^2\Phi_3}{\mathrm{d}s^2} = 20s^3 + 6C_3 s + 2C_2 = 0 \ . \tag{1.139}$$

Although these solutions are possible to find analytically, they are cumbersome to write down and offer little insight. The three-dimensional caustic structure is shown in Fig. 1.5 (a). The grey shading is the bifurcation set, which is now a fold surface which is 'pinched' at the bottom by cusp lines. Intersections of the caustic surface with planes of constant C_3, are also shown for $C_3 < 0$ (b) and $C_3 > 0$ (c). Crossing any line in the $C_3 = \text{const.}$ plane results in the creation/annihilation of pairs of stationary points in the generating function (insets), while for $C_3 < 0$ there exist two cusp points in the lower-half plane where three stationary points annihilate. Only at the origin ($C_1 = C_2 = C_3 = 0$) do these cusps and the self-intersection line meet and all four stationary points of Φ_3 become degenerate.
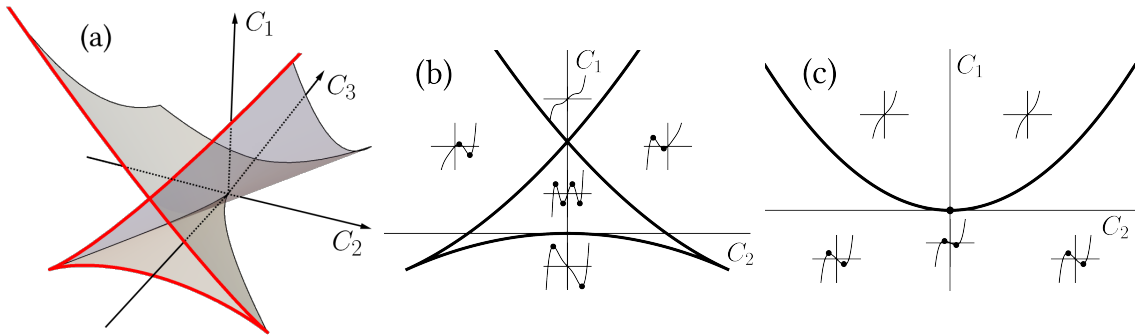

Figure 1.5: Geometry of the swallowtail. **Panel (a):** The full three dimensional caustic surface in the control space. **Panel (b):** Section of the swallowtail for $C_3 < 0$, with the generating function Φ_3 shown as insets. The bifurcation set is shown as a thick black line, clearly showing a pair of cusps in the lower half-plane and a self-intersection in the upper half plane. **Panel (c):** Similar to panel (b), now with for $C_3 > 0$.

Hyperbolic and Elliptic Umbilics

The umbilic catastrophes are so-named since at the centre of their classification lies the notion of *cubic forms*, which describe local curvature near umbilic points: points

on a surface which are locally spherical. A general surface with localized umbilic point
at the origin can be written [85],

$$f(x, y) = \frac{1}{2}K(x^2 + y^2) + \frac{1}{6}\left(ax^3 + 3bx^2y + 3cxy^2 + dy^3\right) + ... \tag{1.140}$$

where the constants $a = f_{xxx}(0,0)$, $b = f_{xxy}(0,0)$, $c = f_{xyy}(0,0)$, $d = f_{yyy}(0,0)$, form
what is sometimes called the 'Monge cubic', which describes the local perturbations
to the spherical curvature of the surface near the umbilic point. By defining the
discriminant [101],

$$D_C = 4(ac - b^2)(bd - c^2) - (ad - bc)^2 , \tag{1.141}$$

the umbilic point is elliptic if $D_C > 0$ and hyperbolic if $D_C < 0$. If $D_C = 0$ we
encounter a *parabolic umbilic* point, which is related to a catastrophe we will not
study here. The germs of the hyperbolic and elliptic umbilic catastrophes correspond
to cubic forms with the appropriate discriminant D_C to their classification.

The hyperbolic umbilic catastrophe has the generating function

$$\Phi_3^{\mathrm{H}} = s_1^3 + s_2^3 + C_3 s_1 s_2 + C_2 s_2 + C_1 s_1 \tag{1.142}$$

where now we have used the superscript "H" to differentiate it from the elliptic umbilic
and swallowtail. The caustic surface must now be determined by calculating the first-
derivatives,

$$\frac{\partial \Phi_3^{\mathrm{H}}}{\partial s_1} = 3s_1^2 + 2C_3 s_1 + C_1 = 0 \tag{1.143}$$

and,

$$\frac{\partial \Phi_3^{\mathrm{H}}}{\partial s_2} = 3s_2^2 + 2C_3 s_2 + C_2 = 0 \tag{1.144}$$

while simultaneously ensuring that the Hessian determinant is zero,

$$\det\left[\frac{\partial^2 \Phi_3^{\mathrm{H}}}{\partial s_i \partial s_j}\right] = \left(\frac{\partial^2 \Phi_3^{\mathrm{H}}}{\partial s_1^2}\right)\left(\frac{\partial^2 \Phi_3^{\mathrm{H}}}{\partial s_2^2}\right) - \left(\frac{\partial^2 \Phi_3^{\mathrm{H}}}{\partial s_1 \partial s_2}\right)^2 = 4\left(3s_1 + C_3\right)\left(3s_2 + C_3\right) = 0 . \tag{1.145}$$

The elliptic umbilic generating function is,

$$\Phi_3^{\mathrm{E}} = 3s_1^2 s_2 - s_2^3 + C_3(s_1^2 + s_2^2) + C_2 s_2 + C_1 s_1 \tag{1.146}$$

The corresponding caustic surface is determined by simultaneous solutions to,

$$\frac{\partial \Phi_3^{\mathrm{E}}}{\partial s_1} = 6s_1 s_2 + 2C_3 s_1 + C_1 = 0 \tag{1.147}$$

$$\frac{\partial \Phi_3^{\mathrm{E}}}{\partial s_2} = 3(s_1^2 - s_2^2) + 2C_3 s_2 + C_2 = 0 \tag{1.148}$$

$$\det\left[\frac{\partial^2 \Phi_3^{\mathrm{E}}}{\partial s_i \partial s_j}\right] = 4C_3^2 - 36(s_1^2 + s_2^2) = 0 \tag{1.149}$$
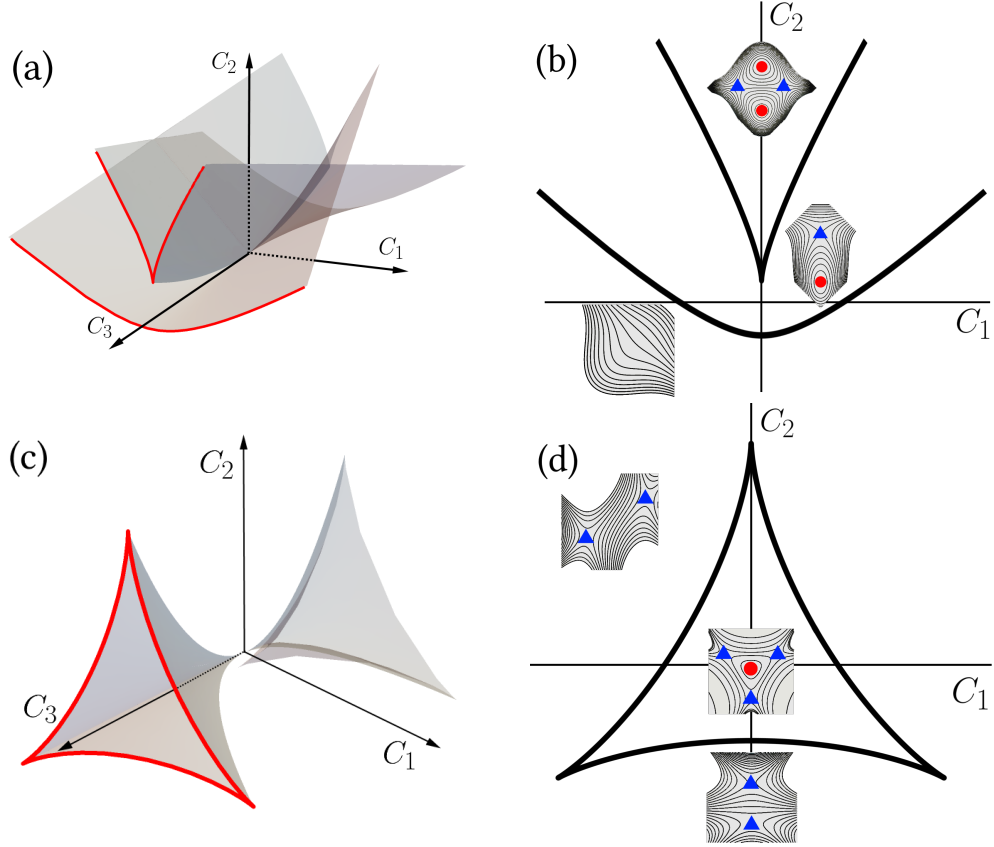
Figure 1.6: Geometry of the D_4 umbilic catastrophes. **Panel (a):** Full three-dimensional hyperbolic umbilic caustic surface. **Panel (b):** Section of the hyperbolic umbilic with fixed $C_3 > 0$. The caustic is shown as a thick black line, which consists of a cusp and a fold. Insets show contour plots of the generating function Φ_Q^H, with minima/maxima indicated with red circles and saddle points indicated with blue triangles **Panel (c):** Full three-dimensional elliptic umbilic caustic surface. **Panel (d):** Section of the elliptic umbilic with fixed $C_3 > 0$, insets are as in panel (b). Panels (a) and (c) are from Paper IV [56].

Like the swallowtail, we shall make no effort to solve the set of equations for the D_4 catastrophes, however we can still visualize them. For convenient parametrization of the surfaces, see Refs. [89, 102]. The hyperbolic and elliptic umbilic catastrophe surfaces are shown in Fig. 1.6, panels (a) and (c), respectively. Panel (b) shows a section of the hyperbolic umbilic cut through the surface at fixed $C_3 > 0$ (although it is symmetric for $\pm C_3$). For corank-2 catastrophes, the generating function Φ_Q becomes two-dimensional, and so now the insets are contour plots where we have labeled the maxima/minima as red circles, and the saddle points are blue triangles. Starting from the bottom of the image, no saddles or local extrema are present. As one crosses the lower fold surface, a local extremum is created plus a saddle point. As one crosses the inner cusp line, a second saddle is created with another extremum

of opposite type so that there is one local minimum, one maximum, and two saddles present inside the cusp. At $C_1 = C_2 = C_3 = 0$ (not shown), only the germ is present, and the corresponding surface consists of two pairs of superimposed fold lines meeting at a right angle (no longer a cusp).

A cut through the elliptic umbilic at $C_3 > 0$ (again symmetric for $\pm C_3$) is shown in panel (d). The contour plots highlight how the overall structure of the elliptic umbilic differs from its hyperbolic cousin. Everywhere outside of the tri-cusped surface, two saddle points can be found. As one crosses into the inner region, a third saddle point is created along with a lone local extremum. In both the hyperbolic and elliptic umbilics, how one chooses to cross the surface affects the way each stationary point is created. Crossing folds, which are planes in 3D catastrophes, extra stationary points are produced such that they arise from doubly-degenerate points, while if one crosses a cusp, which exist as *lines* in this three-dimensional space, the extra stationary points are produced from a triply-degenerate stationary point.

The Catastrophe X_9

The only catastrophe we consider in this thesis which exists beyond Thom's elementary list is known by its group-theoretic symbol, X_9. In Paper IV, we shall find that this catastrophe acts as an organizing centre for caustics in the three-mode Bose-Hubbard model.

The generating function is [85],

$$\Phi_9^\pm = s_2^4 + K s_1^2 s_2^2 \pm s_1^4 + C_7 s_2^2 s_1 + C_6 s_2 s_1^2 + C_5(s_2^2 + s_1^2)$$
$$+ C_4(s_2^2 - s_1^2) + C_3 s_2 s_1 + C_2 s_2 + C_1 s_1 . \tag{1.150}$$

As a corank-2 catastrophe, the generating function is still only two-dimensional, however the control space is relatively enormous, with 7 control parameters. The germ,

$$s_2^4 + K s_1^2 s_2^2 \pm s_1^4 \tag{1.151}$$

contains an additional parameter, the modulus K, which cannot be transformed away by any smooth change of variables, thereby increasing the dimensionality to 8. Because of the sheer size of the space in which the caustic is embedded, a complete analysis is not only laborious, but also impossible to visualize. Thus, we shall examine only three unfoldings of X_9 with codimension 3 which have practical physical applications, and provide some interesting connections to lower-order caustics.

For the remainder of this section, we shall be concerned with the family X_9^+, which corresponds to the '$+$' choice in Eq. (1.150). It can be further divided into two

sub-families [85, 100],

$$
\begin{cases}
{}^0X_9 & K > -2 \qquad \text{and } K \neq 2 \\
{}^4X_9 & K < -2
\end{cases}
\tag{1.152}
$$

where $K = \pm 2$ is excluded because it gives an unstable singularity. The $K = 2$ case is particularly interesting however, and has relevance to physical problems, so we shall also examine it further, even if it cannot be classified as a true catastrophe. Since the method of finding the caustic surfaces is identical to the umbilic cases above, we simply state the generating functions below and will not show the sets of simultaneous equations to be solved for each unfolding.

The first we shall examine is a $K = -6$ partial unfolding, called the 'elliptic' unfolding by Berry [103],

$$
\Phi_9^{\mathrm{E}} = s_2^4 - 6s_1^2 s_2^2 + s_1^4 + C_5(s_2^2 + s_1^2) + C_2 s_2 + C_1 s_1 .
\tag{1.153}
$$

Like in the case of the umbilics, we show the full three-dimensional caustic surface in Fig. 1.7 (a). This unfolding of X_9 can be seen as a generalization of the elliptic umbilic catastrophe D_4^- due to an extra saddle point in the generating function. As shown in the centre of panel (b), there are four saddle points surrounding the local extremum in the generating function. As one crosses the fold surfaces from inside to outside, an extremum and a saddle point coalesce and annihilate, while at each cusp line, however, two saddles and the extremum merge as one to form a single saddle. The result in both cases is the same: only three saddle points exist outside the fourfold cusped structure. One should note that at $C_5 = C_2 = C_1 = 0$ the singularity only appears fivefold degenerate in this reduced space. Since more unfolding terms would have been possible, it is a singularity of codimension eight. Although we do not identify this particular unfolding in Paper IV, this caustic appears in optics [85, 104] (it is Leonardo's cross [87]), and it is instructive to notice that the appearance of additional cusps (compared to, say the elliptic umbilic) is a signature of X_9.

Next, there is the 'hyperbolic' $K = 6$ unfolding,

$$
\Phi_9^{\mathrm{H}} = s_2^4 + 6s_1^2 s_2^2 + s_1^4 + C_4(s_2^2 - s_1^2) + C_2 s_2 + C_1 s_1 .
\tag{1.154}
$$

Now the full caustic surface is shown in panel (c) of Fig. 1.7. Sections of this unfolding are complicated, shown in panel (d) at fixed C_4. Outside the entire surface, there is only one minimum in Φ_9^{H}. Crossing the fold line parallel to the C_2 axis, into the pointed ellipse ('vesica piscis'-like) central section, a new saddle and minimum is created. Inside the small kite-shaped region (shaded, left, in panel (d)) as one crosses the cusp, there are two maxima, one minimum, and two saddles, created either in

pairs or as a triad depending on whether one has crossed the fold surface or cusp line, respectively. Finally there exist long, thin regions (shaded, right) between fold lines which have again two minima and one saddle. This unfolding is seen in Paper IV, when we consider a quench of the Bose-Hubbard trimer with a linear geometry.

The last partial unfolding of X_9 we consider is the rotationally symmetric $K = 2$ case,

$$\Phi_9^{\mathrm{circ}} = s_2^4 + 2s_1^2 s_2^2 + s_1^4 + C_5(s_2^2 + s_1^2) + C_2 s_2 + C_1 s_1 . \tag{1.155}$$

Fig. 1.7 (e) shows the full caustic surface, from which its alternate name 'spun cusp' becomes clear, since it is a circularly symmetric version of the cusp catastrophe. This is in fact not a 'true' catastrophe since it contains an unstable axial caustic along the $C_1 = C_2 = 0$ axis. The insets of Fig. 1.7 demonstrate that anywhere along the axial caustic, the function Φ_9^{circ} contains a local maximum, surrounded by a ring (i.e. an infinite amount, hence why this part of the caustic is sometimes said to have infinite codimension) of local minima, denoted on the figure as a purple ring. Since any perturbation of infinitesimal size will destroy this ring, producing two extrema and one saddle, which are in different locations depending on the perturbation, this cannot represent a 'true' catastrophe since it is unstable.

Although not a member of the X_9 unfoldings, it is still instructive to treat the $K = 2$ case as one, since it has applications in real-world problems where we can sometimes engineer near-perfect symmetry. Furthermore, although a perturbation to Φ_9^{circ} destroys the axial caustic, it will not so drastically destroy the outer circular cusp, where an extremum and saddle point coalesce. The circular unfolding of X_9 is highly relevant to caustics formed via the focusing of light by spherical sources, such as water droplets [104], and gravitational lensing [85].

1.2.3 Catastrophe properties

Stability

Catastrophes exhibit structural stability, they can therefore be distorted in many ways without destroying their overall structure. It is for this reason that the $K = \pm 2$ unfoldings of X_9 are technically excluded from this classification, since it contains an unstable singularity. In a similar vein, other structures such as the line of stationary points generated from $f(x, y) = x^2$ are unstable, since any perturbation εy, εy^2 etc. for any ε will immediately destroy the 'valley' of stationary points.

All non-degenerate (i.e. Morse) stationary points are stable, while degenerate (i.e. non-Morse) stationary points are all unstable [105]. Take, for example, a one
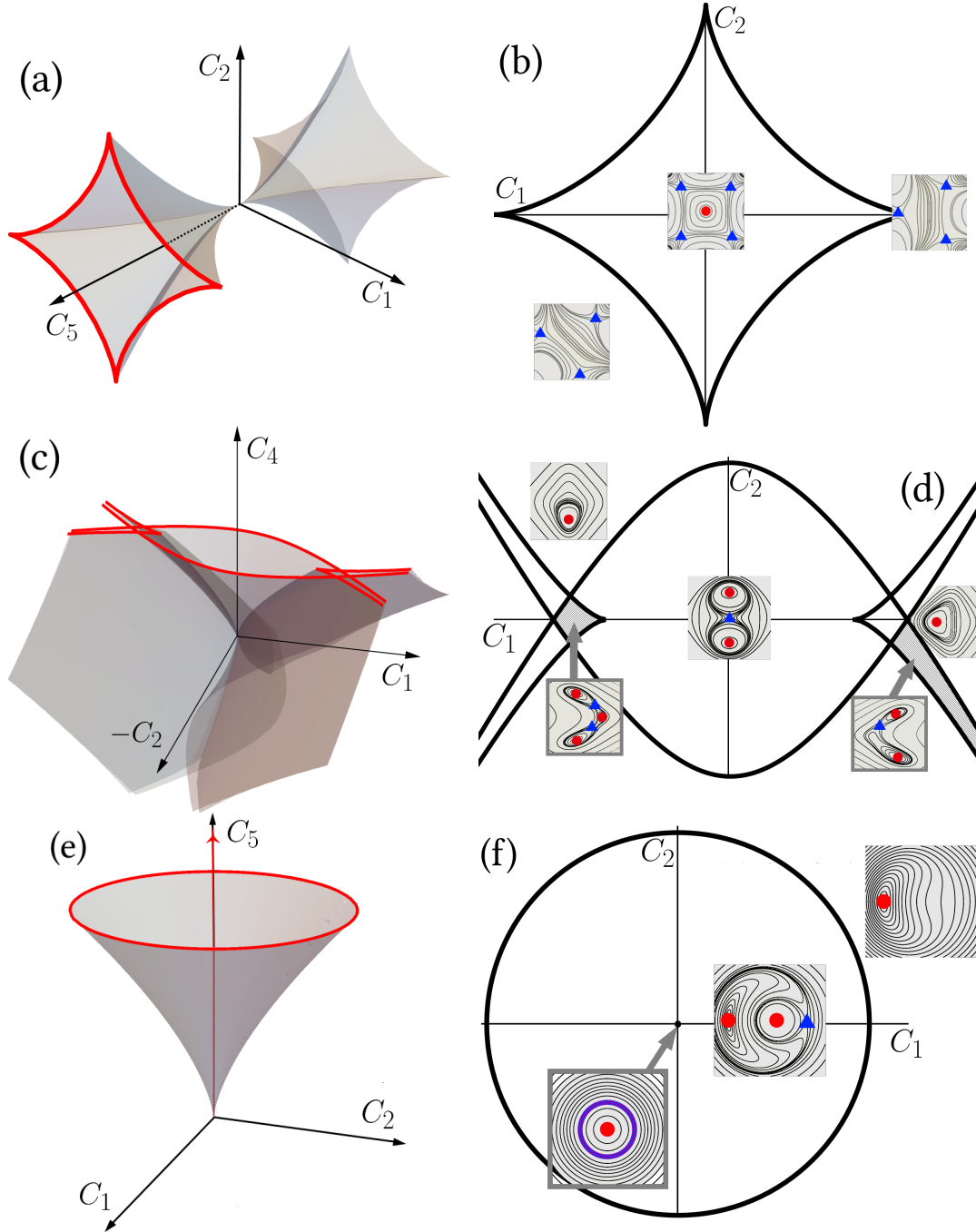
Figure 1.7: Geometry of three partial unfoldings of X_9. All insets on the right column are as in Fig. 1.6, contour plots of Φ_9, with red circles representing local extrema and blue triangles for saddle points. **Panel (a):** Caustic surface of the elliptic unfolding ($K = -6$) caustic surface from X_9^{E} **Panel (b):** Section of the elliptic unfolding caustic at fixed $C_5 > 0$. **Panel (c):** Caustic surface for the hyperbolic unfolding X_9^{H}. **Panel (d):** Section of the hyperbolic caustic at fixed $C_4 > 0$. **Panel (e):** Caustic surface for the circular (excluded) unfolding X_9^{circ}. **Panel (f):** Section of X_9^{circ} at fixed $C_5 < 0$. The inset for the contour plot at the axial caustic indicates an unstable ring of minima, indicated by the purple circle. Panels (c) and (e) are from Paper IV (Ref. [56]).

dimensional function f at a non-degenerate stationary point. By the Morse lemma, in some coordinate system we can write it as $f(x) = x^2$. Let us then perturb the function by $g(x) = \varepsilon x$. By including the perturbation, the stationary point moves from $x^* = 0$ to $x^* = -\varepsilon/2$, which is a smooth translation of the stationary point. I.e. for any $\delta > 0$, you can select an ϵ such that $x^* < \delta$. Also important is that x^* is of the same type, i.e. it remains Morse.

It is by this line of reasoning that the unfolding terms are necessary: catastrophe germs are degenerate stationary points, and hence unstable. A function with a doubly-degenerate critical point is $f(x) = x^3$. Now a perturbation of εx will move the stationary point smoothly to $\pm\sqrt{-\varepsilon/3}$, however the type has changed: it has split from a single non-Morse point to either two Morse points or zero, no matter the size of ε and is thus unstable. This point is, however, stable under perturbations of $g(x) = \varepsilon x^4$ (and similar higher-order perturbations), since a quick calculation shows that the non-Morse critical point remains at $x = 0$, and a new one has been added at $x^* = -3/(3\varepsilon)$, which is arbitrarily far away and hence not locally relevant.

Catastrophes, which form a family of functions which are tuned by their control parameters, are stable to the kinds of perturbations mentioned above, and extended to arbitrary dimensions. The proof is due to Thom [97], and is beyond the scope of this thesis, but the result of the above analysis still applies. A catastrophe function $f : \mathbb{R}^n \times \mathbb{R}^Q \to \mathbb{R}$ is equivalent, in a topological sense, to $f + g : \mathbb{R}^n \times \mathbb{R}^Q \to \mathbb{R}$, where g is the perturbation, and hence is stable.

Consider the cusp catastrophe, Eq. (1.133). First, any perturbation of εx^3 is irrelevant since by redefining the origin, one can 'depress' the quartic and eliminate the cubic term by a smooth change of variables. Next, let us consider a quintic perturbation,

$$\Phi = \varepsilon x^5 + x^4 + C_2 x^2 + C_1 x \tag{1.156}$$

For simplicity, let us set $C_1 = 0$ and $C_2 < 0$ so that we lie inside the canonical cusp along the axis (we know any linear perturbation amounts to a translation of C_1, so this is fine). At lowest order in ε, the stationary points are,

$$x_1^* = 0 \qquad x_2^* = \sqrt{-\frac{C_2}{2}} \qquad x_3^* = -\sqrt{-\frac{C_2}{2}} \qquad x_4^* = -\frac{4}{5\varepsilon} \tag{1.157}$$

We see that x_1^*, x_2^*, and x_3^* are all the expected cusp stationary points, of the same type, while the remaining point x_4^* can again be made arbitrarily far away from any of these points by a small enough perturbation. Hence, the cusp is stable.

Projections

Another important feature of catastrophes is that those of higher-order tend to include those of lower order. We have already encountered many examples of this in our exploration of the various catastrophe geometries. A generating function of high order can still exhibit locations where a single pair of stationary points coalesce and annihilate, which can give rise to fold lines (in 2D), fold surfaces (in 3D), and so on. Similarly, if anywhere in the control space of a high-order catastrophe, three stationary points coalesce into one, then this becomes a cusp line (3D). In higher dimensions, these would become hypersurfaces of dimension $D - q$ where D is the dimension of control space and q is the dimension of the embedded (i.e. lower-order) catastrophe.

Catastrophes of higher-order are not guaranteed to contain all of those of lower order. The catastrophes A_{Q+1}, called the cuspoids, contain one another in succession, and D_5 (the parabolic umbilic) contains $D_4^{\pm}$. Exiting the elementary catastrophes, however, there are complicated relationships between them which are best visualized in so called 'bordering' or 'abutment' diagrams [85, 96]. A bordering diagram adapted from Nye [85] for X_9 can be found in Fig. 15 of Paper IV, showing that different families of X_9 can contain different sub-catastrophes.

1.2.4 Wave catastrophes

Historically, the application of catastrophe theory to physical problems has been dominated by optics. In the vicinity of a caustic, a geometric ray theory of light breaks down and the effects of diffraction are required to ensure that the intensity at the caustic is finite. In the late 20th century this sparked the emergence of 'catastrophe optics', spearheaded by Nye [85] and Berry [99, 106], in which catastrophe theory was combined with a classical wave theory of diffraction to describe the wave nature of focusing events. Mathematically, this corresponds to a local description of a wave near a caustic as,

$$\Psi_Q(\mathbf{C}; \lambda) = \left(\frac{\lambda}{2\pi}\right)^{n/2} \int \ldots \int d\mathbf{s} \, e^{i\lambda\Phi_Q(\mathbf{s};\mathbf{C})} \tag{1.158}$$

where $\Phi_Q(\mathbf{s}; \mathbf{C})$ is a catastrophe function which depends on the nature of the focusing event, n is the corank of the catastrophe, and λ is the wavelength. We will refer to the integral (1.158) as a *diffraction integral* which describes a wave catastrophe.

From a quantum-mechanical perspective, one can view Eq. (1.158) as a Feynman path integral,

$$\Psi(x_0, x(t); t) = \sum_{\text{Paths } x(\cdot)} e^{iS[x(\cdot)]} \tag{1.159}$$

where $\mathcal{S}$ is an action functional and the paths $x(\cdot)$ run from $x(0) = x_0$ to $x(t)$. From this perspective, the catastrophe function Φ_Q plays the role of an action, and the paths being focused are no longer optical paths, but classical paths which the particle takes through phase space. A WKB approximation of the quantum-mechanical path integral breaks down at a caustic [107], and a semiclassical treatment of the wavefunction necessitates the use of diffraction integrals as a local approximation.

Canonical diffraction integrals

Here we demonstrate diffraction integrals associated with each wave catastrophe. The special functions described here will correspond to Eq. (1.158) with $\lambda = 1$, however we shall see that catastrophe diffraction integrals obey scaling identities which allows us to restore the wavelength.

The wave catastrophe of the fold is described by the Airy function [108],

$$\mathrm{Ai}(C) = \frac{1}{\sqrt{2\pi}} \int_{-\infty}^{\infty} \mathrm{d}s \; \mathrm{e}^{\mathrm{i}(s^3 + Cs)} \; , \tag{1.160}$$

which is a solution to the Airy equation,

$$\frac{\mathrm{d}^2 y(x)}{\mathrm{d}x^2} - Cy(x) = 0 \; . \tag{1.161}$$

We plot the Airy function in Fig. 1.8. The caustic is a single point at $C = 0$, however we show it as a dotted line for clarity. Due to the fold catastrophe permitting two solutions for $C < 0$, this is sometimes called the 'bright' region since it will be where two light rays exist. Conversely, since no solutions exist for $C > 0$, this is sometimes called the 'dark' region. The wavefunction on this side is exponentially suppressed, relevant to early-growth behaviour in light cones.

The next wave catastrophe corresponds to the diffraction integral for the cusp, known as the Pearcey function [109]

$$\mathrm{Pe}(C_2, C_1) = \frac{1}{2\pi} \int_{-\infty}^{\infty} \mathrm{d}s \; \mathrm{e}^{\mathrm{i}(s^4 + C_2 s^2 + C_1 s)} \; . \tag{1.162}$$

The Pearcey function is in general complex and hence the simplest wave catastrophe to have both an amplitude and a phase, so we show both in Fig. 1.9. The Pearcey diffraction pattern dresses the classical cusp, which is shown as a black dashed line. This 2D pattern is distinct from, say, a fold extended into a line pattern, which would only give striped Airy fringes rather than the much more complex fringes seen here.

The addition of a phase also introduces us to the notion of dislocations in wave catastrophes which come in the form of phase singularities, i.e. vortices, where the
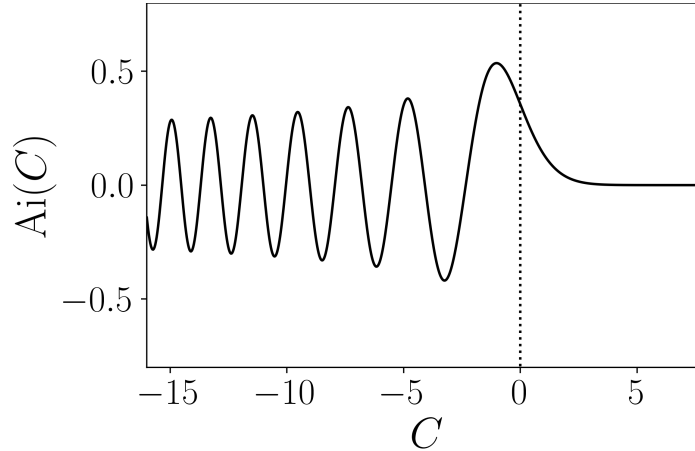
Figure 1.8: Airy function. The caustic lies at $C = 0$, which we have shown as a dotted line.

phase takes all values $\in [0, 2\pi)$ and hence is undefined. Phase singularities appear commonly in optics, for example in Laguerre-Gauss beams [110], in fluid dynamics under rotation, and they even appear in tides as amphidromic points [111]. In order to preserve the single-valuedness of the wavefunction, they occur when the wavefunction has zero amplitude. Furthermore, the phase of the wavefunction winds along a closed contour around these points. For $\Psi = \rho e^{i\phi}$,

$$\oint_{\mathcal{C}} d\phi = \oint_{\mathcal{C}} dr\, \nabla\phi = \pm 2\pi m \tag{1.163}$$

where $\mathcal{C}$ is some closed contour containing one vortex, and m is the topological charge of the vortex, which counts the number of times the phase winds around. As shown in Fig. 1.9 (b), the Pearcey function is populated with a lattice of vortices, mostly contained within the classical cusp. The vortices come in pairs of opposite phase-winding, and so we call these *vortex-antivortex pairs*. The phase winding around multiple phase singularities corresponds to the sum of the individual topological charges m_i times 2π, meaning that a closed contour around a vortex-antivortex pair will contain no net phase winding. A pair of vortices from the Pearcey function are shown in Fig. 1.9 (c).

Vortices are subwavelength structures, and hence represent the finest level of structure in a wave catastrophe, smaller than the fringes and the course classical caustic seen at largest scales. In Paper I, we see that second quantization introduces an additional layer of structure for caustics in Fock space. Vortices in second-quantization no longer correspond to phase singularities: the integral (1.163) becomes a sum across sites on a chain and the vortices become 'phase kinks' (similar to dark solitons).

The remaining catastrophe functions we study in this thesis (which we shall not
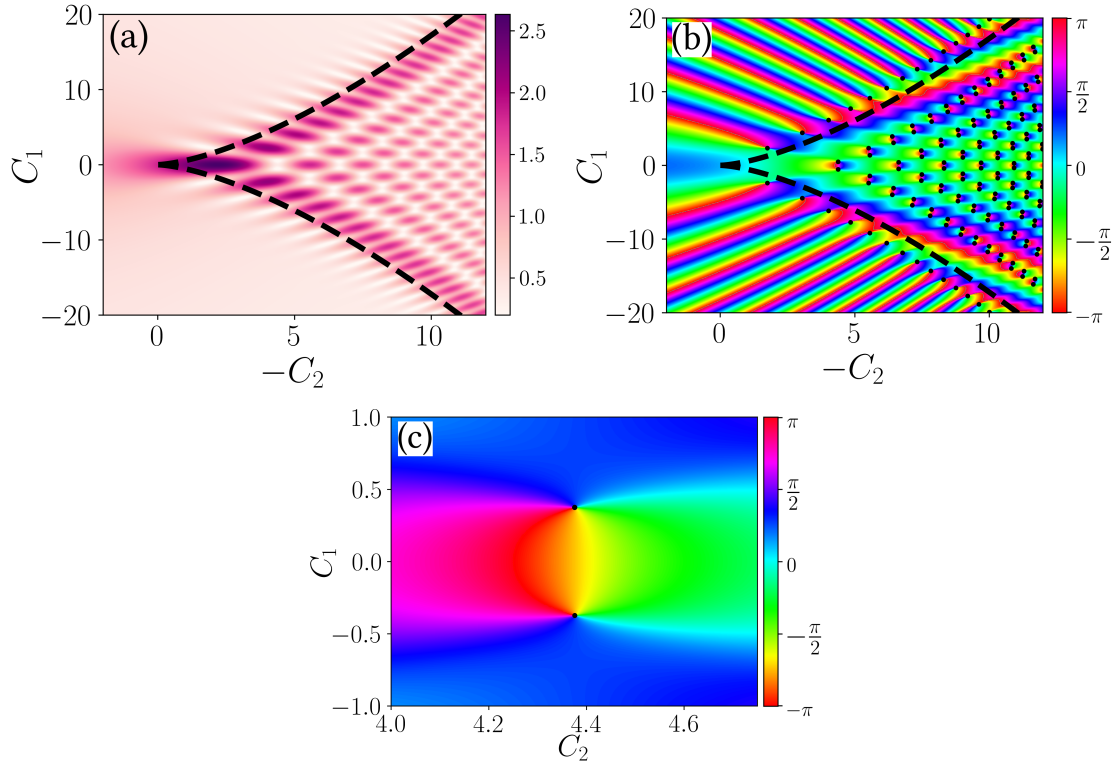
Figure 1.9: Pearcey function. **Panel (a):** Amplitude of the Pearcey function. The diffraction pattern dresses the classical cusp (shown as a dashed line). **Panel (b):** Phase of the Pearcey function. A lattice of vortex-antivortex pairs, indicated as black dots, populate the area between the caustic and line the outside. **Panel (c):** A sample vortex-antivortex pair drawn from the Pearcey function.

specially list because they do not have specific designations) are all of the form given in Eq. (1.158) with $\lambda \to 1$. Since they are three-dimensional, it is impossible to properly visualize the entire pattern at once, so we show relevant two-dimensional sections of each. For these three-dimensional diffraction catastrophes, the phase singularities become generalized to lines of vortices, which have been studied in the case of the elliptic [112,113] and hyperbolic [114] umbilic catastrophes. We will not be concerned with dislocation lines for now, although they present an interesting extension to our present work.

Fig. 1.10 shows diffraction patterns for sections of the umbilic catastrophes. Panels (a) and (b) correspond to sections of the hyperbolic umbilic catastrophe, while panels (c) and (d) are sections of the elliptic umbilic. In every panel, the caustic is shown as a dashed black line, which becomes dressed by an interference pattern. The section shown in panel (a) is along the plane $C_3 = 0$, where two pairs of overlapping fold lines meet at a right angle. This unique section of the elliptic umbilic corresponds to a product of Airy functions, since the cross-term containing C_3 vanishes [114]. Panel

(b) shows $C_3 > 0$, with the familiar cusp with a Pearcey-like interference pattern surrounded by a fold line which generates additional Airy fringes.

Panel (c) shows the diffraction pattern of the elliptic umbilic in the $C_3 = 0$ plane, also called the focus, since the classical catastrophe is simply a point here (the germ). Like in the hyperbolic case, this triple-forked pattern also corresponds to a unique section of the elliptic umbilic integral which can be decomposed directly in terms of Airy functions [112] (in this case the decomposition also involves Airy's second solution, $\mathrm{Bi}(z)$), or a complicated product of 'one-sided Airy functions' [103]. In the $C_3 > 0$ unfolding, shown in panel (d), the threefold cusp gives three interfering Pearcey-like diffraction patterns within the caustic.
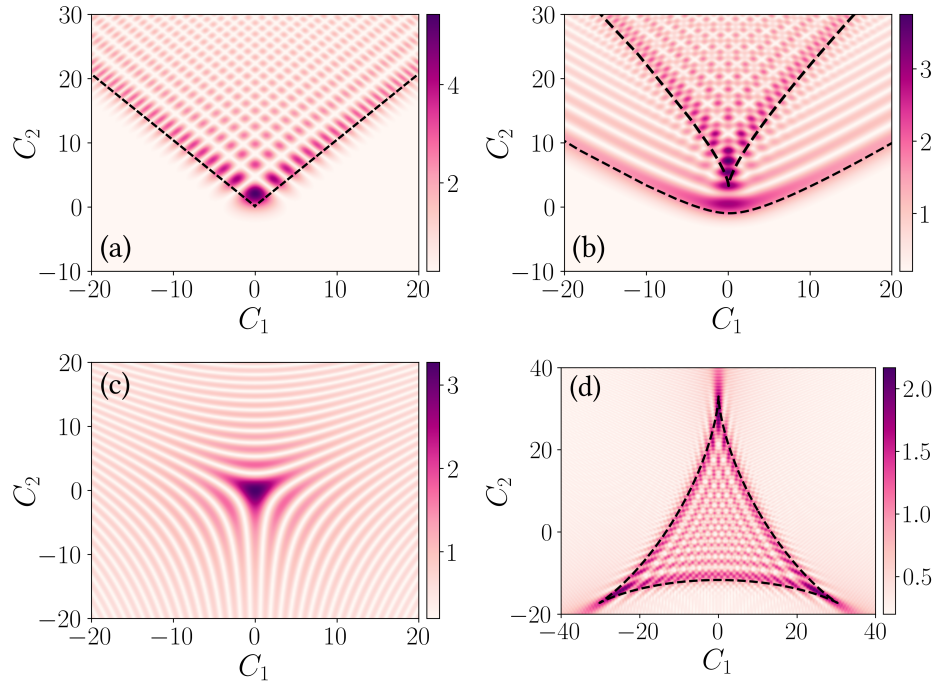

Figure 1.10: Diffraction integrals for the D_4 catastrophes. The classical caustics are shown as dashed lines in each image. **Panel (a):** $C_3 = 0$ plane of the hyperbolic umbilic. **Panel (b):** $C_3 = 3$ plane, with both the cusp and fold lines separate. **Panel (c):** Elliptic umbilic focus, corresponding to the $C_3 = 0$ plane. **Panel (d):** $C_3 = 6$ plane, showing the threefold Pearcey-like interference pattern.

Finally, in Fig. 1.11, we show diffraction patterns for the three sections of X_9 mentioned above. Panel (a) shows the focus of the elliptic unfolding, from the generating function Φ_9^{E} with $C_5 = 0$. In this plane, the function becomes a complicated product of 'one-sided Pearcey functions' [103], and appears to have an apparent eightfold symmetry. Panel (b) shows a fully-unfolded X_9^{E} catastrophe diffraction pattern at $C_5 = 12$, which, due to the four cusps, a fourfold version of a Pearcey diffraction

integral is immediately noticeable.

Panel (c) corresponds to the focal plane ($C_4 = 0$) of the hyperbolic unfolding of X_9, with generating function Φ_9^{H}. This function separates simply into a product of Pearcey functions [103], which is readily seen by a rotating C_1, C_2 coordinates by $\pi/4$. In panel (d), we show the $C_4 = 7$ plane. The fold lines on the top and bottom give rise to Airy fringes inside, while the outward-facing cusps give rise to Pearcey-like fringes pointing in the $\pm C_1$ directions.

Panel (e) shows the focal plane ($C_5 = 0$) of the circular unfolding of X_9 from Φ_9^{circ}. Apart from the origin, there are no distinguishing features of this focus. After unfolding into the $C_5 = -14$ plane, we see the circular nature of the caustic, with fringes inside the classical caustic and none outside. Furthermore the unstable axial caustic at $C_1 = C_2 = 0$ remains the brightest (in this color scheme, it is dark) part of the diffraction catastrophe.

A note on numeric evaluation of these caustics: as one attempts to evaluate the diffraction integrals for systematically higher-order catastrophes, the numerical evaluation of the integrals rapidly becomes more unstable and resource-expensive. For this reason, some of the X_9 caustic patterns are not as sharply defined as the lower-order caustics.

Caustics from water droplet lenses

As mentioned earlier in this section, caustics can be seen in many real-world situations. In this section, we will briefly demonstrate how caustics can be viewed relatively simply even with a simple experimental setup. This setup is inspired by the works of Berry, Nye, Marston and collaborators [104, 112, 115–117], in which they demonstrate that light shone through a single water droplet can yield visible caustics when projected onto a screen.

A relatively simple setup is demonstrated in Fig. 1.12. A glass slide was covered with electrical tape which has been cut to form a small hole. A water droplet is carefully placed so that it resides entirely in the hole without spilling onto the tape. The shape of the droplet is determined by the shape of the hole (boundary conditions) and the surface tension [104]. In turn, the droplet geometry influences how light is focused as it passes through, therefore acting as a control for the types of caustics one can see. The shape can be further influenced by how the slide is oriented: gravity will distort the droplet shape, but surface tension will keep it attached to the slide. A simple portable laser was carefully arranged such that it shines light through the back of the slide, through the droplet and onto a screen. In the case of Nye [104], the
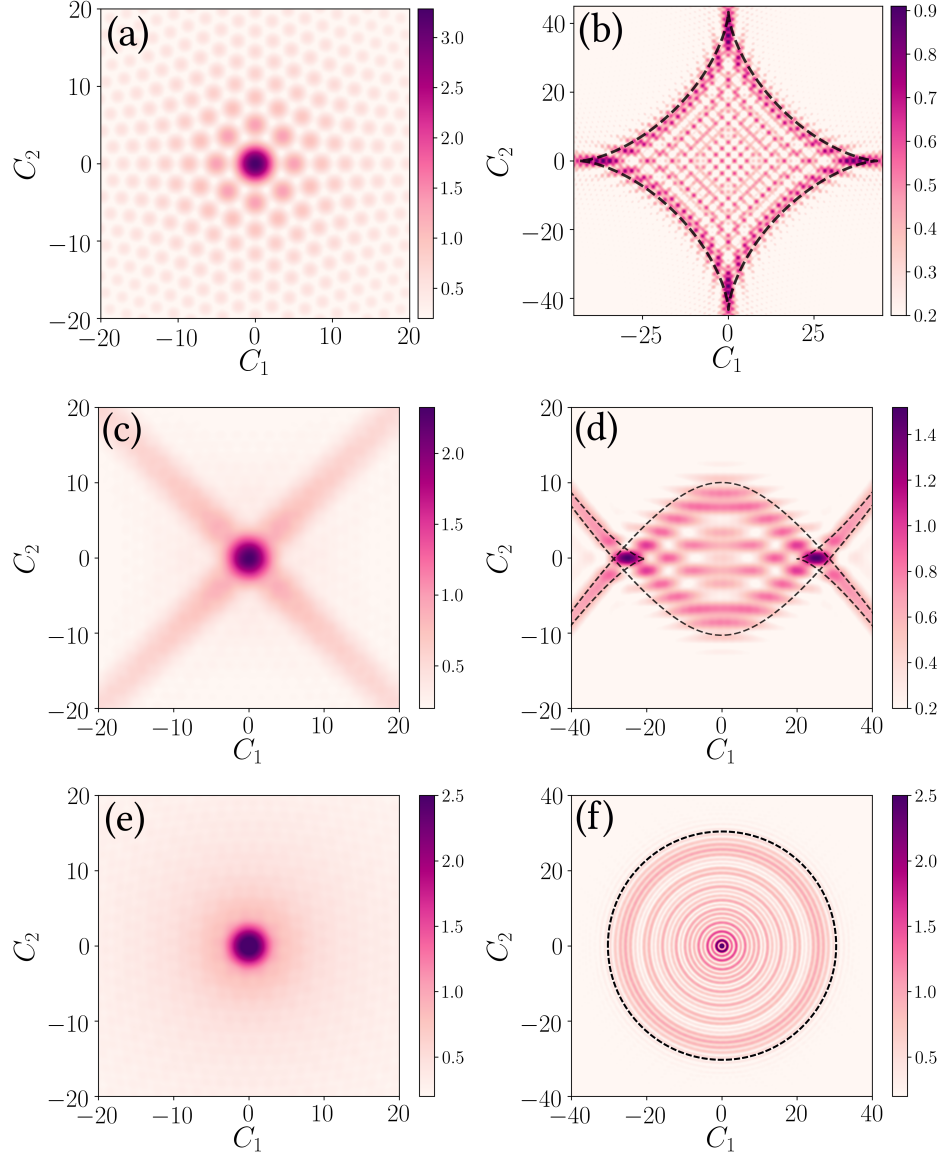
Figure 1.11: Diffraction integrals for X_9 catastrophe unfoldings. The classical caustics are shown as dashed lines in each image. **Panel (a):** $C_5 = 0$ plane of the elliptic unfolding. **Panel (b):** $C_5 = 12$ plane, showing the full fourfold symmetric Pearcey pattern. **Panel (c):** Hyperbolic unfolding $C_4 = 0$ focus plane. **Panel (d):** Hyperbolic unfolding in the $C_4 = 7$ plane. **Panel (e):** Circular unfolding $C_5 = 0$ plane. **Panel (f):** Circular unfolding in the $C_5 = -14$ plane. The central axial caustic continues to dominate the diffraction pattern.

droplets were on the order of 1-8mm in size, and caustics were photographed through a microscope. To capture the images in Fig. 1.13 and Fig. 1 of Ref. [56] (Paper IV, Chapter 5), we used a droplet of approximately 1mm across, however, rather than using a microscope, we place a screen approximately 1m behind the droplet, from which the patterns can be photographed.
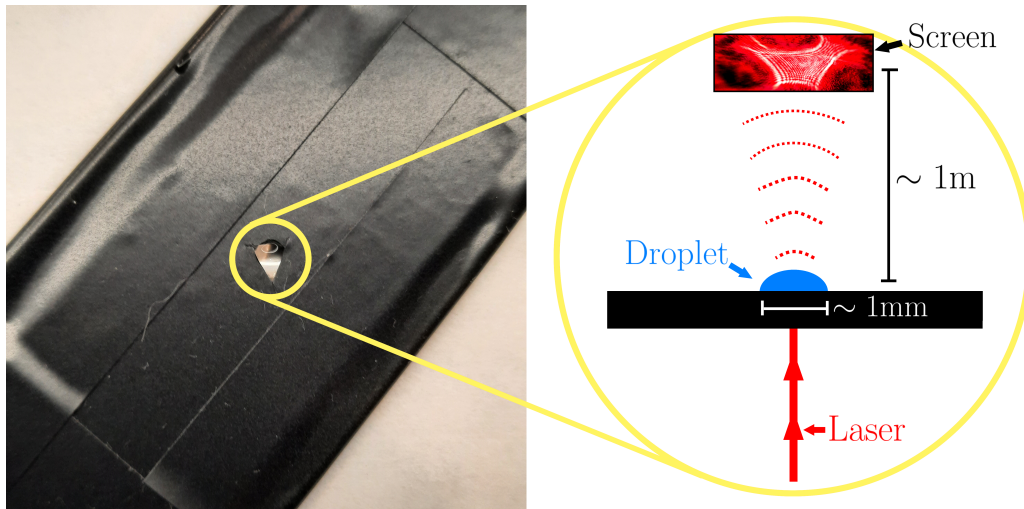
Figure 1.12: Schematic setup for water droplet experiment. The left image shows a glass slide covered in electrical tape, except for a small triangular hole, in which a water droplet is placed. The experimental setup is then shown on the right.

Fig. 1.13 shows three caustics formed using the setup described above using three different laser colours on different droplets. Panel (a) shows a clear Pearcey diffraction pattern, while panel (b) shows an apparent elliptic umbilic catastrophe which has been slightly distorted. The distorted, yet unmistakable interference pattern reinforces the notion that catastrophes are stable to perturbations. Panel (c) shows the distinctive triple fork diffraction pattern, which is indicative of the focus of the elliptic umbilic catastrophe. This experiment demonstrates the genericity of the caustic patterns we have explored above.
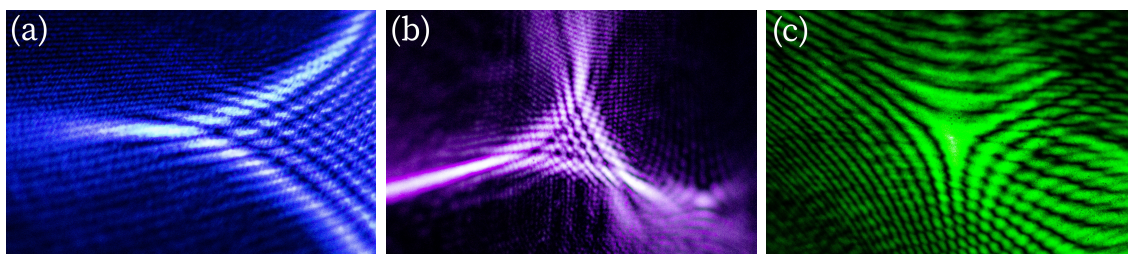

Figure 1.13: Caustics generated by water droplet lenses. Each image is from a different droplet, and the colours correspond to different laser colours used in the experiments.

A lens analogy can be extended to the systems we study in Chapter 5 (Paper IV), where the rays correspond to classical paths through Fock space, and the focusing lens becomes the Hamiltonian itself. Each trajectory corresponds to a classical configuration of the many-body problem. In both the double- and triple-well Bose-Hubbard models, unless the interactions are sufficiently attractive, the Hamiltonian discourages particles to all clump in one well and tends to encourage a roughly equal distribution

of particles in each well. This means that classical rays are 'focused' away from the edges and towards the centre of Fock space, leading to the formation of caustics from imperfect focusing events. In each of these cases, one can view the optical axis as time t, and the water droplet becomes the local energy surface. We also show that the circular symmetry of the quantum phase model gives rise to the circular unfolding of X_9 in (2+1)-dimensional Fock space and time, but perturbations destroy the circular symmetry and lead to bright patches corresponding to valleys of the local energy surface. Small water droplets evaporate quickly, and thus change the shape of the caustic which is projected onto a screen. This effect has been used to track the shape of the droplet as they evaporate [118], and in the same spirit, caustics formed by quantum many-body systems can in principle be a tool to study the nature of the Hamiltonian.

1.3 Measures of Chaos

Chaos corresponds to an extreme sensitivity of a system to its initial conditions: the butterfly effect. A quantitative tool for demonstrating exponential sensitivity to initial conditions, and therefore a diagnostic of classical chaos, is the Lyapunov exponent. Given a dynamical system in D-dimensions,

$$\frac{d\mathbf{x}}{dt} = \boldsymbol{f}(\mathbf{x}) \tag{1.164}$$

with initial condition $\mathbf{x}_0$, we consider a second trajectory with an initial condition perturbed by some small amount $\boldsymbol{\delta}$, so that the distance between these two trajectories is $|\boldsymbol{\delta}(t)|$. There exists a Lyapunov exponent defined by [119],

$$\lambda = \lim_{\substack{t \to \infty \\ \boldsymbol{\delta}(0) \to 0}} \frac{1}{t} \ln \frac{|\boldsymbol{\delta}(t)|}{|\boldsymbol{\delta}(0)|} \tag{1.165}$$

In fact, one can consider the linearized motion of the dynamical system around the perturbation,

$$\frac{d\boldsymbol{\delta}}{dt} = \mathbf{M} \cdot \boldsymbol{\delta} \tag{1.166}$$

where $\mathbf{M} = \partial \boldsymbol{f}/\partial \boldsymbol{x}$ is the Jacobian matrix, to define a set $\lambda_1, ..., \lambda_D$ ordered such that $\lambda_1 \geq \lambda_2 \geq ... \geq \lambda_D$. This set of exponents represents the exponential deviation of trajectories in the direction of the eigenbasis of $\mathbf{M}$ around $\mathbf{x}_0$. The individual λ_i can be positive or negative, but at least one must be zero [119]. For most purposes, however, the definition given in Eq. (1.165) is sufficient because at long enough times,

the spectrum is dominated by the largest exponent, $\lambda_1 = \lambda$, and this is sufficient to diagnose the exponential sensitivity of trajectories. Related to the exponential sensitivity of chaotic systems is the resulting lack of (quasi)periodicity in the long-term dynamics [120] (of closed systems), however, systems which do exhibit long-term periodic dynamics can also be transiently chaotic, such as in the famous Lorenz system [121].

A naive attempt to extend the notion of exponential sensitivity of initial conditions to quantum systems fails: the unitarity of quantum mechanics ensures that the distance between quantum states is preserved in time. Furthermore, the inherent discreteness of quantum spectra results directly in periodicity in closed quantum systems. For this reason, M. Berry proposed the existence of quantum 'chaology' rather than chaos [122] to indicate the study of semiclassical systems whose classical counterparts are chaotic. Modern language surrounding the discussion of chaos in the quantum regime is less prudent than Berry would likely have hoped; the terms 'quantum chaos' and 'quantum chaotic systems' are in widespread use to mean systems which would have fallen under the 'chaology' umbrella. We shall continue the tradition by using these terms interchangeably. Quantum chaos is argued to be the mechanism for thermalization [123, 124], and is therefore a condition for the validity of the Eigenstate Thermalization Hypothesis (ETH).

In this section we shall review signatures of chaos in quantum systems in the following sense: (i) spectra for chaotic systems will follow random matrix theory predictions, and/or (ii) the out-of-time-ordered correlator, which acts as a quantized version of the Poisson bracket, gives 'Lyapunov-like' behaviour. In each case there are exceptions and subtleties, which is a source of a great deal of ongoing research.

1.3.1 Random matrix theory

Random matrix theory (RMT) concerns itself primarily with matrices whose elements obey certain probability distributions, and often will use these probability distributions in order to make statements particularly about the eigenvalues of those matrices. In Paper III, we will make use of RMT in order to identify quantities in a regular system which are typically associated with flags of chaos, and so here we present the relevant background details for those flags.

The use of spectral statistics to distinguish regular and chaotic models is rooted in a pair of conjectures. First, the Berry-Tabor conjecture [125], which states that a generic quantum integrable model will have an eigenspectrum spacing distribution which is Poissonian. Second, the Bohigas-Giannoni-Schmit (BGS) conjecture [126] argues that

the spectra of quantum systems with a chaotic classical counterpart have spectral statistics which obey the 'Wigner surmise', and are described by Gaussian ensembles of RMT. In the following section, we shall examine the statistical difference between the spectra of a matrix (which physically might describe a Hamiltonian) whose elements are randomly drawn from a probability distribution and a set of random numbers. Attempts have been made to prove the Berry-Tabor [128] and BGS [129] conjectures, at least in some limiting cases where there exists a clear classical limit, such as the quantum billiard. However it isn't clear how to include models which do not have a definite classical analogue [130, 131], such as the Sachdev-Ye-Kitaev model [132–134].

Wigner and Poisson Statistics

As a motivation, we consider here the example originally considered by E. P. Wigner [135] in order to characterize the spectral statistics of heavy nuclei. A particularly useful reference for the basics of RMT can be found in Ref. [136]. Suppose we have a real, symmetric random matrix,

$$X = \begin{pmatrix} x_1 & x_3 \\ x_3 & x_2 \end{pmatrix} \tag{1.167}$$

where the elements are drawn from a Gaussian ensemble $\mathcal{N}(\mu, \sigma^2)$, which comes from the probability distribution,

$$p_\sigma(x) = \frac{1}{\sigma\sqrt{2\pi}} e^{-\frac{1}{2}\left(\frac{x-\mu}{\sigma}\right)^2} \tag{1.168}$$

with mean μ and variance σ^2. For this example, suppose $x_1, x_2 \sim \mathcal{N}(0,1)$ and $x_3 \sim \mathcal{N}(0, 1/2)$. The eigenvalues $\lambda_{1,2}$ are therefore real because X is a real, symmetric matrix. The goal is to compute the probability density function (PDF) of the spacing $s = \lambda_2 - \lambda_1$ where λ_2 is the largest eigenvalue and λ_1 is the smallest. Since the original entries are random variables, the object s is therefore a random variable.

The eigenvalues of the matrix are,

$$\lambda_{1,2} = \frac{1}{2}\left[x_1 + x_2 \pm \sqrt{(x_1 + x_2)^2 - 4(x_1 x_2 - x_3^2)}\right] \tag{1.169}$$

thus,

$$s = \sqrt{(x_1 - x_2)^2 + 4x_3^2} \tag{1.170}$$

Now, we wish to change variables in our joint PDF from $P(x_1, x_2, x_3) = p_1(x_1)p_1(x_2)p_{\frac{1}{2}}(x_3)$ to simply $P(s)$. This can be done by making use of $\int d\mathbf{x} g(\mathbf{x})\delta(\mathbf{x} - f(\mathbf{y})) = g(\mathbf{y})$.

Hence,

$$P(s) = \int_{-\infty}^{\infty} \mathrm{d}x_1 \mathrm{d}x_2 \mathrm{d}x_3 \, p_1(x_1)p_1(x_2)p_{\frac{1}{2}}(x_3)\delta\left(s - \sqrt{(x_1 - x_2)^2 + 4x_3^2}\right) \qquad (1.171)$$

$$= \frac{\pi}{2}se^{-\frac{\pi s^2}{4}} \equiv P_W(s) \qquad (1.172)$$

The fact that x_3 had a variance of $1/2$ rather than 1 simplified the results dramatically, and the resulting PDF $P(s)$ would have contained a Bessel function. The distribution in Eq. 1.172 is named "Wigner's surmise". Note that for $s \to 0$, the probability goes to zero, meaning that the odds of finding degeneracies goes to zero, leading to the notion of *level repulsion*. This is quite striking, since the entries of the matrices themselves are independent, while the eigenvalue spacing is correlated. Note this doesn't mean that it's actually impossible to have matrices with degenerate eigenvalues, but that the set of such objects has measure zero.

For completeness, let us compare with what would occur not with a random matrix, but rather a set of independent and identically distributed random variables. These variables $\{\lambda_1, ..., \lambda_N\}$ are described by a probability $\mathcal{P}(\lambda_1, ..., \lambda_N) = p(\lambda_1)p(\lambda_2)...p(\lambda_N)$, meaning that the variables do not depend on one another (since the joint PDF is a product), and they are all governed by the same single-variable PDF, $p(x)$. We now introduce the cumulative distribution function,

$$F(\lambda) = \int_{-\infty}^{\lambda} \mathrm{d}\lambda' \, p(\lambda') \,, \qquad (1.173)$$

which is the probability that any random variable takes a value smaller than λ. Let us suppose we have a random variable at a given value $\lambda_j = \lambda$ and another at a position $\lambda_k = \lambda + s$ with no variables in between. The probability of this event occurring is the simultaneous occurrence of the probabilities $p(\lambda_j = \lambda)$, $p(\lambda_k = \lambda + s)$ and the probability that there is no λ_i between. Furthermore, if we want this to be true for *any* of the random variables $\{\lambda_1, ..., \lambda_N\}$, we sum over N. The (conditional) probability of this event is,

$$P(s|\text{any } \lambda_i = \lambda) = \sum_j p(\lambda)p(\lambda + s)\left[1 - (F(\lambda + s) - F(\lambda))\right]^{N-2} \qquad (1.174)$$

$$= Np(\lambda)p(\lambda + s)\left[1 - (F(\lambda + s) - F(\lambda))\right]^{N-2} \qquad (1.175)$$

where the quantity in the square brackets is the probability that there is no λ_i in the gap between λ and $\lambda + s$ for each of the remaining $N - 2$ random variables. Now, we no longer want the condition that any particular variable must sit at λ, so we

integrate,

$$P_N(s) = \int_\sigma d\lambda \, P(s|\text{any } \lambda_i = \lambda) \tag{1.176}$$

$$= N \int_\sigma d\lambda \, p(\lambda)p(\lambda + s) \left[1 + F(\lambda) - F(\lambda + s)\right]^{N-2} \tag{1.177}$$

where σ is the support (domain) of $p(\lambda)$.

Consider now the case where σ is not infinite, such as a restriction on the total maximum energy of a system. Then, as N increases, the typical spacing must shrink since more λ_i must fit in the same domain. To counter this, we make a local change of variables,

$$s = \frac{\tilde{s}}{Np(\lambda)} \tag{1.178}$$

which scales away the number of samples from our distribution and the local density of random samples. This process of rescaling the gap is sometimes called 'unfolding' (unconnected to the unfolding of catastrophes), so that the mean level spacing is equal to unity across the spectrum, regardless of the size of N, which we will now take to be very large. We can expand the $F\left(\lambda + \frac{\tilde{s}}{Np(\lambda)}\right)$ piece in a Taylor expansion, $F\left(\lambda + \frac{\tilde{s}}{Np(\lambda)}\right) \approx F(\lambda) + \frac{\tilde{s}}{Np(\lambda)}F'(\lambda) + ...$, and note that $F'(\lambda) = p(\lambda)$ which cancels the denominator of the change of variables. The term in the square brackets becomes $\left[1 - \frac{\tilde{s}}{N}\right]^{N-2} \overset{N \to \infty}{=} e^{-\tilde{s}}$. If we also only retain leading order in $p(\lambda + s) \approx p(\lambda)$, we have

$$P_{N \gg 1}(s) \approx N \int_\sigma d\lambda \, p(\lambda)^2 e^{-\tilde{s}} \tag{1.179}$$

and now we use the rule of change of variables for a PDF $[\tilde{P}(x) = P(y = x)\frac{dy}{dx}$ for some PDF $\tilde{P}$ defined on the domain of x and some other PDF P defined on the domain of $y]$, giving,

$$\tilde{P}_{N \gg 1}(\tilde{s}) = P_{N \gg 1}\left(s = \frac{\tilde{s}}{Np(\lambda)}\right)\frac{ds}{d\tilde{s}} = N\frac{1}{N}\int d\lambda \, p(\lambda)^2 \frac{1}{p(\lambda)}e^{-\tilde{s}} \tag{1.180}$$

$$= e^{-\tilde{s}} \equiv P_P(\tilde{s}) \tag{1.181}$$

where we used $\frac{ds}{d\tilde{s}} = \frac{1}{Np(\lambda)}$ and $\int d\lambda \, p(\lambda) = 1$. So in the scaling limit of $N \gg 1$, the PDF of the spacing in local units of $Np(\lambda)$ is an exponential.

This so-called "Poissonian" result is strikingly different from the Wigner surmise in the limit of small s, indicating that for random matrices spectral repulsion is common and for non-random matrix models, there is no spectral repulsion. While this analytic example only applies directly the 2×2 example, these results generalize to $N \times N$ matrices with real entries. The Wigner surmise (1.172) applies only to matrices

with real entries drawn from Gaussian distributions. If the matrix is populated with complex entries, then the expression changes somewhat (see the following section for a more general expression). In general the unfolding of the spectrum should be performed if we wish to check to see whether a matrix obeys Poisson or Wigner-Dyson statistics.
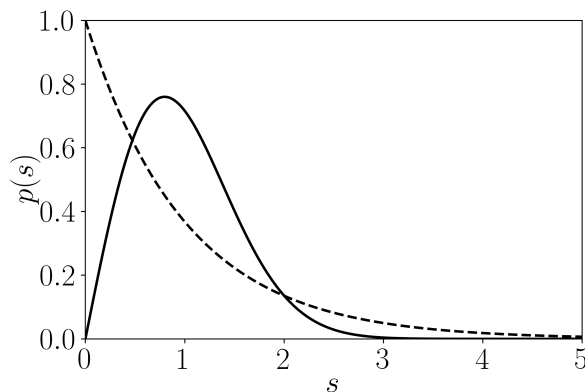

Figure 1.14: **Panel (a):** Wigner surmise, given in Eq. (1.172) is shown as a solid line, while the Poisson distribution from Eq. (1.181) is plotted as a dashed line.

There exist systems which are neither fully chaotic nor completely regular, but are of mixed type in their classical limits. In fact, these types of systems are 'generic' in that they are the more typical case in nature. The level spacing statistics function is therefore an interpolation of the Wigner and Poisson result, which is commonly known as the Berry-Robnik distribution [137],

$$P_{\mathrm{BR}}(s,q) = \left(q + \frac{1}{2}\pi(1-q)s\right)\exp\left(-qs - \frac{1}{4}\pi(1-q)s^2\right) \qquad (1.182)$$

where $q \in [0,1]$ is an interpolation parameter between Wigner and Poisson results in the semiclassical regime ($\hbar \to 0$). In the small s limit, level repulsion in the chaotic regime follows a linear power, such that $P_N(s) \propto s$. However, systems with localized chaotic eigenstates exhibit fractional power-law repulsion between the nearest energy levels [138–140] (localized in the sense that the classically chaotic components occupy less phase space than the regular components). In these cases $P(s) \propto s^{\mathcal{B}}$ with $0 < \mathcal{B} < 1$, and other measures of level-spacing statistics include the Brody distribution [141],

$$P_{\mathrm{B}}(s) = (\mathcal{B}+1)\left[\Gamma\left(\frac{\mathcal{B}+2}{\mathcal{B}+1}\right)\right]^{\mathcal{B}+1} s^{\mathcal{B}} \exp\left\{-\left[\Gamma\left(\frac{\mathcal{B}+2}{\mathcal{B}+1}\right)\right]^{\mathcal{B}+1} s^{\mathcal{B}+1}\right\}, \qquad (1.183)$$

where $\Gamma(x)$ is the Gamma factorial function, and the Izrailev distribution [142],

$$P_{\mathrm{I}}(s) = A\left(\frac{\pi s}{2}\right)^{\mathcal{B}} \exp\left[-\frac{1}{16}\mathcal{B}\pi^2 s^2 - (B - \frac{1}{4}\pi\mathcal{B})s\right] \qquad (1.184)$$

where A and B are constants determined by normalization of $P_{\mathrm{I}}(s)$ and $sP_{\mathrm{I}}(s)$. When dealing with diagnostics of chaos and spectral statistics in Paper III, we shall only be concerned with entirely chaotic or entirely regular systems, in which case the mixed-type distributions are not used. The three-mode Bose-Hubbard model discussed in Paper IV does however exhibit mixed-type behaviour described by the Berry-Robnik distribution [41], so this discussion is relevant for that model. Finally, we note that there exist integrable quantum Hamiltonians which can exhibit the Wigner spacing distribution, however this is either due to fine-tuning such that perturbations destroy the Wigner distribution [143], or finite-size effects [144].

Classification of Ensembles

Suppose we are given a random matrix,

$$X = \begin{pmatrix} x_{11} & \dots & x_{1N} \\ \vdots & \ddots & \vdots \\ x_{N1} & \dots & x_{NN} \end{pmatrix} \tag{1.185}$$

characterized by a certain joint probability density for the entries $\mathcal{P}(x_{11}, ..., x_{NN})$. In order to study 'physical' problems in this thesis, we will be restricting the class of available joint probability density functions from which the entries can be drawn. If the random matrices represent Hamiltonians, such that the eigenvalues correspond to the eigenspectrum of the system, then the first major restriction is natural: X has a real spectrum, $\{\lambda_1, ..., \lambda_N\} \in \mathbb{R}$. Therefore, the matrices studied can be classified into three ensembles which are commonly distinguished by a number β known as the "Dyson index" of the ensemble:

- Real-symmetric ($\beta = 1$)

- Complex Hermitian ($\beta = 2$)

- Quaternion self-dual ($\beta = 4$).

In physical problems, two further restrictions are often imposed:

(i) The matrices/Hamiltonians have independent entries, indicating that the joint PDF is a product of the PDF for each entry,

$$\mathcal{P}(x_{11}, ..., x_{NN}) = p_{11}(x)p_{12}(x)...p_{NN}(x) \tag{1.186}$$

For example, this includes the addition of random interactions or disorder in a system.

(ii) The joint PDF is invariant under rotations (change of basis),

$$\mathcal{P}(X)\mathrm{d}x_{11}\mathrm{d}x_{12}...\mathrm{d}x_{NN} = \mathcal{P}(X')\mathrm{d}x'_{11}\mathrm{d}x'_{12}...\mathrm{d}x'_{NN} \tag{1.187}$$

for some transformation $X' = UXU^{-1}$. This is crucial for physical systems, since the eigenspectrum cannot depend on choice of basis. If X is real symmetric, then U is orthogonal. If X is complex Hermitian, then U is unitary. If X is quaternion self-dual, then U is symplectic.

The Porter-Rosenzweig theorem [135, 145] states that the joint PDF of the matrix X is therefore restricted to,

$$\mathcal{P}(X) = \exp\left[-a\,\mathrm{tr}(X^2) + b\,\mathrm{tr}(X) + c\right] \tag{1.188}$$

where $a, b, c \in \mathbb{R}$ and $a > 0$. That is, the joint PDF must be Gaussian. Returning to the 2×2 example, note that $\mathcal{P}[X] \sim \exp\left[-\frac{1}{2}\,\mathrm{tr}(X^2)\right]$, which required the off-diagonal elements to be drawn from a Gaussian distribution with half the variance of the diagonal elements.

Thus, the classification of relevant ensembles studied in the context of chaotic models is typically reduced to the following ensembles which satisfy the Porter-Rosenzweig condition,

- Gaussian Orthogonal Ensemble (GOE) ($\beta = 1$)

- Gaussian Unitary Ensemble (GUE) ($\beta = 2$)

- Gaussian Symplectic Ensemble (GSE) ($\beta = 4$)

For the purpose of this thesis, we will not concern ourselves with the GSE. Returning to the Wigner surmise in Eq. (1.172), we can write it explicitly for the 2×2 case, which becomes,

$$p(\lambda_1, \lambda_2) = \frac{1}{2}\mathrm{e}^{-\frac{1}{4}(\lambda_1^2 + \lambda_2^2)}|\lambda_1 - \lambda_2| \tag{1.189}$$

In generic ensembles and $N \times N$ matrices, the formula becomes [135],

$$p(\lambda_1, \lambda_2, ..., \lambda_N) \propto \mathrm{e}^{-\frac{1}{2}\sum_i \lambda_i^2} \prod_{j<k} |\lambda_j - \lambda_k|^\beta . \tag{1.190}$$

The product over all $|\lambda_j - \lambda_k|$ (known as a Vandermonde determinant) is somewhat remarkable: it indicates that *all* eigenvalues are connected to each other, since the product will contain terms like $(\lambda_1 - \lambda_N)$. Furthermore, this result is intimately connected with edge physics, for example, it can be shown that Eq. (1.190) can be

reinterpreted as the partition function for the Brownian-motion of a harmonically-trapped 2D Coulomb gas [146]. For each ensemble, the level-spacing distribution generalizes as follows [136],

- GOE:

$$p_1(s) = \frac{\pi}{2} s e^{-\frac{\pi}{4} s^2} \tag{1.191}$$

- GUE:

$$p_2(s) = \frac{32}{\pi^2} s^2 e^{-\frac{4}{\pi} s^2} \tag{1.192}$$

- GSE:

$$p_4(s) = \frac{2^{18}}{3^6 \pi^3} s^4 e^{-\frac{64}{9\pi} s^2} \tag{1.193}$$

Henceforth, we will refer to the distributions in Eqs. (1.191)-(1.193) as 'Wigner-Dyson' distributions for level spacings. $p_1(s)$ and $p_2(s)$ are plotted in Fig. 1.15 panels (a)-(b), respectively, along with the eigenvalue spacings for a single matrix from each ensemble. The most noticeable distinction between each is the different integer exponent representing power-law repulsion, s^β, at low spacing size. In each case, an 'unfolding' of the spectrum is required to match the curves with the data by dividing the numerically calculated eigenvalues by their local density.

The average spectral density $\rho_N(\lambda)$, which measures the distribution of the eigenvalues of an $N \times N$ random matrix is generally impossible to compute for finite N. However, as $N \to \infty$, it follows Wigner's semicircle law, which we shall simply state here,

$$\rho_{N \to \infty}(\lambda, \beta) = \frac{1}{\beta \pi} \sqrt{2\beta - \lambda^2} \tag{1.194}$$

where again β is the Dyson index of the ensemble. For a proof of the semicircle law, see Appendix A. The semicircle law is displayed in Fig. 1.15 (c) for both the GOE and GUE ensembles and compared to a randomly generated matrix from each ensemble.

Oganesyan and Huse introduced a useful method of characterizing each spacing distribution function in terms a single number which does not require 'unfolding' of the spectrum, the consecutive spacing ratio [148],

$$r = \frac{1}{\mathcal{D}} \sum_{n=1}^{\mathcal{D}} r_n \qquad , \qquad r_n = \frac{\min[s_n, s_{n-1}]}{\max[s_n, s_{n-1}]} \tag{1.195}$$

which sums the ratios of all the gaps in the spectrum: $s_n = \lambda_{n+1} - \lambda_n$, with Hilbert space dimension $\mathcal{D}$. The analytic values for the ratio r have been calculated for each ensemble, including for a Poisson spectrum [149, 150]:

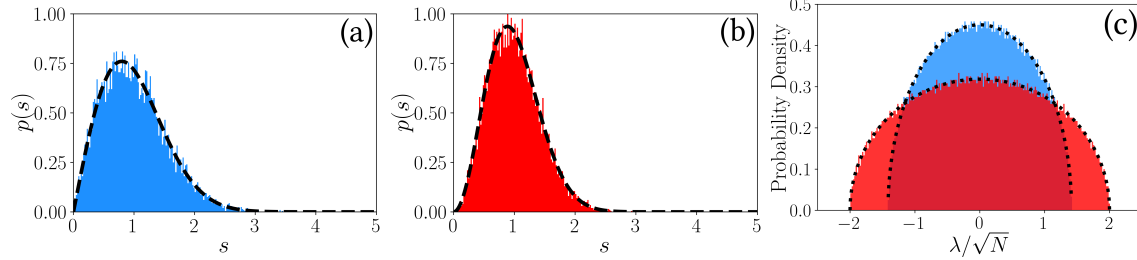- Poisson: $r_P = 2\ln 2 - 1 \approx 0.38629$

Figure 1.15: Eigenvalue statistics for GOE and GUE matrices. In every panel, a single square matrix of size $N = 10^4$ was generated for each ensemble. **Panel (a):** Eigenvalue spacing for the GOE. The Wigner-Dyson distribution $p_1(s)$ is plotted as a dashed line over the histogram. **Panel (b):** Eigenvalue spacing for the GUE. The Wigner-Dyson distribution $p_2(s)$ is plotted as a dashed line. **Panel (c):** Semicircle law for the average spectral density in both the GOE (blue) and GUE (red). Eq. (1.194) is plotted as a dashed line for both ensembles, showing excellent agreement even for a single matrix.

- GOE: $r_1 = 4 - 2\sqrt{3} \approx 0.53590$

- GUE: $r_2 = \frac{2\sqrt{3}}{\pi} - \frac{1}{2} \approx 0.60266$

- GSE: $r_4 = \frac{32\sqrt{3}}{15\pi} - \frac{1}{2} \approx 0.67617$

This ratio therefore allows for a precise statistical test for proximity to a particular ensemble, which we use in Paper III.

In a 1962 paper, Dyson objected to condition (i) above that each $p_{ij}(x)$ be statistically independent absent some physical motivation, since it is impossible to establish a uniform probability distribution on an infinite range (and hence some restriction on $|x_{ij}|$ is necessary). Thus, he proposed instead the introduction of ensembles which replace the symmetric/Hermitian/self-dual matrix X with some orthogonal/unitary/symplectic matrix U whose eigenvalues are distributed on a line/ring/circle. For this reason, these ensembles are given the name 'circular' to replace 'Gaussian' above, and for shorthand will be called COE, CUE, and CSE, respectively. For our purposes in Paper III, however, the results are easily transferable between ensembles, indeed in the limit of large matrix dimension N they give identical behaviour [135], and the relation $U = \exp[-iXt]$ is useful to keep in mind (although Dyson warns against considering this relation to be strictly true).

1.3.2 The Out-of-time-ordered Correlator

In the study of chaos in quantum systems, the use of RMT is largely restricted to static properties, i.e. properties of the spectrum, or relaxation values, and does not act

as a dynamic diagnostic tool for chaos. For this purpose, we introduce a correlation function known as the out-of-time-ordered commutator,

$$C(x,t) \equiv \left\langle \left[\hat{A}(x,t), \hat{B} \right]^{\dagger} \left[\hat{A}(x,t), \hat{B} \right] \right\rangle , \qquad (1.196)$$

where the evaluation of the expectation value $\langle ... \rangle = \mathrm{Tr}\left[\hat{\rho}\,... \right]$ is dependent on the state prepared for measurement, and is often labelled $\langle ... \rangle_{\beta}$ if $\hat{\rho}$ is a Gibbs thermal state with inverse temperature β. The commutator (1.196) was first introduced by Larkin and Ovchinnikov [151] in 1969, but has been more recently revived in the context of quantum information scrambling [152–154] as a measure of chaos in conformal field theory [155]. If the operators $\hat{A}$ and $\hat{B}$ are unitary and Hermitian, one can write,

$$C(x,t) = 2 \left(1 - \mathrm{Re}\left[F(x,t) \right] \right) \qquad (1.197)$$

where the out-of-time-ordered *correlator* (OTOC) is[2],

$$F(x,t) = \langle \hat{A}(x,t)\hat{B}\hat{A}(x,t)\hat{B} \rangle . \qquad (1.198)$$

Typically, the operators $\hat{A}$ and $\hat{B}$ are also selected such that $\left[\hat{A}(x,0), \hat{B} \right] = 0$. For spatially extended systems, such as spin chains, where the operators $\hat{A}(x,0)$ and $\hat{B}$ only have local support, the OTOC can therefore be a measure of information propagation across nonlocal degrees of freedom. The growth of $F(x,t)$ from 0 implies that the support of both operators begins to mix after a certain amount of time, and they lose their ability to commute.
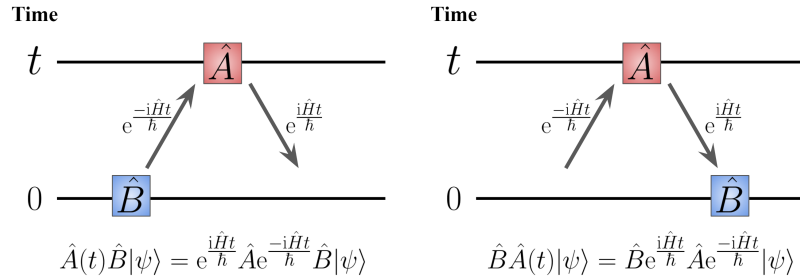

Figure 1.16: Visualization of the OTOC, with time on the vertical axis but application of operators read left to right. On the left, we first apply $\hat{B}$ at time $t = 0$ followed by $\hat{A}$ at time t. On the right, $\hat{A}$ is applied at time t, and then $\hat{B}$ is applied after returning to $t = 0$. The OTOC is the overlap of these two scenarios.

A visualization of the correlator (1.198) as a measure of sensitivity to perturbations can be seen in Fig. 1.16. An OTOC can be thought to be an overlap of the states

---

[2]There is some indecision in the literature as to whether the acronym "OTOC" should refer to the commutator in Eq. (1.196) or the four-point correlation function in Eq. (1.198), since for most operators, both give equivalent information. Here, we shall use the latter convention, unless otherwise noted.

$\hat{A}(t)\hat{B}|\psi\rangle$ (with the spatial degree of freedom suppressed for now) and $\hat{B}\hat{A}(t)|\psi\rangle$. In the first case, we apply $\hat{B}$ at time $t = 0$, evolve forward in time, apply $\hat{A}$, and then backward in time. The second state requires time evolution first to time t, apply operator $\hat{A}$, evolve back to $t = 0$, and then apply $\hat{B}$. Scrambling occurs when this overlap is small, that is, the system is highly sensitive to the order of the operators $\hat{A}$ and $\hat{B}$ on $|\psi\rangle$ after forward and backward time-evolution [154, 157].

Classically, when we consider the exponential sensitivity of trajectories with respect to initial conditions to define a Lyapunov exponent, we can replace the variation with a Poisson bracket,

$$\frac{\partial x(t)}{\partial x_0} = \{x(t), p_0\} \tag{1.199}$$

where $\{A, B\} = \frac{\partial A}{\partial x_0}\frac{\partial B}{\partial p_0} - \frac{\partial A}{\partial p_0}\frac{\partial B}{\partial x_0}$. However, if we are interested in some sort of phase-space average, then it is possible that although for chaotic models, $\frac{\partial x(t)}{\partial x_0} \sim e^{\lambda t}$, the average is zero from cancellations due to some symmetries. Therefore it is preferable to compute the square,

$$\left(\frac{\partial x(t)}{\partial x_0}\right)^2 = |\{x(t), p_0\}|^2 \sim e^{2\lambda t} \tag{1.200}$$

and proceed to average over phase space. In general, we expect this behaviour to carry over to functions of phase space parameters: $|\{W(t), V\}|^2 \sim e^{2\lambda t}$. In the semiclassical limit, the commutator of operators $\hat{A}$ and $\hat{B}$ approaches the Poisson bracket of phase-space functions A and B [158],

$$\frac{1}{i\hbar}\left[\hat{A}(t), \hat{B}\right] \quad \overset{\hbar \lesssim 1}{\Rightarrow} \quad \{A(t), B\} \ . \tag{1.201}$$

Through this, one can define a quantum version of the Lyapunov exponent through early-time exponential growth of the OTOC [152, 154, 157, 159],

$$C(x, t) \sim e^{\lambda_Q t} \tag{1.202}$$

and hence a quantum analogue of the butterfly effect. This exponent, which is not necessarily equal to (twice) its classical counterpart [156], is conjectured to have the bound [154],

$$\lambda_Q \leq \frac{2\pi}{\hbar\beta} \tag{1.203}$$

where β is the inverse temperature. Systems which saturate this bound are known as 'fast scramblers' [160, 161], and display a holographic duality to a black hole [154, 164, 165], an example of which is the Sachdev-Ye-Kitaev model [162, 163]. The quantum Lyapunov exponent is also conjectured to reach a maximum at a quantum critical point [164].

The existence of a nonzero Lyapunov exponent from an OTOC does not necessarily imply a chaotic system, but rather an instability. For example, the inverted harmonic oscillator will exhibit an exponential sensitivity to initial condition, since a perturbation on either side of the unstable point will lead to drastically different behaviour. This effect is replicated in the quantum inverted harmonic oscillator [168], but also in the Lipkin-Meshkov-Glick (LMG) model and the regular phase of the Dicke model [166, 167]. The OTOC can also be exponentially sensitive in quantum systems near a phase transition [169]. This indicates that the OTOC as a diagnostic tool must be treated with some care to avoid 'false flags' in regular systems.

1.3.3   Time Scales

There are a number of important timescales which are relevant to chaotic models, the details of which are still being studied and developed. We shall list a few of the timescales relevant to the problems studied in the remainder of the thesis. In particular, we make use of the early-growth time scales in Paper II, while in Paper III we focus on the Thouless time and relaxation time scales for generalized OTOCs.

In the case of an OTOC for a system with spatial extent, there is an early-time growth which is a power law,

$$C(x,t) \sim \frac{1}{x!} t^{ax} \tag{1.204}$$

where a is a constant. This was originally demonstrated by Lin and Motrunich [170], who argued that it follows directly from the Baker-Campbell-Hausdorff formula,

$$\hat{A}(t) = \hat{A} + \mathrm{i}t \left[\hat{H}, \hat{A} \right] + \frac{(\mathrm{i}t)^2}{2!} \left[\hat{H}, \left[\hat{H}, \hat{A} \right] \right] + ... \tag{1.205}$$

Inserting this into the out-of-time-ordered commutator $C(x,t)$, it becomes evident that the first nonzero term will correspond to that for which the coefficient is $\frac{1}{x!} t^{ax}$. This time scale has been called the 'perturbative' regime [171] and the universal form has been found to hold independent of integrability conditions [172–174].

Following the power-law growth, there is an "early growth" region which precedes the light-cone described in Sec. 1.1.8. This early growth has been conjectured by Xu and Swingle [171], and separately derived by Khemani *et al.* [175] to be of the form,

$$C(x,t) \sim \exp \left[-\lambda_L \frac{(x/v_B - t)^{1+p}}{t^p} \right] . \tag{1.206}$$

where v_B is the 'butterfly velocity', which is a speed at which the OTOC wavefront moves and may be (but not necessarily) equal to the Lieb-Robinson velocity v_{LR}. The exponent p corresponds to an index which depends on the integrability of the model

under consideration. In Paper II, we demonstrate that the $p = 1/2$ case for integrable models can be motivated by catastrophe theory arguments, since the local structure of the wavefront is guaranteed to be an Airy function. One can perform an asymptotic expansion in the 'dark' region of the Airy function to arrive at the analytic form in Eq. (1.206). Models which exhibit $p = 0$ behaviour are 'Lyapunov-like' [175], since there is en explicit exponential growth at $x = v_B t$ and hence one may be tempted to designate such models as chaotic, however $p = 0$ is not necessarily guaranteed to be the case for chaotic models [175], nor is there a well-agreed upon value for p in specific regimes.
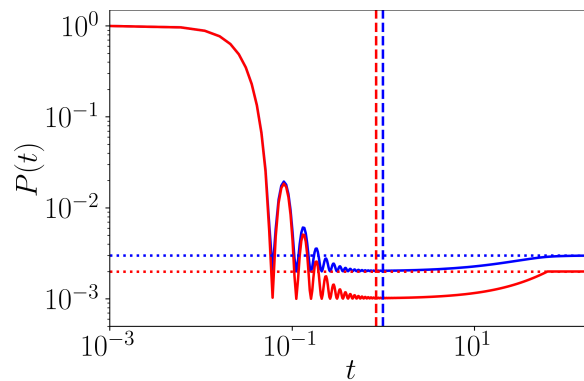

Figure 1.17: Analytic survival probability for random matrices of size 1000×1000 in the GOE (blue, solid) and GUE (red, solid) ensembles, given by Eq. (1.208). The corresponding Thouless times are shown as vertical dashed lines in the same colour of the appropriate ensemble. Saturation values for each ensemble are shown as horizontal dotted lines.

The next important timescale we consider is the Thouless time, t_{Th}, which is the timescale at which the system begins to follow universal RMT forms. The Thouless time was originally introduced to represent the timescale at which a particle can diffuse through and reach the boundary of a disordered conductor [177]. In the context of a return probability for a chaotic system, t_{Th} corresponds to time at which the bottom of the 'correlation hole' is reached [178–180], and the survival probability ramps towards its relaxation value predicted by RMT. In Ref. [182], it is shown that the correlation hole is a feature which is an dynamical manifestation of the level repulsion (i.e. correlations between the eigenvalues) in a chaotic model, as a result of the presence of a 'two-level form factor' appearing in the return probability. In Ref. [176], Alhassid and Levine show that for a Hamiltonian in a Gaussian ensemble, the survival probability $P(t) = |\langle \psi(t)|\psi(0)\rangle|^2$ is,

$$P(t) = \frac{1}{N} \left[2\pi\bar{\rho}\delta(t) + \frac{\beta + 2}{\beta} - b_2\left(\frac{t}{2\pi\bar{\rho}}\right) \right] \qquad (1.207)$$

where N is the linear size of the Hilbert space, β is the Dyson index for the ensemble, $\bar{\rho}$ is the average density of states, and $b_2(x)$ is the two-level form factor, which is the Fourier transform of $Y_2(\omega)$, the two-level cluster function which describes how two eigenvalues 'cluster' in a random matrix [135].

If one chooses a Hamiltonian which consists of a full random matrix from a Gaussian ensemble with an initial semicircular distribution, the density of states has width $\sqrt{2\beta N}$ times some characteristic energy scale call it E (the nature of E is irrelevant, since the matrix is completely random, populated elements drawn from normalized Gaussian distributions). In this case, the survival probability becomes (for $N \gg 1$) [178, 180],

$$P(t) = \frac{1 - \bar{P}}{N} \left[N \frac{J_1^2(\sqrt{2\beta N}t)}{(\sqrt{2\beta N}t)^2} - b_2\left(\frac{\sqrt{2\beta N}t}{2N} \right) \right] + \bar{P} \tag{1.208}$$

where $\bar{P} = (\beta + 2)/(N\beta)$ is the long-time average which is the middle term of Eq. (1.207). The first term has now become $\propto J_1^2(\sqrt{2\beta N}t)/t^2$, where $J_1(x)$ is a Bessel function of the first kind, from the Fourier transform of the semicircle [180, 181]. This term introduces oscillations in the return probability at early times, however the tail end of this piece decays $\sim 1/t^3$ as one enters the correlation hole.

The relevant piece for the correlation hole is the term containing the two-level form factor b_2. Assuming that $N \ll \sqrt{N}t \ll 1$, we approximate the two-level form factor for small arguments ($x \ll 1$) [135, 176],

$$b_2(x) \approx 1 - \frac{2x}{\beta} \tag{1.209}$$

and replace the Bessel function with its late time decay $J_1^2(\sqrt{2\beta N}t)/t^2 \sim 1/t^3$, so that minimizing the return probability $P(t)$ with respect to t gives t_{Th}, since it will occur at the bottom of the correlation hole. For explicit details of this calculation in the GOE ensemble, see Refs. [178, 180, 181]. The resulting Thouless times in each ensemble are then (still in units of E),

$$t_{\text{Th}}^{\text{GOE}} = \left(\frac{3}{\pi} \right)^{\frac{1}{4}} \tag{1.210}$$

$$t_{\text{Th}}^{\text{GUE}} = \left(\frac{3}{2\pi} \right)^{\frac{1}{4}} . \tag{1.211}$$

Fig. 1.17 shows the analytic $P(t)$ for full random matrices in both the GOE and GUE ensembles of size 1000×1000 as blue and red curves, respectively, with the respective Thouless times shown as dashed lines in the same colour. From this figure,

the geometric meaning of the correlation hole becomes clear, and after t_{Th} is crossed, the return probability ramps towards its saturation value.

The saturation values are, for $N \gg 1$,

$$\bar{P}^{\text{GOE}} \approx \frac{3}{N} \tag{1.212}$$

$$\bar{P}^{\text{GUE}} \approx \frac{2}{N} \tag{1.213}$$

and are shown in Fig. 1.17 as horizontal dotted lines in blue and red, respectively. In a more generic system, it is likely that any individual survival probability will fluctuate relatively strongly around any of these curves, and so the average over many realizations will converge to $P(t)$ [180]. The relaxation time, t_R is therefore the time at which one would expect an observable such as the survival probability to fluctuate about its saturation value. At this time, there is no analytic prediction for a value that is independent of tuneable parameters [178], however it appears to be on the order $\sim 10^2$ where the solid curves and dashed horizontal lines meet.

In Paper II, rather than studying a chaotic system directly, we study how generalizations of the OTOC can give the appearance of the markers of chaos mentioned above, by rewriting the OTOC as a survival probability. We therefore use t_{Th} as an estimate for the time at which the generalized OTOC will falsely give a positive chaotic result, and therefore be the time at which chaos 'kicks in' for our probe. The values for the Thouless time (1.210)-(1.211) apply to the system we study, the Bose-Josephson junction coupled to an atomic quantum dot, since the size of the Hilbert space is $\propto N$. For systems which have an exponential Hilbert-space scaling, the expressions (1.210)-(1.211) become no longer valid, and the Thouless time grows exponentially with N, as will the relaxation time.

1.3.4   OTOCs as probes of phase transitions

In this final section we briefly describe some results from Ref. [34]. This work brings together elements from many previous sections by using the OTOC for a single two-level impurity (qubit) connected to a Bose-Josephson junction as a dynamical probe to measure an equilibrium phase transition. The Hamiltonian for the system is,

$$\hat{H} = U\hat{S}_z^2 - 2J\hat{S}_x - NJ^a\hat{\sigma}_x + W\hat{S}_z\hat{\sigma}_z \tag{1.214}$$

where, as usual in the Schwinger prescription, the operators $\hat{S}_\alpha$ correspond to $SU(2)$ spin operators which act on the bosons from Eqs. (1.24)-(1.26), and the $\hat{\sigma}_\alpha$ operators correspond to operators which act on the single two-level system from Eqs. (1.31)-(1.33). U and J correspond to interaction and hopping energies for the N bosons,
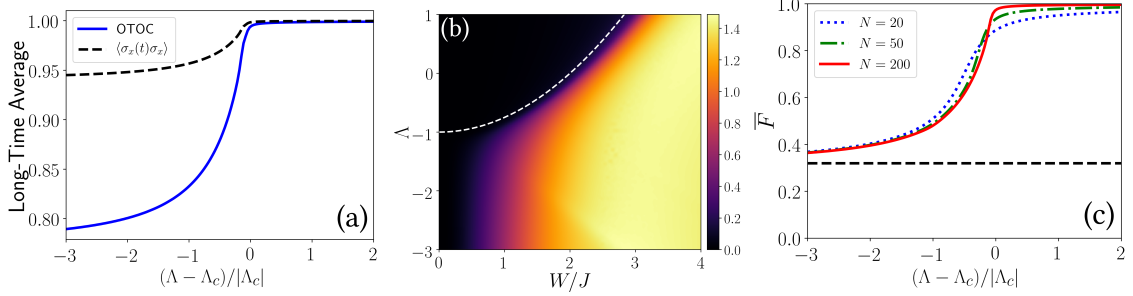
Figure 1.18: OTOC for a qubit probe of the Bose-Josephson junction. **Panel (a):** The long-time average of the OTOC (blue, solid) and long-time average of the two-point correlator (black, dashed) as a function of a reduced critical parameter $(\Lambda - \Lambda_c)/|\Lambda_c|$. Here, $J^a = W = J$ **Panel (b):** Out-of-time-ordered commutator $\overline{C(t)} = 2(1 - \text{Re}[\overline{F}])$ in Λ vs. W/J phase space. Eq. (1.215) is shown as a white dashed curve denoting the phase boundaries. In this panel, $J^a = J$. **Panel (c):** Long-time average of the OTOC as a function of the reduced critical parameter for different boson numbers N. The limit $\overline{F}_{\Lambda \to -\infty}$ is shown as a black dashed line. Here, $J^a = W = J$.

respectively, while J^a is the hopping energy for the qubit, and W is the boson-qubit interaction energy.

Defining, as usual, the critical parameter $\Lambda \equiv UN/(2J)$, there is a $\mathbb{Z}_2$ symmetry breaking transition at $\Lambda = -1$ where the bosons tend to clump in one well or another. With the addition of the qubit, the critical point moves to [31],

$$\Lambda_c = \frac{W^2}{4J^a J} - 1 \tag{1.215}$$

Here, we consider using the OTOC for the qubit,

$$F(t) = \langle \hat{\sigma}_x(t)\hat{\sigma}_x\hat{\sigma}_x(t)\hat{\sigma}_x \rangle \tag{1.216}$$

where $\hat{\sigma}_x(t) = e^{i\hat{H}t}\hat{\sigma}_x e^{-i\hat{H}t}$, and the expectation value $\langle ... \rangle$ here was taken with respect to the ground state of $\hat{H}$. We make use of the long-time average,

$$\overline{F} = \lim_{T \to \infty} \frac{1}{T} \int_0^T dt\, F(t) , \tag{1.217}$$

to detect the quantum phase transition. As shown in Fig. 1.18 (a), the long-time average of the OTOC is more sensitive than the two-point correlator $\overline{\langle \hat{\sigma}_x(t)\hat{\sigma}_x \rangle}$, hence is more sensitive in measuring the phase transition.

Panel (b) of Fig. 1.18 shows the time averaged out-of-time-ordered commutator $\overline{C(t)} = 2(1 - \text{Re}[\overline{F}])$, which carries identical information to the OTOC, in the phase space of Λ and W. The OTOC clearly acts as a good probe for the phase transition boundary described by Eq. (1.215), since the OTOC changes drastically from $\overline{F} \approx 1$

for $\Lambda > \Lambda_c$ to $\overline{F} < 1$ below. The OTOC lacks sensitivity near the $W = 0$ axis, but this is expected since this would correspond to a qubit probe which is completely uncoupled from the system (and hence is no probe at all). The remaining extremes of this phase diagram can be explained in the following way. First, in the $\Lambda \to \infty$ limit, the Hamiltonian becomes dominated by the $\hat{S}_z^2$ term and since $[\hat{H}, \sigma_x] = 0$, then there is no dynamics. The OTOC becomes $\overline{F}_{\Lambda \to +\infty} = \langle (\hat{\sigma}_x)^4 \rangle = 1$. In the opposite extreme, $\Lambda \to -\infty$, the symmetry broken phase corresponds to $\langle \hat{S}_z \rangle = \pm N/2$, thus since the OTOC is evaluated in the ground state of $\hat{H}$, the effective Hamiltonian for the qubit becomes $\hat{H} = -J^a N \hat{\sigma}_x \pm W N \hat{\sigma}_z$. It is possible to calculate $F(t)$ from this expression, and taking the long-time limit gives,

$$\overline{F}_{\Lambda \to -\infty} = \frac{8 J^{a2}(2 J^{a2} - W^2)}{(4 J^{a2} + W^2)^2} \tag{1.218}$$

Fig. 1.18 shows that the long-time average of the OTOC saturates relatively quickly to the two limits $\overline{F}_{\Lambda \to \pm \infty}$ on either side of Λ_c, even for modest N, again demonstrating the sensitivity of OTOCs to quantum phase transitions.

In order to deduce the long-time saturation value of the OTOC, we follow the process outlined in Ref. [183]. Starting with,

$$F(t) = \langle \Psi_0 | e^{i\hat{H}t} \hat{B}^\dagger e^{-i\hat{H}t} \hat{A}^\dagger e^{i\hat{H}t} \hat{B} e^{-i\hat{H}t} \hat{A} | \Psi_0 \rangle \ , \tag{1.219}$$

we insert a resolution of the identity, $\sum_\gamma |\Psi_\gamma\rangle \langle \Psi_\gamma| = \mathbb{1}$, where $\{|\Psi_\gamma\rangle\}$ are the eigenstates of $\hat{H}$, between each of the operators,

$$F(t) = \sum_{\alpha\beta\gamma\delta\epsilon\zeta\eta} \langle \Psi_0| e^{i\hat{H}t} |\Psi_\alpha\rangle \langle \Psi_\alpha| \hat{B}^\dagger |\Psi_\beta\rangle \langle \Psi_\beta| e^{-i\hat{H}t} |\Psi_\gamma\rangle \langle \Psi_\gamma| \hat{A}^\dagger |\Psi_\delta\rangle \langle \Psi_\delta| e^{i\hat{H}t} |\Psi_\epsilon\rangle \langle \Psi_\epsilon| \hat{B} |\Psi_\zeta\rangle$$

$$\tag{1.220}$$

$$\times \langle \Psi_\zeta| e^{-i\hat{H}t} |\Psi_\eta\rangle \langle \Psi_\eta| \hat{A} |\Psi_0\rangle$$

$$= \sum_{\beta\delta\zeta} e^{it(E_0 - E_\beta + E_\delta - E_\zeta)} (B^\dagger)_{0\beta} (A^\dagger)_{\beta\delta} B_{\delta\zeta} A_{\zeta 0} \tag{1.221}$$

Since we are using $\hat{A} = \hat{B} = \hat{\sigma}_x$, and defining $(\hat{\sigma}_x)_{ab} \equiv \sigma_{ab}$,

$$F(t) = \sum_{\alpha\delta\zeta} e^{it(E_0 - E_\alpha + E_\delta - E_\zeta)} \sigma_{0\alpha} \sigma_{\alpha\delta} \sigma_{\delta\zeta} \sigma_{\zeta 0} \tag{1.222}$$

In the normal phase, essentially all matrix elements except one are small. We can take, for example, $W \ll U$, leading to a product state $|\Psi_0\rangle \approx |\psi_0\rangle_B \otimes |X\rangle$, where $|X\rangle$ is the $+1$ eigenstate of $\hat{\sigma}_x$. This leads to a normal phase where $\sigma_{00} \sim \mathcal{O}(1)$, and all other matrix elements $\ll 1$.

The other extreme which leads to equilibration is that a large number of eigenstates are coupled together in such a way that the phases completely decohere and $F(t \to \infty) = 0$. This result is a fully 'scrambled' system [155], however it is not visible within our model here, primarily due to the incredibly small backaction from a single qubit on the N bosons. Although the system studied here is chaotic due to the impurity, it is in a sense 'weak' chaos. Partial revivals occur for long timescales $\sim \mathcal{O}(10^5)$ (in units of J), and only a small number of central eigenstates obey Wigner-Dyson statistics [32].

There are a number of questions as to how weak chaos can lead to equilibration in this system by ensuring more eigenstates are coupled in Eq. (1.222). A natural approach is to change the coupling strength W such that the qubit probe has a stronger effect on the bosons. A convenient measure of how $\hat{\sigma}_x$ couples different eigenstates together is the participation ratio,

$$\mathrm{PR}(|\Psi_0\rangle) = \left(\sum_n |\langle \Psi_n | \hat{\sigma}_x | \Psi_0 \rangle|^4 \right)^{-1} . \tag{1.223}$$

The participation ratio is also useful for predicting the long-time equilibration of the survival probability in chaotic systems [184] when averaged over an entire basis, i.e. $\sum_m \mathrm{PR}(|\Psi_m\rangle) = \bar{P}$, which we make use of in Paper III. $\mathrm{PR}(|\Psi_i\rangle)$ also reaches a maximum in a chaotic system at the Thouless time t_{Th} [178]. In this case, we use it to quantify how many states are coupled by the operators $\hat{\sigma}_x$, and relate it to the long-time average of the variance of the OTOC,

$$\overline{(\Delta F)^2} = \lim_{T \to \infty} \frac{1}{T} \int_0^T \mathrm{d}t \left(\bar{F} - F(t) \right)^2 . \tag{1.224}$$

In Fig. 1.19 (a), we show the logged participation ratio, $\ln[\mathrm{PR}(|\Psi_0\rangle)]$, in the plane of the interaction strength and critical parameter. For each W, there is a peak of the participation ratio at some value of Λ. We plot all of these peaks in panel (b) along with $\overline{(\Delta F)^2}$ at the same values of (Λ, W), and show that a high participation ratio generally correlates to low fluctuations in the OTOC. Panel (c) shows a sample where a relatively 'ideal' value of $W = 7J$ corresponds to an OTOC with a small variation, while a 'non-ideal' example choice of $W = 50J$ has a much larger variation. The choice with the smaller variance ($W = 7J$), which we might expect to be closer to equilibrium, does not oscillate around $F(t) = 0$ (i.e. scrambling), while the $W = 50J$ case does.

One can attempt to deduce a Lyapunov exponent by evaluating the OTOC using a thermal Gibbs ensemble at inverse temperature β to see how close the system comes
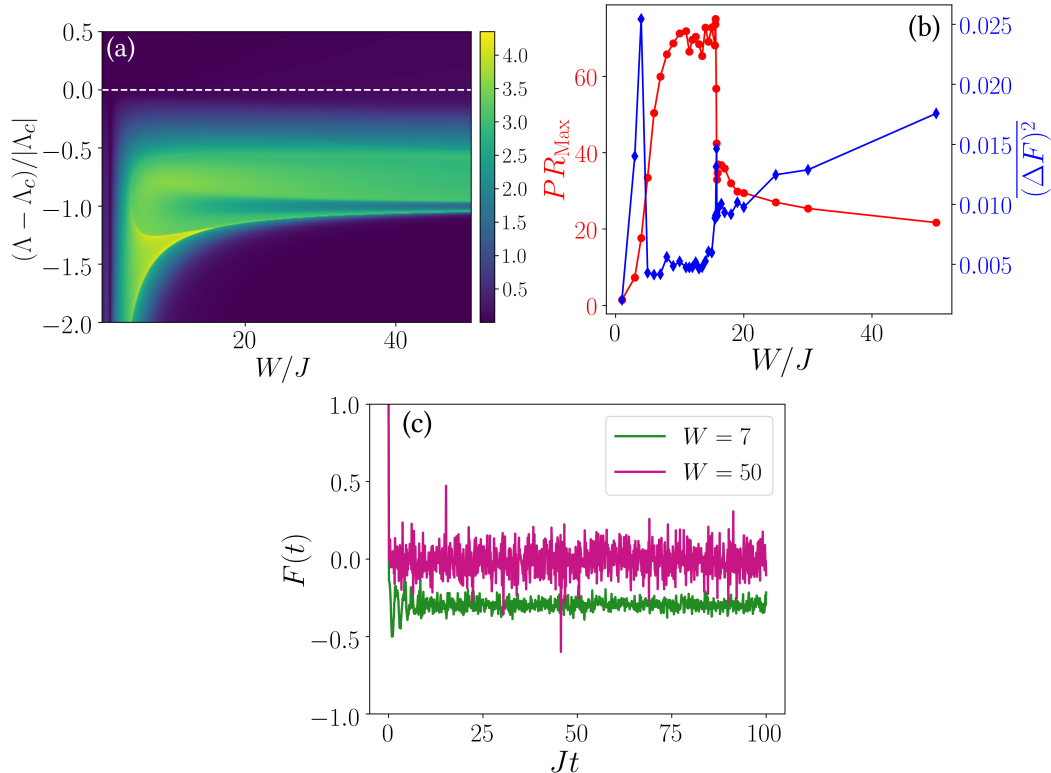
Figure 1.19: Coupling of eigenstates by the OTOC. **Panel (a):** The logged participation ratio $\ln[\mathrm{PR}(|\Psi_0\rangle)]$ as a function of Λ and W. **Panel (b):** Peak participation ratio (selected along the W axis from panel (a)) and the variance $\overline{(\Delta F)^2}$ plotted on the same axes. **Panel (c):** OTOC $F(t)$ for two choices, one with a high participation ratio ($W = 7J$) and one with a low participation ratio ($W = 50J$).

to the bound in Eq. 1.203. In Fig. 1.20 (a), we show the Lyapunov exponent λ_L as a function of the critical parameter Λ (calculated in the same way as was performed in Ref. [164] for longer Bose-Hubbard chain) with $W = J = J^a$, such that $\Lambda_c = -3/4$, and inverse temperature $\beta J = 1$. $F(t)$ is shown for different Λ in panel (b). We see that unlike in Ref. [164], there is no apparent approach of the bound proposed by Maldacena *et al.* [154] for a strong scrambler, reinforcing the notion that this system is only weakly chaotic.

There are some remaining questions as to which diagnostics we have discussed in this section are useful for general weakly chaotic systems. The Bose-Josephson junction connected to a qubit provides an interesting testbed for these diagnostic tools.
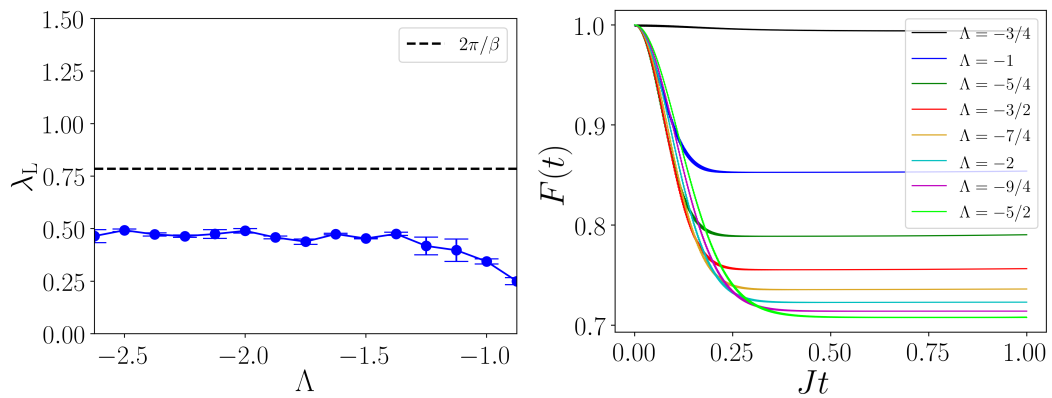
Figure 1.20: Signals of weak chaos. **Panel (a):** Lyapunov exponent calculated from the OTOCs in panel (b). **Panel (b):** The OTOC $F(t)$ for a variety of Λ at $W = J = J^a = 1$, $N = 1000$, and inverse temperature $\beta J = 1$. The decay from $F(t) = 1$ is used to calculate λ_L according to the scheme outlined in Ref. [164].

LIGHT-CONES AS QUANTUM CAUSTICS

In Section 1.1.7, we outlined a general procedure for diagonalizing one-dimensional spin chains using fermion operators via the Jordan-Wigner and Bogoliubov transformations. Using this representation, it is possible to study how local perturbations propagate through the system at a finite velocity as a consequence of the Lieb-Robinson bound (Section 1.1.8), resulting in a 'quantum light cone'. The Lieb-Robinson speed, given by Eq. (1.120), is calculated by maximizing the quasiparticle group velocity, which is mathematically identical to the caustic condition,

$$\frac{\partial \Phi}{\partial k} = \frac{\partial^2 \Phi}{\partial k^2} = 0 \tag{2.1}$$

where $\Phi = \epsilon_k + \ell(k)$, ϵ_k is the quasiparticle dispersion, $\ell(k)$ is at most a linear function of quasiparticle momentum k.

In this paper, we make use of the anisotropic XY model in two limits, and show that catastrophe theory predicts the functional form of the quantum light cone. By creating a single Bogoliubov fermion at a particular site ($x = 0$) and evolving forward

in time, we show that the light cone takes the form of a diffraction integral,

$$\langle x|e^{-i\hat{H}t}\hat{b}_0^\dagger|0\rangle \propto \int dk \; e^{i\Phi(k;x,t)} \tag{2.2}$$

where now $\Phi(k; x, t) = kx - \epsilon_k$ plays the role of a catastrophe function.

By making use of catastrophe theory, we able to put on firm mathematical footing the local description of a light cone as an Airy function. Furthermore, to our knowledge we are the first to correctly predict the functional form of a secondary light cone in the XY model as a Pearcey function. Next, we identify an array of phase dislocations contained within the light cone. In the continuum limit, these are phase singularities (vortex-antivortex pairs), while in the second-quantized limit they correspond to phase-jumps. These dislocations are sensitive to the equilibrium phase transition, and we connect them to critical scaling exponents in a dynamic setting.

Quantum caustics and the hierarchy of light cones in quenched spin chains

W. Kirkby ⬤,[1] J. Mumford ⬤,[1,2] and D. H. J. O'Dell ⬤[1,*]

[1]*Department of Physics and Astronomy, McMaster University, 1280 Main St. W., Hamilton, Ontario, Canada L8S 4M1*
[2]*School of Arts and Sciences, Red Deer College, 100 College Blvd., Red Deer, Alberta, Canada T4N 5H5*

We show that the light conelike structures that form in spin chains after a quench are quantum caustics. Their natural description is in terms of catastrophe theory and this implies (1) a hierarchy of light cone structures corresponding to the different catastrophes, (2) dressing by characteristic wave functions that obey scaling laws determined by the Arnol'd and Berry indices, and (3) a network of vortex-antivortex pairs in space-time inside the cone. We illustrate the theory by giving explicit calculations for the transverse field Ising model and the XY model, finding fold catastrophes dressed by the Airy functions and cusp catastrophes dressed by the Pearcey functions; multisite correlation functions are described by higher catastrophes such as the hyperbolic umbilic. Furthermore, we find that the vortex pairs created inside the cone are sensitive to phase transitions in these spin models with their rate of production being determined by the dynamical critical exponent. More broadly, this work illustrates how catastrophe theory can be applied to singularities in quantum fields.

I. INTRODUCTION

According to Lieb and Robinson [1], there is a maximum speed v_{LR} at which information can propagate in discrete quantum systems that obey the Schrödinger equation and have short range interactions. This is a powerful and generic statement because it implies that, despite the fact there is no intrinsic speed limit in the (nonrelativisitic) Schrödinger equation, the response of these many-particle systems to a sudden quench should be in terms of a light conelike time evolution of spatial correlations [2]. Physically, the "light cone" arises from the maximum group velocity of quasiparticles that are excited by the quench and that subsequently propagate through the sample [3]. Sophisticated methods of analysis have been applied to these quench problems including conformal field theory and tensor networks [3–16], and the theory has been tested in experiments on ultracold atoms [17–19] and ions [20,21] where quantum spin models [18,22–25], the Bose-Hubbard (BH) model [26–29], 1D systems [30–32], and quantum walks on a lattice [33,34] can all be realized. The long coherence times of atomic systems make them particularly suited to studying such dynamics [35,36], and the ability to perform single-site manipulation and detection [37–40] has enabled unprecedented preparation and visualization of the relevant local observables.

In this paper, we show that light cones in quenched spin chains are *quantum caustics*. These are quantum versions of wave focusing phenomena that occur widely in nature in the form of rainbows [41], ship wakes [42–44], tsunamis and tidal

bores [45], and Cherenkov radiation [46] (including superfluid analogs [47–49]). In the geometric ray theory, caustics occur where two or more rays coalesce, giving regions in space where the intensity diverges. By virtue of their singular nature, the natural mathematical description of caustics is via catastrophe theory which partitions them into a hierarchy of equivalence classes, each of which is structurally stable and has its own set of scaling relations [50–52]. To show specifically how this approach can be applied to spin chains, we consider the exactly solvable 1D XY model [53,54], as well as the special case of the 1D transverse-field Ising model (TFIM) [55,56]. While both cases display light conelike behavior, the more general XY model allows for an anisotropic coupling giving rise to a double cone [57,58]. Although we limit our calculations to these exactly solvable models, the structural stability of catastrophes (insensitivity to small perturbations) guarantees they must survive in the presence of weak nonintegrability. This includes weak interactions between quasiparticles or disorder and therefore our results also apply to more general systems than just exactly solvable models.

Wave interference softens caustics and leads to structure on three scales [52]: at large scales, we see divergent ray caustics, whereas at wavelength scales interference smoothes the divergences and dresses each caustic with a characteristic wave function which in the simplest case of two coalescing rays is the Airy function, and finally at subwavelength scales there are networks of vortex-antivortex pairs. These robust features, including vortex-antivortex networks, have been observed in optical fields [41], and more recently in electron microscopy [69]. They have also been discussed theoretically in the context of Bose-Einstein condensates [73,74] and various aspects seen experimentally in these systems [70–72]. Furthermore, the association between the Airy function (and its related kernels) and light cones has previously been noted by various authors [8,14,15,59–64], and recent work has conjectured similar universal forms for wavefronts of out-of-time-ordered correlators [65–68] by examining asymptotic limits of

*Corresponding author: dodell@mcmaster.ca

TABLE I. The seven elementary catastrophes and their generating functions $\Phi_Q(\mathbf{s}; \mathbf{C})$, organized by corank n, and dimension Q of control space [86]. The associated Arnol'd exponents β_Q and Berry exponents ς_m governing the scaling of the wave catastrophes' amplitudes and phase, respectively, are also listed.

Catastrophe	Generating function			Scaling exponents	
	n	Q	$\Phi_Q(\mathbf{s}; \mathbf{C})$	β_Q	$\{\varsigma_m\}$
Fold	1	1	$s^3/3 + Cs$	1/6	$\varsigma = 2/3$
Cusp	1	2	$s^4/4 + C_2 s^2/2 + C_1 s$	1/4	$\varsigma_1 = 3/4, \varsigma_2 = 1/2$
Swallowtail	1	3	$s^5/5 + C_3 s^3/3 + C_2 s^2/2 + C_1 s$	3/10	$\varsigma_1 = 4/5, \varsigma_2 = 3/5, \varsigma_3 = 2/5$
Butterfly	1	4	$s^6/6 + C_4 s^4/4 + C_3 s^3/3 + C_2 s^2/2 + C_1 s$	1/3	$\varsigma_1 = 5/6, \varsigma_2 = 2/3, \varsigma_3 = 1/2, \varsigma_4 = 1/3$
Hyperbolic Umbilic	2	3	$s_1^3/3 + s_2^3/3 + C_3 s_1 s_2 + C_2 s_2 + C_1 s_1$	1/3	$\varsigma_1 = 2/3, \varsigma_2 = 2/3, \varsigma_3 = 1/3$
Elliptic Umbilic	2	3	$3s_1^2 s_2 - s_2^3 + C_3(s_1^2 + s_2^2) + C_2 s_2 + C_1 s_1$	1/3	$\varsigma_1 = 2/3, \varsigma_2 = 2/3, \varsigma_3 = 1/3$
Parabolic Umbilic	2	4	$s_2^4 + s_1^2 s_2 + C_4 s_2^2 + C_3 s_1^2 + C_2 s_2 + C_1 s_1$	3/8	$\varsigma_1 = 5/8, \varsigma_2 = 3/4, \varsigma_3 = 1/2, \varsigma_4 = 1/4$

the Airy function. However, to the best of our knowledge, the present paper is the first to study the hierarchy of universal wave functions that dress light cones, of which the Airy function is only the first, and also point out that light cones should generically contain networks of vortices which in the case of 1D chains appear as space-time vortices.

A fourth scale appears in quantum fields due to discretization of excitations leading to "quantum catastrophes" [75–80] (rippling mirrors give analogous effects [81]). Going to the continuum (classical field) limit returns us to a wave catastrophe. As we shall show, light cones in spin chains have all the features of quantum catastrophes, including *discretized* versions of wave catastrophes and vortices which are regulated by the lattice constant. Although the cone itself is mildly affected by the presence of a quantum critical point (QCP) in the spin models we study, we find by contrast that the vortices are strongly affected and we use this feature to extract the dynamical critical scaling.

The rest of this paper is organized as follows. In Sec. II, we outline the relevant aspects of catastrophe theory, emphasizing the hierarchy of structures and their scaling properties. In Sec. III, we show that light cones are in fact (quantum) caustics and hence their natural mathematical description is via catastrophe theory. In Sec. IV, we introduce the XY and TFIM spin chains focusing on the quasiparticle dispersion relation which is the key ingredient we need to apply catastrophe theory. This program is implemented in Sec. V where we obtain the Airy and Pearcey functions for the wave functions dressing the fold and cusp catastrophes/cones in these models. In Sec. VI, we verify the self-similar scaling properties of light cones that catastrophe theory predicts and in Sec. VII, we describe how higher-order catastrophes arise in the context of correlation functions. In Sec. VIII, we identify and discuss the presence of vortex-antivortex pairs within light cones, while in Sec. IX we touch on the relevance of the theory to quench experiments, and in Sec. X we conclude with a discussion of the broader significance of the results. In order to make this paper self-contained, we have included in Appendices A–F the specifics of quantum spin chain diagonalization methods and various other details of our calculations.

II. GEOMETRIC AND WAVE CATASTROPHES

In what follows, we will not need the full mathematical machinery behind catastrophe theory, but we will make use

of a number of key results and for this reason we give a brief overview here. Our treatment is informal, but we emphasize that these results can be proved rigorously. The main idea can be stated simply: catastrophe theory classifies *structurally stable* singularities of functions and shows that such singularities can only take on certain characteristic shapes [50]. In up to four dimensions, these are René Thom's seven elementary *catastrophes* which are listed in Table I.

Each catastrophe arises from two or more coalescing/bifurcating stationary points of its generating function Φ_Q, the normal forms for which are given in the table. In the physical applications given in this paper, Φ_Q is the action functional and stationary points therefore correspond to classical paths or rays. From an optical/classical mechanics point of view a catastrophe is a caustic, i.e., the locus of points where the ray density diverges.

Thom's theorem states that the local behavior of a function near coalescing stationary points can always be mapped by a smooth change of variables onto one of the catastrophes and in this sense catastrophes are universal. There is also a second sense in which catastrophes are universal: structural stability means stability against perturbations and thus catastrophes do not require special symmetry and hence occur generically in nature. Perturbations do not qualitatively change catastrophes and only quantitatively affect behavior up to the strength of the perturbation.

The catastrophes in Table I are organized by the number n of state variables (their corank), and by the dimension Q of the control parameter space. Control space is the space where the function with its singularities actually lives. The control parameters $\mathbf{C} = \{C_1, C_2, \ldots\}$ could be space and time coordinates as well as any other parameters. The state variables $\mathbf{s} = \{s_1, s_2, \ldots\}$ characterize the rays. The simplest catastrophes (the cuspoids) have $n = 1$ and their generating functions are polynomials of the form

$$\Phi_Q(s; \mathbf{C}) = \frac{s^{Q+2}}{Q+2} + \sum_{m=1}^{Q} \frac{C_m s^m}{m}, \tag{1}$$

with up to Q coalescing stationary points. The stationarity condition reads

$$\frac{\partial \Phi_Q}{\partial s} = 0 \tag{2}$$

and corresponds physically to Hamilton's principle of stationary action, while caustics arise from coalescing stationary

points where the generating function is stationary to higher order [52]

$$\frac{\partial^2 \Phi_Q}{\partial s^2} = 0. \tag{3}$$

In the examples, we provide in subsequent sections, we focus primarily on the fold and cusp catastrophes, as well as a discussion of the hyperbolic umbilic in the context of correlation functions. Folds and cusps are the only structurally stable singularities in the 2D (x, t) control plane where light cones in 1D chains live, while the higher catastrophes (although they may still exist in greater dimensions) can only be projected onto the plane by way of cusps and folds. This property is generic: catastrophes of higher order contain the lower ones [51]. The cusp is the meeting of two fold lines, the swallowtail contains two cusps, and so on.

The wave functions, or wave catastrophes, associated with catastrophes can be obtained in a way analogous to Feynman path integrals by exponentiating the generating function and integrating over all paths,

$$\Psi_Q(\mathbf{C}) \propto \lambda^{n/2} \int_{-\infty}^{\infty} \cdots \int_{-\infty}^{\infty} d^n s \, e^{i\lambda \, \Phi_Q(\mathbf{s};\mathbf{C})}, \tag{4}$$

where λ plays the role of the wave number k or $1/\hbar$ in quantum problems. In this form, the fact that the generating function plays the role of the physical action becomes clear. These functions are also known as diffraction integrals and many of their properties have been tabulated [44]. We emphasize that standard approximations such as the method of stationary phase where the integral over $\mathbf{s}$ is broken up into a sum of independent gaussian integrals around each of the stationary points are doomed to failure when the stationary points coalesce. One must instead keep the full form of Φ_Q to get a result which is uniformly correct through the coalescence regions and this is precisely why diffraction integrals are crucial for treating bifurcation problems where solutions appear or disappear.

The fold has a cubic action $\Phi_1(s; C) = s^3/3 + Cs$, where in the case of a light cone in (1+1) dimensions $C = C(x, t)$. As the control parameter C is taken from positive values down through zero the cubic changes its form so as to describe two coalescing rays. The resulting wave catastrophe can be recognized as the integral form of the Airy function,

$$\Psi_1(C) \propto (2\pi \lambda^{1/6}) \mathrm{Ai}(\lambda^{2/3} C). \tag{5}$$

In the absence of any special symmetry, two fold lines generically meet at cusps. In the region near the cusp point the appropriate action is quartic and features two control parameters $\Phi_2(s; C_1, C_2) = s^4/4 + C_2 s^2/2 + C_1 s$. This normal form, which formally resembles the Landau free energy for a continuous (second-order) phase transition, describes the coalescence of up to three rays and results in a wave catastrophe known as the Pearcey function,

$$\Psi_2(C_1, C_2) \propto (2\pi \lambda^{1/4}) \mathrm{Pe}(C_1 \lambda^{3/4}, C_2 \lambda^{1/2}), \tag{6}$$

which is a complex function of two variables. For our definitions/conventions for the Airy and Pearcey functions, see Eqs. (D5) and (C7), respectively. Plots of the absolute values $|\mathrm{Ai}(C)|$ and $|\mathrm{Pe}(C_1, C_2)|$ of the Airy and Pearcey functions are given in Fig. 1.
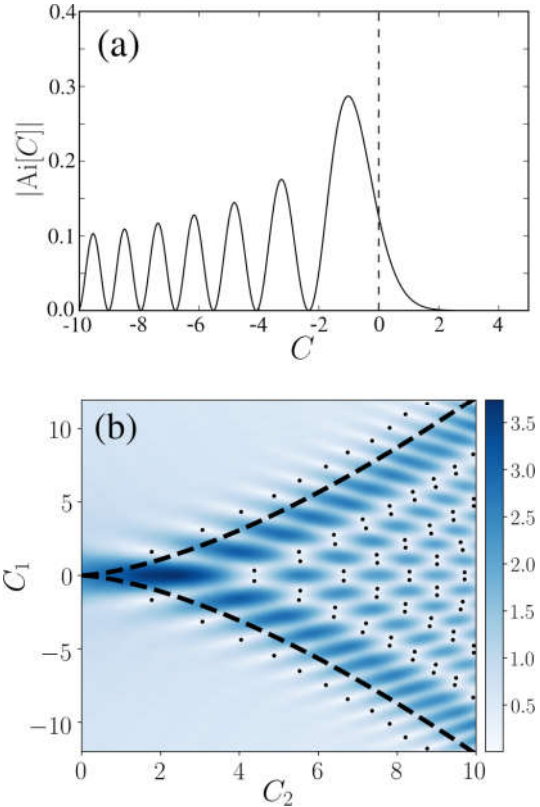

FIG. 1. The Airy and Pearcey functions are the first two wave catastrophes in a hierarchy. (a) Modulus of the Airy function, as defined in Eq. (D5), which dresses a fold catastrophe where two rays coalesce. The location of the fold, or classical caustic, is at $C = 0$ and is indicated by the dashed line. For $C < 0$ there is two-wave interference giving fringes whereas for $C > 0$ there is an evanescent wave. (b) Modulus of the Pearcey function, as defined in Eq. (C7), which dresses the classical cusp caustic $C_1 = 2C_2^{3/2}/(3\sqrt{3})$ and which is shown as a black dashed line. The cusp is made of two fold lines which meet at the cusp tip at $C_1 = C_2 = 0$. There are three rays/waves inside the cusp and only one outside: two coalesce as we cross either of the fold lines, but all three coalesce at the cusp tip which is the most singular part of the classical caustic (a ray picture of the cusp can be seen in Fig. 2(b) in Ref. [80]). However, wave interference removes the classical singularities. The black dots show the locations of vortices: there is a line of vortices outside either edge of the cusp, and vortex-antivortex pairs inside.

The fact that the Pearcey function is a two-dimensional complex function, with an amplitude and a phase at each point, allows for the possibility of vortices. This turns out to be the case: the black dots in Fig. 1(b) show the locations of vortices, or more precisely their cores. There is an ordered network of vortex-antivortex pairs inside the cusp and single rows of vortices lining the outer edges. These are subwavelength features that represent the finest layer of structure of a wave catastrophe. We find the vortices by densely covering the plane with loops around which we integrate the phase of the Pearcey function: loops that contain vortices give a $\pm 2\pi$ phase change (the vortex cores also correspond to nodes of the Pearcey function, although in principle not all nodes need be vortices).

An important feature of wave catastrophes is that they exhibit self-similar scaling. If the parameter λ is changed from λ' to λ the wave functions will retain their functional forms but with rescaled coordinates,

$$\Psi_Q(\{C_m\};\lambda) = \left(\frac{\lambda}{\lambda'}\right)^{\beta_Q} \Psi_Q\left(\left\{\left(\frac{\lambda}{\lambda'}\right)^{\varsigma_m} C_m\right\};\lambda'\right). \quad (7)$$

We can understand this scaling as follows: the overall amplitude scales as λ^{β_Q}, where β_Q is known as the *Arnol'd index*. The distance between interference fringes is also rescaled, but generally the scale factor is different in each direction according to λ^{ς_m}, where ς_m is the *Berry index* associated with coordinate C_m. For the fold wave catastrophe, $\beta_{\text{Ai}} = \frac{1}{6}$ and $\varsigma = \frac{2}{3}$, and for the cusp wave catastrophe, $\beta_{\text{Pe}} = \frac{1}{4}$ and $\varsigma = \{\frac{3}{4}, \frac{1}{2}\}$. A complete list of Arnol'd and Berry indices for the seven elementary catastrophes is displayed in Table I.

The sets of Arnol'd and Berry indices accompanying the different catastrophes are reminiscent of the sets of critical exponents which define universality classes of equilibrium phase transitions. The underlying common cause of this similarity is the presence of singularities, or more precisely non-analyticity, in both cases. We emphasize that in the application to light cones we study here, this universality occurs out of equilibrium, and thus we have an example of universality in quantum dynamics [79,85,87].

III. LIGHT CONES AS QUANTUM CAUSTICS

Our approach to the light cone problem is based upon the idea that the build-up of correlations occurs through quasiparticle propagation [3]; this is known to be the case in a broad range of models including the BH, TFIM, and XY models. The Lieb-Robinson bound can then be expressed in terms of the maximal group velocity of quasiparticles [7,9]

$$v_{\text{LR}} = \max_k \left|\frac{d\epsilon_k}{dk}\right|, \quad (8)$$

where ϵ_k is the dispersion relation for quasiparticles as a function of quasimomentum k. It can be seen immediately that this result is exactly equivalent to Eqs. (2) and (3) which give the conditions for a caustic (note that here we are implicitly considering real solutions to the caustic conditions; imaginary solutions correspond to *phase velocity* across the cone and are discussed in Appendix D. This aspect has also been discussed by Cevolani *et al.* in Ref. [16]). From this simple observation, it follows that light cones are caustics and hence the results and insights of catastrophe theory can be applied to them.

Let us focus on the case of a local quench where a single quasiparticle is created at position $x = 0$ in the middle of a spin chain (we briefly consider weakly nonlocal superpositions of multiple quasiparticles in Sec. IX, and also in Appendix E). Time evolving the state with the Hamiltonian H, the state vector at time t is

$$|\Psi(t)\rangle = e^{-iHt/\hbar} b_{x=0}^\dagger |0\rangle_b \quad (9)$$

where $|0\rangle_b$ is the Bogoliubov quasiparticle ground state and the operator $b_x^\dagger$ creates a quasiparticle at the site located at position x. For the remainder of the paper, we use the subscript "b" to distinguish Fock states in the Bogoliubov basis from the

Jordan-Wigner basis. Introducing the eigenstates $|k\rangle$ of H we can write this as (see Appendix A for details)

$$|\Psi(t)\rangle = \frac{e^{i\theta(t)}}{\sqrt{N}} \sum_k e^{-i\epsilon_k t/\hbar} |k\rangle_b, \quad (10)$$

where N is the number of sites, and the phase $\theta(t) \equiv t/(2\hbar)\sum_k \epsilon_k$ is not observable but is included here for completeness. Projecting onto the position basis, the wave function $\Psi(x_n, t) \equiv \langle x_n|\Psi(t)\rangle$ on the nth lattice site is

$$\Psi(x_n, t) = \frac{e^{i\theta(t)}}{N} \sum_{k_m=-\pi/a}^{\pi/a-\Delta k} e^{i\Phi(k_m;x_n,t)}, \quad (11)$$

where

$$\Phi(k;x,t) = kx - \epsilon_k t/\hbar. \quad (12)$$

In these expressions, n is an integer lying in the range $\{-(N-1)/2, \ldots, (N-1)/2\}$, and the separation between momenta in the sum is $\Delta k = 2\pi/(aN)$.

In the *continuum approximation* (CA), the wave function corresponding to Eq. (11) is (see Appendix A)

$$\Psi_{\text{CA}}(x, t) = \frac{\sqrt{a}\, e^{i\theta(t)}}{2\pi} \int_{-\pi/a}^{\pi/a} dk\, e^{i\Phi(k;x,t)}, \quad (13)$$

where $a = L/N$ is the lattice constant for a lattice of length L, and the quasimomentum k runs over the first Brillouin zone. A comparison of the exact (discrete) and CA wave functions is given in Fig. 8 in the Appendices. In the semiclassical regime, where N is large, the dominant contributions to the integral in Eq. (13) come from values of k where Φ is slowly varying which are the stationary and coalescence points (especially the latter). By Thom's theorem [50–52], we can therefore map Φ onto one of the normal forms Φ_Q. However, although Thom's theorem guarantees that this can be done by smooth transformations, it does not tell us what these transformations actually are. Figuring out the mapping is part of the challenge in applying catastrophe theory to specific physical problems and it is to this task that we now turn.

IV. XY AND TFIM SPIN CHAINS

Let us consider a 1D XY model describing spins on a lattice interacting with a ferromagnetic coupling J, anisotropy parameter γ, and subject to an external field gJ. The Hamiltonian is

$$H = -J \sum_i \left(\frac{(1+\gamma)}{2}\sigma_i^x\sigma_{i+1}^x + \frac{(1-\gamma)}{2}\sigma_i^y\sigma_{i+1}^y - g\sigma_i^z\right), \quad (14)$$

where σ_i^α, $\alpha \in \{x, y, z\}$, are Pauli operators. When $\gamma = 1$ this Hamiltonian reduces to that of the TFIM. The XY Hamiltonian can be diagonalized via the Jordan-Wigner transform followed by a Bogoliubov rotation, which maps spin operators to spinless fermions [82]. As shown in Appendix B, this leads to the free model $H = \sum_k \epsilon_k(\tilde{b}_k^\dagger\tilde{b}_k - 1/2)$, where $\tilde{b}_k^{(\dagger)}$ is the annihilation (creation) operator for Bogoliubov modes with quasimomentum k and dispersion

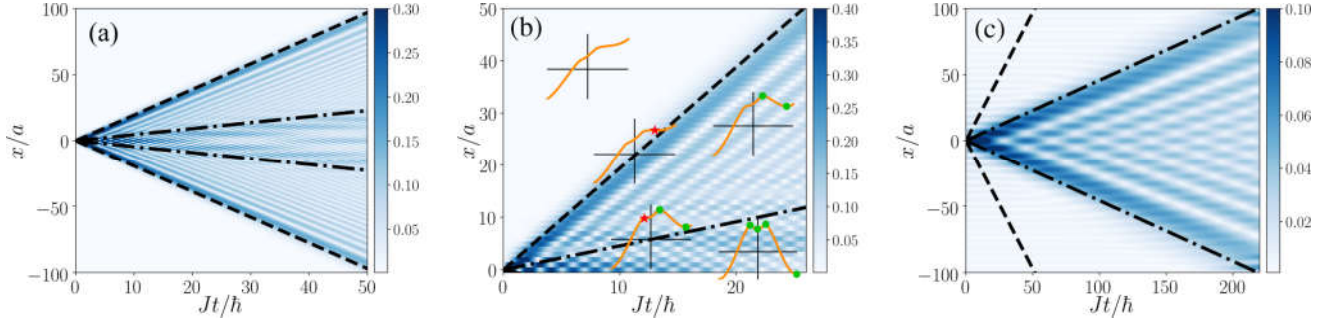$$\epsilon_k = 2J\sqrt{(\cos(ka) - g)^2 + \gamma^2\sin^2(ka)}. \quad (15)$$

FIG. 2. (a) The exact quantum amplitude, obtained by numerically evaluating Eq. (11), for a single Bogoliubov fermion created at the central lattice site, $x = 0$, and propagated under the XY Hamiltonian with $\gamma = 0.2$ and $g = 0.8$. This model gives rise to a double light cone whose boundaries are indicated by the black dashed (LR cone) and dot-dashed (inner cone) lines. (b) A zoom-in of (a) with only half the lattice shown. At five select points (x_n, t), we have overlaid plots of the generating function $\Phi(k; x_n, t)$ [Eq. (16)] as a function of k. Green dots show stationary points of $\Phi(k; x_n, t)$; there are four stationary points in the inner cone and two annihilate (red stars) each time we cross a cone boundary. (c) We can isolate the part of Ψ responsible for the inner cone by only including values of k_m in Eq. (11) that include the three stationary points of Φ that are close to the center of the Brillouin zone (note also the change in timescale). As shown in Sec. V, the inner cone is described by a Pearcey function transformed so as to give a straight cone boundary. Note that in order to keep these figures simple we have not shown the vortices although they are present. See Fig. 3 below, and also Fig. 8 in Appendices, for plots of light cone wave functions with vortices included.

Thus the phase/generating function in Eq. (12) takes the specific form

$$\Phi(k; x, t) = kx - \frac{2Jt}{\hbar}\sqrt{(\cos(ka) - g)^2 + \gamma^2 \sin^2(ka)}. \quad (16)$$

An exact numerical evaluation of the wave function given in Eq. (11) using the generating function $\Phi(k; x, t)$ for the XY model is plotted in Fig. 2. The fact that x_n is discrete means that the light cone actually corresponds to a quantum catastrophe, for more discussion of quantum catastrophes in a spin context see Ref. [80]. However, in the semiclassical regime where N is large, the CA described by Eq. (13) works well. In this case, Φ has the same functional form but with x and k taken as continuous variables, and the integral can be evaluated analytically in terms of the Airy and Pearcey functions as will be explained in the next section.

Dividing $\Phi(k, x, t)$ as given in Eq. (16) by t we can identify three control parameters: $(x/t, \gamma, g)$ [we reserve the energy scale J to play the role of k in Eq. (4)]. However, rays propagate in the 2D (x, t) plane rather than the full 3D control space and thus for generic values of the control parameters catastrophe theory predicts we should see folds and cusps. In fact, we find a double cone made of a cusp enclosed by two folds as shown in Fig. 2 (double cones occur both in spin systems and in coupled 1D gases [57,58]).

Mathematically speaking, the double cone arises because Eq. (16) has up to four stationary points within the first Brillouin zone, as shown by the green dots in the five overlays plotted in Fig. 2(b). Near the origin in Fig. 2 all four stationary points are present, but three are quasidegenerate so Ψ is locally dominated by a Pearcey-like function, which gives the inner cone. As we cross the edges of the inner cone two stationary points annihilate (indicated by red stars in the overlays) leaving two rays which in turn annihilate at the edges of the outer cone so that locally it is dominated by the Airy function. Furthermore, the XY model has a QCP at $g = 1 - \gamma^2$; as the critical regime is approached the inner

cone narrows and eventually collapses because the three inner stationary points in the generating function coalesce at this value of g. In the case of the TFIM ($\gamma = 1$) [4,83,84], Φ has only two stationary points and one finds a single cone with edges that are dressed by Airy functions. The insight from catastrophe theory is that the single cone is nongeneric and only occurs due to the special symmetry of the Hamiltonian when $\gamma = 1$.

Due to the presence of four stationary points, the careful reader might expect the XY model to show signatures of the swallowtail catastrophe. Indeed, this would generically be true, however it can be verified that the quadruple root coalescence do not occur for real k. It is the periodic dispersion relation of the model which keeps us from physically probing the highly singular swallowtail point. The cusp and fold catastrophes that we observe here are however inherited from the part of the swallowtail which is physically permitted.

V. AIRY AND PEARCEY FUNCTIONS

Let us now demonstrate explicitly how the Airy and Pearcey catastrophe integrals emerge in the CA. Starting with the Pearcey integral, consider first the triple stationary point coalescence responsible for the inner cone, which we have isolated in Fig. 2(c). One obvious difference between this wave function and the Pearcey function shown in Fig. 1 is that the cone boundary in the former is straight rather than the standard curved form of the cusp $C_1 = \pm\sqrt{4C_2^3/27}$. Physically, this is due to the free propagation of the fermionic quasiparticles. The required transformation to take us between physical coordinates and those of the standard curved cusp is similar to that used by Kaminski and Paris in Ref. [90]. In Appendix C, we show that for our spin model it is

$$C_1 = -\sqrt{2}x / \left[v_{\rm I}(t\Gamma)^{\frac{1}{4}} \right], \quad (17)$$

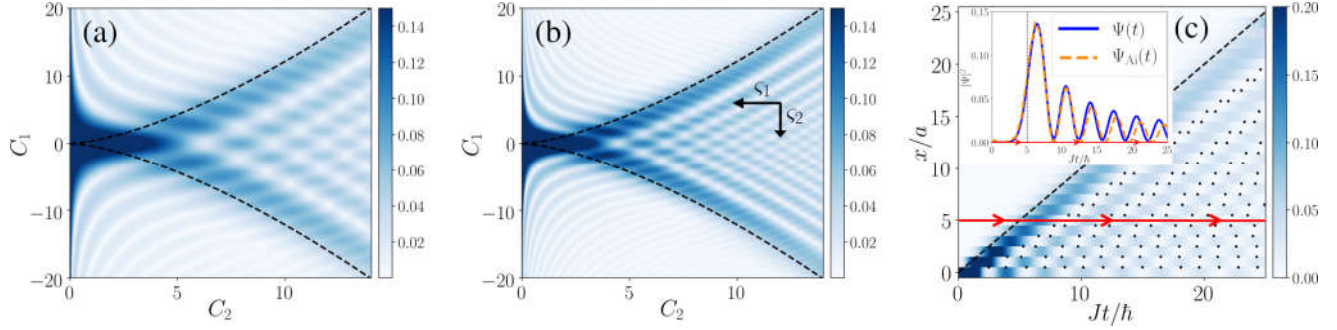$$C_2 = -\sqrt{t}(\gamma^2 + g - 1) / \left[\sqrt{\Gamma}(g - 1) \right], \quad (18)$$

FIG. 3. (a) and (b) Modulus of exact wave function (11) $\Psi[x(C_1, C_2), t(C_1, C_2)]$ plotted in the scaled coordinates for the inner cone only (vortices are present but not shown). It shows a remarkable qualitative resemblance to the Pearcey function (compare with Fig. 1), without performing any approximations. Between (a) and (b), the interaction strength has been changed by a ratio of $J'/J = 2$, so that while the classical ray caustic remains fixed ($C_1 = \pm\sqrt{4C_2^3/27}$, red dashed line), the interference fringes of the wave-function scale according to the Berry indices in the directions indicated. (c) $|\Psi|^2$ for the TFIM (blue shading truncated at 0.2 for clarity) is enclosed by the light cone (black, dashed). Black dots mark the locations of vortices (see Sec. VIII). Slice along the time axis at $x/a = 5$. The local structure of the exact wave function (11) (blue, solid) near the light cone is well-captured by the Airy-like representation of the wave function (21) (orange, dashed). Away from the caustic the Airy function approximation gradually moves out of the phase with the exact result. This is because we have expanded the generating function about the caustic and can be corrected by performing a uniform approximation.

where $\Gamma = \frac{(g^3 - 1 - 2\gamma^2 + 3\gamma^4 + g(3 - 2\gamma^2) + g^2(4\gamma^2 - 3))}{12(g-1)^3}$ and we have defined the *Ising velocity*,

$$v_I \equiv \begin{cases} \frac{2Jag}{\hbar} & 0 < |g| < 1 \\ \frac{2Ja}{\hbar} & 1 < |g| \end{cases}, \tag{19}$$

which is equal to v_{LR} in the TFIM limit (in principle, v_{LR} can be analytically solved for in closed form for general γ,

however, the expression is complicated, and little physical insight is gained from writing it here).

To complete the diffraction integral we also need the integration variable s. This reads $s = \sqrt{2}a(t\Gamma)^{\frac{1}{4}}k$ and results in the Pearcey-like wave function $\Psi_{Pe}(C_1, C_2; J)$ written out in Eq. (20). It rapidly tends to a true Pearcey function at longer times when $S = \sqrt{2}\pi(t\Gamma)^{\frac{1}{4}} \gg 1$.

$$\Psi_{Pe}(C_1, C_2; J) \approx \frac{1}{2\pi}\left(\frac{J(\gamma^2 + g - 1)}{\hbar v_I(g-1)C_2}\right)^{\frac{1}{2}} \int_{-S}^{S} ds \, e^{-\frac{iJ}{\hbar}\Phi_2(s;C_1,C_2)} \overset{Jt/\hbar \gg 1}{\propto} \left(\frac{J}{\hbar}\right)^{\frac{1}{4}} Pe\left[\left(\frac{J}{\hbar}\right)^{\frac{3}{4}}C_1, \left(\frac{J}{\hbar}\right)^{\frac{1}{2}}C_2\right], \tag{20}$$

$$\Psi_{Ai}^{\gamma=1}(C^j; J) \approx \frac{1}{2\pi t^{1/3}}\left(\frac{2Jg^{\frac{2-j}{3}}}{v_I \hbar}\right)^{\frac{1}{2}} \int_{s_j^{Min}}^{s_j^{Max}} ds_j \, e^{\frac{iJ}{\hbar}\Phi_1(s_j;C^j)} \overset{Jt/\hbar \gg 1}{\propto} \left(\frac{J}{\hbar}\right)^{\frac{1}{6}} Ai\left[\left(\frac{J}{\hbar}\right)^{\frac{2}{3}}C^j\right]. \tag{21}$$

In order to display the close resemblance between Ψ_{Pe} and the Pearcey function, we have plotted in Fig. 3 the wave function of the inner cone from Eq. (11) without expansions or approximations in terms of the transformed coordinates C_1 and C_2. This can be compared with the actual Pearcey function plotted in Fig. 1. The only significant deviation is near $C_2 = 0$. Since the limit of integration S tends to 0 as $t \to 0$, the cusp point itself becomes poorly defined, and we get a "smearing" of the wave function as $C_2 \to 0$. As a consequence, we cannot get a Pearcey function exactly at the origin, since the initial boundary condition requires the real-space wave function be entirely localized here. As we move away from the cusp point, however, the Pearcey function is indeed an excellent approximation to the true wave function.

As C_2 increases the Pearcey function can be approximated by two back-to-back Airy functions as the cusp evolves into two fold lines. Indeed, it is a general property of catastrophes that the higher ones evolve into the lower ones as we move away from the former's most singular points. This provides a rigorous explanation for why the Airy functions, which are the simplest of the hierarchy of wave catastrophes, are

commonly encountered in the asymptotics of light cones [8,14,15,59–64].

To examine how the Airy function emerges in the CA, we specialize to $\gamma = 1$ (TFIM Hamiltonian). We stress that the choice of γ does not affect the presence of the fold catastrophe (and thus Airy functions), only the simplicity of the subsequent calculations. To this end, note that for any $g \neq 1$ it can be readily checked that $\Phi(\gamma = 1)$ in Eq. (16) has only two stationary points as a function of k. We can therefore map onto the canonical fold generating function $\Phi_1(s; C)$ by expanding Φ to third order in s. In the CA, and up to a global phase, we show in Appendix D that the correct control parameter in this case is

$$C^j(x, t) = 2(x/v_I - t)(g^{2-j}/\sqrt{t})^{2/3}. \tag{22}$$

The index $j \in \{1, 2\}$ refers to cases $g > 1$, and $g < 1$, corresponding to above and below the QCP, respectively. The integration variable $s_j = (g^{2-j}t)^{\frac{1}{3}}[ka - \arccos(g^{3-2j})]$ and integration limits $s_j^{Min} = -(g^{2-j}t)^{1/3}[\pi + \arccos(g^{3-2j})]$ and $s_j^{Max} = (g^{2-j}t)^{1/3}[\pi - \arccos(g^{3-2j})]$ are also derived in

Appendix D. The resulting wave function $\Psi_{\mathrm{Ai}}^{\gamma=1}(C^j; J)$ is given in Eq. (21).

When $\gamma \neq 1$ this process may be repeated around each fold catastrophe, including for any inner cones, and will result in the emergence of Airy functions with different definitions of the control parameter, C. For example, a particular limit of Eq. (21) has been conjectured to give a universal form for the wavefront of out-of-time-ordered correlators (OTOCs) [65–68]. According to catastrophe theory this is no surprise. Furthermore, closer to the "brightest" parts of the OTOC the hierarchy of catastrophes allows for more elaborate structures beyond the Airy function.

VI. SCALING

The way the spin coupling strength J and the control parameters **C** appear in combination on the right hand sides of Eqs. (20) and (21) shows that light cones have nontrivial scaling properties: varying J is equivalent to rescaling the amplitude and coordinates. More specifically, increasing J causes the amplitude to increase at a rate determined by the Arnol'd index, and the interference patterns to oscillate more quickly in space and time at rates determined by the Berry index for each particular direction. The overall picture is that the fringes flow in towards the origin as J is increased and in the (singular) classical limit, which occurs when $J \to \infty$, all wave structure is pulled into the origin. There are other choices we could have made for the scaling parameter since it need only fill the role of λ in Eq. (4): for the TFIM, we could have alternatively chosen a or g, and in the case of the XY model we could also have chosen either of these or even γ. It is usually necessary to keep some physics constant during the scaling: we can keep the position of the classical ray caustics constant as J is varied by tuning a or g to keep v_I unchanged.

Numerical verification of the catastrophe theory predictions for both the Arnol'd and Berry indices for the exact wave function Eq. (11) is presented in Fig. 4. Panels (a)–(c) show the scaling in the inner cone of the XY model: the fringe scaling is obtained by measuring the distance between peaks of the wave function along coordinates C_1 and C_2 as J is varied and match the Pearcey scaling given in Table I to within 1%. At first glance, it appears that panel (c) shows a contradiction between the expected amplitude scaling of the catastrophe integral and the wave function. However, a quick calculation involving the prefactor of the wave function which ensures that particle number is conserved shows that

$$C_2^{-\frac{1}{2}} \sim \left(\frac{J}{J'}\right)^{-\frac{1}{4}},\qquad(23)$$

which exactly cancels the Arnol'd scaling. This is a peculiarity of our nongeneric initial condition of starting with a completely localized initial state: when tracking a particular fringe, it will move towards the origin but this normalization factor means that its height does not scale with J.

Panel (d) of Fig. 4 shows the predictions in the TFIM for the period T of oscillations near the caustic. Data are shown both for the exact wave function, given in Eq. (11), and also the "spin-flip" state Ψ_X, given in Eq. (33), which is easier to realize experimentally. Since the Berry index ς for the fold
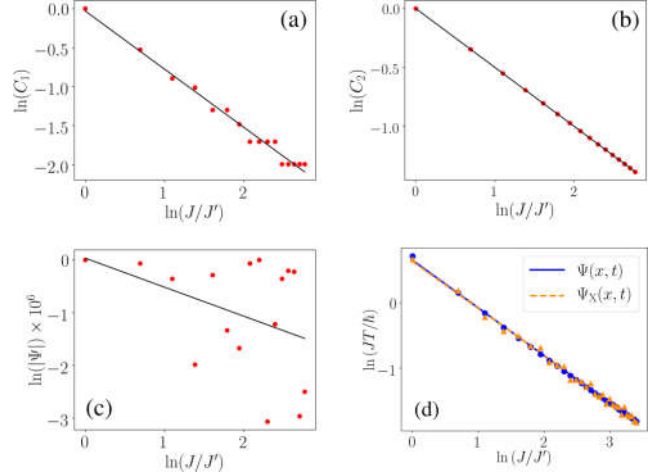

FIG. 4. Self-similar scaling of light cone wave functions. (a) Fringe spacing in the C_1 direction within the inner cone of the XY model scales as J^{ς_1} with a Berry index $\varsigma_1 \approx 0.743 \pm 0.002$ (a range of $1 \leqslant J/J' \leqslant 16$ was used). The staircase pattern is due to the discreteness of the lattice. (b) Fringe spacing scaling in the C_2 direction of the XY model gives a Berry index of $\varsigma_2 \approx 0.500 \pm 0.001$. (c) Wave function amplitude scaling of $\ln |\Psi| \approx (-6 \times 10^{-7} \pm 4 \times 10^{-7}) \ln(J)$, indicating that the amplitude near the cusp has an incredibly weak scaling with J. This effect is explained by Eq. (23), since the initial condition precisely cancels the Arnol'd scaling to preserve particle number. (d) The oscillation period, T, of $\Psi(x_n, t)$ for site $x/a = 5$ in the TFIM with $g = 3$; Eqs. (11) and (33) are plotted in blue circles and orange triangles, with blue-solid and orange-dashed trendlines, respectively (a range of $1 \leqslant J/J' \leqslant 30$ was chosen). Accounting for a geometric factor of $\sin[\arctan(20)]$, we find the Berry index to be 0.654 ± 0.003 and 0.646 ± 0.009 for Ψ and Ψ_X, respectively.

defines scaling perpendicular to the caustic, a geometric factor dependent on v_{LR} must be applied. Numerical agreement to within 3% of Airy scaling given in Table I is found in both cases even for finite-sized systems at finite times.

VII. CORRELATION FUNCTIONS AND HIGHER-ORDER CATASTROPHES

Rather than the probability distribution associated with the wave function itself, light cones are usually observed in correlation functions [17–21]. The equal time site-site correlation function is defined as

$$G(x_n, x_m, t) = \langle b_n^\dagger b_m(t) \rangle - \langle b_n^\dagger(t) \rangle \langle b_m(t) \rangle. \qquad(24)$$

Because Bogoliubov fermions are conserved, $\langle b_n^\dagger(t) \rangle = \langle b_m(t) \rangle = 0$, and the last term vanishes. The remaining piece is

$$\begin{aligned}\langle b_n^\dagger b_m(t) \rangle &= \langle \Psi(t) | b_n^\dagger b_m | \Psi(t) \rangle \\ &= \frac{1}{N} \sum_{k,k'} e^{-i(\epsilon_k - \epsilon_{k'})t/\hbar} {}_b\langle 0 | \tilde{b}_{k'} b_n^\dagger b_m \tilde{b}_k^\dagger | 0 \rangle_b.\end{aligned} \qquad(25)$$

where we have used the state vector $|\Psi(t)\rangle$ given in Eq. (10). Expressing all the operators in terms of quasimomentum (see
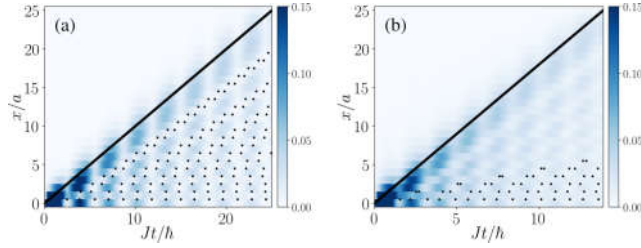
FIG. 5. (a) Correlation function amplitude $|G(0, x_m, t)|$ for $\gamma = 1$, and $g = 0.5$, where the blue shading has been truncated at 0.15 for clarity. Black dots indicate vortices. (b) Same correlation function as in (a), now with $g = 0.9$. Note that the number of vortices within the cone decreases drastically near the critical point (see Sec. VIII).

Appendix A), we obtain

$$G(x_n, x_m, t) = \frac{1}{N^2} \sum_{k,k'} e^{-i(\epsilon_k - \epsilon_{k'})t/\hbar} e^{i(kx_m - k'x_n)}$$

$$= \Psi(x_m, t)\Psi(-x_n, -t). \qquad (26)$$

In Fig. 5, we plot $G(0, x_m, t)$ on the upper half of the spin chain for two different values of g. It displays the same features as the wave function: a light cone, interference fringes, and vortices. In the CA, the equal time site-site correlation function becomes

$$G_{CA}(x, x', t) = \frac{a}{(2\pi)^2} \int_{-\pi/a}^{\pi/a} \int_{-\pi/a}^{\pi/a} dk \, dk' \, e^{i(\Phi(k,x) - \Phi(k',x'))}$$

$$= \Psi_{CA}(x, t)\Psi_{CA}(-x', -t), \qquad (27)$$

and expanding around the cone boundaries gives

$$G_{CA}(x, x', t) \approx \Psi_{Ai}(C(x, t), t)\Psi_{Ai}(C(-x', -t), -t), \quad (28)$$

where $C(x, t)$ is the same function of x and t as that given in Eq. (22).

Measurements and calculations (based on doublon and holon quasiparticles) on the BH model following a quench also find a product of two Airy functions for $G(x_n, x_m, t)$ [8,17]. However, referring to Table I, generic dimension three singularities (i.e., two spatial coordinates x_n and x_m, as well as time t) of corank 2 (i.e., two integration variables, like in the two-site correlation function) are the elliptic umbilic, and hyperbolic umbilic catastrophes. The elliptic umbilic diffraction catastrophe has been studied by Berry, Nye, and Wright [88] via the optics of a triangular water droplet lens, while the hyperbolic umbilic is a direct consequence of the primary coma aberration [86] and has been observed in matter waves using electron microscopy [69]. These catastrophes are generally more complicated than a squared Airy function, however, we note that in a certain plane the hyperbolic umbilic wave catastrophe does indeed reduce to the product of two Airy functions. More precisely, the hyperbolic umbilic wave catastrophe is given by [44]

$$\Psi_{HU}(x, y, z) = \lambda \iint_{-\infty}^{+\infty} ds_1 ds_2 \, e^{i\lambda(s_1^3 + s_2^3 + C_3 s_1 s_2 + C_2 s_2 + C_1 s_1)},$$

$$(29)$$

and when $C_3 = 0$ this reduces exactly to

$$\Psi_{HU}(C_1, C_2, 0) = \frac{4\pi^2 \lambda^{\frac{1}{3}}}{3^{\frac{2}{3}}} Ai\left(\frac{C_1 \lambda^{\frac{2}{3}}}{3^{\frac{1}{3}}}\right) Ai\left(\frac{C_2 \lambda^{\frac{2}{3}}}{3^{\frac{1}{3}}}\right). \qquad (30)$$

Thus, both the XY model and the BH model give rise to a nongeneric special case.

What physical quantity could the C_3 control parameter represent? Studying the form of Ψ_{HU} given in Eq. (29) we note that C_3 controls the coupling between the s_1 and s_2 variables which in a spin chain correspond to the two quasi-momenta k and k'. For noninteracting quasiparticles, which is the case for the exactly solvable models considered in this paper, the two quasimomenta are uncoupled and thus C_3 is zero. Furthermore, the particular regime of the BH model where Refs. [8,17] obtained a product of Airy functions also corresponds to the free quasiparticle case. It is therefore clear that C_3 can be used to parametrize quasiparticle-quasiparticle scattering, and we predict that a model with interacting quasiparticles will give rise to light cones that sample hyperbolic umbilic wave catastrophes. This feature could be verified in an experiment where the strength of the coupling is varied for then the scaling along C_3 should go as $\varsigma_3 = 1/3$.

Other quantities, for example, the spin-spin correlation function, $\Sigma_{nm} = \langle \sigma_n^x \sigma_m^x \rangle - \langle \sigma_n^x \rangle \langle \sigma_m^x \rangle$, may also be calculated exactly via the Jordan-Wigner and Bogoliubov transformations, and simplified using Wick's theorem. The functional forms of these quantities in the continuum approximation remain diffraction integrals, and thus will also display universal behavior corresponding to catastrophes.

VIII. VORTICES AND CRITICALITY

As seen in Figs. 3 and 5, and also Fig. 8 in the Appendices, we find that light cones contain lattices of vortex-antivortex pairs. Vortices form the fine structure of wave catastrophes [86,89–91], and in a continuum are zeros of Ψ where the phase $\chi \equiv Arg\Psi$ is undefined (takes all values) and has the topological property

$$\oint_C d\chi = \pm 2\pi, \qquad (31)$$

where C is any closed path which contains a single vortex. On a discrete lattice we can still use such circuits to find vortices, but across lattice sites one must perform a sum instead of integrating, meaning that their spatial position is only known up to the lattice constant: in figures we place the vortices between lattice sites. Furthermore, vortices on a lattice need not correspond to nodes or even phase singularities, but to points where the phase difference between adjacent sites is $\pm\pi$ (i.e., phase kinks or dark solitons). Thus, while phase interference regulates the amplitude divergence of ray caustics, the effect of a lattice is to regulate the phase singularities of wave theory. In recent work by some of the authors [80], the regularization of phase singularities by a lattice has been considered in Fock space.

Whereas the classical light cone changes smoothly at the QCP [see, e.g., Eq. (19)], there is a sharp minimum in the vortex density, i.e., many vortex-antivortex pairs annihilate, see Fig. 6. In the CA, all vortices except those closest to
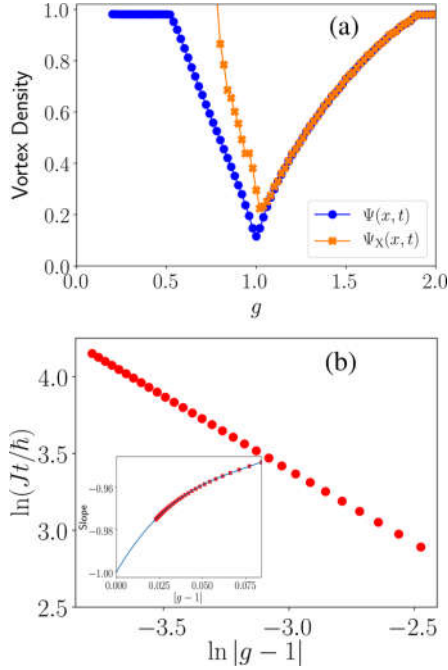
FIG. 6. (a) Vortex density inside the TFIM light cone reaches a sharp minimum at the QCP for both Eq. (11) and the spin-flip state Eq. (33). We define vortex density as being the total number of vortices that occur within a cone up to the time at which the light cone hits the edge of the system, taking care to normalize for different cone sizes at different values of g. (b) Numerical determination of vortex pair creation times at a fixed point in space as $g = g_c = 1$ is approached. In order to extrapolate to the critical point (inset), 30 data points $(g, Jt/\hbar)$ are fitted to a quadratic and then differentiated. The resulting slopes are extrapolated to g_c using a cubic and the intercept gives $\nu z = 0.9999 \pm 0.0004$ (standard error on the fit). The range $0.02 \leqslant |g-1| \leqslant 0.12$ of g was chosen to optimize the proximity to the critical point along with data accuracy, since the wave function becomes highly oscillatory as $g \to 1$. Numerical errors are smaller than the symbol sizes.

the central axis annihilate at the QCP, while on a discrete lattice, more off-axis vortices survive but the same trend is observed. At a fixed point in space, the time at which a vortex is first detected increases as one approaches the critical point, becoming infinite in the CA. This diverging timescale τ is related to critical slowing and suggests a connection to the dynamical critical exponent, z. According to the scaling hypothesis of critical phenomena

$$\tau \propto \xi^z, \tag{32}$$

where $\xi = |g - g_c|^{-\nu}$ is the correlation length and ν is its equilibrium critical exponent. Fig. 5(b) plots τ as found from the wave function Eq. (11) as g is tuned to the QCP. By extrapolating the numerical data [Fig. 5(b) inset] to the critical point we obtain $\nu z = 1$ and hence recover the known critical scaling for the 1D TFIM [92,93]. For purposes of clarity, we have only included the set of vortices which annihilate closest to the axis $x = 0$. Vortices which annihilate farther off-axis also display similar trends, which can be seen in Appendix F, along with further figures which help with visualization of this process.

While a more complete understanding of the nature of the vortex-antivortex pairs within the light cone remains a subject of future work, we wish to highlight that their presence and scaling laws provide an interesting link between the predictions of catastrophe theory and universality (in and out of equilibrium). Due to the self-dual nature of the TFIM, qualitative behavior for $g > 1$ is identical to that of the wave function below the transition with $g \to 1/g$ and $t \to gt$.

IX. EXPERIMENTAL REALIZATION: SPIN-FLIP STATE

The structural stability of catastrophes explains why they occur so frequently in nature. Apart from the examples given in the Introduction, they can also occur in disordered systems such as at the Anderson transition where an evanescent Airy function occurs [94], and it has also been shown that wave catastrophes have the property of self-healing after being disrupted [95]. There are, therefore, a broad range of initial conditions and spin models which will give rise to caustics in their dynamics.

So far we have used the initial condition of a localized single quasiparticle, as given in Eq. (9). This is a nongeneric initial condition and the reader may question how generic the resulting light cones really are. In fact, all our analysis is stable to perturbations around this initial condition. In particular, a state which is naturally generated in trapped ion experiments where individual ions can be addressed is a spin-flip state which starts with all spins polarized in the x direction, except for the central spin, say, which is flipped [21],

$$\Psi_X(x, t) \equiv \langle x | e^{-iHt/\hbar} | \uparrow^x \ldots \uparrow^x \downarrow^x \uparrow^x \ldots \uparrow^x \rangle. \tag{33}$$

It is important to realize that physical spins are in general superpositions of multiple quasiparticles and vice versa. We elaborate upon the mathematical details of this point in Appendix E. What we find is that as long as the quench is not too close to the transition the number of quasiparticles created by a spin flip is close to one and hence we are perturbing around the single quasiparticle state given in Eq. (9). The evidence for this statement can be found in Figs. 4(d) and 6(a), which compare the results of using Ψ_X with those of Ψ. We find that the scaling properties are essentially identical in the two cases whilst the behavior of the vortex density shows some finite differences but is qualitatively the same.

X. DISCUSSION AND CONCLUSIONS

Caustics are a natural phenomenon that can be seen by looking up in the sky on a rainy day. The primary bow of a rainbow is a fold caustic and careful observation reveals supernumerary arcs that are interference fringes described by the Airy function. This is the first in a hierarchy of caustics of increasing complexity whose underlying description is via catastrophe theory. This hierarchy has previously been explored in optics (particularly in the field of gravitational lensing [41]), thermodynamics [96,97], laser physics [98,99], hydrodynamics [43,45,100], and also cosmology [101,102]. By showing that light cones in many-body systems are also caustics, we are able to open the door to the application of a rigorous and unified mathematical framework for describing the dynamics of these systems following a quench.

The main conceptual result of this paper is that there is a hierarchy of light cone structures. They are stable against perturbations and dressed by characteristic wave functions that scale according to the sets of exponents given in Table I. The fold catastrophe and its attendant Airy function features in the TFIM, but breaking the symmetry of the TFIM leads us to the XY model and the second catastrophe, the cusp, which is dressed by the lesser-known Pearcey function. Choosing the spin coupling J as a tuning parameter, we show how the scaling exponents lead to nontrivial scaling of these wave catastrophes as J is varied.

The TFIM and XY models are exactly solvable and hence their quasiparticles are noninteracting. However, the defining feature of catastrophe theory is that it deals with structurally stable singularities and hence the light cone caustics we have described also occur in the presence of perturbations such as weak quasiparticle interactions. A related example of this is provided by the celebrated Kolmogorov-Arnold-Moser (KAM) theorem which shows that tori in the phase space of integrable systems are stable against nonintegrable perturbations. There is in fact a close connection between caustics and the quasiperiodic motion that arises in dynamical systems due to the existence of the tori [103].

Higher-order catastrophes will become important in higher dimension spin lattices. Another way that higher-order catastrophes become important is through n-body correlation functions. For the TFIM we find that the two-site equal time correlation function is described near the cone edge by the product of two Airy functions, which is, however, a special case of the hyperbolic umbilic catastrophe. We predict that adding quasiparticle interactions will lead to the full hyperbolic umbilic catastrophe.

On their finest scales, wave catastrophes contain vortex-antivortex pairs. We have seen that in the case of light cones in 1D spin chains these become vortex-antivortex pairs in space-time. We note in passing that these are reminiscent of the Kosterlitz-Thouless transition that occurs in one space and one time dimension in the quenched 1D Bose-Hubbard model [104] and in quantum wires [105]. Being high-energy features, we find that the vortices are strongly affected by critical slowing near a QCP, unlike the light cone itself which evolves smoothly. The vortices contain all the information about the QCP and can be used to extract the critical scaling behavior.

The fact that light cones are structurally stable and fall into distinct classes, each of which has its own set of scaling exponents, underlines that as a phenomenon they are an example of universality in out-of-equilibrium dynamics, somewhat akin to the universality classes of equilibrium phase transitions. The underlying reason for this universality in both cases is the presence of singularities, and the realization that light cones are caustics aids us in identifying and understanding their properties.

APPENDIX A: DYNAMICS OF A BOGOLIUBOV FERMION

The spin models dealt with in this paper can be exactly diagonalized in terms of Bogoliubov fermions. Their Hamiltonians can therefore be written in the form

$$H = \sum_k \epsilon_k \left(\tilde{b}_k^\dagger \tilde{b}_k - \frac{1}{2} \right), \tag{A1}$$

where ϵ_k is the dispersion relation and the operators $\tilde{b}_k^\dagger$ and $\tilde{b}_k$ create and annihilate, respectively, fermions with quasimomentum k. We shall denote the action of the creation operator on the Bogoliubov vacuum as $\tilde{b}_k^\dagger |0\rangle_b = |k\rangle_b$. These operators are related to their counterparts in position space via a discrete Fourier transform:

$$b_x = \frac{1}{\sqrt{N}} \sum_k e^{-ikx} \tilde{b}_k, \tag{A2}$$

$$\tilde{b}_k = \frac{1}{\sqrt{N}} \sum_x e^{ikx} b_x, \tag{A3}$$

where N is the number of sites/spins.

Applying the time evolution operator to a single Bogoliubov fermion created at the center of the lattice we obtain the state vector:

$$|\Psi(t)\rangle = e^{-iHt/\hbar} b_{r=0}^\dagger |0\rangle_b = e^{-iHt/\hbar} \left(\frac{1}{\sqrt{N}} \sum_k \tilde{b}_k^\dagger \right) |0\rangle_b \tag{A4}$$

$$= \frac{e^{i\theta(t)}}{\sqrt{N}} \sum_k e^{-i\epsilon_k t/\hbar} |k\rangle_b, \tag{A5}$$

where $\theta(t) \equiv (t/2\hbar) \sum_k \epsilon_k$. The corresponding spatial wave function is

$$\Psi(x,t) = {}_b\langle x|\Psi(t)\rangle = \frac{e^{i\theta(t)}}{\sqrt{N}} \sum_k e^{-i\epsilon_k t/\hbar} {}_b\langle x|k\rangle_b, \tag{A6}$$

and inserting the standard result $\langle x|k \rangle = e^{ikx}/\sqrt{N}$ for the overlap gives

$$\Psi(x,t) = \frac{e^{i\theta(t)}}{N} \sum_{k=-\frac{\pi}{a}}^{\frac{\pi}{a} - \frac{2\pi}{Na}} e^{i(kx - \epsilon_k t/\hbar)}. \tag{A7}$$

If we allow $\Delta k = 2\pi/(aN)$ to become very small ($N \gg 1$) we can approximate the sum by the integral

$$\Psi(x,t) = \frac{e^{i\theta(t)} \sqrt{a}}{2\pi} \int_{-\pi/a}^{\pi/a} dk\, e^{i\Phi} \tag{A8}$$

with generating function $\Phi = kx - \frac{t}{\hbar}\epsilon_k$. A comparison of the discrete and continuum cases for the TFIM is given in Fig. 8. In the semiclassical regime ($N \gg 1$), both the sum and the integral are dominated by the points at which Φ is stationary. Along the caustic, however, a saddle-point approximation fails since we are at a degenerate stationary point.

APPENDIX B: DIAGONALIZATION OF THE XY MODEL

The Hamiltonian for the XY model is

$$H = -\sum_{\langle ij \rangle} \left(J_x \sigma_i^x \sigma_j^x + J_y \sigma_i^y \sigma_j^y\right) - h \sum_i \sigma_i^z, \qquad \text{(B1)}$$

where σ_i^α, $\alpha \in \{x, y, z\}$ are the Pauli operators for the ith site. We will use the Jordan-Wigner (JW) transformation, followed by a Bogoliubov rotation, in order to diagonalize H. Following the conventions used by Dutta *et al.* in Ref. [93], the transformation to JW fermions is given by

$$\sigma_i^z = 2c_i^\dagger c_i - 1, \qquad \text{(B2)}$$

$$\sigma_i^- = c_i \prod_{j<i}(1 - 2c_j^\dagger c_j) = -(c_i + c_i^\dagger)e^{i\pi \sum_{j<i} c_j^\dagger c_j}. \qquad \text{(B3)}$$

We note that the JW fermions and Bogoliubov fermions have different vacuua; some more discussion of this point can be found in Appendix E.

Next, we use a Fourier transform, $\tilde{c}_k^\dagger = \sum_j e^{ikx_j} c_j^\dagger$, and then rotate to Bogoliubov fermions via

$$\tilde{b}_k^\dagger = v_k \tilde{c}_k + iu_k \tilde{c}_{-k}^\dagger \qquad \text{(B4)}$$

along with the corresponding destruction operator and transformations for $-k$. Here, $u_k \equiv \cos(\phi_k/2)$, $v_k \equiv \sin(\phi_k/2)$, and $\tan(\phi_k) = (J_y - J_x)\sin(ka)/((J_y + J_x)\cos(ka) + h)$, with properties $u_k = u_{-k}$, $v_k = -v_{-k}$ in order to ensure the anticommutation relations $\{\tilde{c}_k^\dagger, \tilde{c}_{k'}^\dagger\} = \{\tilde{c}_k, \tilde{c}_{k'}\} = 0$ and $\{\tilde{c}_k^\dagger, \tilde{c}_{k'}\} = \delta_{kk'}$ hold. We can simplify the resulting Hamiltonian to get it in the form of Eq. (A1) with $\epsilon_k = 2\sqrt{h^2 + J_x^2 + J_y^2 + 2h(J_x + J_y)\cos(ka) + 2J_x J_y \cos(2ka)}$ being a function of the parameters J_x, J_y, h, and a.

Next we introduce the anisotropy parameter γ so that we can write $J_x \equiv J(1 + \gamma)/2$, $J_y \equiv J(1 - \gamma)/2$ and let $h \equiv gJ$. We thereby arrive at the standard form of the Hamiltonian

$$\frac{H}{J} = -\frac{1}{2} \sum_{\langle ij \rangle} \left((1 + \gamma)\sigma_i^x \sigma_j^x + (1 - \gamma)\sigma_i^y \sigma_j^y\right) - g \sum_i \sigma_i^z \qquad \text{(B5)}$$

with dispersion $\epsilon_k = 2J\sqrt{(\cos(ka) + g)^2 + \gamma^2 \sin^2(ka)}$. If we change our conventions in order to be consistent with Sachdev [82] we must rotate the Hamiltonian by taking $\sigma^x \to \sigma^x$, $\sigma^y \to \sigma^y$, and $\sigma^z \to -\sigma^z$. Then we'll instead
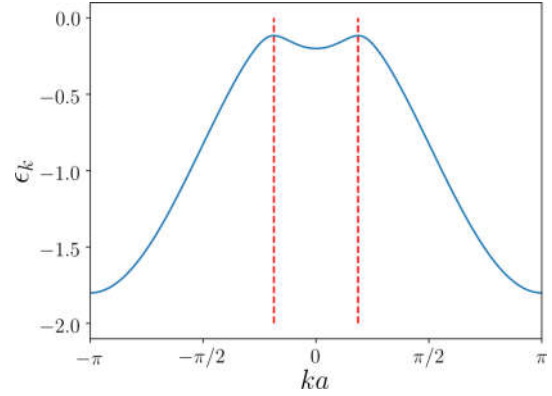

FIG. 7. The XY dispersion relation, given by Eq. (B6), for $\gamma = 0.2$ and $g = 0.8$. Bearing in mind the periodicity of the dispersion relation, one can see that it has four stationary points for these parameter values. The three stationary points that are responsible for the Pearcey function are those that lie between the vertical red dashed lines. The Pearcey function is the wave catastrophe that dresses the inner cone.

have

$$\epsilon_k = 2J\sqrt{(\cos(ka) - g)^2 + \gamma^2 \sin^2(ka)}. \qquad \text{(B6)}$$

Effectively this is like taking $g \to -g$, allowing us to return to the standard form of the transverse-field Ising model in the $\gamma \to 1$ limit, presented in the main text. The dispersion relation given in Eq. (B6) is plotted in Fig. 7.

APPENDIX C: CAUSTICS IN THE XY MODEL

In this Appendix, we give more details of the calculations of the caustics and their wave functions that are presented in the main text. The XY model contains both fold and cusp catastrophes; we focus particularly on the cusp catastrophe and defer some of the treatment of the fold catastrophe to the next Appendix (Appendix D) which is on the TFIM.

1. Calculation of classical caustics in the XY model

The light cone conditions, or equivalently the caustic conditions, are given in Eqs. (2) and (3) in the main text. These correspond to vanishing first and second derivatives of the generating function $\Phi = kx - \epsilon_k t/\hbar$. The vanishing of the first derivative with respect to k gives the equation

$$\frac{\partial \Phi}{\partial k} = x - \frac{Jt(2a\gamma^2 \cos(ka)\sin(ka) + 2a(g - \cos(ka))\sin(ka))}{\hbar\sqrt{(g - \cos(ka))^2 + \gamma^2 \sin^2(ka)}} = 0 \qquad \text{(C1)}$$

bringing x to one side, multiplying both sides by the denominator and squaring gives

$$x^2 \hbar^2 ((g - \cos(ka))^2 + \gamma^2 \sin^2(ka)),$$
$$= 4a^2 J^2 t^2 (g + (\gamma^2 - 1)\cos(ka))^2 \sin^2(ka). \qquad \text{(C2)}$$

Replacing $\sin^2(ka) = 1 - \cos^2(ka)$, putting $z \equiv \cos(ka)$, and collecting as a quartic polynomial gives

$$0 = (\gamma^2 - 1)^2 v_I^2 t^2 z^4 + 2(\gamma^2 - 1)g v_I^2 t^2 z^3 + \left(g^2 v_I^2 t^2 - (\gamma^2 - 1)^2 v_I^2 t^2 - \gamma^2 x^2 + x^2\right)z^2 + \left(-2(\gamma^2 - 1)g v_I^2 t^2 - 2gx^2\right)z$$
$$+ \gamma^2 x^2 - g^2 v_I^2 t^2 + g^2 x^2, \qquad \text{(C3)}$$

where the Ising velocity v_I was defined in Eq. (19). The light cones correspond to the control parameter values where solutions coincide, that is, the stationary points of this equation.

The vanishing of the second derivative of the generating function gives the equation

$$\frac{\partial^2 \Phi}{\partial k^2} = \frac{Jt(2a\gamma^2 \cos(ka)\sin(ka) - 2a(\cos(ka) - g)\sin(ka))^2}{2\hbar((\cos(ka) - g)^2 + \gamma^2 \sin^2(ka))^{3/2}}$$
$$- \frac{Jt(2a^2\gamma^2 \cos^2(ka) - 2a^2 \cos(ka)(\cos(ka) - g))}{\hbar\sqrt{(\cos(ka) - g)^2 + \gamma^2 \sin^2(ka)}} - \frac{Jt(2a^2 \sin^2(ka) - 2a^2\gamma^2 \sin^2(ka))}{\hbar\sqrt{(\cos(ka) - g)^2 + \gamma^2 \sin^2(ka)}} = 0. \quad \text{(C4)}$$

We now multiply both sides by $2\hbar[((\cos(ka) - g)^2 + \gamma^2 \sin^2(ka)]^{3/2}/Jt$ and simplify

$$0 = \tfrac{1}{2}a^2[3(4g^2 + (\gamma^2 - 1)^2) - 2g(9 + 4g^2 - 5\gamma^2)\cos(ka) + 4(\gamma^4 - 1 + g^2(2\gamma^2 - 3))\cos(2ka)$$
$$+ 6g(\gamma^2 - 1)\cos(3ka) + (\gamma^2 - 1)^2 \cos(4ka)]. \quad \text{(C5)}$$

Next we make the replacements $\cos(2ka) = 2\cos^2(ka) - 1$; $\cos(3ka) = 4\cos^3(ka) - 3\cos(ka)$; and $\cos(4ka) = 8\cos^4(ka) - 8\cos^2(ka) + 1$. Defining again $z \equiv \cos(ka)$, and dividing both sides by $a^2/2$,

$$0 = 8(\gamma^2 - 1)^2 z^4 + 24g(\gamma^2 - 1)z^3 - 8(2\gamma^2(\gamma^2 - 1) + g^2(2\gamma^2 - 3))z^2 - 8g(g^2 + \gamma^2)z + 8\gamma^2(g^2 + \gamma^2 - 1). \quad \text{(C6)}$$

The light cones/caustics correspond to simultaneous solutions of Eqs. (C3) and (C6) and hence correspond to the Lieb-Robinson (LR) bound which is the solution which maximizes the propagation speed of the quasiparticles.

In the next section, we describe how the triple coalescence of stationary points give rise to the Pearcey function which provides the inner cone in Fig. 2. The three stationary points which coalesce are those between the dashed lines in Fig. 7. For $0 < \gamma < 1$ and $0 < g < 1$, this coalescence occurs at $k = 0$, thus $z = 1$, and Eq. (C6) yields solutions $g = 1$ and $g = 1 - \gamma^2$. The $g = 1$ solution is highly singular for nonzero anisotropy, while the solution $g = 1 - \gamma^2$ is the key for triple root coalescence.

2. Diffraction integral for the cusp wave catastrophe

Let us begin by defining the Pearcey function which is the canonical form of the wave function corresponding to the cusp catastrophe. The definition of the Pearcey function that we use is

$$\text{Pe}(C_1, C_2) \equiv \frac{1}{2\pi} \int_{-\infty}^{\infty} ds \, e^{-i(C_1 s + \frac{C_2}{2}s^2 + \frac{s^4}{4})}. \quad \text{(C7)}$$

It features two parameters C_1 and C_2 and is generally a complex function. In fact, the common definition of the Pearcey function is the complex conjugate of (C7), however for our purposes, the above definition is more convenient.

Since the coalescence of extrema in Φ occurs at $k = 0$, we expand to fourth order and factor out $J/\hbar$, which we will later use for scaling,

$$\Phi(k; J) \approx \frac{J}{\hbar}\left[2t(g - 1) + \frac{2gax}{v_I}k \right.$$
$$\left. + \frac{1}{2}\frac{2a^2t(\gamma^2 + g - 1)}{(g - 1)}k^2 - \frac{1}{4}4a^4t\Gamma k^4\right], \quad \text{(C8)}$$

where we have defined the following parameter:

$$\Gamma \equiv \frac{(g^3 - 1 - 2\gamma^2 + 3\gamma^4 + g(3 - 2\gamma^2) + g^2(4\gamma^2 - 3))}{12(g - 1)^3}. \quad \text{(C9)}$$

Note that the solution $g = 1 - \gamma^2$ will kill off the quadratic piece.

We now rescale our integration variable

$$s = \sqrt{2}a(t\Gamma)^{\frac{1}{4}}k, \quad \text{(C10)}$$

then our wave function locally takes the form

$$\Psi_{\text{Pe}}(C_1, C_2; J)$$
$$\approx \frac{e^{i\theta(t)}}{2\pi}\sqrt{\frac{J}{\hbar v_I}}\left(\frac{\gamma^2 + g - 1}{(g - 1)C_2}\right)^{\frac{1}{2}}\int_{-S}^{S} ds \, e^{-i\frac{J}{\hbar}(C_1 s + \frac{C_2}{2}s^2 + \frac{s^4}{4})} \quad \text{(C11)}$$

with definitions

$$C_1(g, \gamma; x, t) = -\frac{\sqrt{2}x}{v_I(t\Gamma)^{\frac{1}{4}}}, \quad \text{(C12)}$$

$$C_2(g, \gamma; x, t) = -\frac{\gamma^2 + g - 1}{g - 1}\left(\frac{t}{\Gamma}\right)^{\frac{1}{2}} \quad \text{(C13)}$$

and integration limit

$$S = \sqrt{2}\pi(t\Gamma)^{\frac{1}{4}}. \quad \text{(C14)}$$

Equation (C11) shows that the wave function for the inner cone can locally be expressed as a diffraction integral which is generated by the cusp catastrophe $\Phi_2 = C_1 s + C_2 s^2/2 + s^4$, and is thus directly related to the canonical Pearcey function when t is reasonably large and $J/\hbar = 1$ (below we will see that we can choose any value of $J/\hbar$ and it will simply rescale the coordinates). Note, however, that the normalization of the wave function restricts the bounds of the integral as $t \to 0$, and so no true cusp point can occur at the origin since Φ also vanishes there. Nevertheless, the region of integration is proportional to $t^{1/4}$ and so is larger than the separation between the stationary points as $t \to 0$ since for any quartic equation of the form Φ_2 the position of the stationary points in the s coordinate is proportional to $\sqrt{C_2}$ so that for any infinitesimal time dt the separation between them is proportional to only $(dt)^{1/2}$. Thus it becomes imperative that we
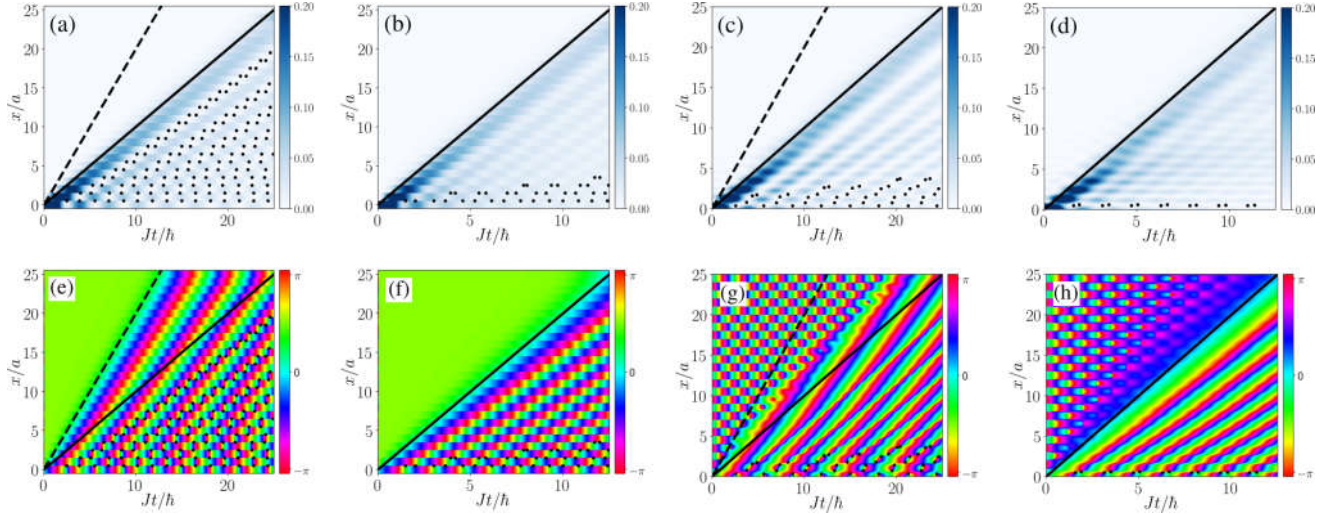
FIG. 8. Caustics and vortices in the TFIM: discrete (exact) versus continuum approximation. The initial condition is a single Bogoliubov fermion created at the center of the chain (only half the chain is shown). The discrete wave function is given by Eq. (A7) whereas the continuum approximation is given by Eq. (A8). [(a)–(d)] Amplitude of the wave function for $g = 0.5$ and 1. [(e)–(h)] Phase of the same wave functions (corresponding to the panels directly above). The caustics are shown as solid black lines, while the imaginary caustics are plotted as dashed lines. The black dots mark the locations of vortices.

consider the effects of all three stationary points, giving rise to the Pearcey-like function described in Eq. (20).

Finally, in order to keep our expressions consistent for $|g| < 1$ and $|g| > 1$, we can instead factor out $Jg/\hbar$ overall. The above results are then identical up to a factor of $1/g$, which can be absorbed into s and is irrelevant for the scaling. Thus the expression v_{I} given in Eq. (19) may be used in Eq. (C12) generally.

3. Self-similar scaling of the cusp wave catastrophe

Now we scale the coupling strength, which corresponds to the width of the dispersion relation, from $J \to J'$. As we do so we enforce $Js^4 = J's'^4$ so that the wave function maintains its basic form. Then, the Berry scaling is

$$JC_1 s = JC_1 \left(\frac{J'}{J}\right)^{\frac{1}{4}} s' = J'C_1 \left(\frac{J}{J'}\right)^{\frac{3}{4}} s' \qquad (C15)$$

and

$$J\frac{C_2}{2} s^2 = J\frac{C_2}{2} \left(\frac{J'}{J}\right)^{\frac{1}{2}} s'^2 = J'\frac{C_2}{2} \left(\frac{J}{J'}\right)^{\frac{1}{2}} s'^2 \qquad (C16)$$

with Arnol'd scaling given by

$$\sqrt{J}ds = \sqrt{J}\left(\frac{J'}{J}\right)^{\frac{1}{4}} ds' = \sqrt{J'}\left(\frac{J}{J'}\right)^{\frac{1}{4}} ds'. \qquad (C17)$$

These are the scaling factors for the cusp wave catastrophe as listed in Table I. As we tune J, it is convenient to keep the caustic in the same place. This is done by simultaneously tuning a such that the Ising velocity v_{I} is constant.

APPENDIX D: CAUSTICS IN THE TRANSVERSE-FIELD ISING MODEL

As mentioned in the main text, the outer light cone in the XY model is dominated by its Airy-like behavior because it

arises from the coalescence of just two stationary points. Since this also occurs in the simpler TFIM (which is obtained by setting $\gamma = 1$), we focus on this case here.

1. Calculation of classical caustics in the TFIM

As shown above for the cusp catastrophe case, we must first calculate the two caustic conditions

$$\frac{\partial \Phi}{\partial k} = 0 = x - \frac{2agJt \sin(ka)}{\hbar\sqrt{g^2 - 2g\cos(ka) + 1}} \qquad (D1)$$

and

$$\frac{\partial^2 \Phi}{\partial k^2} = 0 = -\frac{2a^2 gJt \cos(ka)}{\hbar\sqrt{g^2 - 2g\cos(ka) + 1}}$$
$$+ \frac{2a^2 g^2 Jt \sin^2(ka)}{\hbar(g^2 - 2g\cos(ka) + 1)^{3/2}}, \qquad (D2)$$

which must be simultaneously fulfilled. Rearranging Eq. (D2)

$$g(1 - \cos^2(ka)) = \cos(ka)(g^2 - 2g\cos(ka) + 1) \qquad (D3)$$

leads to $\cos(ka) = g$ or $\cos(ka) = 1/g$, as expected. Inputting this into Eq. (D1), along with $\sin(ka) = \sqrt{1 - g^2}$ [or $\sin(ka) = \sqrt{1 - 1/g^2}$ for $g > 1$], we can solve for the LR velocity, which is identical to the Ising velocity we defined in the previous section,

$$v_{\mathrm{LR}} = v_{\mathrm{I}}. \qquad (D4)$$

Although the caustic lines are determined by the real solutions to Eq. (D3), there exist imaginary solutions for which the Lieb-Robinson velocity g designations are reversed. This seems to be responsible for lines of constant phase across the caustic (see Fig. 8). The presence of two separate speeds within the light cone is also demonstrated by Cevolani et al. in Ref. [16]. We term these imaginary solutions as "imaginary caustics."

2. Diffraction integral for the fold wave catastrophe

The canonical wave catastrophe corresponding to the fold catastrophe is the Airy function. The definition of the Airy function that we use is

$$\text{Ai}(C) \equiv \frac{1}{2\pi} \int_{-\infty}^{\infty} ds \, e^{i(Cs + s^3/3)}. \tag{D5}$$

It features a single parameter C and is a real function if C is real.

The stationary points of Φ coalesce when $k = (1/a)\arccos(g)$ for $g < 1$ and $k = (1/a)\arccos(1/g)$ for $g > 1$, respectively. Thus, for each of these cases, we will expand about these particular k values to third order and factoring out $J/\hbar$ overall,

$$\Phi(k; J) \approx \frac{J}{\hbar}\left(-2t\sqrt{1-g^2} + \frac{x\hbar}{aJ}\arccos(g)\right)$$
$$+ \frac{J}{\hbar}\left(\frac{x\hbar}{aJ} - 2gt\right)(ka - \arccos(g))$$
$$+ \frac{J}{\hbar}\frac{1}{3}gt(ka - \arccos(g))^3 \tag{D6}$$

for $g < 1$ and

$$\Phi(k; J) \approx \frac{J}{\hbar}\left(-2t\sqrt{g^2-1} + \frac{x\hbar}{aJ}\arccos(1/g)\right)$$
$$+ \frac{J}{\hbar}\left(\frac{x\hbar}{aJ} - 2t\right)(ka - \arccos(1/g))$$
$$+ \frac{J}{\hbar}\frac{1}{3}t(ka - \arccos(1/g))^3, \tag{D7}$$

for $g > 1$. Of course, the expansion will only capture the behavior of the wave function close to the light cone, however this is our primary objective. Furthermore, we are guaranteed that (up to a smooth change of variables) this cubic form in particular is structurally stable and will capture the qualitative features of Φ. We now rescale our integration variables as

$$s_1^3 = gt(ka - \arccos(g))^3, \tag{D8}$$

$$s_2^3 = t(ka - \arccos(1/g))^3. \tag{D9}$$

Thus

$$\Phi_{\text{Ai}}(s; J) = \frac{J}{\hbar}\left[\left(-2t\sqrt{1-g^2} + \frac{2gx}{v_{\text{I}}}\arccos(g)\right)\right.$$
$$\left. + 2\left(\frac{x}{v_{\text{I}}} - t\right)\left(\frac{g^2}{t}\right)^{\frac{1}{3}}s_1 + \frac{1}{3}s_1^3\right] \tag{D10}$$

for $g < 1$ and

$$\Phi_{\text{Ai}}(s; J) = \frac{J}{\hbar}\left[\left(-2t\sqrt{g^2-1} + \frac{2x}{v_{\text{I}}}\arccos(1/g)\right)\right.$$
$$\left. + 2\left(\frac{x}{v_{\text{I}}} - t\right)\left(\frac{1}{t}\right)^{\frac{1}{3}}s_2 + \frac{1}{3}s_2^3\right] \tag{D11}$$

for $g > 1$.

Now we define the control variable as

$$C = \begin{cases} 2\left(\frac{x}{v_{\text{I}}} - t\right)\left(\frac{g^2}{t}\right)^{\frac{1}{3}}, & g < 1 \\ 2\left(\frac{x}{v_{\text{I}}} - t\right)\left(\frac{1}{t}\right)^{\frac{1}{3}}, & g > 1 \end{cases}, \tag{D12}$$

so that

$$\Psi(C; J) = \begin{cases} \frac{e^{\Theta_1}}{2\pi(gt)^{\frac{1}{3}}\sqrt{a}} \int_{s^{\text{Min}}}^{s^{\text{Max}}} ds \, e^{\frac{iJ}{\hbar}\Phi_1(C,s)}, & g < 1 \\ \frac{e^{\Theta_2}}{2\pi t^{\frac{1}{3}}\sqrt{a}} \int_{s^{\text{Min}}}^{s^{\text{Max}}} ds \, e^{\frac{iJ}{\hbar}\Phi_1(C,s)}, & g > 1 \end{cases} \tag{D13}$$

with

$$\Phi_1(C, s) = Cs + \frac{1}{3}s^3, \tag{D14}$$

$$\frac{1}{\sqrt{a}}ds = \begin{cases} \sqrt{\frac{2gJ}{v_{\text{I}}\hbar}}ds, & g < 1 \\ \sqrt{\frac{2J}{v_{\text{I}}\hbar}}ds, & g > 1 \end{cases} \tag{D15}$$

and limits

$$s^{\text{Min}} = \begin{cases} (gt)^{\frac{1}{3}}(-\pi - \arccos(g)) & g < 1 \\ t^{\frac{1}{3}}(-\pi - \arccos(1/g)) & g > 1 \end{cases}, \tag{D16}$$

$$s^{\text{Max}} = \begin{cases} (gt)^{\frac{1}{3}}(\pi - \arccos(g)) & g < 1 \\ t^{\frac{1}{3}}(\pi - \arccos(1/g)) & g > 1 \end{cases}. \tag{D17}$$

Note that $s^{\text{Min}} < 0$ and $s^{\text{Max}} > 0$. Thus, if we assume long enough times, then it is reasonable to take these integration limits to plus and minus infinity. We now have a description of the wave function local to the light cone using a fold catastrophe integral, which in the limit of $J/\hbar \to 1$ will become the Airy integral.

3. Self-similar scaling of the fold wave catastrophe

As for the cusp case, we can extract the scaling properties of the fold wave catastrophe by considering the change from $J \to J'$. Under this transformation we assume that $Js^3 = J's'^3$. Then,

$$JCs = JC\left(\frac{J'}{J}\right)^{\frac{1}{3}}s' = J'C\left(\frac{J}{J'}\right)^{\frac{2}{3}}s' \tag{D18}$$

and

$$\sqrt{J}ds = \sqrt{J}\left(\frac{J'}{J}\right)^{\frac{1}{3}}ds' = \sqrt{J'}\left(\frac{J}{J'}\right)^{\frac{1}{6}}ds'. \tag{D19}$$

Taking the integral limits to infinity (long times)

$$\Psi_{\text{Ai}}(C; J) \propto \sqrt{J'}\left(\frac{J}{J'}\right)^{\frac{1}{6}} \int_{-\infty}^{\infty} ds' \, e^{i\frac{J'}{\hbar}\left(\left(\frac{J}{J'}\right)^{\frac{2}{3}}Cs' + \frac{1}{3}s'^3\right)} \tag{D20}$$

or, equivalently,

$$\Psi_{\text{Ai}}(C; J) = \left(\frac{J}{J'}\right)^{\frac{1}{6}}\Psi_{\text{Ai}}\left(\left[\frac{J}{J'}\right]^{\frac{2}{3}}C; J'\right). \tag{D21}$$

We have therefore obtained the scaling factors for the fold wave catastrophe as listed in Table I.

APPENDIX E: SPIN-FLIP STATE $\Psi_{\text{X}}(x, t)$

In this paper, we mainly consider an initial state consisting of a single fermionic quasiparticle localized on a particular site. However, in Sec. IX, we instead consider the initial state where all the spins are polarized along the x direction except

for the central spin which is flipped such that the time evolved wave function is

$$\Psi_X(x,t) \equiv \langle x| e^{-iHt/\hbar} |\uparrow^x \dots \uparrow^x \downarrow^x \uparrow^x \dots \uparrow^x\rangle. \tag{E1}$$

Because experiments with ions can easily address individual spins, and spins and quasiparticles are not quite the same thing, it important to consider this kind of state.

Evaluating the time evolution of spin chains is generally far simpler in the Bogoliubov basis. However, to introduce physical spins, we begin with the JW basis which is related to the Bogoliubov basis by the Bogoliubov rotation:

$$\tilde{c}_k^\dagger = u_k \tilde{b}_k^\dagger - iv_k \tilde{b}_{-k}. \tag{E2}$$

We identify the creation of a JW fermion at the center of the lattice as a spin flip from $\uparrow^x$ to $\downarrow^x$ via the inverse JW transformation:

$$c_j^\dagger = \left(\prod_{i>j} \sigma_i^x\right) \sigma_j^-. \tag{E3}$$

It is also important to note that the JW and Bogoliubov vacuums are related by

$$|0\rangle = \prod_{k>0}(u_k - iv_k\tilde{b}_k^\dagger\tilde{b}_{-k}^\dagger)|0\rangle_b. \tag{E4}$$

Starting with the center spin ($x=0$) down,

$$
\begin{aligned}
|\Psi_0\rangle &= c_{x=0}^\dagger |0\rangle = \sum_{k_1} \tilde{c}_{k_1}^\dagger |0\rangle \\
&= \sum_{k_1} \left(u_{k_1}\tilde{b}_{k_1}^\dagger - iv_{k_1}\tilde{b}_{-k_1}\right) \\
&\quad \times \prod_{k_2>0}\left(u_{k_2} - iv_{k_2}\tilde{b}_{k_2}^\dagger\tilde{b}_{-k_2}^\dagger\right)|0\rangle_b
\end{aligned}
\tag{E5}
$$

and using the following relation

$$
\begin{aligned}
&\tilde{b}_{k_1}^\dagger \prod_{k_2>0}\left(u_{k_2} - iv_{k_2}\tilde{b}_{k_2}^\dagger\tilde{b}_{-k_2}^\dagger\right)|0\rangle_b \\
&= u_{k_1}\tilde{b}_{k_1}^\dagger \prod_{k_2>0,\,|k_2|\neq|k_1|}\left(u_{k_2} - iv_{k_2}\tilde{b}_{k_2}^\dagger\tilde{b}_{-k_2}^\dagger\right)|0\rangle_b,
\end{aligned}
\tag{E6}
$$

we get

$$|\Psi_0\rangle = \sum_{k_1}\tilde{b}_{k_1}^\dagger \prod_{k_2>0,\,|k_2|\neq|k_1|}\left(u_{k_2} - iv_{k_2}\tilde{b}_{k_2}^\dagger\tilde{b}_{-k_2}^\dagger\right)|0\rangle_b. \tag{E7}$$

Next, we evolve in time using a more convenient representation of the time-evolution operator,

$$e^{-\frac{it}{\hbar}\sum_k \epsilon_k(\tilde{b}_k^\dagger\tilde{b}_k - \frac{1}{2})} = e^{i\theta(t)}\prod_k\left[1 - \left(1 - e^{-\frac{it\epsilon_k}{\hbar}}\right)\tilde{b}_k^\dagger\tilde{b}_k\right]. \tag{E8}$$

Dropping the global phase factor, and projecting this state onto real space $\Psi(x_i,t) = \langle x_i|\Psi(t)\rangle$ using

$$
\begin{aligned}
\langle x_i| &= \langle 0| c_i \\
&= \sum_{k_3} e^{ik_3 x_i}{}_b\langle 0| \prod_{\substack{k_4>0 \\ |k_4|\neq|k_3|}}\left(u_{k_4} + iv_{k_4}\tilde{b}_{-k_4}\tilde{b}_{k_4}\right)\tilde{b}_{k_3},
\end{aligned}
\tag{E9}
$$

we arrive at, after a fair amount of algebra,

$$
\begin{aligned}
\Psi(x_i,t) &= \sum_{k_1} e^{-\frac{it\epsilon_{k_1}}{\hbar}} e^{ik_1 x_i}\prod_{\substack{k_2>0 \\ |k_2|\neq|k_1|}}\left(u_{k_2}^2 + v_{k_2}^2 e^{-\frac{it\epsilon_{k_2}}{\hbar}}\right) \\
&\quad + \sum_{k_1} e^{-\frac{2it\epsilon_{k_1}}{\hbar}} e^{ik_1 x_i} v_{k_1}^2 \prod_{\substack{k_2>0 \\ |k_2|\neq|k_1|}}\left(u_{k_2}^2 + v_{k_2}^2 e^{-\frac{it\epsilon_{k_2}}{\hbar}}\right).
\end{aligned}
\tag{E10}
$$

APPENDIX F: VORTEX SCALING

Returning to our original initial condition of a single Bogoliubov fermion created at $x=0$, we can identify space-time vortices in the time evolved system. The discrete (exact) and CA results are compared for the TFIM in Fig. 8 where the same general trend is observed in both cases: fewer vortices at the QCP at $g=1$ than away from it at $g=0.5$. The vortices that survive at the QCP are those near to the center of the chain at $x=0$, i.e., those closest to the position of the original excitation. In fact, in the CA only a single line of vortices on each side of the center line survives.

The vortices are located by breaking the light cone up into small loops and integrating the phase of the wave function around each one. For a loop containing a single vortex,

$$\int_{\mathcal{C}} d\chi = \pm 2\pi, \tag{F1}$$

where the plus sign signifies a vortex and the minus sign an antivortex. For the discrete wave function, the integral along the spatial part of the path $\mathcal{C}$ is replaced by a sum.

If we track the positions of the vortices as g is varied, we find that they flow in space-time in such a way that as the QCP is approached vortices and antivortices annihilate in pairs, each pair annihilating at a different point (x,t). This process is easier to follow in the CA than the discrete case because the discreteness in the lattice direction obscures the spatial location of vortices, so in this Appendix we specialize to the CA case (whereas the data presented in Fig. 6 in the main text are for the discrete case). In particular, Fig. 9 gives a pictorial representation of the annihilations occurring near the center of the lattice for $g=1.75$. We see that vortex-antivortex pairs converge on horizontal lines (i.e., spatial points) located at $x/a = \pm 0.5, \pm 1.5, \pm 2.5, \dots$

The temporal behavior of the vortices can also be seen in Fig. 9. For values of g close the QCP, the vortex-antivortex pairs that occur at short times annihilate and so never occur, or, said another way, as $g \to 1$ the creation time for vortex-antivortex pairs diverges, an example of critical slowing. Thus there are two dimensions along which one can observe critical scaling: along t and along x, and the data for these two directions are shown in Fig. 10. It is clear from the way that the data falls onto straight lines on a log-log scale as $g \to 1$ that the vortices display critical scaling. The figure shows two "sets" of vortices, where each set annihilates within a small region of x/a at diverging timescales. The vortices we call primary vortices annihilate at positions approaching $\bar{x}=1.5a$, while $\bar{x}=2.5a$ for the secondary vortices. In the main text, we focus only on the primary vortices, since a greater number annihilate earlier in time and thus result in a less oscillatory
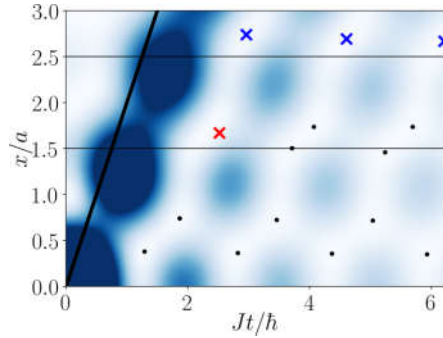
FIG. 9. Graphic depicting vortex annihilation in the CA for the TFIM. Here, $g = 1.75$, and for clarity the lines $x/a = 1.5$ and $x/a = 2.5$ have been drawn. As g is tuned toward the transition, vortex-antivortex pairs (black dots) will approach one another and eventually annihilate at a particular point in space-time, denoted with an "X." It is the vortices which annihilate close to $x/a = 1.5$ that we refer to as 'primary' (red) and those which annihilate close to $x/a = 2.5$ we refer to as "secondary" (blue, all annihilated in this image). In principle, there exist rows of vortices beyond these, but here we focus on those closer to the center of the lattice and short times.

integrand, allowing us to get closer to the transition while maintaining accuracy for a larger number of data points, but we see that the secondary vortices obey the same scaling. The temporal scaling shown in Fig. 10(a) leads to a gradient of -1 and hence the relation $\nu z = 1$ as explained in the main text [see inset in Fig. 6(b)]. The spatial scaling is shown in Fig. 10(b) and leads to a gradient of 0.5.
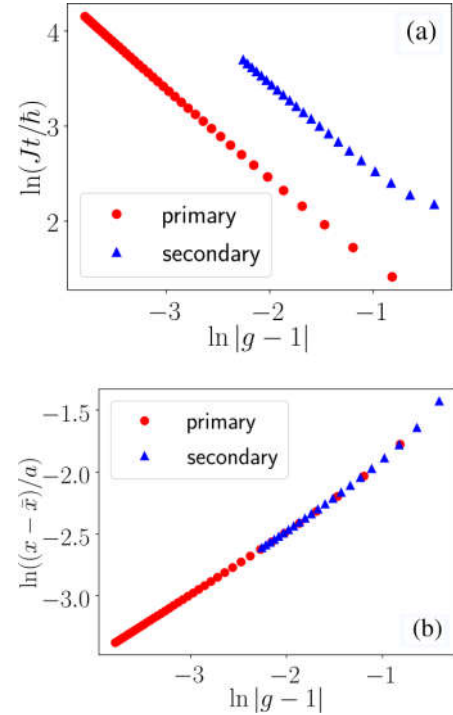

FIG. 10. Vortex annihilation scaling in the TFIM within the CA. (a) The time at which vortex annihilation occurs along a particular set of vortices will diverge as we approach the QCP. (b) Each consecutive vortex pair will annihilate at a point in space (x) which approaches the midpoint between two lattice sites. Thus $\bar{x} = 1.5a$ for the set of primary vortices and $\bar{x} = 2.5a$ for the secondary vortices.

[1] E. H. Lieb and D. W. Robinson, The finite group velocity of quantum spin systems, Commun. Math. Phys. **28**, 251 (1972).

[2] J. Eisert, M. Friesdorf, and C. Gogolin, Quantum many-body systems out of equilibrium, Nat. Phys. **11**, 124 (2015).

[3] P. Calabrese and J. Cardy, Time Dependence of Correlation Functions Following a Quantum Quench, Phys. Rev. Lett. **96**, 136801 (2006).

[4] P. Calabrese and J. Cardy, Evolution of entanglement entropy in one-dimensional systems, J. Stat. Mech. (2005) P04010.

[5] A. M. Läuchli and C. Kollath, Spreading of correlations and entanglement after a quench in the one-dimensional Bose-Hubbard model, J. Stat. Mech. (2008) P05018.

[6] S. R. Manmana, S. Wessel, R. M. Noack, and A. Muramatsu, Time evolution of correlations in strongly interacting fermions after a quantum quench, Phys. Rev. B **79**, 155104 (2009).

[7] J.-M. Stéphan and J. Dubail, Local quantum quenches in critical one-dimensional systems: entanglement, the Loschmidt echo, and light-cone effects, J. Stat. Mech. (2011) P08019.

[8] P. Barmettler, D. Poletti, M. Cheneau, and C. Kollath, Propagation front of correlations in an interacting Bose gas, Phys. Rev. A **85**, 053625 (2012).

[9] P. Calabrese, F. H. L. Essler, and M. Fagotti, Quantum quench in the transverse field Ising chain: I. Time evolution of order parameter correlators, J. Stat. Mech. (2012) P07016.

[10] J. Schachenmayer, B. P. Lanyon, C. F. Roos, and A. J. Daley, Entanglement Growth in Quench Dynamics with Variable Range Interactions, Phys. Rev. X **3**, 031015 (2013).

[11] J. Eisert, M. van den Worm, S. R. Manmana, and M. Kastner, Breakdown of Quasilocality in Long-Range Quantum Lattice Models, Phys. Rev. Lett. **111**, 260401 (2013).

[12] P. Hauke and L. Tagliacozzo, Spread of Correlations in Long-Range Interacting Quantum Systems, Phys. Rev. Lett. **111**, 207202 (2013).

[13] J. Haegeman, C. Lubich, I. Oseledets, B. Vandereycken, and F. Verstraete, Unifying time evolution and optimization with matrix product states, Phys. Rev. B **94**, 165116 (2016).

[14] G. Perfetto and A. Gambassi, Ballistic front dynamics after joining two semi-infinite quantum Ising chains, Phys. Rev. E **96**, 012138 (2017).

[15] M. Kormos, Inhomogeneous quenches in the transverse field Ising chain: scaling and front dynamics, SciPost Phys. **3**, 020 (2017).

[16] L. Cevolani, J. Despres, G. Carleo, L. Tagliacozzo, and L. Sanchez-Palencia, Universal scaling laws for correlation spreading in quantum systems with short- and long-range interactions, Phys. Rev. B **98**, 024302 (2018).

[17] M. Cheneau, P. Barmettler, D. Poletti, M. Endres, P. Schauss, T. Fukuhara, C. Gross, I. Bloch, C. Kollath, and S. Kuhr, Light-cone-like spreading of correlations in a quantum many-body system, Nature (London) **481**, 484 (2012).

[18] T. Fukuhara, P. Schauß, M. Endres, S. Hild, M. Cheneau, I. Bloch, and C. Gross, Microscopic observation of magnon bound states and their dynamics, Nature (London) **502**, 76 (2013).

[19] T. Langen, R. Geiger, M. Kuhnert, B. Rauer, and J. Schmiedmayer, Local emergence of thermal correlations in an isolated quantum many-body system, Nat. Phys. **9**, 640 (2013).

[20] P. Richerme, Z.-X. Gong, A. Lee, C. Senko, J. Smith, M. Foss-Feig, S. Michalakis, A. V. Gorshkov, and C. Monroe, Non-local propagation of correlations in quantum systems with long-range interactions, Nature (London) **511**, 198 (2014).

[21] P. Jurcevic, B. P. Lanyon, P. Hauke, C. Hempel, P. Zoller, R. Blatt, and C. F. Roos, Quasiparticle engineering and entanglement propagation in a quantum many-body system, Nature (London) **511**, 202 (2014).

[22] J. Simon, W. S. Bakr, R. Ma, M. E. Tai, P. M. Preiss, and M. Greiner, Quantum simulation of antiferromagnetic spin chains in an optical lattice, Nature (London) **472**, 307 (2011).

[23] R. Islam, E. E. Edwards, K. Kim, S. Korenblit, C. Noh, H. Carmichael, G.-D. Lin, L.-M. Duan, C.-C. Joseph Wang, J. K. Freericks, and C. Monroe, Onset of a quantum phase transition with a trapped ion quantum simulator, Nat. Commun. **2**, 377 (2011).

[24] K. Kim, M.-S. Chang, S. Korenblit, R. Islam, E. E. Edwards, J. K. Freericks, G.-D. Lin, L.-M. Duan, and C. Monroe, Quantum simulation of frustrated Ising spins with trapped ions, Nature (London) **465**, 590 (2010).

[25] J. Struck, C. Olschlager, R. L. Targat, P. Soltan-Panahi, A. Eckardt, M. Lewenstein, P. Windpassinger, and K. Sengstock, Quantum simulation of frustrated classical magnetism in triangular optical lattices, Science **333**, 996 (2011).

[26] D. Jaksch, C. Bruder, J. I. Cirac, C. W. Gardiner, and P. Zoller, Cold Bosonic Atoms in Optical Lattices, Phys. Rev. Lett. **81**, 3108 (1998).

[27] M. Greiner, O. Mandel, T. Esslinger, T. W. Hänsch, and I. Bloch, Quantum phase transition from a superfluid to a Mott insulator in a gas of ultracold atoms, Nature (London) **415**, 39 (2002).

[28] T. Stöferle, H. Moritz, C. Schori, M. Köhl, and T. Esslinger, Transition from a Strongly Interacting 1D Superfluid to a Mott Insulator, Phys. Rev. Lett. **92**, 130403 (2004).

[29] S. Trotzky, Y.-A. Chen, A. Flesch, I. P. McCulloch, U. Schollwöck, J. Eisert, and I. Bloch, Probing the relaxation towards equilibrium in an isolated strongly correlated one-dimensional Bose gas, Nat. Phys. **8**, 325 (2012).

[30] T. Kinoshita, T. Wenger, and D. S. Weiss, A quantum Newton's cradle, Nature (London) **440**, 900 (2006).

[31] S. Hofferberth, I. Lesanovsky, B. Fischer, T. Schumm, and J. Schmiedmayer, Non-equilibrium coherence dynamics in one-dimensional Bose gases, Nature (London) **449**, 324 (2007).

[32] T. Jacqmin, J. Armijo, T. Berrada, K. V. Kheruntsyan, and I. Bouchoule, Sub-Poissonian Fluctuations in a 1D Bose Gas: From the Quantum Quasicondensate to the Strongly Interacting Regime, Phys. Rev. Lett. **106**, 230405 (2011).

[33] M. Karski, L. Förster, J.-M. Choi, A. Steffen, W. Alt, D. Meschede, and A. Widera, Quantum walk in position space with single optically trapped atoms, Science **325**, 174 (2009).

[34] P. M. Preiss, R. Ma, M. E. Tai, A. Lukin, M. Rispoli, P. Zupancic, Y. Lahini, R. Islam, and M. Greiner, Strongly correlated quantum walks in optical lattices, Science **347**, 1229 (2015).

[35] O. Morsch and M. Oberthaler, Dynamics of Bose-Einstein condensates in optical lattices, Rev. Mod. Phys. **78**, 179 (2006).

[36] R. Blatt and C. F. Roos, Quantum simulations with trapped ions, Nat. Phys. **8**, 277 (2012).

[37] C. Monroe and J. Kim, Scaling the ion trap quantum processor, Science **339**, 1164 (2013).

[38] W. S. Bakr, J. I. Gillen, A. Peng, S. Folling, and M. Greiner, A quantum gas microscope for detecting single atoms in a Hubbard-regime optical lattice, Nature (London) **462**, 74 (2009).

[39] C. Weitenberg, M. Endres, J. F. Sherson, M. Cheneau, P. Schauß, T. Fukuhara, I. Bloch, and S. Kuhr, Single-spin addressing in an atomic Mott insulator, Nature (London) **471**, 319 (2011).

[40] J. F. Sherson, C. Weitenberg, M. Endres, M. Cheneau, I. Bloch, and S. Kuhr, Single-atom-resolved fluorescence imaging of an atomic Mott insulator, Nature (London) **467**, 68 (2010).

[41] J. F. Nye, *Natural Focusing and Fine Structure of Light* (Institute of Physics, Philadelphia, 1999).

[42] L. Kelvin, Deep water ship-waves, Philos. Mag. **9**, 733 (1905).

[43] F. Ursell, *Ship Hydrodynamics, Water Waves and Asymptotics*. Collected works of F. Ursell, 1946–1992 (World Scientific, Singapore, 1994), Vol. 2.

[44] NIST Digital Library of Mathematical Functions, http://dlmf.nist.gov/, Release 1.0.24 of 2019-09-15. F. W. J. Olver, A. B. Olde Daalhuis, D. W. Lozier, B. I. Schneider, R. F. Boisvert, C. W. Clark, B. R. Miller, B. V. Saunders, H. S. Cohl, and M. A. McClain, eds.

[45] M. V. Berry, Tsunami asymptotics, New J. Phys. **7**, 129 (2005); Focused tsunami waves, Proc. R. Soc. London A **463**, 3055 (2007); Minimal analytical model for undular tidal bore profile; quantum and Hawking effect analogies, New J. Phys. **20**, 053066 (2018).

[46] V. L. Ginzburg, Radiation from uniformly moving sources (Vavilov-Cherenkov effect, transition radiation, and some other phenomena), Acoust. Phys. **51**, 11 (2005).

[47] I. Carusotto, S. X. Hu, L. A. Collins, and A. Smerzi, Bogoliubov-Čerenkov Radiation in a Bose-Einstein Condensate Flowing against an Obstacle, Phys. Rev. Lett. **97**, 260403 (2006).

[48] Y. G. Gladush, L. A. Smirnov, and A. M. Kamchatnov, Generation of Cherenkov waves in the flow of a Bose-Einstein condensate past an obstacle, J. Phys. B **41**, 165301 (2008).

[49] J. Marino, A. Recati, and I. Carusotto, Casimir Forces and Quantum Friction from Ginzburg Radiation in Atomic Bose-Einstein Condensates, Phys. Rev. Lett. **118**, 045301 (2017).

[50] R. Thom, *Structural Stability and Morphogenesis* (Benjamin, Reading MA, 1975).

[51] V. I. Arnol'd, Critical points of smooth functions and their normal forms, Russ. Math. Survs. **30**, 1 (1975).

[52] M. Berry, *Singularities in Waves and Rays* in Les Houches, Session XXXV, 1980 Physics of Defects, edited by R. Balian *et al.* (North Holland, Amsterdam, 1981).

[53] E. Lieb, T. Schultz, and D. Mattis, Two soluble models of an antiferromagnetic chain, Ann. Phys. **16**, 407 (1961).

[54] S. Katsura, Statistical mechanics of the anisotropic linear heisenberg model, Phys. Rev. **127**, 1508 (1962).

[55] P. G. de Gennes, Collective motions of hydrogen bonds, Solid State Commun. **1**, 132 (1963).

[56] P. Pfeuty, The one-dimensional Ising model with a transverse field, Ann. Phys. (NY) **57**, 79 (1970).

[57] J. Häppölä, G. B. Halász, and A. Hamma, Universality and robustness of revivals in the transverse field XY model, Phys. Rev. A **85**, 032114 (2012).

[58] T. Langen, T. Schweigler, E. Demler, and J. Schmiedmayer, Double light-cone dynamics establish thermal states in integrable 1D Bose gases, New J. Phys. **20**, 023034 (2018).

[59] V. Eisler and Z. Rácz, Full Counting Statistics in a Propagating Quantum Front and Random Matrix Spectra, Phys. Rev. Lett. **110**, 060602 (2013).

[60] J. Viti, J.-M. Stéphan, J. Dubail, and M. Haque, Inhomogeneous quenches in a free fermionic chain: Exact results, Europhys. Lett. **115**, 40011 (2016).

[61] V. Eisler and F. Maislinger, Hydrodynamical phase transition for domain-wall melting in the XY chain, Phys. Rev. B. **98**, 161117(R) (2018).

[62] V. Hunyadi, Z. Rácz, and L. Sasvári, Dynamic scaling of fronts in the quantum XX chain, Phys. Rev. E **69**, 066103 (2004).

[63] K. Najafi, M. A. Rajabpour, and J. Viti, Light-cone velocities after a global quench in a noninteracting model, Phys. Rev. B. **97**, 205103 (2018).

[64] N. Allegra, J. Dubail, J.-M. Stéphan, and J. Viti, Inhomogeneous field theory inside the arctic circle, J. Stat. Mech. (2016) 053108.

[65] S. Xu and B. Swingle, Accessing scrambling using matrix product operators, arXiv:1802.00801.

[66] C.-J. Lin and O. I. Motrunich, Out-of-time-ordered correlators in quantum Ising chain, Phys. Rev. B **97**, 144304 (2018).

[67] J. Riddell and E. S. Sørensen, Out-of-time ordered correlators and entanglement growth in the random-field XX spin chain, Phys. Rev. B **99**, 054205 (2019).

[68] J. Riddell and E. S. Sørensen, Out of time order correlations in the quasi-periodic aubry-andré model, arXiv:1908.03292

[69] T. C. Petersen, M. Weyland, D. M. Paganin, T. P. Simula, S. A. Eastwood, and M. J. Morgan, Electron Vortex Production and Control Using Aberration Induced Diffraction Catastrophes, Phys. Rev. Lett. **110**, 033901 (2013).

[70] W. Rooijakkers, S. Wu, P. Striehl, M. Vengalattore, and M. Prentiss, Observation of caustics in the trajectories of cold atoms in a linear magnetic potential, Phys. Rev. A **68**, 063412 (2003).

[71] J. H. Huckans, I. B. Spielman, B. L. Tolra, W. D. Phillips, and J. V. Porto, Quantum and classical dynamics of a Bose-Einstein condensate in a large-period optical lattice, Phys. Rev. A **80**, 043609 (2009).

[72] S. Rosenblum, O. Bechler, I. Shomroni, R. Kaner, T. Arusi-Parpar, O. Raz, and B. Dayan, Demonstration of Fold and Cusp Catastrophes in an Atomic Cloud Reflected from an Optical Barrier in the Presence of Gravity, Phys. Rev. Lett. **112**, 120403 (2014).

[73] J. T. Chalker and B. Shapiro, Caustic formation in expanding condensates of cold atoms, Phys. Rev. A **80**, 013603 (2009).

[74] T. P. Simula, T. C. Petersen, and D. M. Paganin, Diffraction catastrophes threaded by quantized vortex skeletons caused by atom-optical aberrations induced in trapped Bose-Einstein condensates, Phys. Rev. A **88**, 043626 (2013).

[75] U. Leonhardt, A laboratory analog of the event horizon using slow light in an atomic medium, Nature (London) **415**, 406 (2002).

[76] M. V. Berry and M. R. Dennis, Quantum cores of optical phase singularities, J. Opt. A **6**, S178 (2004).

[77] M. V. Berry, Three quantum obsessions, Nonlinearity **21**, T19 (2008).

[78] D. H. J. O'Dell, Quantum Catastrophes and Ergodicity in the Dynamics of Bosonic Josephson Junctions, Phys. Rev. Lett. **109**, 150406 (2012).

[79] J. Mumford, W. Kirkby, and D. H. J. O'Dell, Catastrophes in non-equilibrium many-particle wave functions: universality and critical scaling, J. Phys. B **50**, 044005 (2017).

[80] J. Mumford, E. Turner, D. W. L. Sprung, and D. H. J. O'Dell, Quantum Spin Dynamics in Fock Space Following Quenches: Caustics and Vortices, Phys. Rev. Lett. **122**, 170402 (2019).

[81] M. V. Berry, Attenuation and focusing of electromagnetic surface waves rounding gentle bends, J. Phys. A **8**, 566 (1975).

[82] S. Sachdev, *Quantum Phase Transitions*, 2nd ed. (Cambridge University Press, New York, 2011).

[83] P. Calabrese, F. H. L. Essler, and M. Fagotti, Quantum Quench in the Transverse-Field Ising Chain, Phys. Rev. Lett. **106**, 227203 (2011).

[84] L. Bucciantini, Light-cone effect and relaxation after a quantum quench from excited states in the Ising chain, J. Phys.: Conf. Ser. **566**, 012026 (2014).

[85] M. Karl, H. Cakir, J. C. Halimeh, M. K. Oberthaler, M. Kastner, and T. Gasenzer, Universal equilibrium scaling functions at short times after a quench, Phys. Rev. E **96**, 022110 (2017).

[86] M. V. Berry and C. Upstill, Catastrophe optics: morphologies of caustics and their diffraction patterns, Prog. Opt. **18**, 257 (1980).

[87] E. Nicklas, M. Karl, M. Höfer, A. Johnson, W. Muessel, H. Strobel, J. Tomkovič, T. Gasenzer, and M. K. Oberthaler, Observation of Scaling in the Dynamics of a Strongly Quenched Quantum Gas, Phys. Rev. Lett. **115**, 245301 (2015).

[88] M. V. Berry, J. F. Nye, and F. J. Wright, The elliptic umbilic diffraction catastrophe, Philos. Trans. R. Soc. Lond. **291**, 1382 (1979).

[89] J. F. Nye and M. V. Berry, Dislocations in wave trains, Proc. R. Soc. Lond. A **336**, 165 (1974).

[90] D. Kaminski and R. B. Paris, On the zeros of the Pearcey integral, J. Comput. Appl. Math. **107**, 31 (1999).

[91] J. F. Nye, Dislocation lines in the swallowtail diffraction catastrophe, Proc. R. Soc. A **462**, 2299 (2006).

[92] J. E. Bunder and R. H. McKenzie, Effect of disorder on quantum phase transitions in anisotropic XY spin chains in a transverse field, Phys. Rev. B **60**, 344 (1999).

[93] A. Dutta, G. Aeppli, B. Chakrabarti, U. Divakaran, T. Rosenbaum, and D. Sen, *Quantum Phase Transitions in Transverse Field Spin Models: From Statistical Physics to Quantum Information* (Cambridge University Press, Cambridge, 2015).

[94] G. Lemarié, H. Lignier, D. Delande, P. Szriftgiser, and J.-C. Garreau, Critical State of the Anderson Transition: Between a Metal and an Insulator, Phys. Rev. Lett. **105**, 090601 (2010).

[95] J. D. Ring, J. Lindberg, A. Mourka, M. Mazilu, K. Dholakia, and M. R. Dennis, Auto-focusing and self-healing of Pearcey beams, Opt. Express **20**, 18955 (2012).

[96] T. Poston and I. Stewart, *Catastrophe Theory And Its Applications* (Dover, Minola, New York, 1996).

[97] R. Gilmore, *Catastrophe Theory for Scientists and Engineers* (Wiley, New York, 1981).

[98] R. Gilmore, Structural stability of the phase transition in dicke-like models, J. Math. Phys. **18**, 17 (1977).

[99] R. Gilmore and L. M. Narducci, Relation between the equilibrium and nonequilibrium critical properties of the dicke model, Phys. Rev. A **17**, 1747 (1978).

[100] J. T. Stone, R. H. Self, and C. J. Howls, Aeroacoustic catastrophes: Upstream cusp beaming in Lilley's equation, Proc. R. Soc. A **473**, 20160880 (2017).

[101] V. I. Arnold, S. F. Shandarin, and Ya. B. Zeldovich, The large scale structure of the universe I. general properties. one- and two-dimensional models, Geophys. Astrophys. Fluid Dyn. **20**, 111 (1982).

[102] J. Feldbrugge, R. van de Weygaert, J. Hidding, and J. Feldbrugge, Caustic skeleton & cosmic web, J. Cosmol. Astropart. Phys. **2018**, 27 (2018).

[103] V. I. Arnold, *Mathematical Methods of Classical Mechanics* (Springer, New York, 1997).

[104] B. Gardas, J. Dziarmaga, and W. H. Zurek, Dynamics of the quantum phase transition in the one-dimensional Bose-Hubbard model: Excitations and correlations induced by a quench, Phys. Rev. B **95**, 104306 (2017).

[105] A. D. Zaikin, D. S. Golubev, A. van Otterlo, and G. T. Zimanyi, Quantum fluctuations and dissipation in thin super-conducting wires, Usp. Fiz. Nauk **168**, 244 (1998) [Phys. Usp. **41**, 226 (1998)].

CONNECTING CAUSTICS AND INTEGRABILITY: GAUSSIAN WAVES

In this paper, we broaden our analysis of light cones from the previous Chapter to include chaotic models by considering the out-of-time-ordered correlator (OTOC) in integrable and non-integrable limits. We examine the local scaling of the OTOC at the wavefront of the light cone, in contrast to other studies which look at early growth and late-time behaviour, and use it as a tool for distinguishing the integrability limits of the model.

Close to the light cone, we approximate approximating the OTOC as a Gaussian,

$$C(x,t) \approx \exp[-m(x)(x - v_B t)^2 + b(x)t] \tag{3.1}$$

where v_B is the butterfly velocity, $m(x)$ and $b(x)$ are coefficients that scale with position x in a way which depends to the integrability of the model. We generalize the arguments made in Chapter 2 for general free-fermion models, and show analytically that in this case,

$$m(x) \sim \frac{1}{x^{\frac{2}{3}}} \, , \qquad b(x) \sim \frac{1}{x^{\frac{1}{3}}} \, , \tag{3.2}$$

which we then proceed to verify numerically. In the chaotic limit, these scalings change to give exponential decay instead,

$$m(x) \sim \mathrm{e}^{-cx} \, , \qquad b(x) \sim \mathrm{e}^{-wx} \, , \tag{3.3}$$

where c and w are constants.

Scaling at the OTOC Wavefront: Integrable versus chaotic models

Jonathon Riddell,[1] Wyatt Kirkby,[1] D. H. J. O'Dell,[1] and Erik S. Sørensen[1]

[1]*Department of Physics & Astronomy, McMaster University 1280 Main St. W., Hamilton ON L8S 4M1, Canada.*
(Dated: November 11, 2021)

Out of time ordered correlators (OTOCs) are useful tools for investigating foundational questions such as thermalization in closed quantum systems because they can potentially distinguish between integrable and non-integrable dynamics. Here we discuss the properties of wavefronts of OTOCs by focusing on the region around the main wavefront at $x = v_B t$, where v_B is the butterfly velocity. Using a Heisenberg spin model as an example, we find that a propagating Gaussian with the argument $-m(x)(x - v_B t)^2 + b(x)t$ gives an excellent fit for both the integrable case and the chaotic case. However, the scaling in these two regimes is very different: in the integrable case the coefficients $m(x)$ and $b(x)$ have an inverse power law dependence on x whereas in the chaotic case they decay exponentially. In fact, the wavefront in the integrable case is a rainbow caustic and catastrophe theory can be invoked to assert that power law scaling holds rigorously in that case. Thus, we conjecture that exponential scaling at the OTOC wavefront is a robust signature of a nonintegrable dynamics.

Introduction: The hallmark of chaos in classical dynamics is an exponential sensitivity to small changes in initial conditions (butterfly effect). This is at odds with quantum mechanics where unitary time evolution means that the overlap between two states is constant in time. Although quantum systems do not display chaos, there are qualitative differences in behavior depending upon whether their classical limit is integrable or nonintegrable (chaotic) [1]. In the latter case we have 'quantum chaos' which is well studied in single-particle quantum mechanics, including in experiments [2–12]. On the theoretical side, the main approach has traditionally been through spectral statistics [13, 14]. These have universal properties that depend only on the symmetries of the Hamiltonian and show close agreement with the predictions of random matrix theory (RMT)[15–18]. More recently, attention has shifted to many body quantum chaos and particularly its role in foundational issues such as thermalization in closed quantum systems. One limitation of RMT is that it does not describe thermodynamic quantities like temperature and energy that are needed for such analyses [19]. This is remedied by the eigenstate thermalization hypothesis (ETH) [20–24] which has been numerically verified in a range of generic models [25–28] but is violated in integrable and localized systems [29–38], as expected. The ETH generalizes RMT and gives identical predictions if one focuses on a small enough region of the spectrum. Any diagnostic of quantum chaos should therefore clearly differentiate between the integrable and ETH cases. While the ETH does give rise to the notion of chaotic eigenstates, it is a time independent statement and does not resemble classical chaos. In fact, aside from the weak ETH (eigenstate typicality) [39–41], it has no classical counterpart.

The out-of-time-ordered correlator (OTOC) has risen to prominence as a dynamical diagnostic for quantum many body chaos [42–52]. It takes the form

$$C(x,t) = \langle [\hat{A}(t), \hat{B}]^{\dagger}[\hat{A}(t), \hat{B}] \rangle, \qquad (1)$$

where $\hat{A}$ and $\hat{B}$ are operators that at $t = 0$ only have local support (act on different individual lattice sites) and hence commute. The average is usually taken over an ensemble diagonal in the energy basis, but some studies have considered pure states as well [53–55]. As $\hat{A}$ evolves in time it picks up weight throughout the lattice, becoming non-local and causing $C(x,t)$ to become non-zero. This, in effect, tracks the tendency of dynamics to smear information across the system, and it becomes impossible to determine the initial conditions from local data alone. In this respect the OTOC resembles classical chaos where incomplete information leads to exponential inaccuracy. Indeed, the late time value of the OTOC in local spin models does appear to be an indicator of chaos [43, 53–65]. In the classical limit commutators become Poisson brackets which are a diagnostic for classical chaos, and the general expectation is therefore that OTOCs in nonintegrable models experience exponential growth [52],

$$C(0,t) \sim e^{\lambda_L t}, \qquad (2)$$

where λ_L is the quantum Lyapunov exponent and obeys [52],

$$\lambda_L \leq 2\pi k_B T / \hbar. \qquad (3)$$

Models that approach the bound are known as fast scramblers. However, doubt has been cast upon whether exponential growth of the OTOC really is unique to chaotic systems because integrable systems near unstable points behave similarly [66–71].

An OTOC should also display spatial dependence as information propagates across the system. A new conjecture gives the *early time* growth of the OTOC wavefront as [72–74]

$$C(x,t) \sim \exp\left[-\lambda_L \frac{(x/v_B - t)^{1+p}}{t^p} \right]. \qquad (4)$$

This has been verified in several cases and used to study the many body localization transition [72–83]. For interacting models Eq. (4) is usually fitted in regimes where $C(x,t) \ll 1$ [73, 79], corresponding to early times *significantly before* the arrival of the main front. When the broadening coefficient takes the value $p = 0$, it reduces to the simple "Lyapunov-like" exponential growth of Eq. (2), but for quantum spin models expected to obey ETH it is believed that in general $p > 0$ [74]. However, broadening is not necessarily a general

indicator of how close one is to a chaotic model in the sense of ETH [84, 85], and puzzles remain concerning the value of p in this early growth regime. For example, in two dimensions the values of p coincide in chaotic and integrable models, so the broadening coefficient is inadequate for distinguishing them [74], while some studies [72, 74, 86–89] differ on whether the distinction between values of p even exists in either regime.

The aim of this Letter is to show that the main wavefront (region around $x = v_B t$ which is the edge of the OTOC "light cone") carries information on integrability. While there can be signatures of chaos in OTOCs at late times, including long-time oscillations [74, 85, 90–92], it is preferable to examine the main front rather than the signal either at early times (exponentially small) or late times (more contamination from the environment or numerical errors). Recent numerical work in free models has shown that the OTOC in this region is well-fitted by a propagating Gaussian of the form [54, 93],

$$C_G(x,t) \sim e^{-m(x)(x-v_B t)^2 + b(x)t}, \tag{5}$$

where $m(x)$ and $b(x)$ are well behaved functions of x. A Gaussian also occurs in random circuit models [84] and wavefront results suggest it would also be found in the critical Ising model [60]. Here we will employ rigorous arguments from catastrophe theory to show that in many models that can be mapped to free fermions the wavefront takes on a universal Airy function form that can be locally described by Eq. (5). This allows us to extract the scaling of $m(x), b(x)$ analytically, verifying the findings of [54, 93]. For the chaotic case, we numerically verify the Gaussian wave form of Eq. (5) and show that the scaling of $m(x), b(x)$ is very different from the free model. In locally interacting models the Gaussian wave form Eq. (5) therefore carries signatures of whether the model is free or ETH-obeying.

Model: We consider a Heisenberg spin Hamiltonian with nearest and next nearest interactions:

$$\hat{H} = \sum_{j=1}^{L-1} J_1 \left(\hat{S}_j^+ \hat{S}_{j+1}^- + \text{h.c} \right) + \Delta \hat{S}_j^Z \hat{S}_{j+1}^Z$$
$$+ \sum_{j=1}^{L-2} J_2 \left(\hat{S}_j^+ \hat{S}_{j+2}^- + \text{h.c} \right) + \gamma \hat{S}_j^Z \hat{S}_{j+2}^Z, \tag{6}$$

and open boundary conditions. This model has both free and non-integrable regimes. In particular, we consider two choices of the coefficient vector $\vec{c} = (J_1, \Delta, J_2, \gamma)$. The first one, $\vec{c}_f = (-1, 0, 0, 0)$ is the XX chain and is free while the second, $\vec{c}_{\text{ETH}} = (-0.5, 1, -0.2, 0.5)$ has all parameters non-zero which has been verified to obey the ETH with periodic boundary conditions [25]. In the supplementary materials (SM) [94] we demonstrate that an alternative choice of parameters for $\vec{c}_{\text{ETH}}$ leads to the same basic results. Suitable operators for $\hat{A}(t)$ and $\hat{B}$ must be chosen for the OTOC in Eq. (1). In the ETH regime we use spin operators $\hat{A}(t) = \sigma_1^Z$, and $\hat{B} = \sigma_m^Z$, where x is the distance between sites 1 and m, and the average $\langle \ldots \rangle$ is taken over the thermal ensemble restricted to

eigenstates with zero magnetization, $m_z = \sum_{j=1}^{L} \langle \hat{S}_j^Z \rangle = 0$. In the integrable case we perform a Jordan-Wigner transformation from spins to fermions and for simplicity the OTOC we use in this case is

$$C(x,t) = |a_{m,n}(t)|^2 \tag{7}$$

where $a_{m,n}(t) = \{\hat{f}_m^\dagger(t), \hat{f}_n\}$. Here, $\hat{f}_m$ is the annihilation operator for a fermion on site m. Note that if instead of Eq. (7) we use Eq. (1) with operators σ_m^z, then in the case of a pure Gaussian state or a thermal ensemble the dominant dynamical term is in fact $|a_{m,n}(t)|^2$, see Refs. [54, 93] for further details.

Airy light cones in free systems: In 1972 Lieb and Robinson [95] showed that quantum correlations in spin systems propagate at finite speeds and spread out in a light cone-like fashion. Pioneering experiments with ultracold atoms and trapped ions [96–101], where a sudden quench leads to a nonequilibrium state, have confirmed this behavior. In particular, the wavefront for interacting bosonic atoms in an optical lattice was measured to have an Airy function profile [96] in qualitative agreement with theoretical calculations which can be done analytically in certain limits [102]. The associated problem of domain wall propagation [103–110] also yields Airy functions or related kernels for the wavefront. The Airy function shape implies a dynamical scaling behavior, such as a $t^{1/3}$ broadening of the magnetization domain wall in an XX chain [103]. This body of results has led to the notion of an *Airy universality class* for free systems [111–113].

A more general understanding of light cones can be gained by realizing that they are caustics [114]. These are singularities of the ray description of a wave, where in the present case the rays are trajectories of quasiparticles excited by the quench. Caustics are regions where rays coalesce, leading to a diverging probability density in the classical limit. Significantly, only certain morphologies of caustic are structurally stable and hence occur generically in nature; these form a hierarchy described by catastrophe theory where each catastrophe forms an equivalence class with its own scaling properties similar to universality classes for phase transitions [115, 116]. The simplest catastrophe is the fold which occurs where rays coalesce in pairs and an everyday example of this is the rainbow, and another is a ship's wake [117, 118].

In the wave theory each caustic is dressed by a characteristic wavefunction, and in the case of the fold it is the Airy function [119]. To see how this works, consider the case where the quench excites a Bogoliubov fermion on the site at $x = 0$, say. The resulting wavefunction is

$$\Psi(x,t) = \langle x_b | e^{-i\hat{H}t} \hat{b}_{x=0}^\dagger | 0_b \rangle = \langle x_b | \sum_k e^{-i\epsilon(k)t} | k \rangle$$
$$\approx \frac{\sqrt{a}}{2\pi} \int_{-\frac{\pi}{a}}^{\frac{\pi}{a}} dk \, e^{i[kx - \epsilon(k)t]} \tag{8}$$

where a is the lattice constant. The operators $\hat{b}_x$ are the linear combinations of $\hat{f}_m$ and $\hat{f}_m^\dagger$ that diagonalize the Hamiltonian via a Bogoliubov transformation and $\epsilon(k)$ is the Bogoliubov dispersion relation [for the XX chain $\epsilon(k) = J_1 \cos ka$].
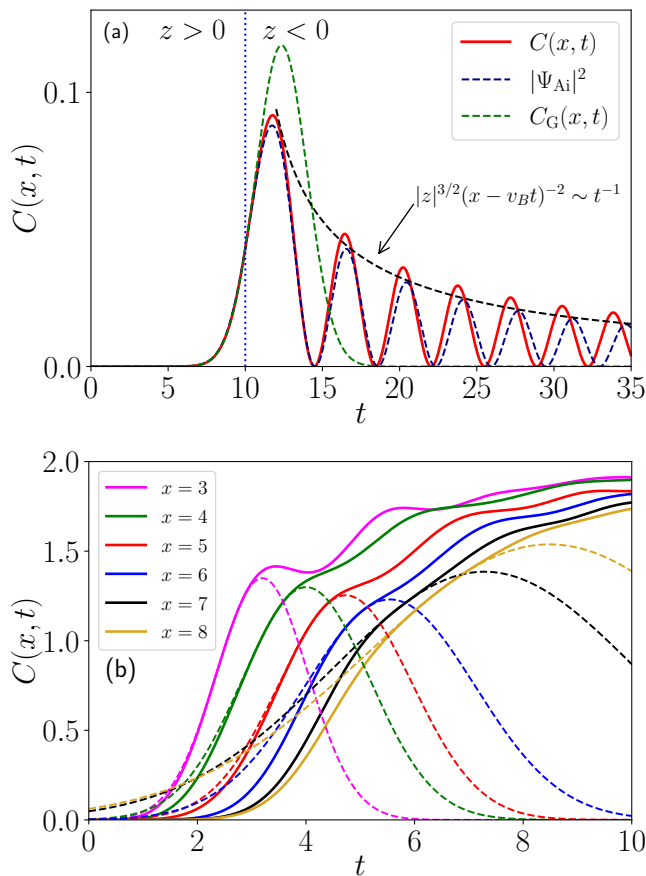
Figure 1. Wavefronts of $C(x,t)$. **(a)** The integrable case, $\vec{c}_f$. Here $x = 10$. Exact numerical results (solid red) along with a fit to the Gaussian form Eq. (5) (green), and the Airy result from Eq. (9) (blue). The expected t^{-1} decay in the amplitude is also shown (black). **(b)** ETH case, $\vec{c}_{\mathrm{ETH}}$, at different positions x. Solid lines indicate the OTOC data, and dashed lines are fits to Eq. (5) centered at $x = v_B t$.

Defining $\Phi(k, x, t) = kx - \epsilon(k)t$, a caustic occurs at quasi-momentum k_c, where two conditions are satisfied [119]: $(\partial\Phi/\partial k)_{k_c} = 0$ and $(\partial^2\Phi/\partial k^2)_{k_c} = 0$. The first condition is Fermat's principle that gives classical rays as saddles of the action $k\dot{x} - \epsilon(k)$ and the second defines the caustic as the place where saddles coalesce. These conditions correspond exactly to the Lieb-Robinson (LR) bound for a light cone as being determined by the maximum value of the group velocity $d\epsilon/dk$ of the fermions [114, 120, 121], $v_{\mathrm{LR}} = \max_k |d\epsilon/dk|$.

The fact that light cones are caustics allows a number of powerful results from catastrophe theory to be applied: *i)* The only structurally stable catastrophes in two dimensions (the space-time formed by x and t) are fold lines that meet at cusp points, as anyone who has ironed a shirt knows. For a light cone the only place a cusp could occur is at the origin where the two edges meet. However, in the present case of the XX model the dispersion relation is so simple that only two rays can coalesce and no cusp occurs, just two pure fold lines that meet at $x = t = 0$. This result is special and

if a symmetry breaking term is added the two folds will instead generically meet at a cusp (coalescence of three rays) and the back-to-back Airy functions are locally replaced by a Pearcey function [114]; *ii)* The defining feature of a fold catastrophe is that the phase $\Phi(k, x, t)$ is cubic in k. This is why the Airy function is the universal wavefunction at a fold because $\mathrm{Ai}(z) = (1/2\pi) \int_{-\infty}^{\infty} ds \, \exp[i(zs + s^3/3)]$; *iii)* There exists a diffeomorphism from the physical variables (k, x, t) to the canonical Airy cubic form (s, z). Therefore, a Taylor expansion truncated at precisely third order about the caustic gives the exact semiclassical description in the neighborhood of that point. Performing the transformation of variables, $s^3 = 2(k - k_c)^3/[t\partial_k^3\epsilon(k_c)]$ gives [72, 74, 94]

$$\Psi_{\mathrm{Ai}}(x,t) \sim \sqrt{a}\left(\frac{-2}{\partial_k^3\epsilon(k_c)t}\right)^{1/3} e^{i\Phi(k_c,x,t)} \, \mathrm{Ai}(z), \quad (9)$$

$$\text{where} \quad z = (x - v_B t)\left|t\partial_k^3\epsilon(k_c)/2\right|^{-1/3}. \quad (10)$$

In Fig. 1(a), we plot $|\Psi_{\mathrm{Ai}}(x,t)|^2$ alongside the numerical result at the point $x = 10$, with the caustic ($z = 0$) marked by the vertical dotted line. The Airy wavefunction gradually goes out of phase at longer times because the Taylor expansion was made at a single point, but the range could be extended via a uniform mapping [122]. From the asymptotics of the Airy function as $z \to -\infty$ it follows that the amplitude of the OTOC wavefront decays as $|z|^{3/2}/(x - vt)^2 \sim 1/t$ (in agreement with Refs. [60, 61]), and the fringe spacing becomes *constant*. In this way one also finds that the amplitude along the wavefront $x/t = v_B$ decays as $x^{-2/3}$ [94]. Furthermore, Eq. (9) also correctly predicts the early time growth. Keeping just the first term of the $z \to \infty$ asymptotic series for the Airy function [94] gives the universal $p = 1/2$ form of the OTOC in Eq. (4) [72–74].

While an Airy function has been derived for OTOCs before [72, 74, 113], the point we emphasize here is that catastrophe theory guarantees that this result is rigorously true and robust to perturbations. Hence, deviations from it imply some qualitative change to the dynamics. One possibility is the presence of a symmetry breaking term which gives one of the higher catastrophes [114] (such as a cusp in the XY model which has a double cone). Another possibility is nonintegrable dynamics, and it is to that case we now turn.

Profile of the wavefront in the ETH case: In Fig. 1(b) we plot the exact results for the OTOC for $\vec{c}_{\mathrm{ETH}}$. Fringes are partially visible at smaller x but the Airy nodes have disappeared. Although structural stability implies that catastrophes are stable against weak chaos, $\vec{c}_{\mathrm{ETH}}$ corresponds to strong chaos which disrupts the rays and their interference significantly. At $x = 3$ the wavefront has quite a sharp slope, indicating that the process of scrambling (the increase in non-locality of the observable) is still in full swing. By $x = 8$, the slope of the OTOC at the wavefront has significantly decreased. The Gaussian waveform of Eq. (5) provides an excellent local fit to the wavefront in both the integrable [54, 93] and chaotic regimes, as seen from the dashed curves in Fig. 1(a) and 1(b), respectively. The fit is performed over the range $t = \frac{x}{v_B} \pm \Delta$

where $\Delta \approx 0.5$ gives a reasonably large window to describe the shape of $C(x,t)$. Within the fitting window, for a fixed x, the parameters $m(x)$ and $b(x)$ in Eq. (5) can be determined with very high precision with errors on each term of the order of 10^{-7} to 10^{-9}. A crucial ingredient to identify the parameters in the ETH case is to first determine the butterfly velocity v_B, which can be done using velocity-dependent Lyapunov exponents [74, 123], as demonstrated in the SM [94]. We find that the velocity for the ETH model characterized by $\vec{c}_{\text{ETH}}$ is roughly $v_B \approx 1.28$ (in contrast to $v_B = 1$ for $\vec{c}_f$). Although the integrable and ETH wavefronts both display flattening, the scaling properties of $m(x)$ and $b(x)$ are fundamentally different in the two regimes as we now show.

Scaling in Free Models: By expanding the Airy wavefunction given in Eq. (9) about the caustic at $z = 0$ we obtain

$$m(x) = \frac{c_m}{x^{\frac{2}{3}}} , \quad b(x) = \frac{c_b}{x^{\frac{1}{3}}} , \tag{11}$$

where c_m and c_b are constants that depend explicitly on the dispersion relation (see the SM [94] for details). Due to the universality of the Airy wavefunction, this scaling is expected to hold for many models which can be written in terms of freely propagating quasiparticles. Furthermore, corrections beyond quadratic order in $x - v_B t$ can be obtained. However, the cubic term in the exponent falls off rapidly (at least as x^{-1}), and so it is reasonable, even at moderate distances, to keep only the Gaussian approximation. We have numerically verified Eq. (11) and the results are shown in Fig. 2(a). Fitting the scaling of each parameter for distances $0 < x \leq 650$ we find,

$$m(x) \propto \frac{1}{x^{a_m}} , \quad b(x) \propto \frac{1}{x^{a_b}} , \tag{12}$$

with $a_m = 0.68857 \pm 0.00008$, and $a_b = 0.33043 \pm 0.00002$, indicating good agreement with the expected values. We also note that because $m(x) \propto b(x)^2$, $m(x)$ falls off significantly quicker than $b(x)$. This may point to an intermediate regime in x where the OTOC is well described by $C(x,t) \sim e^{b(x)t}$.

Scaling in ETH regime: In Fig. 2(b) we show a plot of the data for the $\vec{c}_{\text{ETH}}$ case. A linear trend emerges, implying that the spatial dependence on $m(x)$ and $b(x)$ in the ETH regime exhibits exponential rather than power-law decay,

$$b(x) \sim e^{-cx}, \quad m(x) \sim e^{-wx}, \tag{13}$$

where $c, w > 0$ are constants. We find that $c = 0.38 \pm 0.02$ and $w = 0.66 \pm 0.05$. Like the free case, $m(x) \propto b(x)^2$, however, as shown in the SM [94], this is not generally the case.

The exponentially decaying behavior of $m(x)$ and $b(x)$ is clearly distinct from the free fermion case. This indicates that the Gaussian waveform can distinguish ETH-obeying from free dynamics. In both Figs. 2(a) and (b) $m(x), b(x)$ decay by upwards of two orders of magnitude as a function of position, however the exponential decay in the ETH regime ensures that this occurs over a short distance of $x \approx 10$ while in the free
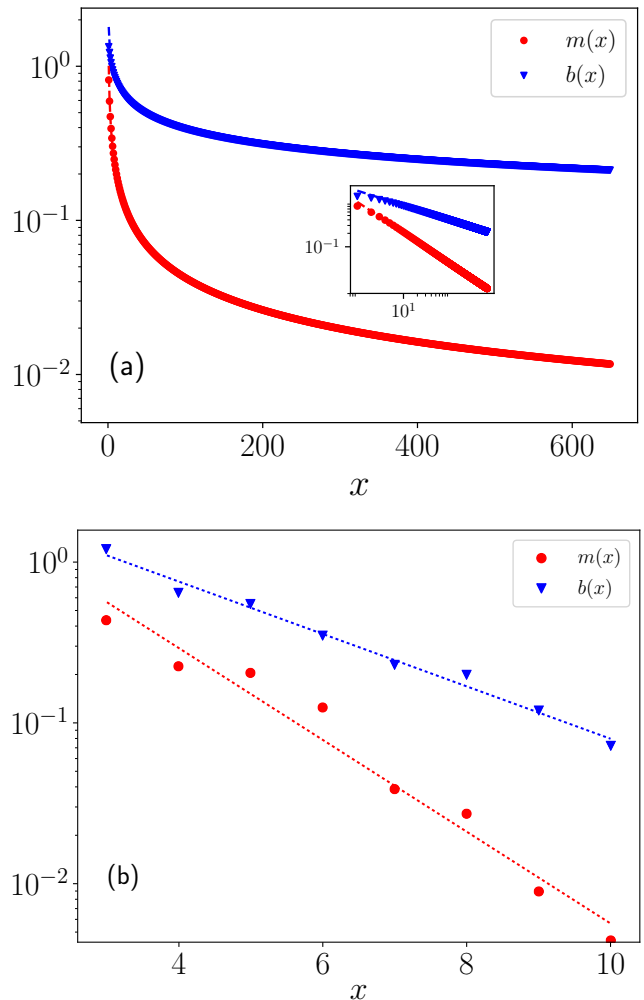

Figure 2. Log-linear plots for the Gaussian parameters $m(x)$ (red) and $b(x)$ [blue]. **(a)** The free Hamiltonian, $\vec{c}_f$. Dashed lines are fits to Eq. 12. Inset is a log-log plot of the same data. **(b)** The ETH Hamiltonian, $\vec{c}_{\text{ETH}}$, using the same data as in Fig. 1(b) indicating exponential decay of $m(x), b(x)$.

model it takes a distance of $x \approx 600$. Thus, the general flattening of the OTOC at the wavefront (see e.g. Fig. 1) occurs *much* faster in thermalizing models.

Conclusions: Close to the wavefront, integrable and ETH models can be distinguished by the difference in scaling of the parameters $m(x), b(x)$ in Eq. (5). The ability of modern experiments to measure quantum light cone profiles [96–101] and OTOCs [124–129] holds out the possibility that this prediction can be tested in the laboratory. A remaining open question concerns the transition from integrable to ETH dynamics [130–132] and the degree to which structural stability protects the Airy wavefront. A resolution of this question would constitute a quantum version of the celebrated KAM theorem [133].

SHARCNET (www.sharcnet.ca) and Compute/Calcul Canada (www.computecanada.ca).

————————

[1] M. V. Berry, Quantum chaology (The Bakerian Lecture), Proc. R. Soc. A **413**, 183 (1987).

[2] R. A. Jalabert, H. U. Baranger, and A. D. Stone, Conductance fluctuations in the ballistic regime: A probe of quantum chaos?, Phys. Rev. Lett. **65**, 2442 (1990).

[3] C. M. Marcus, A. J. Rimberg, R. M. Westervelt, P. F. Hopkins, and A. C. Gossard, Conductance fluctuations and chaotic scattering in ballistic microstructures, Phys. Rev. Lett. **69**, 506 (1992).

[4] V. Milner, J. L. Hanssen, W. C. Campbell, and M. G. Raizen, Optical billiards for atoms, Phys. Rev. Lett. **86**, 1514 (2001).

[5] N. Friedman, A. Kaplan, D. Carasso, and N. Davidson, Observation of chaotic and regular dynamics in atom-optics billiards, Phys. Rev. Lett. **86**, 1518 (2001).

[6] H. J. Stockmann and J. Stein, "Quantum" chaos in billiards studied by microwave absorption, Phys. Rev. Lett. **64**, 2215 (1990).

[7] S. Sridhar, Experimental observation of scarred eigenfunctions of chaotic microwave cavities, Phys. Rev. Lett. **67**, 785 (1991).

[8] F. L. Moore, J. C. Robinson, C. Bharucha, P. E. Williams, and M. G. Raizen, Observation of dynamical localization in atomic momentum transfer: A new testing ground for quantum chaos, Phys. Rev. Lett. **73**, 2974 (1994).

[9] D. A. Steck, W. H. Oskay, and M. G. Raizen, Observation of chaos-assisted tunneling between islands of stability, Science **293**, 274 (2001).

[10] W. K. Hensinger, H. Häffner, A. Browaeys, N. R. Heckenberg, K. Helmerson, C. McKenzie, G. J. Milburn, W. D. Phillips, S. L. Rolston, H. Rubinsztein-Dunlop, and B. Upcroft, Dynamical tunnelling of ultracold atoms, Nature **412**, 52 (2001).

[11] S. Chaudhury, A. Smith, B. E. Anderson, S. Ghose, and P. S. Jessen, Quantum signatures of chaos in a kicked top, Nature **461**, 768 (2009).

[12] Y. S. Weinstein, S. Lloyd, J. Emerson, and D. G. Cory, Experimental implementation of the quantum baker's map, Phys. Rev. Lett. **89**, 157902 (2002).

[13] M. C. Gutzwiller, Periodic orbits and classical quantization conditions, J. Math. Phys. **12**, 343 (1971).

[14] M. V. Berry and M. Tabor, Closed orbits and the regular bound spectrum, Proc. R. Soc. A **349**, 101 (1976).

[15] E. P. Wigner, On the statistical distribution of the widths and spacings of nuclear resonance levels, Proc. Cambridge Philos. Soc. **47**, 790 (1951).

[16] C. E. Porter, *Statistical theories of spectra: fluctuations* (Academic Press, New York, 1965).

[17] M. V. Berry and M. Tabor, Level clustering in the regular spectrum, Proc. R. Soc. A **356**, 375 (1977).

[18] O. Bohigas, M. J. Giannoni, and C. Schmit, Characterization of chaotic quantum spectra and universality of level fluctuation laws, Phys. Rev. Lett. **52**, 1 (1984).

[19] L. D'Alessio, Y. Kafri, A. Polkovnikov, and M. Rigol, From quantum chaos and eigenstate thermalization to statistical mechanics and thermodynamics, Advances in Physics **65**, 239 (2016), https://doi.org/10.1080/00018732.2016.1198134.

[20] J. M. Deutsch, Quantum statistical mechanics in a closed system, Phys. Rev. A **43**, 2046 (1991).

[21] M. Srednicki, Chaos and quantum thermalization, Phys. Rev. E **50**, 888 (1994).

[22] M. Srednicki, The approach to thermal equilibrium in quantized chaotic systems, Journal of Physics A: Mathematical and General **32**, 1163 (1999).

[23] M. Rigol, V. Dunjko, and M. Olshanii, Thermalization and its mechanism for generic isolated quantum systems, Nature **452**, 854 (2008).

[24] G. De Palma, A. Serafini, V. Giovannetti, and M. Cramer, Necessity of eigenstate thermalization, Phys. Rev. Lett. **115**, 220401 (2015).

[25] T. LeBlond, K. Mallayya, L. Vidmar, and M. Rigol, Entanglement and matrix elements of observables in interacting integrable systems, Phys. Rev. E **100**, 062134 (2019).

[26] H. Kim, T. N. Ikeda, and D. A. Huse, Testing whether all eigenstates obey the eigenstate thermalization hypothesis, Phys. Rev. E **90**, 052105 (2014).

[27] R. Mondaini, K. R. Fratus, M. Srednicki, and M. Rigol, Eigenstate thermalization in the two-dimensional transverse field Ising model, Phys. Rev. E **93**, 032104 (2016).

[28] K. Kaneko, E. Iyoda, and T. Sagawa, Work extraction from a single energy eigenstate, Phys. Rev. E **99**, 032128 (2019).

[29] G. Biroli, C. Kollath, and A. M. Läuchli, Effect of rare fluctuations on the thermalization of isolated quantum systems, Phys. Rev. Lett. **105**, 250401 (2010).

[30] H.-H. Lai and K. Yang, Entanglement entropy scaling laws and eigenstate typicality in free fermion systems, Phys. Rev. B **91**, 081110(R) (2015).

[31] J. Riddell and M. P. Müller, Generalized eigenstate typicality in translation-invariant quasifree fermionic models, Phys. Rev. B **97**, 035129 (2018).

[32] P. Ribeiro, M. Haque, and A. Lazarides, Strongly interacting bosons in multichromatic potentials supporting mobility edges: Localization, quasi-condensation, and expansion dynamics, Phys. Rev. A **87**, 043635 (2013).

[33] L. Vidmar and M. Rigol, Generalized Gibbs ensemble in integrable lattice models, Journal of Statistical Mechanics: Theory and Experiment **2016**, 064007 (2016).

[34] R. Nandkishore and D. A. Huse, Many-body localization and thermalization in quantum statistical mechanics, Annual Review of Condensed Matter Physics **6**, 15 (2015).

[35] S. Iyer, V. Oganesyan, G. Refael, and D. A. Huse, Many-body localization in a quasiperiodic system, Phys. Rev. B **87**, 134202 (2013).

[36] M. Schreiber, S. S. Hodgman, P. Bordia, H. P. Lüschen, M. H. Fischer, R. Vosk, E. Altman, U. Schneider, and I. Bloch, Observation of many-body localization of interacting fermions in a quasirandom optical lattice, Science **349**, 842 (2015).

[37] H. P. Lüschen, P. Bordia, S. S. Hodgman, M. Schreiber, S. Sarkar, A. J. Daley, M. H. Fischer, E. Altman, I. Bloch, and U. Schneider, Signatures of Many-Body Localization in a Controlled Open Quantum System, Phys. Rev. X **7**, 011034 (2017).

[38] H. P. Lüschen, P. Bordia, S. Scherg, F. Alet, E. Altman, U. Schneider, and I. Bloch, Observation of Slow Dynamics near the Many-Body Localization Transition in One-Dimensional Quasiperiodic Systems, Physical Review Letters **119**, 260401 (2017).

[39] T. Mori, Weak eigenstate thermalization with large deviation bound (2016), arXiv:1609.09776.

[40] F. G. S. L. Brandão, E. Crosson, M. B. Şahinoğlu, and J. Bowen, Quantum error correcting codes in eigenstates of translation-invariant spin chains, Phys. Rev. Lett. **123**, 110502 (2019).

[41] A. M. Alhambra, J. Riddell, and L. P. García-Pintos, Time evolution of correlation functions in quantum many-body systems, Phys. Rev. Lett. **124**, 110605 (2020).

[42] B. Yoshida, Firewalls vs. scrambling, Journal of High Energy Physics **10**, 132 (2019).

[43] B. Swingle and D. Chowdhury, Slow scrambling in disordered quantum systems, Phys. Rev. B **95**, 060201(R) (2017).

[44] J. R. González Alonso, N. Yunger Halpern, and J. Dressel, Out-of-time-ordered-correlator quasiprobabilities robustly witness scrambling, Phys. Rev. Lett. **122**, 040404 (2019).

[45] B. Yan, L. Cincio, and W. H. Zurek, Information scrambling and Loschmidt echo, Phys. Rev. Lett. **124**, 160603 (2020).

[46] J. Tuziemski, Out-of-time-ordered correlation functions in open systems: A Feynman-Vernon influence functional approach, Phys. Rev. A **100**, 062106 (2019).

[47] D. Mao, D. Chowdhury, and T. Senthil, Slow scrambling and hidden integrability in a random rotor model, Phys. Rev. B **102**, 094306 (2020).

[48] R. J. Lewis-Swan, A. Safavi-Naini, J. J. Bollinger, and A. M. Rey, Unifying scrambling, thermalization and entanglement through measurement of fidelity out-of-time-order correlators in the Dicke model, Nature Communications **10**, 1581 (2019).

[49] S. Nakamura, E. Iyoda, T. Deguchi, and T. Sagawa, Universal scrambling in gapless quantum spin chains (2019), arXiv:1904.09778.

[50] Y. Gu and A. Kitaev, On the relation between the magnitude and exponent of OTOCs, Journal of High Energy Physics **2019**, 75 (2019).

[51] R. Belyansky, P. Bienias, Y. A. Kharkov, A. V. Gorshkov, and B. Swingle, Minimal model for fast scrambling, Phys. Rev. Lett. **125**, 130601 (2020).

[52] J. Maldacena, S. H. Shenker, and D. Stanford, A bound on chaos, Journal of High Energy Physics **2016**, 106 (2016).

[53] J. Lee, D. Kim, and D.-H. Kim, Typical growth behavior of the out-of-time-ordered commutator in many-body localized systems, Phys. Rev. B **99**, 184202 (2019).

[54] J. Riddell and E. S. Sørensen, Out-of-time ordered correlators and entanglement growth in the random-field XX spin chain, Phys. Rev. B **99**, 054205 (2019).

[55] X. Chen, T. Zhou, D. A. Huse, and E. Fradkin, Out-of-time-order correlations in many-body localized and thermal phases, Annalen der Physik **529**, 1600332 (2017).

[56] Y. Huang, Y.-L. Zhang, and X. Chen, Out-of-time-ordered correlators in many-body localized systems, Annalen der Physik **529**, 1600318 (2017).

[57] R. Fan, P. Zhang, H. Shen, and H. Zhai, Out-of-time-order correlation for many-body localization, Science Bulletin **62**, 707 (2017).

[58] Y. Chen, Universal logarithmic scrambling in many body localization (2016), arXiv:1608.02765.

[59] R.-Q. He and Z.-Y. Lu, Characterizing many-body localization by out-of-time-ordered correlation, Phys. Rev. B **95**, 054201 (2017).

[60] C.-J. Lin and O. I. Motrunich, Out-of-time-ordered correlators in a quantum Ising chain, Phys. Rev. B **97**, 144304 (2018).

[61] J. Bao and C. Zhang, Out-of-time-order correlators in one-dimensional XY model (2019), arXiv:1901.09327.

[62] D. A. Roberts and B. Yoshida, Chaos and complexity by design, Journal of High Energy Physics **2017**, 121 (2017).

[63] Y. Huang, F. G. S. L. Brandão, and Y.-L. Zhang, Finite-size scaling of out-of-time-ordered correlators at late times, Phys. Rev. Lett. **123**, 010601 (2019).

[64] Y. Chen, Universal logarithmic scrambling in many body localization (2016), arXiv:1608.02765.

[65] J. K. Max McGinley, Andreas Nunnenkamp, Slow growth of entanglement and out-of-time-order correlators in integrable disordered systems (2018), arXiv:1807.06039.

[66] S. Pappalardi, A. Russomanno, B. B. Žunkovic, F. Iemini, A. Silva, and R. Fazio, Scrambling and entanglement spreading in long-range spin chains, Phys. Rev. B **98**, 134303 (2018).

[67] Q. Hummel, B. Geiger, J. D. Urbina, and K. Richter, Reversible quantum information spreading in many-body systems near criticality, Phys. Rev. Lett. **123**, 160401 (2019).

[68] K. Hashimoto, K.-B. Huh, K.-Y. Kim, and R. Watanabe, Exponential growth of out-of-time-order correlator without chaos: inverted harmonic oscillator, Journal of High Energy Physics **2020**, 68 (2020).

[69] S. Pilatowsky-Cameo, J. Chávez-Carlos, M. A. Bastarrachea-Magnani, P. Stránský, S. Lerma-Hernández, L. F. Santos, and J. G. Hirsch, Positive quantum Lyapunov exponents in experimental systems with a regular classical limit, Phys. Rev. E **101**, 010202(R) (2020).

[70] T. Xu, T. Scaffidi, and X. Cao, Does scrambling equal chaos?, Phys. Rev. Lett. **124**, 140602 (2020).

[71] W. Kirkby, D. H. J. O'Dell, and J. Mumford, False signals of chaos from quantum probes, Phys. Rev. A **104**, 043308 (2021).

[72] S. Xu and B. Swingle, Accessing scrambling using matrix product operators, Nature Physics **16**, 199–204 (2019).

[73] S. Xu and B. Swingle, Locality, quantum fluctuations, and scrambling, Physical Review X **9**, 031048 (2019).

[74] V. Khemani, D. A. Huse, and A. Nahum, Velocity-dependent Lyapunov exponents in many-body quantum, semiclassical, and classical chaos, Phys. Rev. B **98**, 144304 (2018).

[75] A. Nahum, S. Vijay, and J. Haah, Operator spreading in random unitary circuits, Phys. Rev. X **8**, 021014 (2018).

[76] C. W. von Keyserlingk, T. Rakovszky, F. Pollmann, and S. L. Sondhi, Operator hydrodynamics, OTOCs, and entanglement growth in systems without conservation laws, Phys. Rev. X **8**, 021013 (2018).

[77] S.-K. Jian and H. Yao, Universal properties of many-body quantum chaos at Gross-Neveu criticality (2018), arXiv:1805.12299.

[78] Y. Gu, X.-L. Qi, and D. Stanford, Local criticality, diffusion and chaos in generalized Sachdev-Ye-Kitaev models, Journal of High Energy Physics **2017**, 125 (2017).

[79] S. Sahu, S. Xu, and B. Swingle, Scrambling dynamics across a thermalization-localization quantum phase transition, Phys. Rev. Lett. **123**, 165902 (2019).

[80] T. Rakovszky, F. Pollmann, and C. W. von Keyserlingk, Diffusive hydrodynamics of out-of-time-ordered correlators with charge conservation, Phys. Rev. X **8**, 031058 (2018).

[81] S. H. Shenker and D. Stanford, Black holes and the butterfly effect, Journal of High Energy Physics **2014**, 67 (2014).

[82] A. A. Patel, D. Chowdhury, S. Sachdev, and B. Swingle, Quantum butterfly effect in weakly interacting diffusive metals, Phys. Rev. X **7**, 031047 (2017).

[83] D. Chowdhury and B. Swingle, Onset of many-body chaos in the $O(N)$ model, Phys. Rev. D **96**, 065005 (2017).

[84] V. Khemani, A. Vishwanath, and D. A. Huse, Operator Spreading and the Emergence of Dissipative Hydrodynamics under Unitary Evolution with Conservation Laws, Physical Review X **8**, 031057 (2018).

[85] N. Anand, G. Styliaris, M. Kumari, and P. Zanardi, Quantum coherence as a signature of chaos (2020), arXiv:2009.02760.

[86] S. Gopalakrishnan, D. A. Huse, V. Khemani, and R. Vasseur, Hydrodynamics of operator spreading and quasiparticle diffusion in interacting integrable systems, Phys. Rev. B **98**, 220303(R) (2018).

[87] P. L. Doussal, S. N. Majumdar, and G. Schehr, Large deviations for the height in 1D Kardar-Parisi-Zhang growth at late times, EPL (Europhysics Letters) **113**, 60004 (2016).

[88] C. Monthus and T. Garel, Probing the tails of the ground-state energy distribution for the directed polymer in a random medium of dimension $d = 1, 2, 3$ via a Monte Carlo procedure in the disorder, Phys. Rev. E **74**, 051109 (2006).

[89] I. V. Kolokolov and S. E. Korshunov, Universal and nonuniversal tails of distribution functions in the directed polymer and Kardar-Parisi-Zhang problems, Phys. Rev. B **78**, 024206 (2008).

[90] E. M. Fortes, I. García-Mata, R. A. Jalabert, and D. A. Wisniacki, Gauging classical and quantum integrability through out-of-time-ordered correlators, Phys. Rev. E **100**, 042201 (2019).

[91] E. M. Fortes, I. García-Mata, R. A. Jalabert, and D. A. Wisniacki, Signatures of quantum chaos transition in short spin chains, EPL (Europhysics Letters) **130**, 60001 (2020).

[92] J. Wang, G. Benenti, G. Casati, and W. Wang, Quantum chaos and the correspondence principle (2020), arXiv:2010.10360.

[93] J. Riddell and E. S. Sørensen, Out-of-time-order correlations in the quasiperiodic Aubry-André model, Phys. Rev. B **101**, 024202 (2020).

[94] J. Riddell, W. Kirkby, D. H. J. O'Dell, and E. S. Sørensen, Supplementary material (2021).

[95] E. H. Lieb and D. W. Robinson, The finite group velocity of quantum spin systems, Commun. Math. Phys. **28**, 251 (1972).

[96] M. Cheneau, P. Barmettler, D. Poletti, M. Endres, P. Schauß, T. Fukuhara, C. Gross, I. Bloch, C. Kollath, and S. Kuhr, Light-cone-like spreading of correlations in a quantum many-body system, Nature **481**, 484–487 (2012).

[97] T. Fukuhara, P. Schauß, M. Endres, S. Hild, M. Cheneau, I. Bloch, and C. Gross, Microscopic observation of magnon bound states and their dynamics, Nature **502**, 76–79 (2013).

[98] T. Langen, R. Geiger, M. Kuhnert, B. Rauer, and J. Schmiedmayer, Local emergence of thermal correlations in an isolated quantum many-body system, Nat. Phys. **9**, 643 (2013).

[99] P. Jurcevic, B. P. Lanyon, P. Hauke, C. Hempel, P. Zoller, R. Blatt, and C. F. Roos, Quasiparticle engineering and entanglement propagation in a quantum many-body system, Nature **511**, 202–205 (2014).

[100] P. M. Preiss, R. Ma, M. E. Tai, A. Lukin, M. Rispoli, P. Zupancic, Y. Lahini, R. Islam, and M. Greiner, Strongly correlated quantum walks in optical lattices, Science **347**, 1229 (2015).

[101] Y. Takasu, T. Yagami, H. Asaka, Y. Fukushima, K. Nagao, S. Goto, I. Danshita, and Y. Takahashi, Energy redistribution and spatiotemporal evolution of correlations after a sudden quench of the Bose-Hubbard model, Sci. Adv. **6**, eaba9255 (2020).

[102] P. Barmettler, D. Poletti, M. Cheneau, and C. Kollath, Propagation front of correlations in an interacting Bose gas, Phys. Rev. A **85**, 053625 (2012).

[103] V. Hunyadi, Z. Rácz, and L. Sasvári, Dynamic scaling of fronts in the quantum XX chain, Phys. Rev. E **69**, 066103 (2004).

[104] V. Eisler and Z. Rácz, Full counting statistics in a propagating quantum front and random matrix spectra, Phys. Rev. Lett. **110**, 060602 (2013).

[105] V. Eisler and F. Maislinger, Hydrodynamical phase transition for domain-wall melting in the XY chain, Phys. Rev. B **98**, 161117(R) (2018).

[106] V. Eisler and F. Maislinger, Front dynamics in the XY chain after local excitations, SciPost Physics **8**, 10.21468/scipostphys.8.3.037 (2020).

[107] M. Kormos, Inhomogeneous quenches in the transverse field Ising chain: scaling and front dynamics, SciPost Physics **3**,

[108] V. B. Bulchandani and C. Karrasch, Subdiffusive front scaling in interacting integrable models, Physical Review B **99**, 121410(R) (2019).

[109] J. Viti, J.-M. Stéphan, J. Dubail, and M. Haque, Inhomogeneous quenches in a free fermionic chain: Exact results, EPL (Europhysics Letters) **115**, 40011 (2016).

[110] G. Perfetto and A. Gambassi, Ballistic front dynamics after joining two semi-infinite quantum Ising chains, Physical Review E **96**, 012138 (2017).

[111] J.-M. Stéphan, Free fermions at the edge of interacting systems, SciPost Physics **6**, 10.21468/scipostphys.6.5.057 (2019).

[112] M. Fagotti, Higher-order generalized hydrodynamics in one dimension: The noninteracting test, Physical Review B **96**, 220302(R) (2017).

[113] S. Bhanu Kiran, D. A. Huse, and M. Kulkarni, Spatiotemporal spread of perturbations in power-law models at low temperatures: Exact results for OTOC (2020), arXiv:arXiv:2011.09320.

[114] W. Kirkby, J. Mumford, and D. H. J. O'Dell, Quantum caustics and the hierarchy of light cones in quenched spin chains, Phys. Rev. Research **1**, 033135 (2019).

[115] R. Thom, *Structural Stability and Morphogenesis* (Benjamin, Reading MA, 1975).

[116] V. I. Arnol'd, Critical points of smooth functions and their normal forms, Russ. Math. Survs. **30**, 1 (1975).

[117] L. Kelvin, Deep water ship-waves, Philos. Mag. **9**, 733 (1905).

[118] F. Ursell, *Ship Hydrodynamics, Water Waves and Asymptotics. Collected works of F. Ursell, 1946–1992*, Vol. 2 (World Scientific, Singapore, 1994).

[119] M. V. Berry, Singularities in waves and rays, in *Physics of Defects (1980)*, Vol. XXXV, edited by R. Balian and et al. (North-Holland Publishing, Amsterdam, 1981).

[120] J.-M. Stéphan and J. Dubail, Local quantum quenches in critical one-dimensional systems: entanglement, the Loschmidt echo, and light-cone effects, J. Stat. Mech. , P08019 (2011).

[121] P. Calabrese, F. H. L. Essler, and M. Fagotti, Quantum quench in the transverse field Ising chain: I. time evolution of order parameter correlators, J. Stat. Mech. , P07016 (2012).

[122] M. V. Berry and K. E. Mount, Semiclassical approximations in wave mechanics, Rep. Prog. Phys. **35**, 315 (1972).

[123] Y.-L. Zhang and V. Khemani, Asymmetric butterfly velocities in 2-local hamiltonians, SciPost Phys. **9**, 24 (2020).

[124] J. Li, R. Fan, H. Wang, B. Ye, B. Zeng, H. Zhai, X. Peng, and J. Du, Measuring out-of-time-order correlators on a nuclear magnetic resonance quantum simulator, Phys. Rev. X **7**, 031011 (2017).

[125] M. Gärttner, J. G. Bohnet, A. Safavi-Naini, M. L. Wall, J. J. Bollinger, and A. M. Rey, Measuring out-of-time-order correlations and multiple quantum spectra in a trapped-ion quantum magnet, Nat. Phys. **13**, 781 (2017).

[126] K. X. Wei, C. Ramanathan, and P. Cappellaro, Exploring localization in nuclear spin chains, Phys. Rev. Lett. **120**, 070501 (2018).

[127] K. A. Landsman, C. Figgatt, T. Schuster, N. M. Linke, B. Yoshida, N. Y. Yao, and C. Monroe, Verified quantum information scrambling, Nature **567**, 61 (2019).

[128] E. J. Meier, J. Ang'ong'a, F. A. An, , and B. Gadway, Exploring quantum signatures of chaos on a Floquet synthetic lattice, Phys. Rev. A **100**, 013623 (2019).

[129] M. Niknam, L. F. Santos, and D. G. Cory, Sensitivity of quantum information to environment perturbations measured with a nonlocal out-of-time-order correlation function, Phys. Rev.

10.21468/scipostphys.3.3.020 (2017).

Research **2**, 013200 (2020).

[130] M. Gring, M. Kuhnert, T. Langen, T. Kitagawa, B. Rauer, M. Schreitl, I. Mazets, D. Adu Smith, E. Demler, and J. Schmiedmayer, Relaxation and pre-thermalization in an isolated quantum system, Science **337**, 1318 (2012).

[131] F. H. L. Essler, S. Kehrein, S. R. Manmana, and N. J. Robin-son, Quench dynamics in a model with tuneable integrability breaking, .

[132] B. Bertini and M. Fagotti, Pre-relaxation in weakly interacting models, J. Stat. Mech. , P07012 (2015).

[133] G. Brandino, J.-S. Caux, and R. Konik, Glimmers of a quantum KAM theorem: Insights from quantum quenches in one-dimensional Bose gases, Phys. Rev. X **5**, 041043 (2015).

Supplementary Material for "Scaling of wavefronts of out-of-time-ordered-correlators: integrable versus chaotic systems"

Jonathon Riddell,[1] Wyatt Kirkby,[1] D. H. J. O'Dell,[1] and Erik S. Sørensen[1]

[1]*Department of Physics & Astronomy, McMaster University 1280 Main St. W., Hamilton ON L8S 4M1, Canada.*
(Dated: November 11, 2021)

In these supplementary materials we give the details of the Airy function and its asymptotics, the calculation of OTOC wavefront in terms of the Airy function, the extraction of the butterfly velocity from the OTOC and also provide some alternative examples to those presented in the main text.

I. THE AIRY FUNCTION

The Airy function was constructed by the astronomer G. B. Airy in 1838 in order to describe the interference of light at a rainbow which is the simplest example of a caustic [1]. It has the integral representation

$$\text{Ai}(z) = \frac{1}{2\pi} \int_{-\infty}^{\infty} ds \; e^{i(zs + \frac{1}{3}s^3)} \;, \tag{SM1}$$

which can be interpreted as an elementary path integral where the paths being summed are labeled by s [2]. The key feature is that the phase is cubic in s; this means that it has a maximum of two stationary points (corresponding to two rays according to Fermat's principle) that merge at the point $z = 0$ which is the location of the caustic. Thus, the Airy function describes the interference between two waves when $z < 0$ (the interference fringes are the supernumerary arcs which can sometimes be observed inside the main bow) and one single evanescent wave when $z > 0$. For the calculation of the profile at very early times (far from the wavefront) we can use the $z \to \infty$ asymptotics of the Airy function which are given by [3],

$$\text{Ai}(z) \sim \frac{e^{-\frac{2}{3}z^{3/2}}}{2\sqrt{\pi}z^{1/4}} \sum_{n=0}^{\infty} (-1)^n \frac{u_n}{(\frac{2}{3})^n z^{3n/2}} \;, \tag{SM2}$$

where $u_n = (2n+1)(2n+3)...(6n-1)/(216^n n!)$. Truncating this series at $n = 0$ gives the universal $p = 1/2$ form of the OTOC in Eq. (4) in the main text for early entanglement growth in free systems. However, this asymptotic expansion is not valid close to the wavefront and that case is dealt with in the next section.

II. DERIVATION OF GAUSSIAN IN FREE MODELS

For models which can be mapped onto free-fermions, the Hamiltonian is,

$$\hat{H} = \sum_k \epsilon(k) \left(\tilde{b}_k^\dagger \tilde{b}_k - \frac{1}{2} \right) \tag{SM3}$$

where $\epsilon(k)$ is the dispersion relation. Starting with a single Bogoliubov localized Fermion,

$$\langle x_b | e^{-i\hat{H}t} \hat{b}_{x=0}^\dagger | 0_b \rangle = \langle x_b | \sum_k e^{-i\epsilon(k)t} | k \rangle = \frac{1}{N} \sum_{k=-\frac{\pi}{a}}^{\frac{\pi}{a} - \frac{2\pi}{Na}} e^{i(kx - \epsilon(k)t)} \approx \frac{\sqrt{a}}{2\pi} \int_{-\frac{\pi}{a}}^{\frac{\pi}{a}} dk \; e^{i(kx - \epsilon(k)t)} \;. \tag{SM4}$$

Now, we want to calculate the local form of the light cone via the focusing of trajectories. Using $\Phi = kx - \epsilon(k)t$, we require the conditions

$$\left. \frac{\partial \Phi}{\partial k} \right|_{k_c} = \left. \frac{\partial^2 \Phi}{\partial k^2} \right|_{k_c} = 0 \;, \tag{SM5}$$

to define the k_c. Hence, near the coalescing saddles of Φ,

$$\Phi \approx k_c x - \epsilon(k_c)t + (x - v_B t)(k - k_c) - \frac{1}{6} t \partial_k^3 \epsilon(k_c)(k - k_c)^3 + \mathcal{O}(k^4) \;, \tag{SM6}$$

where $v_B = \partial_k \epsilon(k_c)$ is the butterfly velocity, and the second-order term vanishes since $\partial_k^2 \Phi(k_c) = \partial_k^2 \epsilon(k_c) = 0$. Assuming that the dispersion $\epsilon(k)$ only has two coalescing saddles, catastrophe theory indicates that the cubic form (a fold) is sufficient to qualitatively describe the local form of Φ. When a larger number of saddles coalesce one obtains one of the higher catastrophes (sometimes called generalized Airy functions), which we will not discuss here but an introduction in the context of spin chains can be found in Ref. [2]. Now, letting,

$$s^3 \equiv \frac{-t}{2} \partial_k^3 \epsilon(k_c)(k - k_c)^3 \tag{SM7}$$

and

$$z \equiv (x - v_B t) \left(\frac{-2}{\partial_k^3 \epsilon(k_c) t} \right)^{1/3} \tag{SM8}$$

Thus,

$$\Psi(x, t) \approx \frac{\sqrt{a}}{2\pi} \left(\frac{-2}{\partial_k^3 \epsilon(k_c) t} \right)^{1/3} e^{i(k_c x - \epsilon(k_c) t)} \int_{s_-}^{s_+} ds \ e^{i(zs + \frac{1}{3} s^3)} \ , \tag{SM9}$$

where,

$$s_\pm = \left(\frac{-t}{2} \partial_k^3 \epsilon(k_c) \right)^{1/3} \left(\pm \frac{\pi}{a} - k_c \right) \ . \tag{SM10}$$

At sufficiently long times, these limits approach infinity and we recover the Airy function, which was defined in Eq. (SM1). $\text{Ai}[z]$ can be approximated near $z = 0$ by making use of,

$$\ln\left(\text{Ai}[z]\right) \approx -\frac{2}{3} \ln 3 - \ln(\Gamma[\tfrac{2}{3}]) - 3^{1/3} \frac{\Gamma[\frac{2}{3}]}{\Gamma[\frac{1}{3}]} z - \frac{1}{2} \left(3^{1/3} \frac{\Gamma[\frac{2}{3}]}{\Gamma[\frac{1}{3}]} \right)^2 z^2 + \frac{1}{3} \left(\frac{1}{2} - \frac{3\Gamma\left(\frac{2}{3}\right)^3}{\Gamma\left(\frac{1}{3}\right)^3} \right) z^3 + \mathcal{O}(z^4) \tag{SM11}$$

Thus, we expect the above wavefunctions to locally take the form,

$$\Psi(x, t) \approx \tilde{A} e^{-\tilde{m}(x - v_B t)^2} e^{-\tilde{b}(x - v_B t)} e^{-\zeta(x - v_B t)^3} ..., \tag{SM12}$$

where,

$$\tilde{A} = \frac{\sqrt{a}}{\pi \Gamma[\frac{2}{3}]} \left(\frac{-1}{36 \partial_k^3 \epsilon(k_c) t} \right)^{1/3} e^{i(k_c x - \epsilon(k_c) t)} \tag{SM13}$$

$$\tilde{m} = \frac{1}{2} \left(\frac{-6}{\partial_k^3 \epsilon(k_c)} \right)^{2/3} \left(\frac{\Gamma[\frac{2}{3}]}{\Gamma[\frac{1}{3}]} \right)^2 t^{-2/3} \tag{SM14}$$

$$\tilde{b} = \frac{\Gamma[\frac{2}{3}]}{\Gamma[\frac{1}{3}]} \left(\frac{-6}{\partial_k^3 \epsilon(k_c)} \right)^{1/3} t^{-1/3} \tag{SM15}$$

$$\zeta = -\frac{2}{3 \partial_k^3 \epsilon(k_c)} \left(\frac{1}{2} - \frac{3\Gamma\left(\frac{2}{3}\right)^3}{\Gamma\left(\frac{1}{3}\right)^3} \right) t^{-1} \tag{SM16}$$

Each term in the exponential contains factors of the form $\frac{(x - v_B t)^n}{t^{n/3}}$ for integer n. Assuming close proximity to the light cone relative to the distance from the origin, such that $\delta x \equiv x - v_B t$, with $\delta x / x \ll 1$, then,

$$\frac{\delta x}{t^{1/3}} \approx \left(\frac{v_B}{x} \right)^{1/3} \delta x + \frac{1}{3} \left(\frac{v_B}{x^4} \right)^{1/3} \delta x^2 + \frac{2}{9} \left(\frac{v_B}{x^7} \right)^{1/3} \delta x^3 + ... \tag{SM17}$$

$$\frac{\delta x^2}{t^{2/3}} \approx \frac{1}{3} \left(\frac{v_B^2}{x^2} \right)^{1/3} \delta x^2 + \frac{2}{3} \left(\frac{v_B^2}{x^5} \right)^{1/3} \delta x^3 + \frac{5}{9} \left(\frac{v_B^2}{x^8} \right)^{1/3} \delta x^4 + ... \tag{SM18}$$

$$\frac{\delta x^3}{t} \approx \left(\frac{v_B}{x} \right) \delta x^3 + \left(\frac{v_B}{x} \right) \delta x^4 + \left(\frac{v_B}{x} \right) \delta x^5 + ... \tag{SM19}$$

Keeping terms of order lower than $\mathcal{O}(\delta x / x)$, amounts to replacing each factor of t with x / v_B. Note that the second-order term in Eq. (SM17) is suppressed by a factor of $x^{-2/3} v_B^{-1/3}$ when compared to the lowest-order term of Eq. (SM18), and so at

large x there is no need to consider both, although including them will provide lowest-order corrections to $\tilde{m}$ and $\tilde{b}$ at fixed x. Furthermore, all the terms in Eq. (SM19) can be neglected since any term of cubic order or above in δx will not only be small, but also further suppressed by at least x^{-1}. Therefore our Gaussian approximation remains valid, and we can then rewrite Eq. (SM12) by replacing $t \to x/v_B$ in Eqs. (SM13)-(SM16). Thus we define the Gaussian form,

$$\Psi_G(x,t) \equiv A e^{-m(x-v_B t)^2} e^{-b(x-v_B t)} \tag{SM20}$$

such that $C_G(x,t) = |\Psi_G(x,t)|^2$ approximates the OTOC near the wavefront according to Eq. (5) of the main text, now with,

$$A = \frac{\sqrt{a}}{\pi \Gamma[\frac{2}{3}]} \left(\frac{-v_B}{36 \partial_k^3 \epsilon(k_c) x} \right)^{1/3} e^{i(k_c x - \epsilon(k_c)t)} \tag{SM21}$$

$$m = \frac{1}{2} \left(\frac{-6 v_B}{\partial_k^3 \epsilon(k_c)} \right)^{2/3} \left(\frac{\Gamma[\frac{2}{3}]}{\Gamma[\frac{1}{3}]} \right)^2 x^{-2/3} \tag{SM22}$$

$$b = \frac{\Gamma[\frac{2}{3}]}{\Gamma[\frac{1}{3}]} \left(\frac{-6 v_B}{\partial_k^3 \epsilon(k_c)} \right)^{1/3} x^{-1/3} \tag{SM23}$$

from which Eq. (11) of the main text follows directly.

From Eq. (SM20), and $C_G(x,t) = |\Psi_G(x,t)|^2$, it follows that exactly along the wavefront, there is a scaling $C(x = v_B t, t) \sim x^{-2/3}$. This was verified numerically for the XX model in Fig. SM1, for $1 \le x \le 100$, giving an approximate amplitude scaling of $C(x = v_B t, t) \sim x^{-0.664}$ at less than 0.5% error.
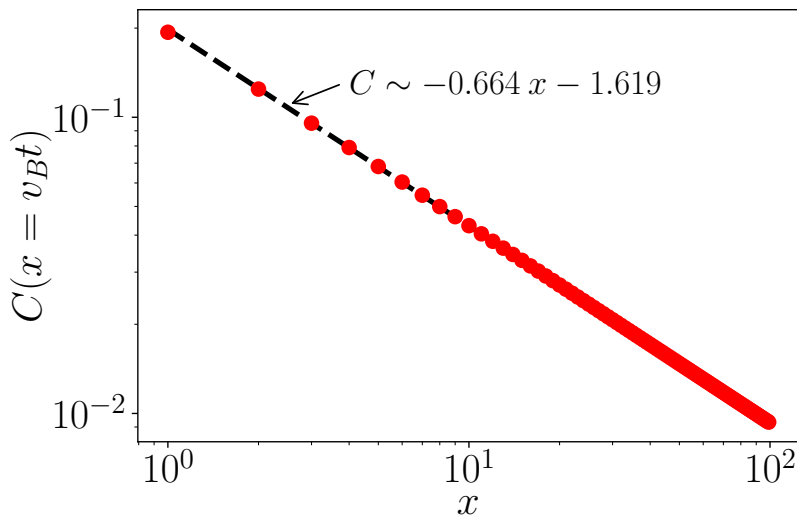

Figure SM1. OTOC amplitude scaling at the wavefront. Red circles indicate the amplitude of C evaluated along the light cone $(x = v_B t)$ as a function of the site number. A linear fit to the log-log data is shown as a black-dashed line.

III. VELOCITY

In this section we follow [4, 5] and extract the butterfly velocity from the OTOC using velocity dependent Lyapunov exponents. This method supposes that,

$$C(x,t) \sim e^{\lambda(v)t}, \tag{SM24}$$

such that,

$$\lambda(v) \sim -(v - v_B)^\alpha. \tag{SM25}$$

We can therefore find the butterfly velocities by looking for constant rays in the OTOC data such that $\lambda(v) = 0$. In this study however we do not limit ourselves to rays $x = vt$ for a set of velocities, we instead allow the rays to have a constant shift in
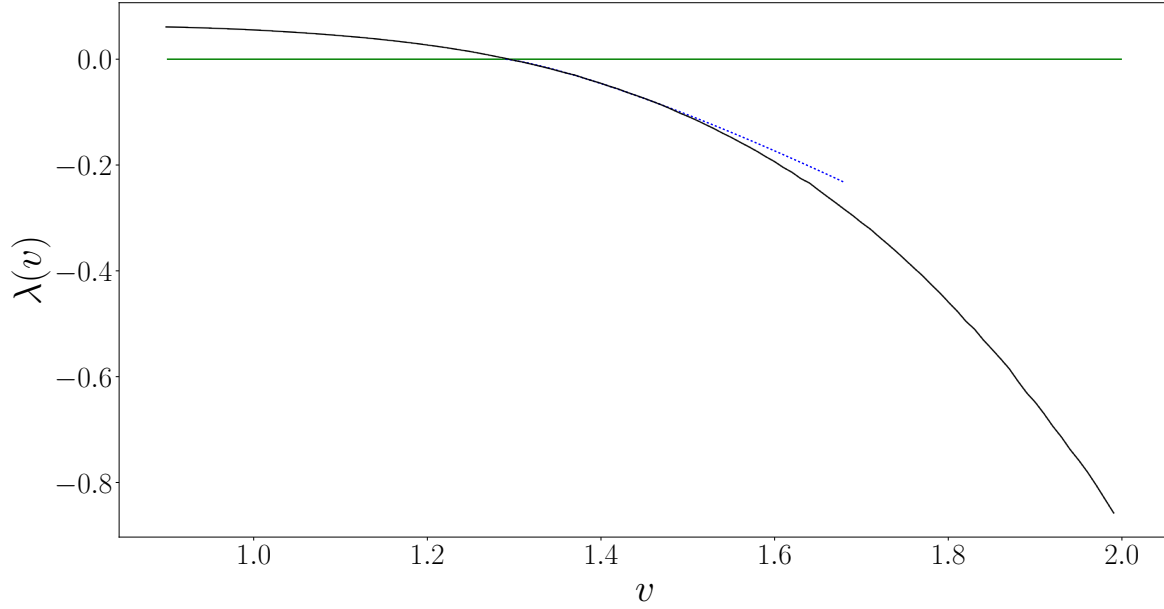
Figure SM2. Velocity dependent Lyapunov exponent plotted against velocities v. Horizontal green line indicates the velocity axis, the solid black line is $\lambda(v)$ and the blue dotted line is our fit for $\lambda(v) \sim -(v - v_B)^{\alpha}$.

time to account for the possibility that the form in Eq. (SM24) fits better before the classical wave-front arrives. We therefore investigate and fit the contours given by,

$$t = \frac{x}{v} - t_s, \qquad (SM26)$$

where t_s is the shift time we vary from $t_s = 0 \to 1$. We then select the time shift with the most numerical agreement with Eq. (SM24).

We find numerically that,

$$\alpha \approx 1.2801 \pm 0.0009, \ \ v_B = 1.29, \ \ t_s \approx 0.108 \qquad (SM27)$$

IV. ALTERNATIVE EXAMPLE

In this section we discuss an example where $m(x)$ does not scale as $\sim b(x)^2$ demonstrating that this behavior is not generic and the ETH obeying models may have corrections to the scaling of $m(x)$ independent of $b(x)$. We start be re-parametrizing our Hamiltonian in Eq. (6) for convenience. We restrict the possible parameter choices in our Hamiltonian as,

$$\hat{H} = \sum_{n=1,2} J_n \sum_j \left(\hat{S}_j^X \hat{S}_{j+n}^X + \hat{S}_j^Y \hat{S}_{j+n}^Y + \Delta \hat{S}_j^Z \hat{S}_{j+n}^Z \right). \qquad (SM28)$$

Here we choose values of $J_1 = -1$, $J_2 = 0.3703704$ and $\Delta = 0.75$ which corresponds to a chiral phase of the ground state [6]. We similarly determine the butterfly velocity as in section III, and find that,

$$\alpha \approx 1.2964 \pm 0.0004, \ \ v_B = 1.26, \ \ t_s \approx 0.06. \qquad (SM29)$$

This then allows us to reconfirm that the Gaussian wave can be confirmed for each x, shown in Fig. SM3. The fitting interval was again on an interval of length $\Delta t = 1$ indicating a large dynamical regime of validity. With this we can extract the forms of $m(x)$ and $b(x)$ which again decay exponentially.

In Fig. SM4 we again see that,

$$b(x) \sim e^{-cx}, \quad m(x) \sim e^{-wx}. \tag{SM30}$$

However this time, we get the behavior that, $c = 0.2666 \pm 0.0003$ and $w = 0.398 \pm 0.0009$, therefore we see that $w \napprox 2c$. We can see why this might be the case with a simple derivation of the form of Eq. (5) in the main text.

We are interested solely in the dynamical region centred around $t = x/v_B$. With standard expansions one can arrive at the propagating Gaussian form. Let $\tau = t - \frac{x}{v_B}$ and $\Delta = \frac{\dot{C}\left(x, \frac{x}{v_B}\right)}{C\left(x, \frac{x}{v_B}\right)}$. Since $C(x,t)$ is a positive function for the regime we are interested in,

$$C(x,t) = \exp\left[\ln C(x,t)\right], \tag{SM31}$$

this allows us to expand inside the logarithm,

$$C(x,t) = K e^{\ln\left(1 + \Delta\tau + \mathbb{O}\left[\frac{\ddot{C}\left(x,\frac{x}{v_B}\right)}{C\left(x,\frac{x}{v_B}\right)}\tau^2\right]\right)}, \tag{SM32}$$

$$= K e^{\ln(1+\Delta\tau) + \ln\left(1 + \mathbb{O}\left[\frac{\ddot{C}\left(x,\frac{x}{v_B}\right)}{C\left(x,\frac{x}{v_B}\right)\Delta(1+\tau)}\tau^2\right]\right)}. \tag{SM33}$$

Expanding one more time we arrive at,

$$C(x,t) = K e^{\Delta\tau - \frac{1}{2}\Delta^2\tau^2 + \mathbb{O}\left(\frac{1}{3}\Delta^3\tau^3\right) + \mathbb{O}\left[\frac{\ddot{C}\left(x,\frac{x}{v_B}\right)}{\dot{C}\left(x,\frac{x}{v_B}\right)(1+\tau)}\tau^2\right]}. \tag{SM34}$$

In Eq. (SM34) we see that the first order term and the second order term are related by squaring the first order term if,

$$\frac{\ddot{C}\left(x, \frac{x}{v_B}\right)}{\dot{C}\left(x, \frac{x}{v_B}\right)(1+\tau)} \approx 0. \tag{SM35}$$
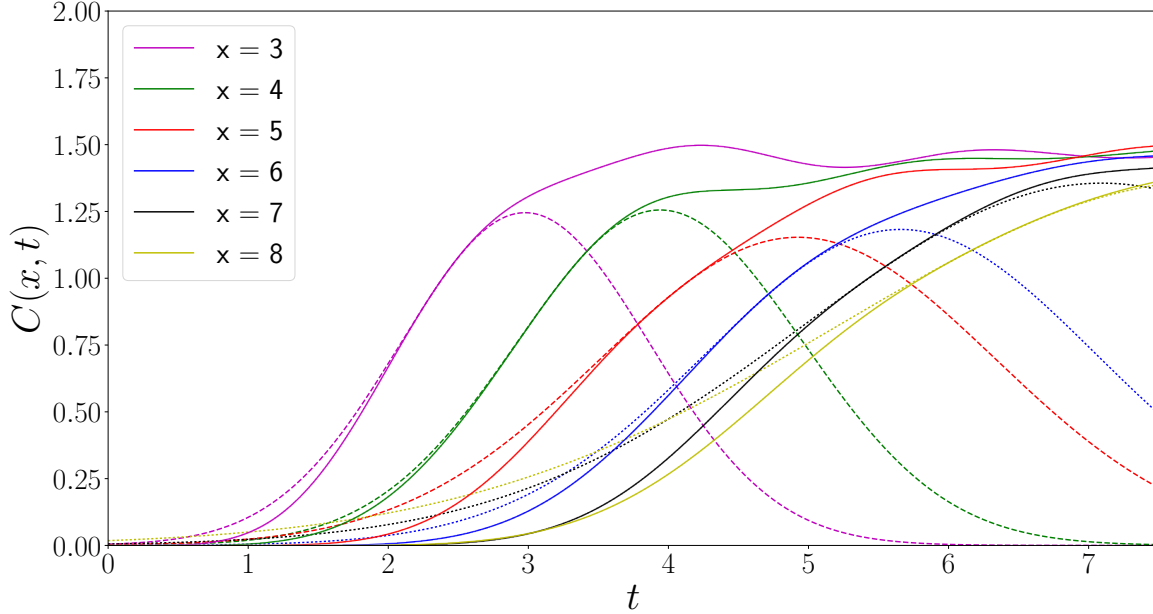

Figure SM3. $C(x,t)$ for the Hamiltonian in Eq. (SM28). Solid lines indicate the OTOC data, and dashed lines are the fitted Gaussian waveform given in Eq. (5) in the main text. Errors on the fits are on the order of 10^{-7} to 10^{-9} for all fitting parameters. The interval fitted is of total length $\Delta t = 1$ centred around $x = v_B t$.
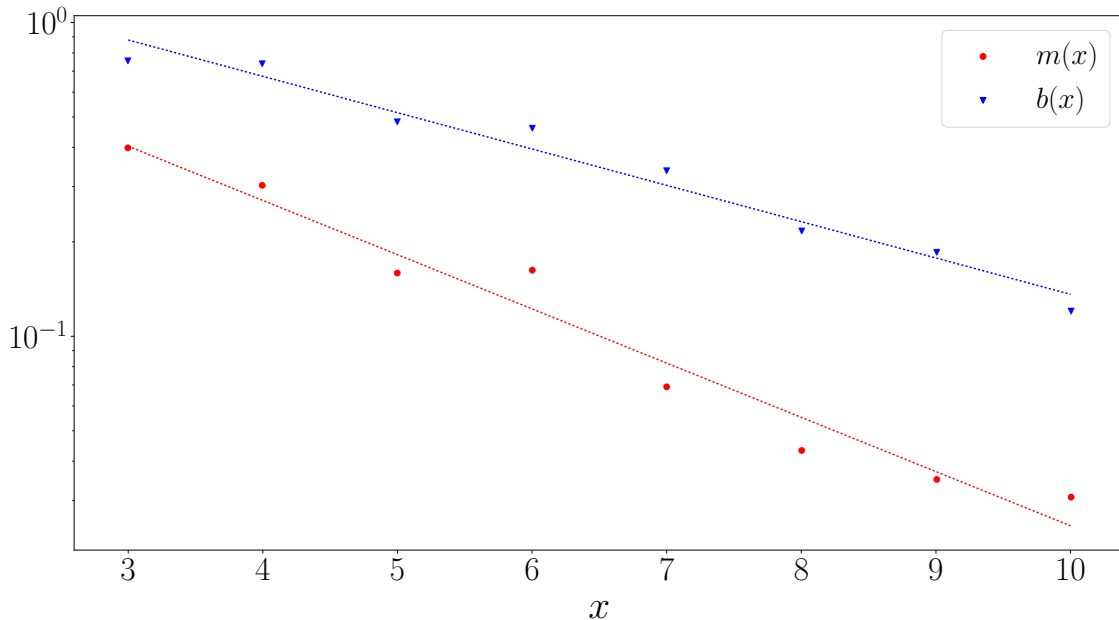
Figure SM4. Log-linear plot for $m(x)$ and $b(x)$ for the Hamiltonian characterized by the Hamiltonian in Eq. (SM28). Solid circles indicate data points from the fitting in Fig. SM3 and dashed lines indicate a fit to a linear equation. This rough linear scaling indicates the points are falling off exponentially fast.

This is of course not always the case. However for free fermions it turns out this is true for sufficiently large x. In the case of free fermions, the OTOC given in Eq. (7) in the main text experiences a change in curvature at the light cone. At a given fixed lattice point at large x, $C(x, t = \frac{x}{v_B})$ is an inflection point in a slice along the temporal direction. This property is inherited from the local Airy description, where $\text{Ai}''[z] = z\text{Ai}[z]$, and hence $\text{Ai}''[0] = 0$. This interestingly allows one to approximate the butterfly velocity (for free models) as,

$$v_B \equiv \frac{x}{t_*} \quad , \tag{SM36}$$

for which one defines t_* such that,

$$\left. \frac{d^2}{dt^2} C(x, t) \right|_{t=t^*} = 0 \tag{SM37}$$

In Fig. SM5 we see that for free fermions this conjecture approximates the butterfly velocity to $v_B \approx 0.988$ which corresponds to a 1.21% difference. This method is however unreliable in the cases where only small x are accessible.

---

[1] G. B. Airy, On the intensity of light in the neighbourhood of a caustic, Trans. Cambridge Philos. Soc. **6**, 379 (1838).

[2] W. Kirkby, J. Mumford, and D. H. J. O'Dell, Quantum caustics and the hierarchy of light cones in quenched spin chains, Phys. Rev. Research **1**, 033135 (2019).

[3] NIST Digital Library of Mathematical Functions. http://dlmf.nist.gov/, Release 1.1.1 of 2021-03-15. F. W. J. Olver, A. B. Olde Daalhuis, D. W. Lozier, B. I. Schneider, R. F. Boisvert, C. W. Clark, B. R. Miller, B. V. Saunders, H. S. Cohl, and M. A. McClain, eds.

[4] V. Khemani, D. A. Huse, and A. Nahum, Velocity-dependent Lyapunov exponents in many-body quantum, semiclassical, and classical chaos, Phys. Rev. B **98**, 144304 (2018).

[5] Y.-L. Zhang and V. Khemani, Asymmetric butterfly velocities in 2-local hamiltonians, SciPost Phys. **9**, 24 (2020).

[6] S. Furukawa, M. Sato, and S. Onoda, Chiral order and electromagnetic dynamics in one-dimensional multiferroic cuprates, Phys. Rev. Lett. **105**, 257205 (2010).
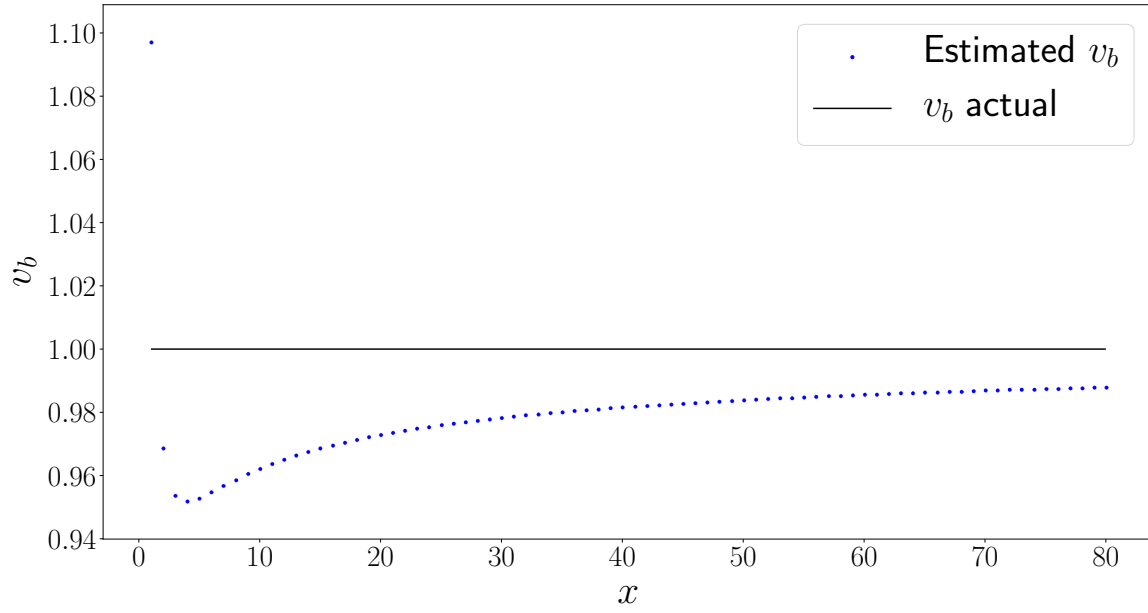
Figure SM5. Numerical estimate of v_B for the free model characterized by $\vec{c}_f$. Where $m = \frac{L}{2}$ and $x = |m - n|$. The system size used was $L = 1600$, and the data estimated roots with time steps of $\Delta t = 10^{-4}$. Roots were estimated within $\pm 10^{-5}$ of zero.

FALSE FLAGS OF CHAOS WITH GENERALIZED OTOCS

We consider two-time correlation (TTC) function of the form,

$$F_n(t) = \langle [\hat{A}(t), \hat{B}]^n \rangle , \qquad (4.1)$$

which is a generalization of the four-point out-of-time-ordered correlator (OTOC). We demonstrate that for a completely regular system, this function can exhibit traditional signals of chaos and hence must be treated with some care.

We consider a two-mode Bose-Hubbard system coupled to an atomic quantum dot (AQD) which mediates the tunnelling of the bosonic system. Since both systems are independently integrable and can't exchange energy, the system as a whole is also integrable. It becomes possible to express $F_n(t)$ as a return amplitude for a system undergoing effective stroboscopic dynamics. From this perspective, the model appears to yield typical signals associated with chaotic systems, such as a positive Lyapunov exponent, spectral repulsion, and a self-averaging survival probability (i.e. relaxation). We numerically verify these signals using random matrix theory, and find that the onset of chaotic signals corresponds to the Thouless time.

False signals of chaos from quantum probes

W. Kirkby ◉,[1] D. H. J. O'Dell ◉,[1] and J. Mumford ◉[1,2]

[1]*Department of Physics and Astronomy, McMaster University, 1280 Main Street West, Hamilton, Ontario, Canada L8S 4M1*
[2]*School of Arts and Sciences, Red Deer College, 100 College Boulevard, Red Deer, Alberta, Canada T4N 5H5*

We demonstrate that two-time correlation functions, which are generalizations of out-of-time-ordered correlators (OTOCs), can show "false flags" of chaos by exhibiting behavior predicted by random matrix theory even in a system with classically regular dynamics. In particular, we analyze a system of bosons trapped in a double-well potential and probed by a quantum dot which is coupled to the bosons dispersively. This system is integrable. Despite the continuous time evolution generated by the true Hamiltonian, we find that the n-fold two-time correlation function for the probe describes an effective stroboscopic or Floquet dynamics. From this perspective, the bosons appear to be alternately driven by two different noncommuting Hamiltonians in a manner reminiscent of the Trotterized time evolution that occurs in digital quantum simulation. The classical limit of this effective dynamics can have a nonzero Lyapunov exponent, while the effective level statistics and return probability show traditional signatures of chaotic behavior. In line with several other recent studies, this work highlights the fact that the behavior of OTOCs and their generalizations must be interpreted with some care.

I. INTRODUCTION

Two-time correlation (TTC) functions are indispensable tools in the investigation of the dynamics of quantum many-body systems. For example, a TTC of the form $\langle [\hat{A}(t), \hat{B}(t')] \rangle$ enters Kubo's formula for the linear response of the observable A at time t due to the time-dependent perturbation at earlier times t' by the drive B [1]. The wide utility of linear response theory means that TTCs are therefore a vital ingredient in calculations in quantum many-particle kinetics ranging from absorption spectra to reaction rates and diffusion constants. They are also useful in assessing "quantumness" through their connection to Leggett-Garg inequalities [2,3].

In this paper we consider a general n-fold TTC function [4–8] which for Hermitian operators we define as

$$F_n(t) \equiv \langle [\hat{A}(t)\hat{B}(0)]^n \rangle, \quad (1)$$

where $\hat{A}(t) = e^{i\hat{H}t}\hat{A}(0)e^{-i\hat{H}t}$, and $\langle \cdots \rangle$ is the expectation value taken with respect to a pure or mixed state. The first-order TTC function $F_1 = \langle \hat{A}(t)\hat{B}(0) \rangle$ describes a perturbation by operator $\hat{B}$ at time $t = 0$ followed by a "probe" by operator $\hat{A}$ at time t like in the Kubo formula. This function is related to quantities such as the quantum fidelity which has been successfully employed as a means of detecting and characterizing quantum phase transitions (QPTs) [9–13]. However, in general, the first-order TTC fails to capture the spread of information across a system from an initial perturbation. Thus, in recent years the second-order TTC function $F_2 = \langle \hat{A}(t)\hat{B}(0)\hat{A}(t)\hat{B}(0) \rangle$ has gained popularity and is often referred to as the out-of-time-ordered correlation (OTOC) function.

In addition to being more sensitive to QPTs than first-order TTCs [14–16], OTOCs have been used to identify the "scrambling" of information across a system's degrees of freedom [17–19]. For this purpose it is useful to express the OTOC function as an overlap between two states, $F_2(t) = \langle \psi_1(t) | \psi_2(t) \rangle$, where $|\psi_1(t)\rangle = \hat{B}(0)\hat{A}(t)|\psi\rangle$ and $|\psi_2(t)\rangle = \hat{A}(t)\hat{B}(0)|\psi\rangle$ and $|\psi\rangle$ is some general state. When the operators are chosen such that they initially commute, $[\hat{A}(0), \hat{B}(0)] = 0$, then F_2 is unity at $t = 0$, and at later times it decays as correlations build up and these operators no longer commute. For some systems, for example, the Sachdev-Ye-Kitaev [20] or Bose-Hubbard [21] models, there is a quantum analog of the "butterfly effect" whereby there is an exponential decay $F_2(t) \approx a - ce^{\lambda t}$ where a and c are constants and λ is the decay rate. There is, however, evidence that some nonintegrable short-range models, such as Ising chains [22] and Luttinger liquids [23], do not display such exponential dependence.

The exponential sensitivity of OTOCs to information scrambling has led to the exciting idea that OTOCs might be capable of quantifying many-body quantum chaos (or stated more carefully, dynamics which would be chaotic in the classical limit) [20,24–37]. The defining feature of classical chaos is an exponential sensitivity to initial conditions, i.e., the exponential increase in separation over time of initially close points in phase space, and is quantified by Lyapunov exponents. This behavior is considered to be a prerequisite for ergodicity and thermalization which destroys any memory of the initial state and it therefore seems natural enough from an information-theoretic perspective that chaos should be related to information scrambling. It has been demonstrated in a number of specific examples that the OTOC decay rate λ is directly related (but not necessarily equal [28]) to the Lyapunov exponent λ_L in the classical limit of a chaotic quantum system; these cases include the kicked rotor [28,38], stadium billiard [30], Dicke model [37], and kicked Dicke model [39].

110

However, recently it has been shown that having $\lambda > 0$ for an OTOC does not necessarily indicate that the system is chaotic, but instead can be caused by information scrambling from dynamics near an unstable fixed point [40,41]. The simplest example of such cases is the exponential separation of trajectories at short times in the inverted harmonic oscillator, which in single-particle quantum mechanics gives rise to $\lambda > 0$ at finite and infinite temperatures from the OTOC [42]. Furthermore, OTOCs in integrable many-particle systems such as the Lipkin-Meshkov-Glick model and the Dicke model (in the latter's integrable phase) [43,44] also exhibit positive λ near unstable points resulting from second-order QPTs.

In this paper we provide another example of how TTCs can exhibit false flags of chaos. In particular, we show that for a regular (i.e., nonchaotic) system, the dynamics of Eq. (1) can be governed by a time-evolution operator which displays Wigner-Dyson-type spectral statistics described by random matrix theory (RMT). RMT was first used in the 1950s to understand the statistical properties of the spectra of complex nuclei [45] and reached maturity in the 1980s with the realization (as encapsulated by conjectures such as that due to Bohigas, Giannoni, and Schmit [46,47]) that fluctuations in the distances between energy levels have universal properties in the semiclassical regime (far above the ground state) that distinguish chaotic from nonchaotic systems. In fact, it seems that apart from a few atypical exceptions the spectral statistics of physical systems fall into one of four classes determined by ensembles of random Hermitian matrices. For classically integrable systems the statistics of the corresponding quantum energy levels are Poissonian, whereas for classically chaotic systems the corresponding energy level fluctuations follow those of either the Gaussian orthogonal ensemble (GOE), the Gaussian unitary ensemble (GUE), or the Gaussian symplectic ensemble (GSE) independent of the details of the system and depending only on the symmetry properties of the Hamiltonian under canonical transformations. For a Floquet-type unitary operator [such as that effectively given by Eq. (1)], these ensembles are changed from Gaussian to circular ensembles (COE, etc.) because the eigenvalues should have a magnitude of 1.

The system we use to illustrate these features is a simple model consisting of N identical bosons occupying two modes and coupled to a single qubit probe (atomic quantum dot) and has previously been discussed in a considerable number of theoretical proposals (e.g., [48–56]). In general this system is chaotic [52,56], but in this paper we do not allow the qubit to exchange energy with the bosons (dispersive limit of the interaction) and since the bosonic part of the Hamiltonian is integrable [57,58], this renders the entire model integrable. Our model is relevant to experiments with bosonic Josephson junctions, e.g., Bose-Einstein condensates (BECs) in double-well potentials [59–62], or spinor condensates with two internal states [63,64], if an additional impurity atom or ion [65–68] is added. Alternatively, the same Hamiltonian (Ising model with long-range interactions) can be realized with trapped ions, again with two internal states [69], and again a distinguished "impurity" atom or ion should be added to the system. Solid-state Josephson junctions might offer another route to realize the type of dynamics we will discuss here [70–72].

The structure of the rest of this paper is as follows: Section II presents the details of the model (bosons + probe) to be used and Sec. III examines how a TTC of operators in the subspace belonging to the probe can be written as a periodic Floquet operator acting purely on the bosons. In Sec. IV the classical dynamics generated by this Floquet operator is examined, including the classical Lyapunov exponent which is a signature of chaos. Section V turns to quantum properties: Sec. V A examines the quasienergy level spacings of the Floquet operator and compares against the results of RMT, while Sec. V B treats the quantum TTC as a survival amplitude which leads naturally to computations of the inverse participation ratio and further comparisons against RMT. Conclusions are presented in Sec. VI. This paper also has three Appendixes where details of the calculations and some extra supporting results are given.

II. MODEL

Our model couples the two-mode Bose-Hubbard model, which describes N interacting bosons hopping between two sites, to a single two-state atomic quantum dot (AQD), i.e., a qubit. In order to put the qubit and the bosons on a similar footing it is convenient to express the boson operators in terms of collective spin operators:

$$\hat{S}_\alpha \equiv 1/2 \sum_i^N \hat{\sigma}_\alpha^i, \qquad (2)$$

where $\alpha \in \{x, y, z\}$. Using the Schwinger representation the same collective spin operators can alternatively be defined via annihilation and creation operators acting on the sites: If we label the two sites of the Bose-Hubbard model as L (left) and R (right) then the number difference between the left and right sites can be written $(\hat{b}_L^\dagger \hat{b}_L - \hat{b}_R^\dagger \hat{b}_R) \equiv 2\hat{S}_z$, where $\hat{b}_{L/R}^\dagger$ ($\hat{b}_{L/R}$) is the creation (annihilation) operator for a boson on the left or right site obeying the usual commutation relations $[\hat{b}_i, \hat{b}_j^\dagger] = \delta_{i,j}$ where $i, j \in [L, R]$. Similarly, we have $(\hat{b}_R^\dagger \hat{b}_L + \hat{b}_L^\dagger \hat{b}_R) \equiv 2\hat{S}_x$ which takes a boson from one site and puts it onto the other (plus the reverse process to make the operator hermitian), thus producing mode coupling (tunneling).

In this way one finds that, up to constant terms, the total Hamiltonian can be written (for full details see [50]) as

$$\hat{H} = \hat{H}_B + \hat{H}_d + \hat{H}_{Bd}, \qquad (3)$$

where H_B, H_d, and H_{Bd} are the N boson, dot, and boson-dot interaction Hamiltonians, respectively, and are given by

$$\hat{H}_B = k_z \hat{S}_z^2/(N+1) - \alpha_x \hat{S}_x + \alpha_z \hat{S}_z, \qquad (4)$$

$$\hat{H}_d = -\Delta(1 + \hat{\sigma}_z)/2, \qquad (5)$$

$$\hat{H}_{Bd} = \beta \hat{S}_x(1 + \hat{\sigma}_z). \qquad (6)$$

Here, the AQD operators are single Pauli matrices and are distinguished from the boson Pauli matrices by the absence of a superscript. The parameters in this Hamiltonian have the following definitions: k_z is the boson-boson interaction energy, α_x is the boson hopping and/or tunneling energy, α_z is the energy imbalance between the two boson modes, Δ is the energy imbalance between the two AQD modes, and β is the coupling energy between the AQD and the N boson hopping or tunneling energy.
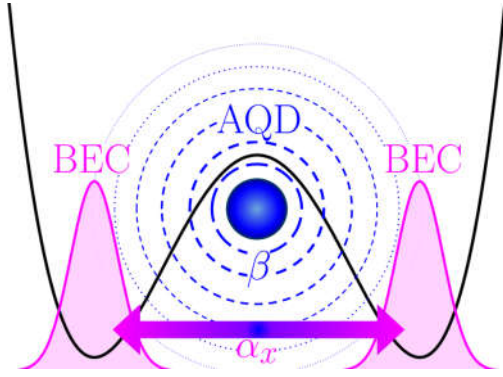
FIG. 1. Schematic of system being considered: a BEC trapped in a double-well potential with interwell hopping moderated by a trapped AQD. Tuning the parameter β in $\hat{H}_{Bd}$ will effectively modify the hopping strength α_x. The BEC has a self-interaction strength k_z, and a bias or tilt in the double well can be controlled by α_z.

It is important to note that there is no hopping term ($\hat{\sigma}_x$ operator) in the dot's Hamiltonian and so it cannot make transitions between its two states, i.e., $[\hat{\sigma}_z, \hat{H}] = 0$, and this gives a dispersive interaction between the bosons and the AQD. The AQD therefore plays a somewhat passive role in the dynamics of the bosons: from $\hat{H}_{Bd}$ we see that the effect of the AQD is to modify the tunneling energy of the bosons, either having no effect or suppressing it depending on whether the AQD is initialized in its excited or ground state, respectively. It has previously been shown that when the AQD is allowed to make transitions the classical dynamics displays chaos above a certain critical value of β [52], and without these transitions the dynamics is regular. Nevertheless, we will show in this paper that when AQD operators are used in Eq. (1), apparently chaotic dynamics emerge in the TTC due to the presence of the AQD.

One way to realize the Hamiltonian in Eq. (3) is with a BEC trapped in a double-well potential in the two-mode regime and coupled to a distinguishable atom trapped between the two wells (see Fig. 1). This dot atom could be a different species to the rest of the atoms or simply be in a different hyperfine state. In fact the dot atom need not even be trapped between the two wells, and could instead be allowed to tunnel back and forth between the two wells like the bosons [49,50,56]. Recent experimental realizations [73–75] of ^{133}Cs atoms immersed in an ultracold ^{87}Rb gas allow for individual impurities to be controlled and used as nondestructive quantum probes. In order for the interaction to be dispersive, however, in this case the energy difference between the symmetric and antisymmetric states of the dot atom should be much greater than all the other energies so that it remains in just one state during the dynamics.

For such an ultracold atom realization the parameters in Eqs. (4)–(6) can all be controlled using external fields: k_z and β contain the boson-boson and boson-dot s-wave scattering lengths, respectively, and can be controlled via the Feshbach resonance technique [76,77]; α_x is the tunneling energy between the two BEC wells and can be controlled by raising or lowering the height of the barrier, e.g., by laser intensity; α_z is the energy imbalance between the two wells and can be controlled by providing a tilt between them via external fields

with spatial gradients; Δ is the energy difference between the first two states of the AQD. An alternative realization, with slightly modified parameter definitions, makes use of internal states (for both the bosons and the AQD) rather than spatial states, although all the atoms should then be tightly trapped so that they occupy a single spatial mode. The tunneling between states in this case must be driven by laser or radio frequency radiation depending on whether the different internal states are different electronic orbitals or hyperfine states.

Yet another way to realize the boson-impurity model is via ions immersed in a BEC. In the experiment discussed in Ref. [65] a single ^{171}Yb$^+$ ion was trapped inside a ^{87}Rb BEC and the experiment demonstrated independent control of the ion and the BEC. More recent experiments have demonstrated control and transport of a single ^{87}Rb$^+$ [66,67] ion impurity immersed in a BEC. In these experiments, the ion is created by ionizing a Rydberg atom, and Rydberg blockade ensures the creation of only a single impurity in the BEC. Furthermore, temperatures where ion-atom collisions are dominated by the s-wave channel are being approached [78]. The Hamiltonian $\hat{H}_B$ can also be realized using a linear ion trap system using ^{171}Yb$^+$ with effective magnetic fields generated by stimulated Raman transitions [79].

III. CORRELATION FUNCTION DYNAMICS: FLOQUET OPERATOR

Our philosophy in this paper is to treat the AQD as a probe of the boson dynamics and hence the operators we use in Eq. (1) are all AQD operators. In fact, for simplicity we use $\hat{\sigma}_x$ for both operators $\hat{A}$ and $\hat{B}$ where, of course, we evolve $\hat{A}(t) = \hat{\sigma}_x(t)$ as a function of time but keep $\hat{B}(0) = \hat{\sigma}_x(0)$ at $t = 0$. Furthermore, we assume that at $t = 0$ the probe and bosons are uncorrelated so that the initial state of the system is a product state of the form $|\Psi\rangle = |\psi\rangle_B \otimes |+\rangle_d$ where $|\psi\rangle_B$ is the state of the BEC and $|+\rangle_d$ is the excited state of the quantum dot (starting the dot in the ground state works as well). This is, therefore, the state we use for evaluating the correlator $\langle \cdots \rangle$. In addition, we make two simplifications to Eqs. (4)–(6): first, since $[\hat{H}_d, \hat{H}] = 0$ the AQD Hamiltonian will only produce an overall dynamical phase in our calculations which will not affect the results, so we set $\Delta = 0$, and second, without loss of generality we set $\beta = \alpha_x/2$ (we explain this last condition below).

Under these conditions we find that the n-fold TTC reduces to a correlation function evaluated purely within the bosonic state,

$$F_n(t) = {}_B\langle\psi|\hat{\mathcal{F}}^n|\psi\rangle_B, \tag{7}$$

where $\hat{\mathcal{F}}^n$ is a Floquet operator that repeatedly applies (n times) the unitary operator

$$\hat{\mathcal{F}} = e^{-i\hat{H}_1 t} e^{-i\hat{H}_2 t}. \tag{8}$$

The derivation of this result is given in Appendix A where it is shown that the two Hamiltonians appearing in $\hat{\mathcal{F}}$ are given by

$$\hat{H}_1 = -\hat{H}_B = -k_z\hat{S}_z^2/(N+1) + \alpha_x\hat{S}_x - \alpha_z\hat{S}_z, \tag{9}$$

$$\hat{H}_2 = \hat{H}_B\big|_{\alpha_x=0} = k_z\hat{S}_z^2/(N+1) + \alpha_z\hat{S}_z. \tag{10}$$

In line with the reduction of the full state to only the bosonic state in Eq. (7), it is notable that these effective Hamiltonians depend only on the boson operators and are different versions of $\hat{H}_B$ given in Eq. (4). Hence, the general TTC has turned into a survival amplitude for the BEC part $|\psi\rangle_B$ of the total state after n applications of the operator $\hat{\mathcal{F}}$. The different signs in front of the two Hamiltonians mean that the Floquet operator describes a system being shaken forwards and backwards (with slightly different forwards and backwards evolution) in time where the elapsed time $t = T$ is the length of each part of the shake and the order n of the TTC is the number of cycles.

Our choice of $\beta = \alpha_x/2$ simplifies the Hamiltonian $\hat{H}_2$ so that $\hat{S}_x$ does not appear, as explained in Appendix A. This tuning is not central to the validity of our results: other choices will simply add a finite hopping term to $\hat{H}_2$. However, the vanishing of the β term in the other Hamiltonian is a robust feature of having an uncorrelated initial state. This is a special choice, but also a very reasonable one. As long as the initial state is separable, one will always get forward and backward pieces like in Eqs. (9) and (10).

We note in passing that a related issue to the one discussed in this paper is also an important consideration in digital quantum simulation, i.e., the breakup of continuous time evolution into separate steps. This sometimes goes under the name of Trotterization (after Trotter-Suzuki decompositions) and careful control of the errors induced by this process is critical to the accuracy of such simulations. In fact, it has been shown that there is a deep connection to chaos because chaotic systems are intrinsically less stable against such errors than nonchaotic ones [80].

IV. CLASSICAL CORRELATION FUNCTION DYNAMICS

We begin our analysis of the correlation function dynamics by checking for classical chaos. The classical theory is given by the mean-field approximation and it is known that in this limit the two-mode Bose-Hubbard model, which describes the bosonic part of the system, is equivalent to a nonrigid pendulum which is an integrable system [81]. When coupled to an impurity spin the total system can be mapped in certain regimes onto a double pendulum [50] which is in general chaotic, although in the present dispersive case the second pendulum has a constant angular momentum which keeps the model integrable.

The mean-field versions of our various Hamiltonians are derived in Appendix B. It is shown that the mean-field version $\mathcal{H}$ of the total Hamiltonian $\hat{H}$ is given by

$$\mathcal{H} = \frac{k_z}{4}z^2 - \frac{\alpha_x}{2}\sqrt{1-z^2}\cos\phi + \frac{1}{2}\alpha_z z - \frac{\Delta}{2N}\left(1+\frac{y}{2}\right) + \frac{\beta}{2}\sqrt{1-z^2}\cos\phi\left(1+\frac{y}{2}\right), \quad (11)$$

which is obtained by replacing the mode operators with complex numbers and taking the thermodynamic limit $\mathcal{H} = \lim_{N\to\infty}\hat{H}/N$. From there, Hamilton's equations of motion can be used to generate the dynamics. The mean-field limits of $\hat{H}_1$ and $\hat{H}_2$ are

$$\mathcal{H}_1 = -\frac{k_z}{4}z^2 + \frac{\alpha_x}{2}\sqrt{1-z^2}\cos\phi - \frac{\alpha_z}{2}z, \quad (12)$$

$$\mathcal{H}_2 = \frac{k_z}{4}z^2 + \frac{\alpha_z}{2}z. \quad (13)$$
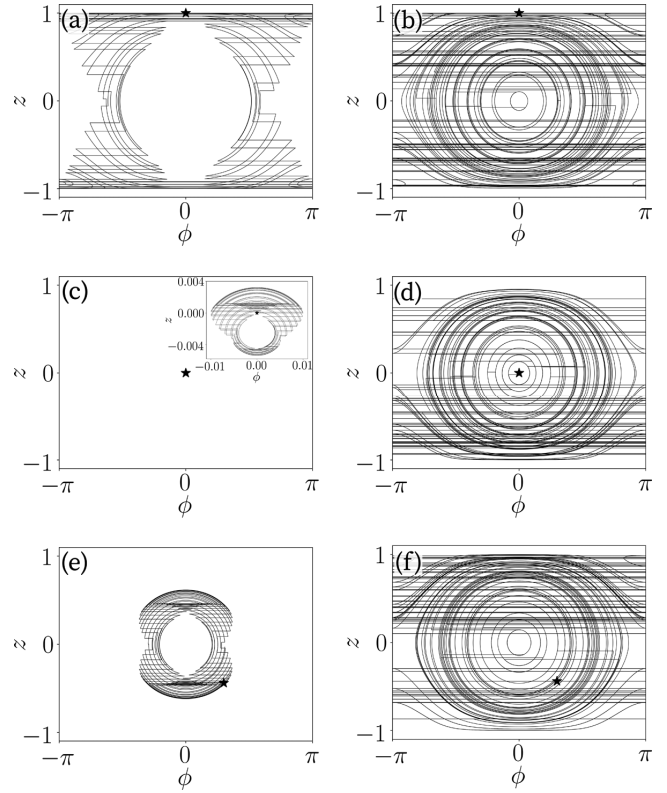

FIG. 2. Classical phase-space portraits of the n-fold TTC obtained using the mean-field Hamiltonians $\mathcal{H}_1$ and $\mathcal{H}_2$ given in Eqs. (B12) and (B13), respectively. As explained in the text, the choices we make for the operators and states in the correlation function mean that the probe drops out of the problem and the correlation dynamics is purely for the bosons: z is the number difference and ϕ the phase difference between the two bosonic modes. The star in each panel indicates the starting point. Time evolution proceeds with repetitive application of each Hamiltonian and since $\hat{H}_2$ is diagonal in the $\hat{S}_z$ basis, then in z coordinates $\mathcal{H}_2$ will evolve the classical trajectory in a straight horizontal line to another constant energy contour of $\mathcal{H}_1$. The left column shows classical trajectories with $\alpha_x T = 1$ (weakly chaotic) while the right column shows $\alpha_x T = 5$ (strongly chaotic). (a, b) Initial state has all spins pointing along S_z axis. (c, d) Initial state has all spins pointing along the S_x axis. Panel (c) has such little variation from the initial state that it must be shown in an inset. (e, f) Randomly selected initial classical vector with no special symmetry. For all panels, $k_z = 3\alpha_x$, $\alpha_z = 0.01\alpha_x$, and $n = 50$.

The dynamics are produced by using Hamilton's equations of motion for $\mathcal{H}_2$ for a period of time T; then we switch to Hamilton's equations for $\mathcal{H}_1$ for the same period of time and repeat this intertwining process for n cycles.

In Fig. 2 we plot the phase-space dynamics of the BEC mean-field variables

$$z = (n_L - n_R)/N, \quad \phi = \phi_L - \phi_R, \quad (14)$$

which are the scaled number difference and phase difference between the left and right wells, respectively. Each row has a different initial condition represented by a black star. At short times (left column) the dynamics only accesses limited regions of phase space, especially if the system is initialized near the stable fixed point at $\phi = z = 0$. However, at
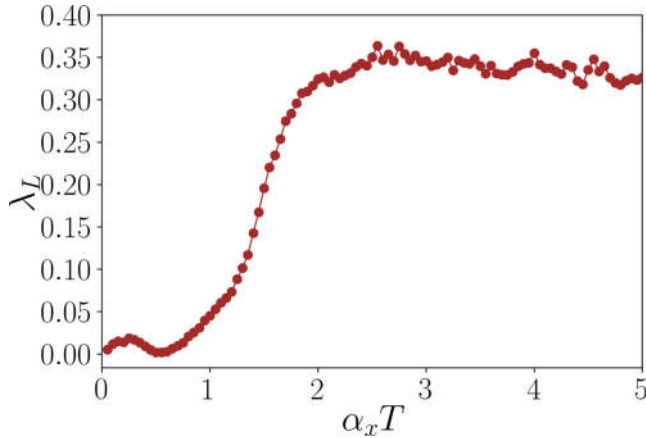
FIG. 3. The Lyapunov exponent, λ_L, as a function of the classical kick period $\alpha_x T$ for dynamics produced by the repeated application of the mean-field Hamiltonians in Eqs. (9) and (10). At short times, $\lambda_L \approx 0$, suggesting the system is regular while for longer times a clear nonzero Lyapunov exponent develops, suggesting chaotic dynamics. Each data point is the maximum λ_L which is then averaged over 1500 random initial states in phase space. Here, $\alpha_z = 0.01\alpha_x$ and $k_z = 3\alpha_x$ while the Hamiltonians $\mathcal{H}_1$ and $\mathcal{H}_2$ are cycled $n = 20$ times. These results can be contrasted with those shown in Fig. 6 in Appendix B where it is shown that the true (continuous) dynamics of the full Hamiltonian has $\lambda_L = 0$.

longer times (right column) the dynamics becomes ergodic and independent of the initial conditions which is a hallmark of classical chaos. In fact, Fig. 2 shows how ergodicity is established despite the two parts of the time evolution being separately integrable: the $\mathcal{H}_2$ trajectories conserve z, so they travel only along the ϕ direction, essentially providing a pathway to different energy contours of $\mathcal{H}_1$, along which the orbit proceeds.

To quantify the chaotic dynamics we numerically compute the Lyapunov exponent λ_L and the results are plotted in Fig. 3 as a function of $\alpha_x T$. Each data point is obtained from a phase-space average taken with respect to many random initial states. When $\lambda_L > 0$ the trajectories are exponentially separating in time and hence we have chaos. As expected from Fig. 2, for relatively short periods ($\alpha_x T \lesssim 1$) the trajectories tend to stay in a small subregion of phase space leading to $\lambda_L \approx 0$. As the shake period is increased ($\alpha_x T \gtrsim 1$) the Lyapunov exponent becomes nonzero and the correlator dynamics becomes chaotic. For a comparison with the actual model see Fig. 6 in Appendix B, where a plot of λ_L versus k_z shows that $\lambda_L = 0$, demonstrating that $\mathcal{H}$ is regular. These results give us the first hint that the dynamics of the general TTC function can be chaotic even for a nonchaotic system.

V. QUANTUM CORRELATION FUNCTION DYNAMICS

We now turn to the fully quantum problem to look for evidence of so-called quantum chaos in the correlator dynamics. To this end we first examine the spectral statistics of the Floquet operator and compare to RMT and, second, we calculate the survival probability.

A. Eigenphases and spacings of the Floquet operator

We first consider the Floquet operator $\hat{\mathcal{F}}$ in Eq. (8). Recently it was shown that in a quantum stadium billiard model (which has a classical limit which is chaotic) the spectral statistics of the operator $\hat{\Lambda}(t) = \ln(-[\hat{x}(t), \hat{p}_x(0)]^2)/(2t)$, which contains an out-of-time-ordered *commutator*, aligns well with the predictions from RMT [30]. Similar results were found when analyzing the spectral statistics of a Floquet operator for a shaken system when its corresponding classical system is chaotic [80]. We will follow this route here and analyze the spectrum of $\hat{\mathcal{F}}$. This is a unitary operator, but rather than work with its complex eigenvalues $e^{i\theta_j}$, we instead examine the statistical properties of its eigenphases θ_j.

First, we note that the eigenphases are time dependent in a nontrivial way which can be seen by writing $\hat{\mathcal{F}}$ in terms of a single effective Hamiltonian $\hat{\mathcal{F}} = e^{-i\hat{H}_{\text{eff}} t} = e^{-i\hat{H}_1 t} e^{-i\hat{H}_2 t}$. Using the Baker-Campbell-Hausdorff formula,

$$e^{\hat{X}} e^{\hat{Y}} = \exp\left(\hat{X} + \hat{Y} + \tfrac{1}{2}[\hat{X}, \hat{Y}] + \cdots\right), \qquad (15)$$

we find that $\hat{H}_{\text{eff}}$ for our system can be written at short times as

$$\hat{H}_{\text{eff}}(t) = \hat{H}_1 + \hat{H}_2 - \frac{it}{2}[\hat{H}_1, \hat{H}_2] + O(t^2). \qquad (16)$$

At each moment in time the effective Hamiltonian yields a set of instantaneous eigenstates $\{|v_i(t)\rangle\}$ such that $\hat{H}_{\text{eff}}(t)|v_i(t)\rangle = \epsilon_i(t)|v_i(t)\rangle$ where $\{\epsilon_i(t)\}$ is the set of instantaneous eigenenergies. From Eq. (16), we can see at early times the dynamics is simply due to $\exp[-i(\hat{H}_1 + \hat{H}_2)t]$; however, as t increases, more terms contribute to $\hat{H}_{\text{eff}}$ and the dynamics of the eigenenergies becomes complicated. Since $\epsilon_i t = \theta_i \pmod{2\pi}$, we expect the eigenphases to inherit this complicated behavior and this can indeed be seen in Fig. 4(a) where they are plotted as a function of time. At early times the magnitude of the eigenphases increases linearly until at around $\alpha_x t \approx 0.4$ they begin to wind around the interval $[-\pi, \pi)$ at which point tiny avoided crossings form (they are at first too small to see at the scale of the figure; however, when zoomed in incredibly narrow avoided crossings become visible). At around $\alpha_x t \approx 1.3$ the avoided crossings begin to widen and at late times the eigenphases are well separated and display the equivalent of level repulsion found in time-independent chaotic systems.

Rather than examine the full statistical distribution of the eigenphases, we instead calculate the average spacing ratio [82],

$$r_n = \frac{\min(\delta_n, \delta_{n+1})}{\max(\delta_n, \delta_{n+1})}, \qquad r = \frac{1}{\mathcal{D}} \sum_{n=1}^{\mathcal{D}} r_n, \qquad (17)$$

where $\delta_n = \theta_{n+1} - \theta_n$ is the difference between adjacent eigenphases and $\mathcal{D} = N + 1$ is the size of the BEC Hilbert space. The spacing ratio takes on distinct values depending on which RMT ensemble the eigenphases follow, if they follow any at all. For our case, having $\alpha_z \neq 0$ destroys the parity symmetry of the system, leaving only time-reversal symmetry. We therefore expect that r should obey the circular orthogonal example (COE) result of $r_{\text{COE}} = 4 - 2\sqrt{3} \approx 0.536$. Figure 4(b) shows clearly that r does indeed oscillate around the COE result provided we consider longer times $\alpha_x t > 2.0$. In fact, comparing Figs. 4(a) and 4(b), we see that the dip in r in the
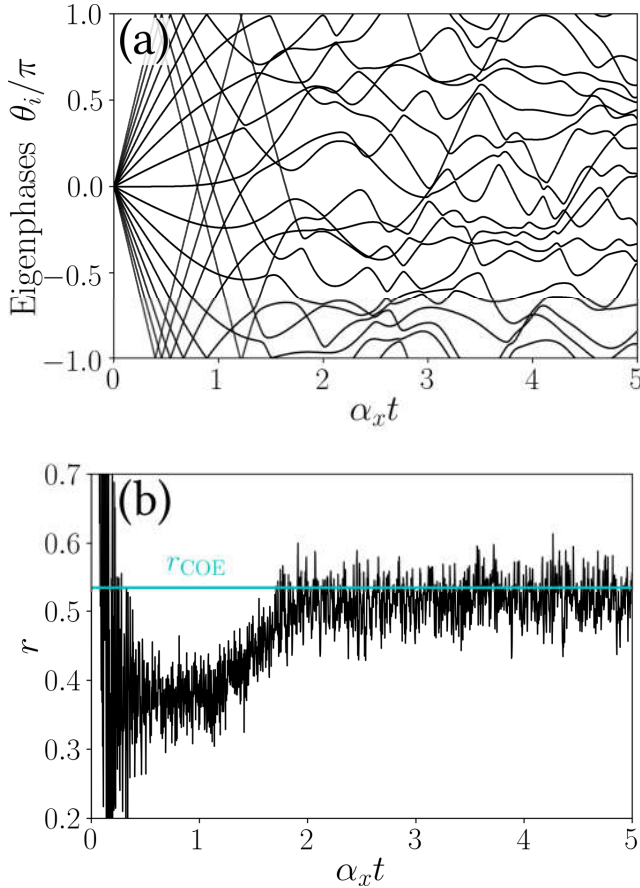
$\hat{H}_{\mathrm{eff}}$), into $P_n(t)$. This gives

$$P_n(t) = \left| \sum_{i=1}^{\mathcal{D}} \langle \psi | \hat{\mathcal{F}}^n | v_i \rangle \langle v_i | \psi \rangle \right|^2$$

$$= \sum_{i,j}^{\mathcal{D}} e^{in(\epsilon_i - \epsilon_j)t} |\langle v_i | \psi \rangle|^2 |\langle v_j | \psi \rangle|^2. \qquad (18)$$

Here, and from now on, we suppress the subscript "B" on $|\psi\rangle_B$. Since the eigenstates and eigenenergies of H_{eff} are complicated functions of time, even the qualitative behavior of the long-time average of Eq. (18) is not immediately clear. For large enough TTC order n, the phase factor will oscillate rapidly, making all terms where $\epsilon_i \neq \epsilon_j$ approximately equal to zero (the "diagonal approximation"). This condition is satisfied naturally in the chaotic regime due to level repulsion of the eigenenergies. The level repulsion of the corresponding eigenphases is shown in Fig. 4, so we should expect the same for the eigenenergies resulting in no degeneracies in the spectrum. Thus, when n is large enough, the long-time average of $P_n(t)$, $P = \lim_{T \to \infty} \frac{1}{T} \int_0^T P_n(t) dt$, can be written as

$$P \approx \sum_{i,j}^{\mathcal{D}} \delta_{i,j} |\langle v_i | \psi \rangle|^2 |\langle \psi | v_j \rangle|^2 = I\{|\psi\rangle\}. \qquad (19)$$

Thus, the survival probability becomes equal to the inverse participation ratio (I) of the state $|\psi\rangle$ over the basis states of $\hat{H}_{\mathrm{eff}}$ (or $\hat{\mathcal{F}}$) where the participation ratio (R) is defined as

$$R\{|\psi\rangle\} \equiv \frac{1}{\sum_a^{\mathcal{D}} |\langle v_a | \psi \rangle|^4}, \qquad (20)$$

and is used to quantify how spread a state of interest $|\psi\rangle$ is over a reference basis $\{|v_a\rangle\}$. What remains to be done is to explore the effect of different BEC states $|\psi\rangle$ in which the correlation function is evaluated, and we will see that this choice can affect the outcome of P.

A generic state $|\psi\rangle$ (e.g., one taken at random, absent any special symmetry) has complex coefficients in the basis of $\hat{S}_z$ (i.e., the set of Fock states $\{|m\rangle\}$ where the eigenvalues $\{m\}$ are half the boson number difference between the two sites) and is best modeled by a circular unitary ensemble (CUE), whose states are uniformly distributed on the unit sphere in $\mathbb{C}^{\mathcal{D}}$. If, however, we select a single eigenstate $|m\rangle$ of the $\hat{S}_z$ operator for our TTC, there is a shift instead to COE statistics due to the fact that these are eigenstates of $\hat{H}_2$, ultimately changing the symmetry of $\hat{\mathcal{F}}$. This can be seen explicitly from the TTC, using Eq. (7):

$$F_n(t) = \langle m | (e^{-i\hat{H}_1 t} e^{-i\hat{H}_2 t})^n | m \rangle$$

$$= e^{-i\phi(m)t} \langle m | \underbrace{(e^{-i\hat{H}_1 t} e^{-i\hat{H}_2 t})^{n-1} e^{-i\hat{H}_1 t}}_{\hat{U}_t} | m \rangle, \qquad (21)$$

where the phase $\phi(m) = k_z m^2/(N+1) + \alpha_z m$ can be neglected because we are interested in the survival probability $P_n(t) = |F_n(t)|^2$. The evolution operator $\hat{U}_t$ in Eq. (21) is related to the Floquet operator by

$$\hat{U}_t = \hat{\mathcal{F}}^n e^{i\hat{H}_2 t} \qquad (22)$$

FIG. 4. (a) Eigenphases θ_i of the Floquet operator $\hat{\mathcal{F}}$ as a function of time for $N = 16$. At early times the eigenphases evolve regularly, but as time goes on they begin to wind around the interval $[-\pi, \pi)$ and avoided crossings form. These are initially tiny but gradually widen and result in the familiar level repulsion seen in chaotic systems. (b) Average eigenphase spacing ratio r as a function of time for $N = 100$. At later times r oscillates around the RMT prediction of r_{COE}, shown as a horizontal cyan line, coinciding with the occurrence of level repulsion in (a). The other parameters for both images are $k_z = 3\alpha_x$ and $\alpha_z = 0.01\alpha_x$.

range $0.4 \leqslant \alpha_x t \leqslant 1.3$ corresponds to the range of times when the eigenphases first begin to wind around the full interval $[-\pi, \pi)$ and form small avoided crossings. The time at which the dip occurs and how low it is are nonuniversal features that depend on the parameters of the system. For $\alpha_x t > 1.3$ the avoided crossings of the eigenphases begin to widen and eventually show the chaotic result of level repulsion quantified by $r \approx r_{\mathrm{COE}}$.

B. Survival probability

Returning to Eq. (7), we focus our attention back on $F_n(t)$. More precisely, we study its squared absolute value which corresponds to the return probability $P_n(t) = |F_n(t)|^2$. Furthermore, based on the results of the last section we expect the clearest evidence of chaos to come from the long-time average of $P_n(t)$. We start by inserting the resolution of identity, $\mathbb{1} = \sum_i |v_i\rangle\langle v_i|$ (expressed in terms of the eigenvectors of

and has the additional symmetry $\hat{U}_t = \hat{U}_t^T$, meaning its eigenstates have real components. Therefore, when considering the $\hat{S}_z$ eigenstates as our basis, the time-dependent eigenstates of $\hat{U}_t$ are not taken from matrices in the CUE (since those states have complex components) and instead are best modeled by random matrices in the COE, for which the states are distributed uniformly on the unit sphere in $\mathbb{R}^{\mathcal{D}}$.

There exist signatures of chaos in both the survival probability of a single state, P_n, and for ensembles of states. For the purposes of this article, we will focus on general features of the survival probability and so we will average over an *entire* basis; however, a more in-depth discussion of individual survival probabilities can be found in Appendix C. Performing the average over a basis $\{|\psi_i\rangle\}$, we can write the sum over individual $I\{|\psi_i\rangle\}$ as

$$I = \sum_i I\{|\psi_i\rangle\} = \sum_{i,j} |\langle v_j|\psi_i\rangle|^4 = \overline{P}, \qquad (23)$$

where the bar over P signals the average over the entire basis. If we use a random basis or the basis states of the $\hat{S}_x$ operator [80], we expect the average I to take on the CUE prediction,

$$I_{\text{CUE}} = \frac{2\mathcal{D}}{\mathcal{D}+1}, \qquad (24)$$

where in the thermodynamic limit, $N \to \infty$, and hence $I_{\text{CUE}} \to 2$. Meanwhile, if we use the basis of $\hat{S}_z$ eigenstates, we expect the average I to take on the COE prediction,

$$I_{\text{COE}} = \frac{3\mathcal{D}}{\mathcal{D}+2}, \qquad (25)$$

for which $I_{\text{COE}} \to 3$ as $N \to \infty$.

Following Schiulaz *et al.* [83], we can also calculate the Thouless time t_{Th} for a fully connected model like ours in the COE and CUE ensembles. t_{Th} describes the time at which the wave function first extends over the entire many-body Hilbert space, and is thus the time at which universal RMT predictions begin to govern the dynamics. For spatially extended systems, t_{Th} generally depends on the system size [83,84]; however, for a fully connected model and $N \gg 1$,

$$t_{\text{Th}}^{\text{CUE}} = \left(\frac{3}{2\pi}\right)^{\frac{1}{4}}, \qquad (26)$$

$$t_{\text{Th}}^{\text{COE}} = \left(\frac{3}{\pi}\right)^{\frac{1}{4}}, \qquad (27)$$

where these times are expressed in units of α_x^{-1}.

In Fig. 5(a) we plot numerical evaluations of $P_n(t)$ averaged over the $\hat{S}_x$ basis. Since at short times $H_{\text{eff}} \approx \hat{S}_x$, the survival probability is briefly constant and subsequently drops off to fluctuate near its relaxation value. The red dashed line is the long-time average and takes the value $\overline{P}_x \approx 2.105$, an approximately 7% error from its expected value of $I_{\text{CUE}}|_{N=60} \approx 1.968$, shown as a solid cyan line. Although the survival probability has large-amplitude oscillations, the long-time average agrees well with the RMT prediction in Eq. (24). It is not required that we average over any particular basis in order to agree with the prediction in Eq. (24), only that the basis does not introduce any special symmetries to $F_n(t)$.
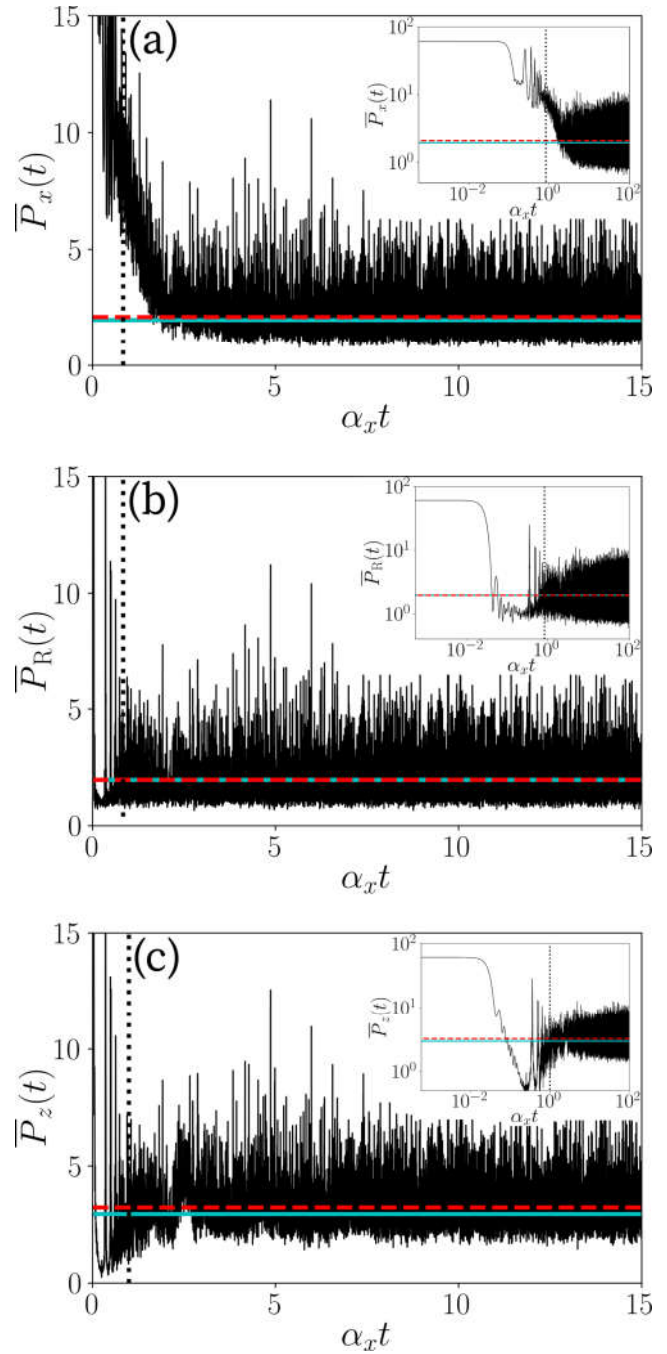

FIG. 5. The survival probability averaged over bases as a function of time. (a) Averaged over the $\hat{S}_x$ basis. The long-time average $\overline{P}_x \approx 2.106$ is shown as a red dashed line, while the predicted $I_{\text{CUE}} \approx 1.968$ is shown as a solid cyan line. (b) Averaged over a randomly selected basis. Here, the long-time average is $\overline{P}_R \approx 1.971$. (c) Averaged over the $\hat{S}_z$ basis. Here, $\overline{P}_z \approx 3.242$ and $I_{\text{COE}} \approx 2.905$ are shown as red dashed lines and cyan solid lines, respectively. Insets are identical, but plotted on a log-log scale, highlighting the transition from regular to chaotic dynamics. The Thouless time t_{Th} is shown in every panel as a vertical dotted line. The parameter values in all images are $k_z = 3\alpha_x$, $\alpha_z = 0.01\alpha_x$, $N = 60$, and $n = 50$.

As a demonstration, Fig. 5(b) shows the survival probability averaged over a randomly generated complex orthonormal

basis (via a QR decomposition of a randomly populated complex matrix), which we denote $\overline{P}_R(t)$. The long-time average in the random basis is $\overline{P}_R \approx 1.969$, and agrees extremely well (within $<0.1\%$) with $I_{\mathrm{CUE}}|_{N=60}$. Finally, Fig. 5(c) shows $P_n(t)$ averaged over the $\hat{S}_z$ basis. The long-time average is $\overline{P}_z \approx 3.229$, again shown as a red dashed line, and has an approximately 11% deviation from $I_{\mathrm{COE}}|_{N=60} \approx 2.905$. In each image, the TTC order is $n = 40$ and the system size is $N = 60$.

Taken together, the plots shown in Fig. 5 (see especially the log-log plots in the insets) indicate that the effective dynamics of the n-fold TTC are regular at short times, then undergo a transition period until approximately t_{Th}, shown in all panels as a vertical dashed line according to Eqs. (26) and (27), after which the survival probability settles down, or at least oscillates about a universal value given by its RMT prediction in the respective ensemble. In general, we expect the agreement between the numerical result and the theoretical predictions given in Eqs. (24) and (25) to improve for higher TTC order n and correspondingly longer time averages.

VI. SUMMARY AND CONCLUSION

In this paper, we have given a proof of concept that conventional signals of chaotic behavior, including level statistics, classical Lyapunov exponents, and RMT predictions, can arise from generalized n-fold TTCs even when starting from a nonchaotic Hamiltonian. This is significant because TTCs, and more specifically OTOCs (the $n = 2$ case), are commonly used as diagnostic tools for what is often called quantum chaos. Higher-order TTCs have been the focus of some previous studies [4–8], including as an improvement of the standard four-point OTOC as a diagnostic of chaos, and so the emergence of signatures of chaos as a result of the form of the TTC is therefore of interest.

In our case we chose a rather simple system consisting of a bosonic Josephson junction coupled dispersively to an AQD or impurity spin. This has the benefit of being integrable and thus all the signals of chaos we find are genuinely in the TTC, not the original dynamics. Importantly, both the parameters α_x and α_z must be nonzero in the system we are considering so that there are noncommuting pieces in the Hamiltonian. In particular, $\alpha_x = 0$ would allow the vanishing of the commutator $[\hat{H}_1, \hat{H}_2] = 0$, resulting in trivial dynamics, while α_z is

necessary to destroy the parity symmetry and thereby allow the eigenstates of $\hat{\mathcal{F}}$ and $\hat{U}_t$ to be modeled by the appropriate ensembles in RMT. However, the simplicity of our system also means that even the effectively shaken n-fold TTC is only weakly chaotic and thus our survival probabilities do not rapidly converge to the RMT values (for our parameters the deviation can be as large as 11%). However, we also saw evidence that the bases of $\hat{S}_x$ and $\hat{S}_z$ remain in some sense special (being the eigenstates of the two pieces of the Hamiltonian), whereas when a truly random basis was chosen we obtained excellent agreement with deviation of less than 0.1%.

There remain signatures of chaos which we have not addressed here. For example, we have not attempted to identify a *quantum* Lyapunov exponent [one typically uses $F_2(t)$ and finds that $F_2(t) \approx a - ce^{\lambda t}$, where c is some constant]. Rather, in Sec. IV we have merely looked directly at the classical Lyapunov exponent obtained from the mean-field equations of motion for the n-fold TTC. Furthermore, for a chaotic system obeying the RMT predictions outlined in this paper, it is expected that there exists a "correlation hole" (a signature of correlations in level statistics) in the survival probability with a minimum at t_{Th} [83,85–88], which proceeds to ramp towards the saturation value. We have not identified a correlation hole in the TTCs studied here, likely because the transition from a regular to chaotic system occurs explicitly in time, so level correlations will not be detectable prior to t_{Th}.

ACKNOWLEDGMENTS

APPENDIX A: TTC CALCULATION

We consider the two-time correlator,

$$F_n(t) = \langle [\hat{A}(t)\hat{B}(0)]^n \rangle, \tag{A1}$$

where $\hat{A}(t) = e^{i\hat{H}t}\hat{A}e^{-i\hat{H}t}$ and assume that $\hat{A}$ and $\hat{B}$ initially commute. Selecting $\hat{A} = \hat{B} = \hat{\sigma}_x$, that is, the hopping operator on the Hilbert space of the quantum dot,

$$
\begin{aligned}
F_n(t) &= \left\langle \left\{ \exp\left[i\left(\frac{k_z}{N+1}\hat{S}_z^2 - \alpha_x \hat{S}_x + \alpha_z \hat{S}_z - \frac{\Delta}{2}(\mathbb{1} + \hat{\sigma}_z) + \beta \hat{S}_x(\mathbb{1} + \hat{\sigma}_z) \right)t \right] \right. \right. \\
&\quad \times \hat{\sigma}_x \exp\left[-i\left(\frac{k_z}{N+1}\hat{S}_z^2 - \alpha_x \hat{S}_x + \alpha_z \hat{S}_z - \frac{\Delta}{2}(\mathbb{1} + \hat{\sigma}_z) + \beta \hat{S}_x(\mathbb{1} + \hat{\sigma}_z) \right)t \right] \hat{\sigma}_x \Big\}^n \right\rangle \tag{A2} \\
&= \left\langle \left\{ \exp\left[i\left(\frac{k_z}{N+1}\hat{S}_z^2 - \alpha_x \hat{S}_x + \alpha_z \hat{S}_z - \frac{\Delta}{2}(\mathbb{1} + \hat{\sigma}_z) + \beta \hat{S}_x(\mathbb{1} + \hat{\sigma}_z) \right)t \right] \right. \right. \\
&\quad \times \exp\left[-i\left(\frac{k_z}{N+1}\hat{S}_z^2 - \alpha_x \hat{S}_x + \alpha_z \hat{S}_z - \frac{\Delta}{2}(\mathbb{1} - \hat{\sigma}_z) + \beta \hat{S}_x(\mathbb{1} - \hat{\sigma}_z) \right)t \right] \Big\}^n \right\rangle, \tag{A3}
\end{aligned}
$$

where we have made use of the fact that for some function of the Pauli spin matrices $f(\hat{\sigma}_x, \hat{\sigma}_y, \hat{\sigma}_z)$, $\hat{\sigma}_x f(\hat{\sigma}_x, \hat{\sigma}_y, \hat{\sigma}_z)\hat{\sigma}_x = f(\hat{\sigma}_x, -\hat{\sigma}_y, -\hat{\sigma}_z)$.

For the expectation value we assume a product state $|\psi\rangle_B \otimes |+\rangle_d$, where $|\psi\rangle_B$ is a general state of the BEC and $|+\rangle_d$ is the excited state of the AQD. The $(\mathbb{1} - \hat{\sigma}_z)$ and $(\mathbb{1} + \hat{\sigma}_z)$ factors in Eq. (A3) act as projectors onto the excited and ground AQD states, respectively. In particular, the operator $(\mathbb{1} - \hat{\sigma}_z)$ appearing in the right-hand exponential acts as twice the identity operator on the ket $|+\rangle_d$ and thus $|+\rangle_d$ passes through this exponential replacing all the $(\mathbb{1} - \hat{\sigma}_z)$ factors by the number 2. Meanwhile, the other exponential contains $(\mathbb{1} + \hat{\sigma}_z)$ which annihilates $|+\rangle_d$ and so expanding out the exponential in a Taylor series we find all the AQD operators vanish and we can resum the exponential with only the boson operators. As a result we find the surprising result that the correlation function becomes completely independent of the AQD and we are left with

$$F_n(t) = \left\langle \left\{ e^{i\left(\frac{k_z}{N+1}\hat{S}_z^2 - \alpha_x \hat{S}_x + \alpha_z \hat{S}_z\right)t} e^{-i\left(\frac{k_z}{N+1}\hat{S}_z^2 - \alpha_x \hat{S}_x + \alpha_z \hat{S}_z - \Delta + 2\beta \hat{S}_x\right)t} \right\}^n \right\rangle_B. \tag{A4}$$

The Δ term results in a global phase which we can choose to set to zero, and we are free to select β as we wish; we choose $\beta = \alpha_x/2$ to remove all $\hat{S}_x$ terms in $\hat{H}_2$ as described in the main text, so that we finally achieve

$$F_n(t) = \left\langle \left\{ \exp\left[i\left(\frac{k_z}{N+1}\hat{S}_z^2 - \alpha_x \hat{S}_x + \alpha_z \hat{S}_z\right)t\right] \right.\right.$$
$$\left.\left. \times \exp\left[-i\left(\frac{k_z}{N+1}\hat{S}_z^2 + \alpha_z \hat{S}_z\right)t\right] \right\}^n \right\rangle_B \tag{A5}$$

$$\equiv \langle \hat{\mathcal{F}}^n \rangle_B = \langle [e^{-i\hat{H}_1 t} e^{-i\hat{H}_2 t}]^n \rangle_B. \tag{A6}$$

APPENDIX B: MEAN-FIELD HAMILTONIAN AND EQUATIONS OF MOTION

In order to write down the mean-field approximation to the quantum Hamiltonians given in Eqs. (3), (9), and (10), we first write the spin operators in terms of their corresponding Schwinger representations,

$$\hat{S}_z = (\hat{b}_L^\dagger \hat{b}_L - \hat{b}_R^\dagger \hat{b}_R)/2, \tag{B1}$$

$$\hat{S}_x = (\hat{b}_R^\dagger \hat{b}_L + \hat{b}_R^\dagger \hat{b}_R)/2, \tag{B2}$$

where $\hat{b}_{L/R}^{(\dagger)}$ annihilates (creates) a boson in the left or right well. The quantum dot operators can be similarly written, using $\hat{d}_{u/d}^{(\dagger)}$:

$$\hat{\sigma}_z = (\hat{d}_u^\dagger \hat{d}_u - \hat{d}_d^\dagger \hat{d}_d)/2. \tag{B3}$$

Next, we assume that in the classical limit $N \to \infty$, we can replace the boson operators by complex numbers $\hat{b}_i \to \sqrt{n_i} e^{i\phi_i}$. We can also make a similar replacement for the dot $\hat{d}_i \to \sqrt{n_i} e^{i\varphi_i}$ (the "mean-field" theory is in fact exact for the dot, since any state on the Bloch sphere is uniquely characterized by two angles), and then defining $n_L = N - n_R$, $\phi = \phi_L - \phi_R$, $z = (n_L - n_R)/N$, and $y = n_u - n_d$ we have the substitution

rules,

$$\hat{S}_x \to \sqrt{n_L n_R} \cos(\phi_L - \phi_R) = \frac{N}{2}\sqrt{1 - z^2} \cos\phi, \tag{B4}$$

$$\hat{S}_z \to \frac{1}{2}(n_L - n_R) = \frac{Nz}{2}, \tag{B5}$$

$$\hat{\sigma}_z \to \frac{1}{2}(n_u - n_d) = \frac{y}{2}. \tag{B6}$$

Hence, the mean-field Hamiltonian $(\mathcal{H} = \lim_{N\to\infty} \hat{H}/N)$ is [also in the main text as Eq. (11)]

$$\mathcal{H} = \frac{k_z}{4}z^2 - \frac{\alpha_x}{2}\sqrt{1 - z^2}\cos\phi + \frac{1}{2}\alpha_z z - \frac{\Delta}{2N}\left(1 + \frac{y}{2}\right)$$
$$+ \frac{\beta}{2}\sqrt{1 - z^2}\cos\phi\left(1 + \frac{y}{2}\right), \tag{B7}$$

where all energies on the right-hand side are measured in terms of α_x. Hamilton's equations give

$$\dot{z} = -\frac{\partial\mathcal{H}}{\partial\phi} = -\frac{\alpha_x}{2}\sqrt{1 - z^2}\sin\phi$$
$$+ \frac{\beta}{2}\sqrt{1 - z^2}\sin\phi\left(1 + \frac{y}{2}\right), \tag{B8}$$

$$\dot{\phi} = \frac{\partial\mathcal{H}}{\partial z} = \frac{k_z}{2}z + \frac{\alpha_z}{2} + \frac{\alpha_x z \cos\phi}{2\sqrt{1 - z^2}}$$
$$- \frac{\beta z \cos\phi}{2\sqrt{1 - z^2}}\left(1 + \frac{y}{2}\right), \tag{B9}$$

$$\dot{y} = -\frac{\partial\mathcal{H}}{\partial\varphi} = 0, \tag{B10}$$

$$\dot{\varphi} = \frac{\partial\mathcal{H}}{\partial y} = \frac{\beta}{4}\sqrt{1 - z^2}\cos\phi - \frac{\Delta}{4N}. \tag{B11}$$

Likewise, the mean-field approximations for $\hat{H}_1$ and $\hat{H}_2$ are [also in the main text as Eqs. (12) and (13), respectively]

$$\mathcal{H}_1 = -\frac{k_z}{4}z^2 + \frac{\alpha_x}{2}\sqrt{1 - z^2}\cos\phi - \frac{\alpha_z}{2}z, \tag{B12}$$

$$\mathcal{H}_2 = \frac{k_z}{4}z^2 + \frac{\alpha_z}{2}z. \tag{B13}$$

The classical trajectories for $\mathcal{H}_1$ and $\mathcal{H}_2$ are similarly calculated using Hamilton's equations; however, the set of conjugate variables $\{y, \varphi\}$ is no longer present:

$$\dot{z}_1 = -\frac{\alpha_x}{2}\sqrt{1 - z^2}\sin\phi, \tag{B14}$$

$$\dot{\phi}_1 = -\frac{k_z z}{2} - \frac{\alpha_z}{2} - \frac{\alpha_x z \cos\phi}{2\sqrt{1 - z^2}}, \tag{B15}$$

$$\dot{z}_2 = 0, \tag{B16}$$

$$\dot{\phi}_2 = \frac{k_z z}{2} + \frac{\alpha_z}{2}. \tag{B17}$$

The dynamics are governed by repeatedly alternating between $\mathcal{H}_1$ and $\mathcal{H}_2$ for a time $\alpha_x T$.

In Fig. 3 of the main text, we show the effects of tuning the time at which the TTC is measured on the Lyapunov exponent for the classical Hamiltonians (B12) and (B13). Alternatively, in Fig. 6, we demonstrate the presence of a positive classical Lyapunov exponent for the system alternating between $\mathcal{H}_1$ and $\mathcal{H}_2$ as a function of the bosonic interaction energy.
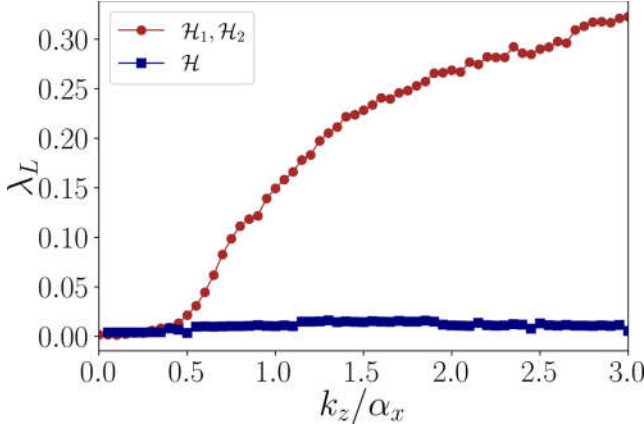
FIG. 6. The Lyapunov exponent, λ_L, as a function of k_z for dynamics produced by the mean-field version of Eq. (3) (blue squares) and the mean-field versions of Eqs. (9) and (10) (red dots). We can see for $\mathcal{H}$, $\lambda_L \approx 0$, suggesting the system is regular while for the combination of $\mathcal{H}_1$ and $\mathcal{H}_2$, $\lambda_L > 0$, suggesting chaotic dynamics. Each data point is the maximum λ_L averaged over 1500 random initial states in phase space. For both sets of data $\alpha_z = 0.01\alpha_x$ and for the red data the dynamics is cycled through $\mathcal{H}_1$ and $\mathcal{H}_2$ $n = 20$ times.

The original Hamiltonian has no appreciable Lyapunov exponent while the shaken system rapidly develops exponential separation of trajectories after $k_z/\alpha_x > 0.5$. The distance d between trajectories $\{z_n, \phi_n\}$ and $\{z_m, \phi_m\}$ in the BEC coordinates corresponds to a great-circle distance on the Bloch sphere,

$$d = \cos^{-1}\left[z_n z_m + \sqrt{\left(1 - z_n^2\right)\left(1 - z_m^2\right)} \cos(\phi_n - \phi_m)\right],$$
(B18)

which can be used to calculate λ_L.

APPENDIX C: INDIVIDUAL SURVIVAL PROBABILITY

In Sec. V B of the main text we concerned ourselves mainly with the general features of the survival probability without specifically selecting states. The qualitative nature of $P_n(t)$ broadly follows $\overline{P}_n(t)$ (the average), although it is more sensitive due to the lack of averaging over initial states. The saturation values when not averaged over the bases are then

$$P^{\text{CUE}} = \frac{2}{\mathcal{D} + 1},$$
(C1)

$$P^{\text{COE}} = \frac{3}{\mathcal{D} + 2}.$$
(C2)

In Fig. 7, we show the survival probability $P_n(t)$ for three different states using $n = 50$ and $N = 200$ at $k_z = 3\alpha_x$ and $\alpha_z = 0.01\alpha_x$. Figure 7(a) shows the survival probability for $|\psi\rangle = |N/2\rangle_x = e^{-i\hat{S}_y\pi/2}|N/2\rangle$, which is the ground state of the $\hat{S}_x$ operator and also a coherent state. Much like the average, the survival probability is roughly constant for short times, then drops off, saturating at approximately 8.521×10^{-3}, which is within 14% of the CUE value of 9.901×10^{-3}. For Fig. 7(b), we chose an initial state which is Gaussian (but
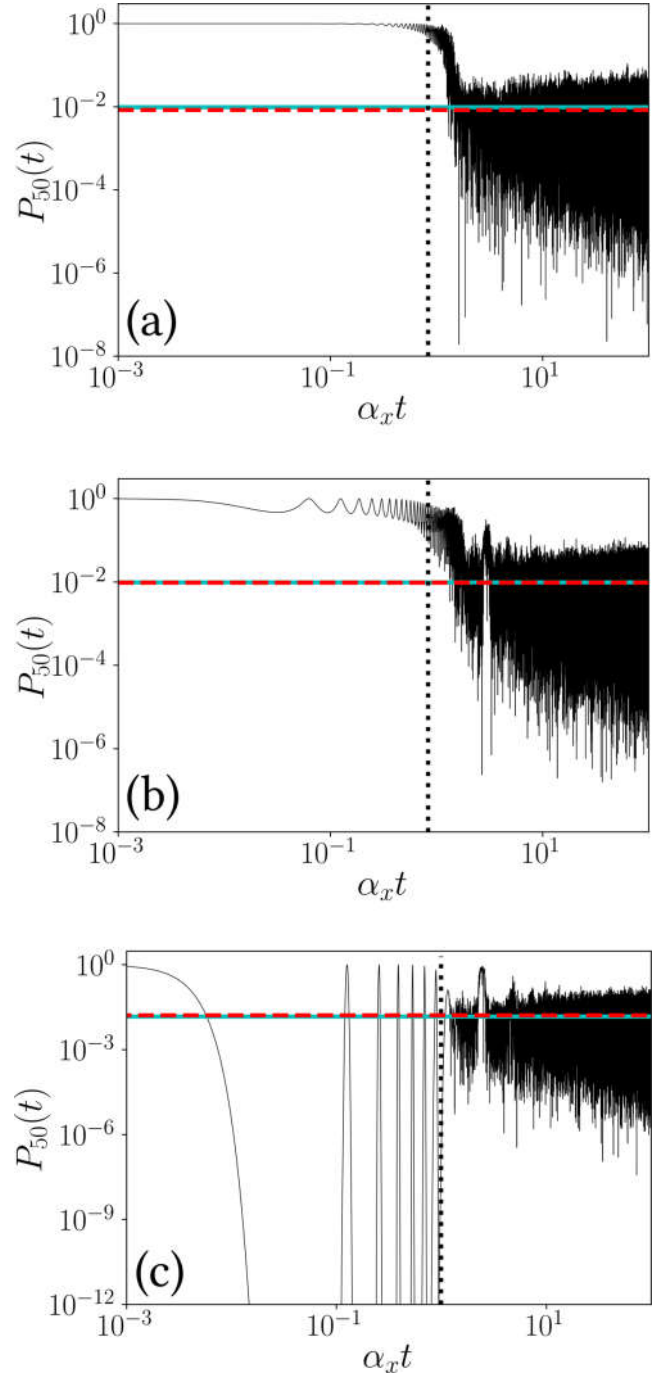

FIG. 7. Survival probability $P_n(t)$ for two different choices of $|\psi\rangle$ (a) using $|\psi\rangle = |N/2\rangle_x = e^{-i\hat{S}_y\pi/2}|N/2\rangle$, (b) using the Gaussian state given in Eq. (C3), and (c) using $|\psi\rangle = |N/2\rangle$. t_{Th} is shown as a vertical dotted line, the long-time average of the data is given as a horizontal solid cyan line, and the corresponding RMT prediction is given by a dashed red line. The parameter values in each image are $k_z = 3\alpha_x$, $\alpha_z = 0.01\alpha_x$, $N = 200$, and $n = 50$.

not a coherent state) in the $\hat{S}_z$ basis,

$$|\psi\rangle = \frac{1}{(2\pi N)^{1/4}} \sum_{m=-N/2}^{N/2} e^{-\frac{m^2}{4N}} |m\rangle.$$
(C3)

This broader state has excellent agreement with the CUE value at approximately 9.757×10^{-3}, within 1.5%. Finally, in Fig. 7(c), we instead choose a member of the $\hat{S}_z$ basis, $|\psi\rangle = |N/2\rangle$. The return probability of this state demonstrates sharp peaks reminiscent of dynamical phase transitions (DPTs) and subsequently saturates at 16.605×10^{-3}, approximately 12% higher than P^{COE}.

Comparing the actual saturation values with those predicted in Eqs. (C1) and (C2), we find that the relative errors can be fairly large, on the order of 10–15 %. However, the errors on individual states can be extremely sensitive to parameter shifts. For example, a change to $k_z = 8\alpha_x$ (deeper into the "chaotic" region, extrapolated from Fig. 6) can reduce the

error from the coherent state $(|\psi\rangle = |N/2\rangle_x)$ to approximately 9.393×10^{-3}, which is 5.1% error from the P^{COE} value.

The return probability can occasionally reach extremely small orders of magnitude, especially for larger N, at which machine-precision exact diagonalization becomes insufficient to properly resolve $P_n(t)$. This effect occurs in the regular regions prior to t_{Th} in Fig. 7(c), where DPT-like sharp valleys can only be resolved with precision on the order of 80 decimal places (increasing with N). The extreme sensitivity of numerical noise in the Loschmidt echo in similar systems has been identified in Ref. [89]. The region which requires high sensitivity to properly resolve the dynamics is, however, not our primary concern since it is not the chaotic region.

[1] P. M. Chaiken and T. C. Lubensky, *Principles of Condensed Matter Physics* (Cambridge University Press, New York, 1995).

[2] A. J. Leggett, Realism and the physical world, Rep. Prog. Phys. **71**, 022001 (2008).

[3] C. Emary, N. Lambert, and F. Noric, Leggett-Garg inequalities, Rep. Prog. Phys. **77**, 016001 (2014).

[4] A. Bhattacharyya, W. Chemissany, S. Shajidul Haque, B. Yan, Towards the web of quantum chaos diagnostics, arXiv:1909.01894.

[5] F. M. Haehl, R. Loganayagam, P. Narayan and M. Rangamani, Classification of out-of-time-order correlators, SciPost Phys. **6**, 001 (2019).

[6] N. Y. Halpern, B. Swingle, and J. Dressel, Quasiprobability behind the out-of-time-ordered correlator, Phys. Rev. A **97**, 042105 (2018).

[7] S. H. Shenker and D. Stanford, Multiple shocks, J. High Energy Phys. 12 (2014) 046.

[8] D. A. Roberts and B. Yoshida, Chaos and complexity by design, J. High Energy Phys. 04 (2017) 121.

[9] P. Zanardi and N. Paunkovic, Ground state overlap and quantum phase transitions, Phys. Rev. E **74**, 031123 (2006).

[10] S. Chen, L. Wang, S. J. Gu, and Y. Wang, Fidelity and quantum phase transition for the Heisenberg chain with next-nearest-neighbor interaction, Phys. Rev. E **76**, 061108 (2007).

[11] P. Buonsante and A. Vezzani, Ground-State Fidelity and Bipartite Entanglement in the Bose-Hubbard Model, Phys. Rev. Lett. **98**, 110601 (2007).

[12] H. T. Quan, Z. Song, X. F. Liu, P. Zanardi, and C. P. Sun, Decay of Loschmidt Echo Enhanced by Quantum Criticality, Phys. Rev. Lett. **96**, 140604 (2006).

[13] W. Q. Ning, S. J. Gu, Y. G. Chen, C. Q. Wu, and H. Q. Lin, Concurrence and fidelity of a Bose-Fermi mixture in a one-dimensional optical lattice, J. Phys.: Condens. Matter **20**, 235236 (2008).

[14] M. Heyl, F. Pollman, and B. Dora, Detecting Equilibrium and Dynamical Quantum Phase Transitions in Ising Chains via Out-of-Time-Ordered Correlators, Phys. Rev. Lett. **121**, 016801 (2018).

[15] Z.-H. Sun, J.-Q. Cai, Q.-C. Tang, Y. Hu, and H. Fan, Out-of-time-order correlators and quantum phase transitions in the rabi and dicke models, Ann. Phys. (Berlin) **532**, 1900270 (2019).

[16] J. Mumford, W. Kirkby, and D. H. J. O'Dell, Measuring out-of-time-ordered correlation functions with a single impurity qubit

in a bosonic Josephson junction, J. Phys. B: At. Mol. Opt. Phys. **53**, 145301 (2020).

[17] N. Y. Yao, F. Grusdt, B. Swingle, M. D. Lukin, D. M. Stamper-Kurn, J. E. Moore, and E. A. Demler, Interferometric approach to probing fast scrambling, arXiv:1607.01801.

[18] B. Swingle, G. Bentsen, M. Schleier-Smith, and P. Hayden, Measuring the scrambling of quantum information, Phys. Rev. A **94**, 040302(R) (2016).

[19] A. Bohrdt, C. B. Mendl, M. Endres, and M. Knap, Scrambling and thermalization in a diffusive quantum many-body system, New J. Phys. **19**, 063001 (2017).

[20] J. Maldacena and D. Stanford, Remarks on the Sachdev-Ye-Kitaev model, Phys. Rev. D **94**, 106002 (2016).

[21] H. Shen, P. Zhang, R. Fan, and H. Zhai, Out-of-time-order correlation at a quantum phase transition, Phys. Rev. B **96**, 054503 (2017).

[22] C.-J. Lin and O. I. Motrunich, Out-of-time-ordered correlators in a quantum Ising chain, Phys. Rev. B **97**, 144304 (2018).

[23] B. Dóra and R. Moessner, Out-of-Time-Ordered Density Correlators in Luttinger Liquids, Phys. Rev. Lett. **119**, 026802 (2017).

[24] D. A. Roberts and D. Stanford, Diagnosing Chaos Using Four-Point Functions in Two-Dimensional Conformal Field Theory, Phys. Rev. Lett. **115**, 131603 (2015).

[25] J. Maldacena, S. H. Shenker, and D. Stanford, A bound on chaos, J. High Energy Phys. 08 (2016) 106.

[26] G. Zhu, M. Hafezi, and T. Grover, Measurement of many-body chaos using a quantum clock, Phys. Rev. A **94**, 062329 (2016).

[27] I. Kukuljan, S. Grozdanov, and T. Prosen, Weak quantum chaos, Phys. Rev. B **96**, 060301(R) (2017).

[28] E. B. Rozenbaum, S. Ganeshan, and V. Galitski, Lyapunov Exponent and Out-of-Time-Ordered Correlator's Growth Rate in a Chaotic System, Phys. Rev. Lett. **118**, 086801 (2017).

[29] J. S. Cotler, D. Ding, G. R. Penington, Out-of-order operators and the butterfly effect, Ann. Phys. **396**, 318 (2018).

[30] E. B. Rozenbaum, S. Ganeshan, and V. Galistski, Universal level statistics of the out-of-time-ordered operator, Phys. Rev. B **100**, 035112 (2019).

[31] J. Kurchan, Quantum bound to chaos and the semiclassical limit, J. Stat. Phys. **171**, 965 (2018).

[32] X. Chen and T. Zhou, Operator scrambling and quantum chaos, arXiv:1804.08655.

[33] I. García Mata, M. Saraceno, R. A. Jalabert, A. J. Roncaglia, and D. A. Wisniacki, Chaos Signatures in the Short and Long

Time Behavior of the Out-of-Time Ordered Correlator, Phys. Rev. Lett. **121**, 210601 (2018).

[34] R. A. Jalabert, I. García-Mata, and D. A. Wisniacki, Semiclassical theory of out-of-order correlators for low-dimensional classically chaotic systems, Phys. Rev. E **98**, 062218 (2018).

[35] R. Hamazaki, K. Fujimoto, and M. Ueda, Operator noncommutativity and irreversibility in quantum chaos, arXiv:1807.02360.

[36] E. J. Torres-Herrera, A. M. García-García, and L. F. Santos, Generic dynamical features of quenched interacting quantum systems: Survival probability, density imbalance, and out-of-time-ordered correlator, Phys. Rev. B **97**, 060303(R) (2018).

[37] J. Chávez-Carlos, B. López-del-Carpio, M. A. Bastarrachea-Magnani, P. Stránský, S. Lerma-Hernández, L. F. Santos, and J. G. Hirsch, Quantum and Classical Lyapunov Exponents in Atom-Field Interaction Systems, Phys. Rev. Lett. **122**, 024101 (2019).

[38] K. Hashimoto, K. Murata, and R. Yoshii, Out-of-time-order correlators in quantum mechanics, J. High Energy Phys. 10 (2017) 138.

[39] S. Sinha, S. Ray, and S. Sinha, Fingerprint of chaos and quantum scars in kicked Dicke model: An out-of-time-order correlator study, J. Phys.: Condens. Matter **33**, 174005 (2021).

[40] S. Pappalardi, A. Russomanno, B. Žunkovic, F. Iemini, A. Silva, and R. Fazio, Scrambling and entanglement spreading in long-range spin chains, Phys. Rev. B **98**, 134303 (2018).

[41] Q. Hummel, B. Geiger, J. D. Urbina, and K. Richter, Reversible Quantum Information Spreading in Many-Body Systems near Criticality, Phys. Rev. Lett. **123**, 160401 (2019).

[42] K. Hashimoto, K.-B. Huh, K.-Y. Kim, and R. Watanabe, Exponential growth of out-of-time-order correlator without chaos: Inverted harmonic oscillator, J. High Energy Phys. 11 (2020) 68.

[43] S. Pilatowsky-Cameo, J. Chávez-Carlos, M. A. Bastarrachea-Magnani, P. Stránský, S. Lerma-Hernández, L. F. Santos, and J. G. Hirsch, Positive quantum Lyapunov exponents in experimental systems with a regular classical limit, Phys. Rev. E **101**, 010202(R) (2020).

[44] T. Xu, T. Scaffidi, and X. Cao, Does Scrambling Equal Chaos? Phys. Rev. Lett. **124**, 140602 (2020).

[45] E. P. Wigner, On the statistical distribution of the widths and spacings of nuclear resonance levels, Proc. Cambridge Philos. Soc. **47**, 790 (1951).

[46] O. Bohigas, R. U. Haq, and A. Pandey, Fluctuation properties of nuclear energy levels and widths: Comparison of theory with experiment, in *Nuclear Data for Science and Technology* (Reidel, Dordrecht, Netherlands, 1983), pp. 809–813.

[47] O. Bohigas, M. J. Giannoni, and C. Schmit, Characterization of Chaotic Quantum Spectra and Universality of Level Fluctuation Laws, Phys. Rev. Lett. **52**, 1 (1984).

[48] I. Bausmerth, U. R. Fisher, and A. Posazhennikova, Quantum top inside a Bose-Einstein-condensate Josephson junction, Phys. Rev. A **75**, 053605 (2007).

[49] M. Rinck and C. Bruder, Effects of a single fermion in a Bose Josephson junction, Phys. Rev. A **83**, 023608 (2011).

[50] F. Mulansky, J. Mumford, and D. H. J. O'Dell, Impurity in a Bose-Einstein condensate in a double well, Phys. Rev. A **84**, 063602 (2011).

[51] R. Gerritsma, A. Negretti, H. Doerk, Z. Idziaszek, T. Calarco, and F. Schmidt-Kaler, Bosonic Josephson Junction Controlled by a Single Trapped Ion, Phys. Rev. Lett. **109**, 080402 (2012).

[52] J. Mumford, J. Larson, and D. H. J. O'Dell, Impurity in a bosonic Josephson junction: Swallowtail loops, chaos, self-trapping, and Dicke model, Phys. Rev. A **89**, 023620 (2014).

[53] J. Mumford and D. H. J. O'Dell, Critical exponents for an impurity in a bosonic Josephson junction: Position measurement as a phase transition, Phys. Rev. A **90**, 063617 (2014).

[54] J. Joger, A. Negretti, and R. Gerritsma, Quantum dynamics of an atomic double-well system interacting with a trapped ion, Phys. Rev. A **89**, 063621 (2014).

[55] M. R. Ebgha, S. Saeidian, P. Schmelcher, and A. Negretti, Compound atom-ion Josephson junction: Effects of finite temperature and ion motion, Phys. Rev. A **100**, 033616 (2019).

[56] J. Chen, K. Keiler, G. Xianlong, and P. Schmelcher, Impurity-induced quantum chaos for an ultracold bosonic ensemble in a double well, Phys. Rev. A **104**, 033315 (2021).

[57] J. Links, A. Foerster, A. P. Tonel, and G. Santos, The two-site Bose-Hubbard model, Ann. Henri Poincaré **7**, 1591 (2006).

[58] M. T. Batchelor and A Foerster, Yang-Baxter integrable models in experiments: From condensed matter to ultracold atoms, J. Phys. A: Math. Theor. **49**, 173001 (2016).

[59] M. Albiez, R. Gati, J. Fölling, S. Hunsmann, M. Cristiani, and M. K. Oberthaler, Direct Observation of Tunneling and Nonlinear Self-Trapping in a Single Bosonic Josephson Junction, Phys. Rev. Lett. **95**, 010402 (2005).

[60] S. Levy, E. Lahoud, I. Shomroni, and J. Steinhauer, The a.c. and d.c. Josephson effects in a Bose-Einstein condensate, Nature (London) **449**, 579 (2007).

[61] L. J. LeBlanc, A. Bardon, J. McKeever, M. Extavour, D. Jervis, J. Thywissen, F. Piazza, and A. Smerzi, Dynamics of a Tunable Superfluid Junction, Phys. Rev. Lett. **106**, 025302 (2011).

[62] A. Trenkwalder, G. Spagnolli, G. Semeghini, S. Coop, M. Landini, P. Castilho, L. Pezzè, G. Modugno, M. Inguscio, A. Smerzi, and M. Fattori, Quantum phase transitions with parity-symmetry breaking and hysteresis, Nat. Phys. **12**, 826 (2016).

[63] T. Zibold, E. Nicklas, C. Gross, and M. K. Oberthaler, Classical Bifurcation at the Transition from Rabi to Josephson Dynamics, Phys. Rev. Lett. **105**, 204101 (2010).

[64] C. S. Gerving, T. M. Hoang, B. J. Land, M. Anquez, C. D. Hamley, and M. S. Chapman, Non-equilibrium dynamics of an unstable quantum pendulum explored in a spin-1 Bose-Einstein condensate, Nat. Commun. **3**, 1169 (2012).

[65] C. Zipkes, S. Palzer, C. Sias, and M. Köhl, A trapped single ion inside a Bose-Einstein condensate, Nature (London) **464**, 388 (2010).

[66] T. Dieterle, M. Berngruber, C. Hölzl, R. Löw, K. Jachymski, T. Pfau, and F. Meinert, Transport of a Single Cold Ion Immersed in a Bose-Einstein Condensate, Phys. Rev. Lett. **126**, 033401 (2021).

[67] T. Dieterle, M. Berngruber, C. Hölzl, R. Löw, K. Jachymski, T. Pfau, and F. Meinert, Inelastic collision dynamics of a single cold ion immersed in a Bose-Einstein condensate, Phys. Rev. A **102**, 041301(R) (2020).

[68] E. Astrakharchik, L. A. P. Ardila, R. Schmidt, K. Jachymski, and A. Negretti, Ionic polaron in a Bose-Einstein condensate, Commun. Phys. **4**, 94 (2021).

[69] J. G. Bohnet, B. C. Sawyer, J. W. Britton, M. L. Wall, A. M. Rey, M. Foss-Feig, and J. J. Bollinger, Quantum spin dynamics and entanglement generation with hundreds of trapped ions, Science **352**, 1297 (2016).

[70] Y. Zhu, Q. Sun, and T. Lin, Andreev bound states and the π-junction transition in a superconductor/quantum-dot/superconductor system, J. Phys.: Condens. Matter **13**, 8783 (2001).

[71] S. De Franceschi, L. Kouwenhoven, C. Schönenberger, and W. Wernsdorfer, Hybrid superconductor-quantum dot devices, Nat. Nanotechnol. **5**, 703 (2010).

[72] S. Pal and C. Benjamin, Tuning the 0-π Josephson junction with a magnetic impurity: Role of tunnel contacts, exchange coupling, e-e interactions and high-spin states, Sci. Rep. **8**, 5208 (2018).

[73] F. Schmidt, D. Mayer, Q. Bouton, D. Adam, T. Lausch, N. Spethmann, and A. Widera, Quantum Spin Dynamics of Individual Neutral Impurities Coupled to a Bose-Einstein Condensate, Phys. Rev. Lett. **121**, 130403 (2018).

[74] Q. Bouton, J. Nettersheim, D. Adam, F. Schmidt, D. Mayer, T. Lausch, e. Tiemann, and A. Widera, Single-Atom Quantum Probes for Ultracold Gases Boosted by Nonequilibrium Spin Dynamics, Phys. Rev. X **10**, 011018 (2020).

[75] D. Adam, Q. Bouton, J. Nettersheim, S. Burgardt, and A. Widera, Coherent and dephasing spectroscopy for single-impurity probing of an ultracold bath, arXiv:2105.03331.

[76] W. Muessel, H. Strobel, D. Linnemann, T. Zibold, B. Juliá-Díaz, and M. K. Oberthaler, Twist-and-turn spin squeezing in Bose-Einstein condensates, Phys. Rev. A **92**, 023603 (2015).

[77] H. Perrin, Ultra cold atoms and Bose-Einstein condensation for quantum metrology, Eur. Phys. J. Spec. Top. **172**, 37 (2009).

[78] M. Pinkas, Z. Meir, T. Sikorsky, R. Ben-Shlomi, N. Akerman, and R. Ozeri, Effect of ion-trap parameters on energy distributions of ultra-cold atom-ion mixtures, New J. Phys. **22**, 013047 (2020).

[79] P. W. Hess, P. Becker, H. B. Kaplan, A. Kyprianidis, A. C. Lee, B. Neyenhuis, G. Pagano, P. Richerme, C. Senko, J. Smith, W. L. Tan, J. Zhang, and C. Monroe, Nonthermalization in trapped atomic ion spin chains, Philos. Trans. R. Soc. A **375**, 20170107 (2017).

[80] L. M. Sieberer, T. Alsacher, A. Elben, M. Heyl, P. Hauke, F. Haake, and P. Zoller, Digital quantum simulation, Trotter errors, and quantum chaos of the kicked top, npj Quantum Inf. **5**, 78 (2019).

[81] A. Smerzi, S. Fantoni, S. Giovanazzi, and S. R. Shenoy, Quantum Coherent Atomic Tunneling between Two Trapped Bose-Einstein Condensates, Phys. Rev. Lett. **79**, 4950 (1997).

[82] V. Oganesyan and D. A. Huse, Localization of interacting fermions at high temperature, Phys. Rev. B **75**, 155111 (2007).

[83] M. Schiulaz, E. J. Torres-Herrera, and L. F. Santos, Thouless and relaxation time scales in many-body quantum systems, Phys. Rev. B **99**, 174313 (2019).

[84] P. Sierant, D. Delande, and J. Zakrzewski, Thouless Time Analysis of Anderson and Many-Body Localization Transitions, Phys. Rev. Lett. **124**, 186601 (2020).

[85] P. Pechukas, Remarks on "quantum chaos", J. Phys. Chem. **88**, 4823 (1984).

[86] L. Leviandier, M. Lombardi, R. Jost, and J. P. Pique, Fourier Transform: A Tool to Measure Statistical Level Properties in Very Complex Spectra, Phys. Rev. Lett. **56**, 2449 (1986).

[87] Y. Alhassid and R. D. Levine, Spectral autocorrelation function in the statistical theory of energy levels, Phys. Rev. A **46**, 4650 (1992).

[88] E. J. Torres-Herrera and L. F. Santos, Signatures of chaos and thermalization in the dynamics of many-body quantum systems, Eur. Phys. J. Spec. Top. **227**, 1897 (2019).

[89] I. Homrighausen, N. O. Abeling, V. Zauner-Stauber, and J. C. Halimeh, Anomalous dynamical phase in quantum spin chains with long-range interactions, Phys. Rev. B **96**, 104436 (2017).

CAUSTICS IN MANY-BODY QUANTUM DYNAMICS

This paper consists of a large-scale program seeking to unify the dynamics of nonequilibrium systems using the mathematics of catastrophe theory. We begin with an introduction to caustics appearing in optical systems, and proceed to review the formation of fold and cusp catastrophes in (1+1)-dimensional Fock space plus time for the two-mode Bose-Hubbard model. Next, we extend the available parameter space, and hence potential caustic dimension, by considering the three-mode Bose-Hubbard model, giving a (2+1)-dimensional Fock space plus time. In the higher-dimensional space, the set available caustics is greatly increased. We first identify the presence of hyperbolic and elliptic umbilic caustics following a quench.

Next, we perform analytics on a simplified 'kicked' system in order to gain some insight into catastrophe organization. The result is a diffraction integral which shows that caustics in this model are organized by an eight-dimensional corank-2 catastrophe known as X_9. This catastrophe lies beyond Thom's original elementary list, and is the first to have a geometric parameter called a 'modulus'. We compare this integral form of the wavefunction against both classical trajectories and the fully second-quantized dynamics. By tuning parameters in the three-mode model, we demonstrate how special (hyperbolic and circular) unfoldings of X_9 appear in the dynamics according

to different geometries of the Bose-Hubbard chain. The stability of the caustics is also investigated by perturbing the kicked model. Finally, we show that at long times, chaos in the three-mode model apparently destroys any visible signs of caustics.

Caustics in quantum many-body dynamics

W. Kirkby, Y. Yee, K. Shi, and D. H. J. O'Dell

Department of Physics and Astronomy, McMaster University,
1280 Main St. W., Hamilton, Ontario, Canada, L8S 4M1
(Dated: February 9, 2022)

We describe a new class of nonequilibrium quantum many-body phenomena in the form of networks of caustics that dominate the many-body wavefunction in the semiclassical regime following a sudden quench. It includes the light cone-like propagation of correlations as a particular case. Caustics are singularities formed by the birth and death of waves and form a hierarchy of universal patterns whose natural mathematical description is via catastrophe theory. Examples in classical waves range from rainbows and gravitational lensing in optics to tidal bores and rogue waves in hydrodynamics. Quantum many-body caustics are discretized by second-quantization ("quantum catastrophes") and live in Fock space which can potentially have many dimensions. We illustrate these ideas using the Bose Hubbard dimer and trimer models which are simple enough that the caustic structure can be elucidated from first principles and yet run the full range from integrable to nonintegrable dynamics. The dimer gives rise to discretized versions of fold and cusp catastrophes whereas the trimer allows for higher catastrophes including the codimension-3 hyperbolic and elliptic umbilics which are organized by, and projections of, an 8-dimensional corank-2 catastrophe known as X_9. These results describe a hitherto unrecognized form of universality in quantum dynamics organized by singularities that manifest as strong fluctuations in mode population probabilities.

I. INTRODUCTION

Despite playing a fundamental role in many-body dynamics, the first observations of light cone-like spreading of correlations were only made recently using ultracold atomic gases in optical lattices [1–3] and trapped ions [4, 5]. These systems offer long relaxation times, the ability to vary external potentials and interparticle interactions, and spatially resolved imaging at the level of single sites/ions. The experiments proceed by creating a highly nonequilibrium state through a sudden quench, e.g. by rapidly changing the lattice depth, and then monitoring the time evolution of site occupations. This success has been followed-up with observations of the many-body localization transition [6–9] to a non-thermalizing dynamical phase of matter [10, 11] related to localization in Fock space [12]. Another highly controllable system which allows individual site addressing and imaging is provided by arrays of Rydberg atoms; starting from high-energy states experiments have revealed the surprising existence of long-lived periodic revivals [13–15], dubbed 'quantum many-body scars' [16–21]. These discoveries have foundational implications for our understanding of how isolated quantum systems reach thermal equilibrium [22–25] and whether nonequilibrium dynamics can display universality akin to that seen at equilibrium phase transitions [26–30]. There are also technological implications because quantum information processors are themselves out-of-equilibrium many-particle systems [31].

In this paper we introduce the idea of quantum many-body caustics. Like the above-mentioned phenomena, caustics occur in out-of-equilibrium quantum many-body wavefunctions but unlike scars, which arise from individual eigenstates, these come from the interference of multiple eigenstates. Caustics are the result of wave bifurcations, which are violent events where waves are born or die. This results in a locally large amplitude that diverges in the classical (mean-field) limit and caustics can thus dominate wavefields. Remarkably, certain shapes of caustic are *structurally stable* against perturbations and hence occur generically. These form a hierarchy described by catastrophe theory [32–34]. They also obey scaling laws in which each member of the hierarchy has its own set of scaling exponents comprised of Arnold and Berry indices [35]. This universality, like that in equilibrium phase transitions, ultimately derives from the presence of singularities. In previous work we have considered caustics in integrable systems such as the Bose-Hubbard (BH) dimer (bosonic Josephson junction) [36–38] and the transverse field Ising model with infinite-range [39] and short-range [40] interactions, respectively. In particular, the latter paper showed that light-cone wave fronts on a spin chain are in fact caustics arising from the coalescence of two waves (fold catastrophe). This allowed us to predict new properties of cones including a nontrivial scaling with respect to the spin coupling strength and the existence of a hierarchy of new structures such as double cones when the spin-spin coupling symmetry is broken, e.g. in the anisotropic XY model where three waves coalesce (cusp catastrophe).

The present work has two goals: firstly to explore higher catastrophes beyond the fold and cusp in Fock space, and secondly to see if caustics occur in nonintegrable systems and hence are a generic feature of many-body wavefunctions. For this purpose we choose the BH trimer which is simple enough to permit exact numerical solutions for moderate particle numbers, and even analytic calculations in the case of a δ-kicked Hamiltonian, such that the caustics can be easily identified, and yet is nonintegrable (classically chaotic) with direct connections to current experiments in optical lattices and spin-1 Bose-Einstein condensates (BECs) [41]. The power of the

catastrophe theory approach, which derives from its origins in topology, lies in its ability to make robust qualitative predictions for the hierarchy of allowed caustics and their morphologies. In this paper we verify these mathematically rigorous predictions with detailed numerical and analytical calculations.

Some images of caustics are shown in Fig. 1. They were made by shining laser pointers through water droplets and photographing the resulting pattern on a screen. These striking morphologies occur without special tuning: they are structurally stable and hence occur in 'typical' or generic situations [42, 43]. For example, an isolated point focus arising from a perfect lens is not structurally stable in two or more dimensions and instead evolves into an extended caustic in the presence of aberrations. Note that higher catastrophes contain the lower ones. Indeed, the structurally stable catastrophe in 2D is the cusp and in both panels (a) and (b) we can see, respectively, one and three cusp shapes embedded in these slices through what are actually patterns in 3D space. The wave catastrophe dressing the cusp is known as the Pearcey function [44], and is defined through a so-called 'diffraction integral' (which can be viewed as an elementary form of path integral, see Eq. 18) [45]. The threefold forked pattern panel (c) of Fig. 1 corresponds to a section of the elliptic umbilic catastrophe which can be described by a pair of separable Airy functions [42]. Zooming out to larger scales the fringes bunch up so that the caustics appear as singular intersecting lines with diverging intensity, but at the wavelength scale we see that they are softened by interference. At the finest scales (not shown) the interference pattern contains a network of vortices [35] that we predict are also present in light cones and many-body caustics more generally.

Everyday optical examples of caustics include rainbows, bright lines on the bottom of swimming pools, and twinkling starlight [46]. Less everyday examples include Cherenkov radiation [47, 48] and gravitational lensing [49]. As understood by Kelvin [50], caustics appear in hydrodynamics as ship wakes, tsunamis [51, 52], and tidal bores [53], and have been identified as one of the causes of freak waves and extreme events [54–58]. This has inspired recent studies comparing freak waves in linear and nonlinear optical systems [59–67]. Cosmology is another field where caustics appear because smooth distributions of matter evolving under gravity will generically develop caustics (singularities in the density distribution) and this has been proposed as an explanation for the large scale structure of the universe [68, 69].

Caustics also occur in quantum waves. Historically, rainbows have been studied in nuclear scattering [70], and more recently have been observed in electron microscopy [71], atom optics [72–75], and in the experiment described in reference [76] a cusp caustic was recorded in the time-dependent atom density distribution of a dilute BEC moving in a 1D optical lattice. In these examples the matter waves are adequately described by the single-particle Schrödinger wave equation, but caustics are not
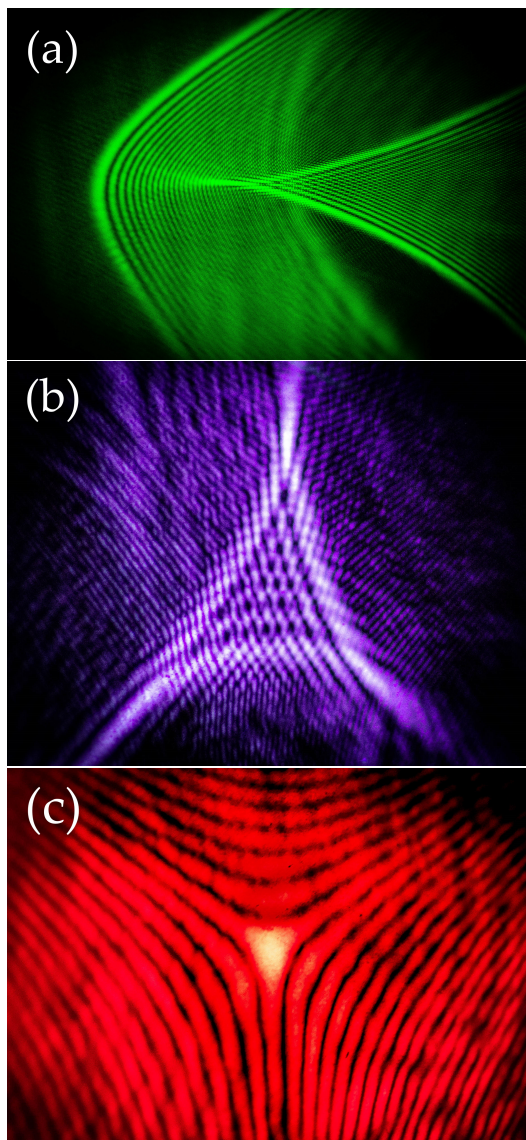

FIG. 1. Real optical caustics made by shining a laser pointer through a water droplet of radius ∼ 1mm and photographed on a screen at a distance of several meters. The droplet has a triangular perimeter imposed by placing it in a triangle cut out of tape stuck on a microscope slide. This mimics the triangular Fock space found in the BH trimer model and leads to the same families of caustics. **Panel (a):** Hyperbolic umbilic, **Panel (b):** Elliptic umbilic, **Panel (c):** Elliptic umbilic near its most singular point. What we see in these photos are slices through three dimensional catastrophes that also contain lower catastrophes: the hyperbolic umbilic contains a single cusp (which is the only structurally stable catastrophe in 2D and is dressed by the Pearcey function wave catastrophe) and the elliptic umbilic contains three cusps. Taking a 1D slice across a cusp gives the simplest catastrophe of all, the fold catastrophe (whose wave pattern is the Airy function), and in fact folds and cusps are the basic elements in 'light cones' in Ising and XY models, see Fig. 2 in reference [40]. These images and the methods used to make them were inspired by the experiments reported in reference [42]. The different colors arise from using three different color lasers.

limited to this scenario and also arise in solutions of the Gross-Pitaevskii equation (nonlinear Schrödinger equation) which can equally describe self-interacting BECs [77] and nonlinear optics in a fibre [59]. Nevertheless, these cases still correspond mathematically to the "classical" wave scenario, i.e. an actual or effective single-particle wave, whether linear or nonlinear. The many-body caustics we study in this paper are a new kind of object: they live in Fock space which is fundamentally discrete. This second quantization is crucial for regulating the singularities present in the classical (mean-field) limit [36], and thus they are in the same spirit as quantized phase singularities in quantum optics [78, 79].

The BH dimer and trimer models we focus on here give rise to dynamical caustics that live in (1+1)- and (2+1)-dimensional spaces: 1- and 2-dimensional Fock space plus time, respectively (assuming total number conservation). Catastrophe theory predicts, and we shall indeed find, that the dimer displays discretized fold and cusp catastrophes which are the simplest two in Thom's hierarchy, while the trimer hosts the codimension-3 catastrophes: the hyperbolic elliptic and umbilic catastrophes. Our results are the first steps in elaborating the hierarchy of many-body caustics and, by fully incorporating quantum fluctuations, they go beyond previous applications of catastrophe theory to many particle systems such as equilibrium thermodynamic [80, 81] and quantum [82–85] phase transitions in the Lipkin-Meshkov-Glick and Dicke models, which were limited to mean-field theory.

The plan for the rest of this paper is as follows: in Section II we present the BH dimer and trimer models and in Section III explain the relevant parts of catastrophe theory, including the associated interference patterns. In Sections IV and V we present a gallery of images of caustics in the dimer and trimer found using exact numerical solutions of the quantum equations of motion. However, although we can numerically compute the wavefunction for $N \sim 150$ particles, we are unable to obtain analytic mappings onto the canonical catastrophe wavefunctions for the trimer because it is non-integrable. In order to provide some analytic examples, in Section VI we instead study δ-kicked dynamics where the interactions are flashed on and off such that the mapping can be achieved analytically (interactions can be engineered in cold atom experiments using Feshbach resonances, see e.g. [86]). In Section VII we go beyond the quantum phase model (rigid pendulum model), which assumes all three modes are significantly occupied, and find corrections that break circular symmetry in Fock space in favor of triangular symmetry and identify the particular sub-family of the X_9 catastrophe at work. In order to do this we introduce a path integral representation for the wavefunction. In Section VIII we compare repulsive and attractive interactions and discuss the crucial role interactions play in the formation of caustics in BH dynamics. Finally, in Section IX we give our conclusions. There are also three appendices which contain details of some of the calculations, including a derivation of the path integral.

As the caustics described in this paper live in Fock space, their main experimental signature would be singularity dominated fluctuations in mode populations, e.g. populations of sites in an optical lattice or populations of spin states in a spinor gas. Experimental considerations are discussed mainly in Sections II and IX.

II. TWO- AND THREE-MODE BOSE-HUBBARD MODELS: EXPERIMENT AND THEORY

We choose the BH model to illustrate the basic ideas of many-body caustics because it is a key model in statistical physics [87, 88] that describes interacting bosons hopping on a lattice, and has been realized in celebrated experiments using ultracold atoms [89, 90]. Due to the ability of these experiments to create sudden quenches, the dynamical states of the BH model have received ongoing theoretical [24, 91–105] and experimental [1, 2, 106–113] attention including: studies of the timescales for many-body quantum revivals and the establishment of coherence, light-cone-like propagation of correlations, effective Hamiltonians in periodically driven "Floquet" systems, and relaxation to equilibrium, to name just a few. The BH dimer and trimer models are particular cases that consider two and three lattice sites (modes), respectively. The dimer describes bosonic Josephson junctions [114–121] that have been realized experimentally with BECs trapped in double-well potentials [122–127], and also with spinor BECs exhibiting the internal version of the Josephson effect [128]. Additionally, the same Hamiltonian describes trapped ions with two internal states and long-range interactions [4, 5, 129, 130].

The BH trimer model describes BECs in triple-well potentials as well as spin-1 BECs [131–133] where the atoms share a common external state (as in a tight trap). Spin-1 BECs have been realized in experiments on ^{23}Na [41, 134–136] and ^{87}Rb [137–142] where the three internal states are provided by the Zeeman sublevels of the F=1 hyperfine manifold. Due to conservation of the angular momentum during collisions, these models do not naturally realize the full trimer model, but this can enforced by applying an integrability breaking RF field that drives transitions between the $|m\rangle$ and $|m \pm 1\rangle$ states [41, 143]. Like the dimer, these systems can display macroscopic quantum self-trapping [144–146]. However, unlike the dimer the trimer is nonintegrable and its classical dynamics exhibits chaos [143, 144, 147–151, 222] giving behaviour qualitatively closer to the many-site model. The trimer also accomodates next-to-nearest-neighbor interactions which are important when the atoms have dipole-dipole interactions [152–155].

A. Two-Mode Equations of Motion

We first consider the BH dimer, which will form up to (1+1)-dimensional caustics in the dynamics [36, 37]. The Hamiltonian is [156, 157]

$$\hat{H}^{\text{dimer}} = -J\left(\hat{a}_l^\dagger\hat{a}_r + \hat{a}_r^\dagger\hat{a}_l\right) + U\left(\hat{a}_l^\dagger\hat{a}_l - \hat{a}_r^\dagger\hat{a}_r\right)^2 , \quad (1)$$

where $\hat{a}_{l/r}^{(\dagger)}$ annihilates (creates) a particle in the left/right well, J is the hopping energy and U is the on-site inter-action energy between particles. The operators obey the usual bosonic commutation relations $[\hat{a}_i,\hat{a}_j^\dagger] = \delta_{ij}$, where i and j correspond to either l or r.

In this paper we study caustics that form in Fock space. The Fock states $|n\rangle$ are eigenstates of the half-number-difference operator $\hat{n} \equiv (\hat{a}_l^\dagger\hat{a}_l - \hat{a}_r^\dagger\hat{a}_r)/2$. A general quantum state can be expanded as

$$|\Psi(t)\rangle = \sum_n c_n(t)|n\rangle . \quad (2)$$

Inserting Eq. (2) into the time-dependent Schrödinger equation, $i\hbar\partial_t|\Psi(t)\rangle = \hat{H}|\Psi(t)\rangle$, we obtain a set of $N+1$ coupled differential equations for the Fock-space amplitudes $c_n(t)$ which we refer to as the generalized Raman-Nath (RN) equations (a similar set of differential difference equations were derived by Raman and Nath in the context of dynamical diffraction [158–160]),

$$i\hbar\dot{c}_n(t) = 4Un^2 c_n(t) - Jc_{n-1}(t)\sqrt{\frac{N^2}{4}+\frac{N}{2}-n^2+n}$$
$$- Jc_{n+1}(t)\sqrt{\frac{N^2}{4}+\frac{N}{2}-n^2-n} \quad (3)$$

where the dot represents a time derivative.

The mean-field limit is given by the Heisenberg substitution rules, replacing operators with complex amplitudes [148, 161]

$$\hat{a}_{r/l} \to \sqrt{N_{r/l}}e^{i\theta_{r/l}} , \quad (4)$$

and leads to the Hamiltonian

$$H_{\text{MF}}^{\text{dimer}} = 4Un^2 - J\sqrt{N^2-4n^2}\cos\phi , \quad (5)$$

where $\phi = \theta_r - \theta_l$ is the phase difference between the two modes and is the conjugate variable to n. $H_{\text{MF}}^{\text{dimer}}$ describes a classical nonrigid pendulum where n is angular momentum and ϕ angular position. The variable length of the nonrigid pendulum is accounted for by the square root factor [115]. In fact, because they have simultaneously well-defined position and momentum as a function of time, the mean-field solutions are analogous to geometric rays. Hamilton's equations of motion give Josephson's equations for two coupled superfluids [162]

$$\dot{n} = -\frac{1}{\hbar}\frac{\partial}{\partial\phi}H_{\text{MF}}^{\text{dimer}} = -\frac{J}{\hbar}\sqrt{N^2-4n^2}\sin\phi \quad (6)$$

$$\dot{\phi} = \frac{1}{\hbar}\frac{\partial}{\partial n}H_{\text{MF}}^{\text{dimer}} = 8\frac{U}{\hbar}n + \frac{J}{\hbar}\frac{8n}{\sqrt{N^2-4n^2}}\cos\phi . \quad (7)$$

Attempts to semiclassically quantize the mean-field problem are complicated by the appearance of both number and phase variables in the potential energy term, meaning that the Hamiltonian is not separated into the sum of a 'kinetic' term proportional to n^2 and a 'potential' term $V(\phi)$, but can be pushed through with some care [119, 163]. However, providing the population difference is always small in comparison to the total particle number ($n \ll N$) the square root term in $H_{\text{MF}}^{\text{dimer}}$ can be set to unity reducing it to that of a standard rigid pendulum. This is the relevant Hamiltonian in atomic BECs in optical lattices when there are many atoms per site [164–169], and also in superconducting Josephson junctions where it is known as the *quantum phase model* (QPM) [170, 171]. In this paper we shall sometimes make use of the QPM for simplicity but will also consider corrections to it (we will see in Section VII that this can make a difference to the caustics that occur).

B. Three-mode Equations of Motion

The Hamiltonian for the BH trimer can be written as

$$\hat{H} = -K_L(\hat{a}_1^\dagger\hat{a}_2 + \hat{a}_2^\dagger\hat{a}_1) - K_R(\hat{a}_2^\dagger\hat{a}_3 + \hat{a}_3^\dagger\hat{a}_2) \quad (8)$$
$$- K_X(\hat{a}_3^\dagger\hat{a}_1 + \hat{a}_1^\dagger\hat{a}_3) + \frac{U}{2}\sum_{i=1}^3\hat{n}_i(\hat{n}_i-1) + \sum_{i=1}^3\epsilon_i\hat{n}_i .$$

The parameters K_L, K_R, K_X correspond to the hopping energies between wells 1 and 2, 2 and 3, and 1 and 3, respectively. The ϵ_i allow for different well depths.

In its linear configuration ($K_X = 0$), the BH trimer system has been used as a spatial model for rapid adiabatic passage by controlling the well depths $\epsilon_i(t)$ as functions of time [172–177]. Indeed, adding a magnetically-induced tilt to the lattice allows additional rich behaviour including control of correlations [186, 187]. The linear configuration has also been studied from the point of view of an ultracold atom transistor-like device [178–181]. In its fully-connected triangular configuration ($K_X \neq 0$), the trimer system provides a minimal model for superfluid circuits and discrete vortices [182–185]. Both chain and triangle have been discussed in the context of quantum steering [188–191]. To the best of our knowledge the BH trimer has not been studied experimentally using triple-well BECs, although detailed proposals with tuneable hopping and interaction parameters via Feshbach resonances exist [192]. As mentioned above, spin-1 BECs provide another physical system where the three mode BH model can provide the natural theoretical description [143].

When $U = 0$, the mean-field BH trimer model exhibits regular dynamics, while for nonzero interactions it exhibits chaos indicating nonintegrability. Close to the ground state chaotic trajectories are mixed with islands of regular dynamics [144, 161]. Energy level statistics in the quantum version tell a similar story: in general they obey neither the Poisson nor Wigner distributions but

are better described by a Berry-Robnic distribution [193] which is a signature of a classical limit containing both regular and chaotic dynamics [194]. The significance of this for the results we present below is that we find caustics in a nonintegrable model even though caustics are usually associated with integrable behavior [195]. We therefore conjecture that the caustics are at least stable against weak integrability breaking terms as described by the famous Kolmogorov-Arnold-Moser theorem [196].

The quantum many-body state can be expanded as

$$|\Psi(t)\rangle = \sum_{n_1 n_2 n_3} M_{n_1 n_2 n_3}(t) |n_1, n_2, n_3\rangle \qquad (9)$$

$$= \sum_{n_1 n_X} M_{\delta n_2 n_X}(t) |\delta n_2, n_X\rangle \qquad (10)$$

where we have introduced new Fock space coordinates $\delta n_2 \equiv n_2 - N/3$ and $n_X \equiv n_1 - n_3$, and have assumed the total particle number is conserved so that one of the sums is eliminated (the variables δn_2 and n_X are similar to those used by Arwas et al [182]). The allowed Fock space is then triangular in shape and the schematic in Fig. 2 depicts a small region of it. Since each Fock state is coupled to six others by all the possible hopping terms, Fock space can be tiled by a hexagonal pattern as shown.

Inserting Eq. (10) into Schrödinger's equation gives the following generalized Raman-Nath equations for the Fock space amplitudes $M_{ij}(t)$ (we have put all $\epsilon_i = 0$)

$$i\hbar \dot{M}_{\delta n_2, n_X}(t) =$$

$$- \frac{K_L}{\sqrt{2}} \sqrt{\left(\frac{N}{3} + \delta n_2 + 1\right)\left(\frac{2N}{3} - \delta n_2 + n_X\right)} M_{\delta n_2 + 1, n_X - 1}$$

$$- \frac{K_L}{\sqrt{2}} \sqrt{\left(\frac{N}{3} + \delta n_2\right)\left(\frac{2N}{3} - \delta n_2 + n_X + 2\right)} M_{\delta n_2 - 1, n_X + 1}$$

$$- \frac{K_R}{\sqrt{2}} \sqrt{\left(\frac{N}{3} + \delta n_2\right)\left(\frac{2N}{3} - \delta n_2 - n_X + 2\right)} M_{\delta n_2 - 1, n_X - 1}$$

$$- \frac{K_R}{\sqrt{2}} \sqrt{\left(\frac{N}{3} + \delta n_2 + 1\right)\left(\frac{2N}{3} - \delta n_2 - n_X\right)} M_{\delta n_2 + 1, n_X + 1}$$

$$- \frac{K_X}{2} \sqrt{\left(\frac{2N}{3} - \delta n_2 + n_X + 2\right)\left(\frac{2N}{3} - \delta n_2 - n_X\right)} M_{\delta n_2, n_X + 2}$$

$$- \frac{K_X}{2} \sqrt{\left(\frac{2N}{3} - \delta n_2 - n_X + 2\right)\left(\frac{2N}{3} - \delta n_2 + n_X\right)} M_{n_2, n_X - 2}$$

$$+ \frac{U}{4} \left[3\delta n_2^2 + n_X^2\right] M_{\delta n_2, n_X}. \qquad (11)$$

The mean-field approximation is obtained as above by replacing operators with complex amplitudes, $\hat{a}_i \to \sqrt{n_i}e^{i\phi_i}$. The resulting Hamiltonian is,

$$H_{\mathrm{MF}} = - 2K_L \sqrt{n_1 n_2} \cos(\varphi_2 - \varphi_1)$$
$$- 2K_R \sqrt{n_2 n_3} \cos(\varphi_3 - \varphi_2) \qquad (12)$$
$$- 2K_X \sqrt{n_3 n_1} \cos(\varphi_1 - \varphi_3)$$
$$+ \frac{U}{2} \sum_{i=1}^{3} n_i(n_i - 1) + \sum_{i=1}^{3} \epsilon_i n_i.$$

Like in the quantum case, we can change our coordinates to δn_2 and n_X and eliminate the third member due to
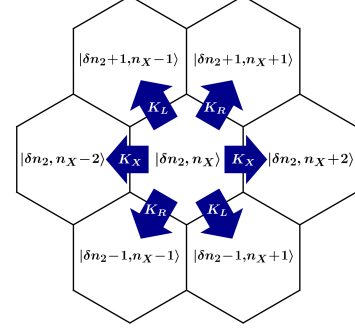

FIG. 2. A small region of Fock space for the BH trimer. It can be tiled by hexagonal cells in the coordinates $\{\delta n_2, n_X\}$ we use throughout this paper. Hopping terms shift δn_2 by only 1 unit, while $n_X \equiv n_1 - n_3$ can change by 1 or 2 units.

number conservation. However, in the mean-field problem we also require the phase variables conjugate to the number variables and these are $\phi_X \equiv \frac{1}{2}(\varphi_1 - \varphi_3)$ and $\phi_C \equiv \frac{1}{2}(2\varphi_2 - \varphi_1 - \varphi_3)$, respectively. The third phase variable $\Theta \equiv \varphi_1 + \varphi_2 + \varphi_3$ is irrelevant to the mean-field dynamics studied here, and in the quantum wavefunction becomes a global phase. The resulting mean-field equations of motion in these variables come out to be:

$$\dot{n}_X = - K_L \sqrt{2\left(\frac{N}{3} + \delta n_2\right)\left(\frac{2N}{3} - \delta n_2 + n_X\right)} \sin\left(\phi_X - \phi_C\right)$$
$$- K_R \sqrt{2\left(\frac{N}{3} + \delta n_2\right)\left(\frac{2N}{3} - \delta n_2 - n_X\right)} \sin\left(\phi_X + \phi_C\right)$$
$$- 2K_X \sqrt{\left(\frac{2N}{3} - \delta n_2\right)^2 - n_X^2} \cos\left(2\phi_X\right) \qquad (13)$$

$$\dot{\delta n_2} = K_L \sqrt{2\left(\frac{N}{3} + \delta n_2\right)\left(\frac{2N}{3} - \delta n_2 + n_X\right)} \sin\left(\phi_X - \phi_C\right)$$
$$- K_R \sqrt{2\left(\frac{N}{3} + \delta n_2\right)\left(\frac{2N}{3} - \delta n_2 - n_X\right)} \sin\left(\phi_X + \phi_C\right) \qquad (14)$$

$$\dot{\phi}_X = \frac{U}{2} n_X - K_L \frac{\left(\frac{N}{3} + \delta n_2\right)\cos(\phi_X - \phi_C)}{\sqrt{2\left(\frac{N}{3} + \delta n_2\right)\left(\frac{2N}{3} - \delta n_2 + n_X\right)}}$$
$$+ K_R \frac{\left(\frac{N}{3} + \delta n_2\right)\cos(\phi_X + \phi_C)}{\sqrt{2\left(\frac{N}{3} + \delta n_2\right)\left(\frac{2N}{3} - \delta n_2 - n_X\right)}}$$
$$+ K_X \frac{n_X \cos(2\phi_X)}{\sqrt{\left(\frac{2N}{3} - \delta n_2\right)^2 - n_X^2}} \qquad (15)$$

$$\dot{\phi}_C = \frac{3U}{2} \delta n_2 - K_L \frac{\left(\frac{N}{3} - 2\delta n_2 + n_X\right)\cos(\phi_X - \phi_C)}{\sqrt{2\left(\frac{N}{3} + \delta n_2\right)\left(\frac{2N}{3} - \delta n_2 + n_X\right)}}$$
$$- K_R \frac{\left(\frac{N}{3} - 2\delta n_2 - n_X\right)\cos(\phi_X + \phi_C)}{\sqrt{2\left(\frac{N}{3} + \delta n_2\right)\left(\frac{2N}{3} - \delta n_2 - n_X\right)}}$$
$$+ K_X \frac{\left(\frac{2N}{3} - \delta n_2\right)\cos(2\phi_X)}{\sqrt{\left(\frac{2N}{3} - \delta n_2\right)^2 - n_X^2}}. \qquad (16)$$

While the dimer case gave mean-field equations describing a non-rigid pendulum, the trimer case can be interpreted as describing three coupled anharmonic oscillators

Catastrophe	Symbol	n	Q	$\Phi_Q(\mathbf{s};\mathbf{C})$
Fold	A_2	1	1	$s^3 + Cs$
Cusp	A_3	1	2	$s^4 + C_2 s^2 + C_1 s$
Swallowtail	A_4	1	3	$s^5 + C_3 s^3 + C_2 s^2 + C_1 s$
Butterfly	A_5	1	4	$s^6 + C_4 s^4 + C_3 s^3 + C_2 s^2 + C_1 s$
Hyperbolic Umbilic	D_4^+	2	3	$s_1^3 + s_2^3 + C_3 s_1 s_2 + C_2 s_2 + C_1 s_1$
Elliptic Umbilic	D_4^-	2	3	$3 s_1^2 s_2 - s_2^3 + C_3(s_1^2 + s_2^2)$ $+ C_2 s_2 + C_1 s_1$
Parabolic Umbilic	D_5	2	4	$s_2^4 + s_1^2 s_2 + C_4 s_2^2 + C_3 s_1^2$ $+ C_2 s_2 + C_1 s_1$

TABLE I. Thom's seven elementary catastrophes, their symbols, and generating functions $\Phi_Q(\mathbf{s};\mathbf{C})$, organized by corank n, and codimension Q [43].

Symbol	n	$\Phi_Q(\mathbf{s};\mathbf{C})$
A_{Q+1}	1	$s^{Q+2} + \sum_{i=1}^{Q-1} C_i s^i$
$D_{Q+1}^\pm$	2	$s_1^Q \pm s_1 s_2^2 + C_{Q+1} s_2^2 + \sum_{i=2}^{Q-1} C_i s_1^i + C_1 s_2$
E_6	2	$s_1^3 + s_2^4 + C_5 s_1 s_2^2 + C_4 s_2^2 + C_3 s_1 s_2 + C_2 s_2 + C_1 s_1$
E_7	2	$s_1^3 + s_1 s_2^3 + C_6 s_2^4 + C_5 s_2^3 + C_4 s_2^2$ $+ C_3 s_1 s_2 + C_2 s_1 + C_1 s_2$
E_8	2	$s_1^3 + s_2^5 + C_7 s_1 s_2^3 + C_6 s_1 s_2^2 + C_5 s_2^3$ $+ C_4 s_1 s_2 + C_3 s_2^2 + C_2 s_1 + C_1 s_2$
$X_9^\pm$	2	$s_2^4 + K s_1^2 s_2^2 \pm s_1^4 + C_7 s_2^3 s_1 + C_6 s_2 s_1^3$ $+ C_5(s_2^2 + s_1^2) + C_4(s_2^2 - s_1^2)$ $+ C_3 s_2 s_1 + C_2 s_2 + C_1 s_1$

TABLE II. Catastrophe organization beyond Thom's seven elementary list [49], with general control space dimension Q. Many of the higher catastrophes do not have names, and are referenced by their group-theoretic symbol, yet are often split into cuspoids A_{Q+1}, and umbilics $\{D_{Q+1}, E_{Q+1}, X_9\}$.

[161]. Eqns. (13)-(16) must in general be solved numerically, but a problem can potentially arise for trajectories that touch the boundaries of Fock space where the square root factors in the denominators vanish. Physically, the boundaries correspond to situations where one of the modes is empty. We find empirically that this becomes less of a problem as N is increased and almost never occurs in the semiclassical regime we consider in this paper where $N \sim 150$ because trajectories spend most of their time in the central region of Fock space.

III. WAVE CATASTROPHES

Catastrophe theory describes the structurally stable singularities of gradient maps. This applies to problems posed in terms of a minimum principle, e.g. principle of stationary action. The seven elementary catastrophes introduced by René Thom [32] are listed in Table I, and some examples of higher catastrophes are listed in Table II. They are organized by corank (number of "state" variables $\mathbf{s} = \{s_1, s_2, \ldots\}$ that label paths) and codimension (number of control parameters $\mathbf{C} = \{C_1, C_2, \ldots\}$ which in our case is the dimension of Fock space plus time and any other parameters in the Hamiltonian). The key objects are the generating functions $\Phi_Q(\mathbf{s};\mathbf{C})$, and in physical applications they give the *local action* close to the caustic. Stationary points $\partial_s \Phi_Q = 0$ specify classical paths or rays, which are the mean-field solutions. Caustics occur where the action is stationary to higher order, i.e. $\partial_s^2 \Phi_Q = 0$ (in two or more dimensions this condition becomes the vanishing of the Hessian matrix), and thus are regions where classical paths either coalesce or are born (bifurcations). The main point is that this can only happen in certain ways if the bifurcation is to be structurally stable against perturbations.

For example, in the case of light-like cones the action is $\Phi(k; x, t) = kx - \epsilon_k t/\hbar$, where ϵ_k is the dispersion relation for quasiparticles of wavenumber k [40]. The Lieb-Robinson bound, which gives the maximum speed

of quasiparticles and hence defines the cone is [197, 198]

$$v_{\text{LR}} = \max_k \left| \frac{d\epsilon_k}{dk} \right| \qquad (17)$$

which is exactly equivalent to the two conditions $\partial_s \Phi_Q = 0$ and $\partial_s^2 \Phi_Q = 0$ defining caustics.

Each catastrophe has a 'germ', which is the part of Φ_Q that remains when it is evaluated at the origin of control space $\mathbf{C} = 0$. The germ characterizes the order of the singularity. The other terms show how the catastrophe 'unfolds' as one moves away from the origin of control space. The corank 1 catastrophes, A_{Q+1} are called the *cuspoids*, and extend beyond the butterfly to the *wigwam* and *star* catastrophes (not listed). The remaining catastrophe types, D_{Q+1}, E_{Q+1}, and above are typically called *umbilics*, referring to the classification of cubic forms near an umbilic point (a point on a surface with locally spherical curvature) which become the germs for these catastrophes.

Catastrophes obey projection identities: higher catastrophes contain lower ones, e.g. the swallowtail contains two cusps and three fold lines when projected into two dimensions. It is not, however, guaranteed that catastrophes of high order (i.e. higher codimension and/or corank) contain all catastrophes of lower order. In section VI, we will briefly discuss distinctions between families of the high-order catastrophe X_9, which have different projection identities (X_9 is the catastrophe that organizes all the structures we see in the BH trimer dynamics). With special tuning one could engineer focusing events with any shape, but catastrophe theory instead describes structurally stable caustics that result from natural focusing, and so are more likely to appear generically.

The geometric ray theory (mean-field theory in Fock space) gives the basic shape of the caustic, but these ray sums give divergent amplitudes. To remove these one should include interference and we enter the realm of wave catastrophes (diffraction integrals) [43, 49]. Each

ray catastrophe is dressed by a characteristic wave interference pattern described by a diffraction integral,

$$\Psi(\mathbf{C}) \propto \lambda^{n/2} \int ... \int d\mathbf{s} \, e^{i\lambda\Phi_Q(\mathbf{s};\mathbf{C})} \, . \qquad (18)$$

This wavefunction lives in the space of control parameters (Fock space + time) and resembles a path integral where the generating function plays the role of the action and we integrate over state variables $\mathbf{s}$ which label paths. The parameter λ acts as the inverse of Planck's constant, and in the BH model is proportional to the total number of particles N. The precise connection to path integrals will be explained in Section VII and Appendix C. It is interesting to note that while wave theory removes geometric singularities it also introduces new ones, namely phase singularities where the phase takes all values and hence is undefined [199]. These are more commonly known as dislocations in optics and vortices in condensed matter systems. A genuinely new feature of caustics in quantum many-body wavefunctions in comparison to classical waves is that phase singularities are removed by second-quantization because it discretizes the vortices [39]. We shall not dwell on this 'fine structure' of caustics here, and focus instead on their gross features.

In the semiclassical regime $N \gg 1$ the discretization is hardly visible and we tend to a continuous theory. However, there are two possible limits that distinguish many-body versus one-body interference [39, 163]

1. A wave-like theory where commutators between operators like $[\hat{a}, \hat{a}^\dagger] = 1$, or approximate macroscopic versions such as $[\hat{\phi}, \hat{n}] \approx i$, are maintained (*interference fringes in Fock space preserved*)

2. A geometric ray-like theory where commutators vanish. This is the Gross-Pitaevskii equation limit (*interference fringes in Fock space removed*)

In Fig. 3 we compare the mean-field (ray) and fully quantum (2nd quantized) theories for a caustic in the 3-mode BH model. Although present, the discretization of Fock space is not visible and the quantum waves appear smooth. The interference fringes in Fig. 3(b) are true many-body fringes not present in the one-body (ray) theory shown in Fig. 3(a). The ray theory we apply is the truncated Wigner approximation (TWA) where an *ensemble* of classical rays are propagated using the classical equations (13)–(16) with initial conditions sampled from a quantum quasiprobability distribution (the Wigner function) [200–203]. Summing these rays gives the mean-field approximation to the quantum dynamics. The initial state in Fig. 3 is a phase state, which is a state with narrow relative phase distributions but which consequently has a flat probability distribution in Fock space because number and phase are conjugate variables. In the mean-field case shown in panel (a), we see that the first time slice contains a representative set of points approximating an equal superposition of Fock states. Panel (b) plots the absolute values of the quantum amplitudes
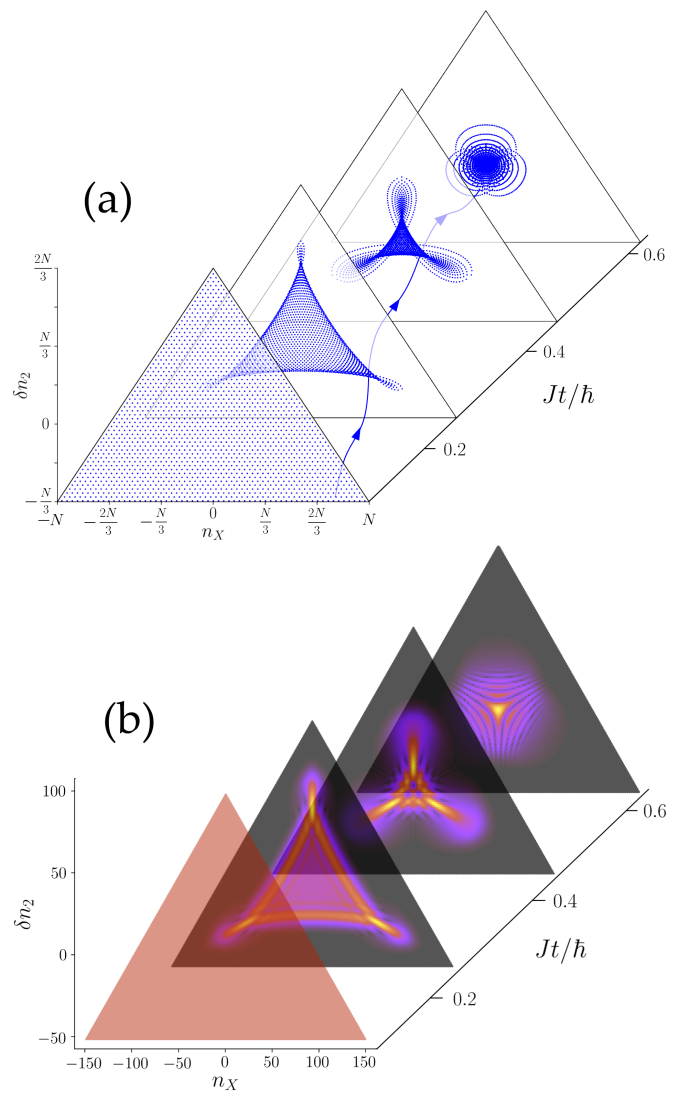

FIG. 3. Time slices comparing mean-field and quantum dynamics in the triangular Fock space found in the BH trimer under the constraint of total number conservation. **Panel (a):** An ensemble of initial points are evolved in time using the classical equations of motion Eqns. (13)–(16) and form a space-time version of the elliptic umbilic catastrophe, with one particular trajectory picked out for illustration. In the TWA the initial conditions are drawn from a quantum probability distribution and in this simple case the initial state is a phase state meaning that the relative phases are sharply defined (here taken to be $\phi_X = \phi_C = 0$) but with the consequence that their conjugate number differences take all possible values with equal probability, thereby uniformly populating the allowed triangular region of Fock space. **Panel (b):** The quantum dynamics are obtained by solving Eq. (11). The initial phase state appears as a discretized plane wave in Fock space (although here $N = 150$ and the discreteness of Fock space is not visible). The correspondence between the quantum and classical dynamics is clear: the quantum wavefunction is brightest where the density of trajectories is highest. In both images, $K_L = K_R = K_X \equiv J$, $U = -0.005J$, and $\epsilon_i = 0$.
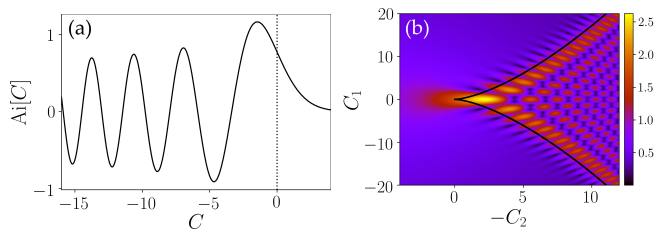
FIG. 4. The wave catastrophes associated with the fold and the cusp. **Panel (a):** The fold catastrophe is decorated by an Airy function, Eq. (20). The location of the classical caustic is indicated by a vertical dotted line. In the classical (ray) theory the intensity is divergent at this point and falls off as $1/\sqrt{-C}$ on the bright side. By contrast, the Airy function is finite at the caustic and two-wave interference gives rise to oscillations; these two waves coalesce at $C = 0$ and become evanescent on the dark side. **Panel (b):** The cusp catastrophe is decorated by the Pearcey function which is a complex-valued function (here we plot the modulus) given by Eq. (22), with the divergent classical cusp caustic shown as a solid black curve.

of the Fock states found by solving the Raman-Nath equations Eq. (11). In both cases the dynamics leads to focusing and clearly forms an elliptic umbilic caustic which can be compared to those shown in Fig. 1. An equal superposition of Fock states is a plane wave-like state analogous to the initial state often considered in optics, but here it is the BH dynamics that acts as an imperfect lens which focuses the wave in Fock space. The key feature of this initial state is that it is broad in Fock space, and structural stability means that the caustics it generates will not be qualitatively different from those generated by other broad states such as the gaussian-shaped ground state in the case with strongly coupled sites such that the hopping dominates interactions (this case will be discussed in Section VI B).

In the next two sections we investigate the hierarchy of wave catastrophes that appear in BH dimer and trimer dynamics, building up to the high-order catastrophe X_9 which ultimately organizes the lower catastrophes we see. It should be borne in mind that because the trimer is not integrable our ability to analytically describe the appearance of each catastrophe is limited and for this reason we go to δ-kicked dynamics in Section VI. Furthermore, unlike free-space optics, classical rays in Fock space do not travel in straight lines in the BH model even for the integrable case ($U = 0$).

IV. CAUSTICS IN THE DIMER

Dynamical caustics in the BH dimer live in the (1+1)D space formed by Fock space and time. The only structurally stable catastrophes in two dimensions are fold lines which can meet at cusp points.
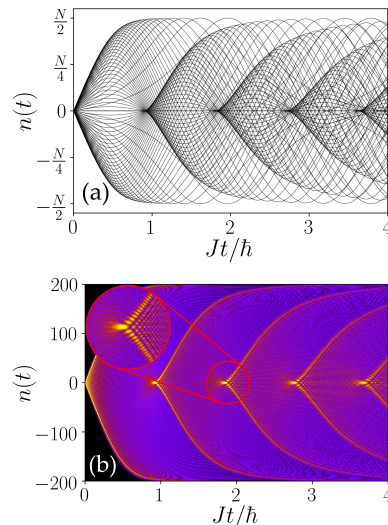

FIG. 5. Recurring cusp caustics in the two-mode BH model. **Panel (a):** Each curve is a mean-field configuration obtained from Eqns. (6)–(7) starting from $n = 0$ and with an initial phase sampled from the distribution $\phi = [0...2\pi)$ corresponding to a definite (equal) number of bosons in each well. **Panel (b):** Modulus of the quantum wavefunction calculated using the two-mode RN equations Eq. (3) with $N = 400$ and where the initial state is the single Fock state $|n = 0\rangle$. In both cases we can identify a series of cusp caustics corresponding to partial revivals of the initial state. In the inset we see that in the immediate vicinity of each cusp the wavefunction is a Pearcey function [36, 39] (the discretization of Fock space is not visible here so the wavefunction appears continuous).

A. Fold

The simplest catastrophe is the fold. Folds are corank-1, codimension-1 objects with a cubic generating function,

$$\Phi_1(s; C) = s^3 + Cs .\tag{19}$$

Folds arise where two families of rays coalesce and this can be at a point on a line, a line in a plane, a surface in 3D etc. The corresponding wave catastrophe is

$$\frac{2\pi}{3^{1/3}} \text{Ai}\left(\frac{C}{3^{1/3}}\right) = \int_{-\infty}^{\infty} ds \, e^{i(s^3 + Cs)}\tag{20}$$

and is plotted in Fig. 4(a). This function is the well-known Airy function introduced as the wave description for light at rainbows in 1838 [204]. It not only removes the singularity in the ray theory but its interference fringes also explain the supernumerary arcs that are sometimes visible inside the main bow in optical rainbows.

B. Cusp

In two dimensions, generic focusing events are fold lines that meet at cusps. These have quartic generating func-

tions,

$$\Phi_2(s; C_1, C_2) = s^4 + C_2 s^2 + C_1 s \ . \qquad (21)$$

Inside the cusp, three families of classical rays coexist, while only one family exists outside. This means that along each fold line, two sets of rays coalesce, while at the highly singular cusp point, all three families coalesce. The wave catastrophe associated with the cusp is a 2D wavefunction known as the Pearcey function [44, 45],

$$\mathrm{Pe}[C_1, C_2] = \int_{-\infty}^{\infty} \mathrm{d}s \ \mathrm{e}^{\mathrm{i}(s^4 + C_2 s^2 + C_1 s)} \ , \qquad (22)$$

and is plotted in Fig. 4(b). As can be seen, the Pearcey function consists of an interference pattern inside the cusp (due to three-wave interference), while outside it becomes exponentially suppressed. Since the cusp catastrophe consists of the meeting of two fold lines, a one-dimensional slice of the Pearcey function across one of these lines projects onto an Airy function.

We show examples of these two wave catastrophes appearing in Fock-space dynamics of the BH dimer following a quench in Fig. 5. The initial condition is a single Fock state $|n = 0\rangle$ (which is the opposite case to the phase state shown in Fig. 3). Physically, it describes the situation where two independent BECs are suddenly coupled so that at $t = 0$ particles can begin to hop between them, thereby building up coherence [205]. The structural stability of catastrophes means that qualitatively similar behaviour is found for similar initial states such as narrow gaussians in Fock space that can also be centered away from $n = 0$. Fig. 5(a) shows the set of TWA trajectories propagating from $n = 0$, each with a different relative phase ϕ. The complete certainty in n means complete uncertainty in ϕ so the phases are drawn with equal probability from the interval $\phi = [0...2\pi)$. The imperfect focusing of trajectories leads to cusps which revive at times $Jt = m\pi/(2\sqrt{1 + 2NU/J})$ for $m = 1, 2, 3, ...$ Cusps only form because of the nonlinearity due to interactions: setting $U = 0$ leads to isolated focal points. In the quantum theory Pearcey patterns dress each cusp. Moving away from the cusp tip, the wavefunction rapidly tends to back-to-back Airy functions describing the two fold lines emanating from the cusp [36].

V. CAUSTICS IN THE TRIMER

The BH trimer model also yields cusps if we restrict attention to just one of the Fock space variables, as illustrated in Fig. 6. For variety the initial condition is this time chosen to be an equal superposition of all Fock states. Like an individual Fock state, this does not correspond to an eigenstate of the Hamiltonian that we use to propagate the system in time. Instead it is a highly-excited state made up of a broad superposition of eigenstates, and this allows the system to explore its nonlinearity and produce caustics which revive periodically.

When we examine the full (2+1)D space available in the trimer then, as expected, we discover codimension-3 catastrophes, namely the elliptic and hyperbolic umbilics. This is shown in Figs. 7 and 8 which compare numerical solutions of the generalized Raman-Nath equations given in Eq. (11) with the canonical wave catastrophes. According to Table I, there is a third codimension-3 catastrophe known as the swallowtail, but this is a corank 1 catastrophe meaning that it only has a single state variable. To realize the swallowtail catastrophe in the trimer we could freeze one of the conjugate phases $\{\phi_X, \phi_C\}$, but we will not pursue this possibility here.

It is important to emphasize that although we have chosen parameters where the match in Figs. 7 and 8 between the numerical results and the canonical catastrophes is quite good, we have not optimized the parameters and these catastrophes occur generically. If we could solve the trimer model analytically we could perform an exact mapping but due to its nonintegrability this is not possible. We must therefore satisfy ourselves with qualitative rather than quantitative matches which are in any case fully within the spirit of catastrophe theory which is a topological theory [32–34]. In Section VI we consider simplified kick dynamics where we *can* precisely map the wavefunctions onto canonical wave catastrophes. A brief note on the figures in this paper: we present the bifurcation sets in orientations that are convenient to visualize, hence some of the caustic surfaces are plotted using the negative axis of control parameters, specifically Figs. 4, 10, and 11.

A. Elliptic Umbilic

The elliptic umbilic catastrophe,

$$\Phi_{D_4^-}(\mathbf{C}) = 3s_1^2 s_2 - s_2^3 + C_3(s_1^2 + s_2^2) + C_2 s_2 + C_1 s_1 \ , \ (23)$$

is one of the two catastrophes of codimension 3 with corank 2. As can be seen in Fig. 7, the dominant feature of the elliptic umbilic is its three-fold symmetry. Taking two-dimensional slices at fixed values of C_3 (which for us is the time direction), the elliptic umbilic appears as three curved fold lines that meet at three cusps. In its full three dimensional form we see that these are really three fold surfaces that meet at cusp shaped ribs. In the geometric theory, there are four rays at all points inside the caustic, while only two exist at any point outside because two coalesce on the caustic.

The corresponding diffraction catastrophe has been studied both theoretically and experimentally by Berry *et al.* in Ref. [42] by focusing light through a triangular water droplet lens (as repeated by us in Fig. 1). A Pearcey diffraction pattern locally dresses each cusp, as apparent by considering any particular corner of Fig. 7(d). The three-fold cusp structure expands/contracts as the control parameter C_3 is changed until it collapses at $C_3 = 0$. The most singular part of the caustic, the umbilic focus, is at the centre of control space ($\mathbf{C} = \mathbf{0}$). In the wave
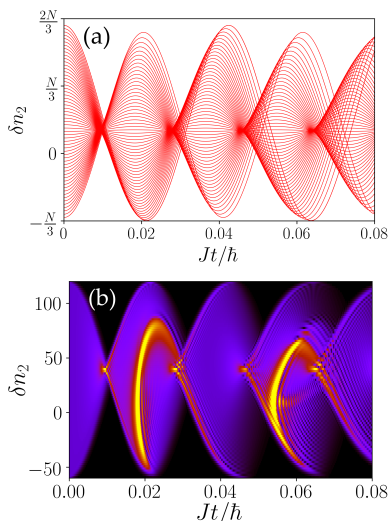
FIG. 6. Recurring cusps in the BH trimer model, starting from an equal superposition of Fock states, the three-mode version of a phase state. **Panel (a):** Classical trajectories along the plane of fixed $n_X = 0$. **Panel (b):** Quantum dynamics in the same plane as (a) where the classical cusps are now dressed by interference fringes, locally approximated by the Pearcey function. The bright streaks are finite-size effects due to reflections off the Fock-space boundary in the n_X direction, but structural stability ensures the cusps survive. In both panels, $K_L = K_R \equiv J = 100U$, $K_X = 0$ (linear configuration), while for the quantum dynamics we used $N = 180$.

theory the focus is dressed by a diffraction pattern composed of a three-fold symmetric fork with the brightest patch at the center and surrounded by an Airy fringe pattern, as shown in Fig. 7(b).

B. Hyperbolic Umbilic

The hyperbolic umbilic catastrophe,

$$\Phi_{D_4^+} = s_1^3 + s_2^3 + C_3 s_1 s_2 + C_2 s_2 + C_1 s_1 , \qquad (24)$$

is the remaining catastrophe of codimension 3 with corank 2. The hyperbolic umbilic caustic surface corresponds to an overlapping cusp and fold extended into three-dimensional space, as shown in Fig. 8(e). Within the cusp, there are four classical rays at every point, two of which annihilate each other as the cusp surface is crossed. The remaining two rays annihilate as the fold is crossed. The resulting diffraction pattern projected on a plane of constant C_3 is a Pearcey-like function surrounded by an Airy fringe pattern as seen in Fig. 8(d). At the plane $C_3 = 0$, the caustic is only partially unfolded, and now two sets of fold lines overlap to form a right-angle corner, dressed by a pattern described by a product of Airy functions in two dimensions, as shown in Fig. 8(b).

We can observe the hyperbolic umbilic in the dynamics of the trimer system by starting from the single Fock
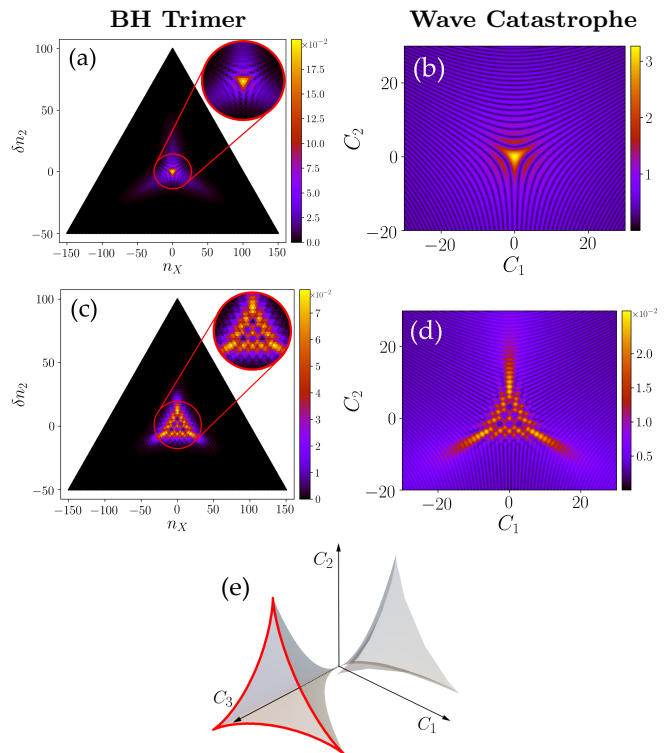

FIG. 7. Comparison of BH trimer dynamics with the canonical elliptic umbilic catastrophe. **Panel (a):** Fock-space amplitudes starting from an even superposition of Fock states [Eq. (29)] for $K_L = K_R = K_X \equiv J$, $U = 0.01J$ and $N = 150$ at $Jt/\hbar = 0.47$. **Panel (b):** Diffraction pattern amplitude in the plane around the elliptic umbilic focus. **Panel (c):** Same conditions as panel (a), but now at $Jt/\hbar = 0.54$. **Panel (d):** Diffraction pattern for a slice of the elliptic umbilic at $C_3 = 3.8$. **Panel (e):** Caustic surface of the elliptic umbilic catastrophe. The triple-cusped intersection with a $C_3 = $ const. plane is highlighted in red.

state $|\delta n_2, n_X\rangle = |0, 0\rangle$ and with $K_X = 0$ (linear spatial configuration of the triple-well). The initial compact state spreads non-uniformly into a two-fold symmetric polygon with partially unfolded hyperbolic umbilic corners as shown in Fig. 8(a). As the dynamics continue, the edges unfold completely, and the cusps separate from the fold lines (moving off the $C_3 = 0$ plane), as is first visible in the bottom corner of Fig. 8(c).

C. The X_9 catastrophe

In the absence of tilts ($\epsilon_i = 0$), the BH trimer can be seen to have six independent control parameters: $\{U, K_R, K_X, \delta n_2, n_X, NK_L t\}$ (or transformations thereof), thus the codimension-3 catastrophes that we have discussed are merely projections of a catastrophe embedded in a higher dimensional space. We shall argue in this and the following sections that the higher catastrophe that organizes the BH trimer dynamics is in fact the high order umbilic catastrophe known by its
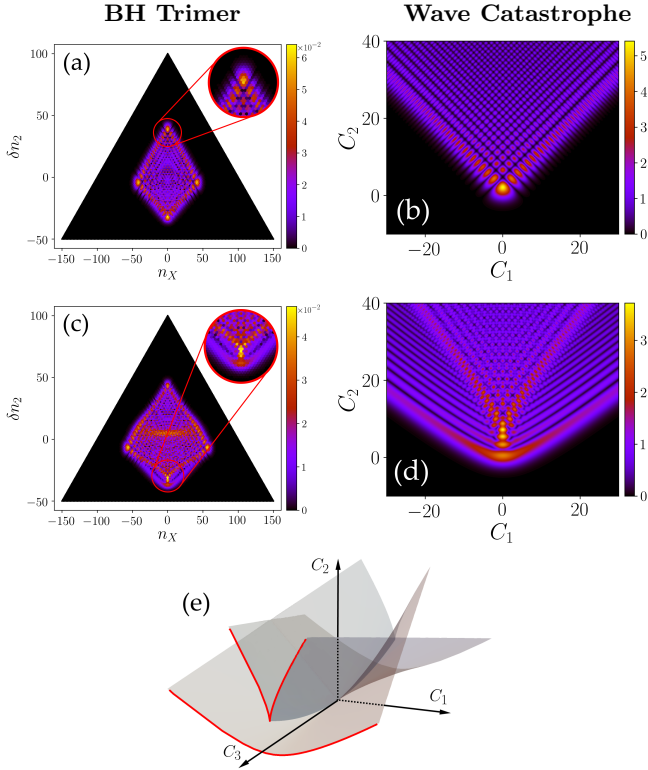
BH Trimer   **Wave Catastrophe**

FIG. 8. Comparison of BH trimer dynamics with the canonical hyperbolic umbilic catastrophe. **Panel (a):** Wavefunction amplitudes for hopping strengths $K_L = K_R \equiv J = 4U$, $K_X = 0$, and $N = 150$ at $Jt/\hbar = 0.24$. The initial state was $|\delta n_2, n_X\rangle = |0, 0\rangle$. **Panel (b):** Hyperbolic umbilic diffraction pattern on the plane $C_3 = 0$. **Panel (c):** Same conditions as panel (a) now at $Jt/\hbar = 0.34$. The bottom umbilic is now completely unfolded. **Panel (d):** Diffraction pattern for the hyperbolic umbilic in the plane $C_3 = 3$. **Panel (e):** Caustic surface of the elliptic umbilic catastrophe. A projection onto the plane $C_3 = \text{const.}$ is highlighted in red.

group-theoretic symbol, X_9. This complicated object has previously been the subject of detailed theoretical analysis by Borghi [206] and by Berry and Howls [207], and plays an important role in optical refraction through two-dimensional surfaces, such as water droplets [208], glass junctions [209], gravitational lensing [49], and has also been discussed in the context of stochastic resonance in two dimensions [210]. X_9 acts as an organizing centre for a multitude of lower catastrophes and we refer the reader to Fig. 15 for a "bordering" diagram showing its relationship to these subcatastrophes.

The X_9 catastrophe is of corank 2 and its complete 8-dimensional unfolding can be written as [49],

$$\Phi_{X_9^\pm} = s_2^4 + K s_1^2 s_2^2 \pm s_1^4 + C_7 s_2^2 s_1 + C_6 s_2 s_1^2 + C_5(s_2^2 + s_1^2)$$
$$+ C_4(s_2^2 - s_1^2) + C_3 s_2 s_1 + C_2 s_2 + C_1 s_1 . \qquad (25)$$

Although X_9 appears 8-dimensional, its control space has only seven parameters, while the eighth, K, is known as the *modulus*. Catastrophes beyond codimension 5 (or
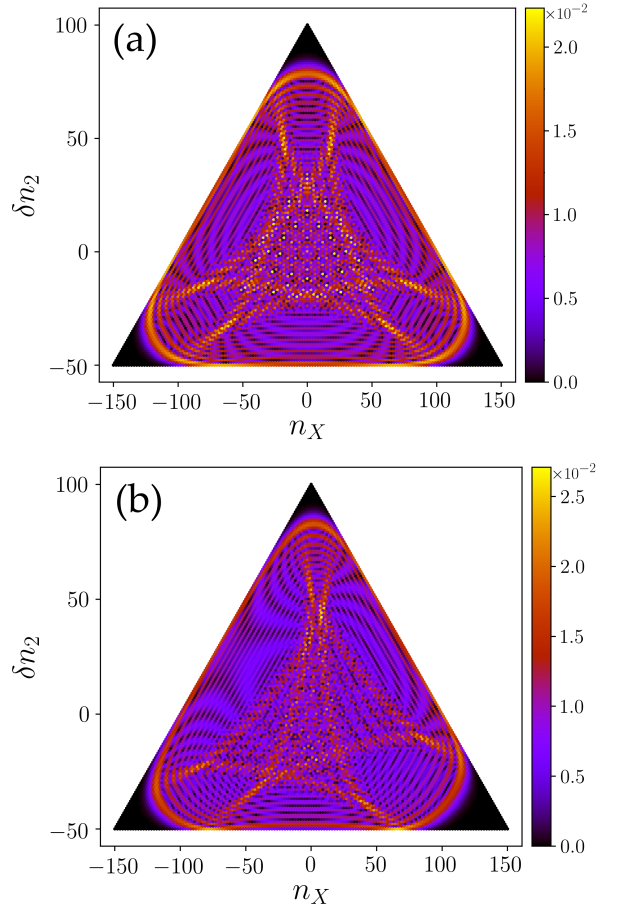

FIG. 9. 6-cusped diffraction pattern surrounded by a fold line, typical of systems with 3-fold symmetry also organized by X_9. **Panel (a):** Fock space amplitudes after a quench starting from all particles evenly distributed in each well, $|\delta n_2, n_X\rangle = |0, 0\rangle$. Here, $N = 150$, $K_L = K_R = K_X \equiv J$, $U/J = 0.04$ at $Jt/\hbar = 0.475$. **Panel (b):** As panel (a), now with $K_R = J$, $K_L = 1.2J$, and $K_X = 0.8J$, showing how an absence of symmetry does not destroy the caustics.

above corank 3) can contain moduli which are different from regular control parameters in that they can only alter the caustic pattern geometrically [85] (rather than topologically by changing the number of critical points [208]), and cannot be removed via scaling arguments. This modulus has two excluded values: $K \neq \pm 2$, where the singularities achieve infinite codimension, meaning there are an infinite number of ways to unfold the singularity, and perturbations can lead to any number of coalescing critical points. As we shall see in the following sections, the X_9 germ $\Phi_{X_9^\pm}[\mathbf{C = 0}]$ arises naturally as the base singularity in all the cases we study.

The high dimension of X_9 makes it hard to visualize and we shall therefore concentrate on particular projections. An example from BH trimer dynamics is shown in Fig. 9(a) where all the hopping amplitudes are equal and leads to two superimposed elliptic umbilics slightly rotated from each other. More precisely, the character-

istic features are a three-fold symmetric caustic featuring a six-cusped figure encapsulated by Airy-like fringes. This type of caustic is commonly encountered when light passes through liquid drops, where a $2n$-cusped pattern is formed by drops with n-fold symmetry, all surrounded by an 'oval' fold line [208]. Perturbing the symmetry will not destroy this caustic structure, as shown in Fig. 9(b) where the symmetry of the hopping terms is broken. It can only be altered dramatically by changing the symmetry in a fundamental way, such as setting a hopping term to 0.

It may appear that the control space of X_9 contains one too many parameters for the BH trimer. This is because the physical constraint of number conservation restricts us from exploring the full mathematical control space. We shall see [Fig. 10] that loosening the restriction $n_1 + n_2 + n_3 = N$ allows us to access a complete section of the X_9 catastrophe since a point in Fock space is then specified by three coordinates rather than two, bringing the total number of control parameters to seven.

The case $K = +2$ in Eq. (25) does not give a proper structurally stable catastrophe but is conceptually important because it arises in models with circular symmetry, wherein a perfectly circular 'spun cusp' is realized, punctured by an unstable axial caustic line. This is in fact the case we shall find within the QPM and for a perfectly triangular trimer (all hopping amplitudes equal) to be discussed in Section VI B. The value $K = -2$ is also not a proper catastrophe but is important because it separates X_9 into two distinct sub-families $^0X_9$ and $^4X_9$ which will come up in Section VII when we go beyond the QPM. The catastrophe germ for $K = 0$, which for $C_7 = C_6 = C_3 = 0$ is equal to $\Phi_2(s_1) + \Phi_2(s_2)$, has led to the X_9 family being known as the 'double cusp', sometimes even for $K \neq 0$ [211–213].

VI. KICKED DYNAMICS

The patterns and shapes exhibited in Figs. 6–9 are exact numerical solutions for the BH trimer model which is in general analytically intractable. They clearly resemble the caustics that catastrophe theory predicts, and also have the expected properties. However, it would be reassuring to have an analytical demonstration that in some tractable limit we really can map the dynamics to catastrophes. This is what we now do using a simplified kicked Hamiltonian. This not only allows us to analytically realize various versions of the X_9 catastrophe but also suggests an experimentally viable method for engineering precisely defined caustics.

Following an optical analogy where caustics are formed after light passes through 'bad' lenses which deform the wavefront (an ideal lens will produce a perfect hemispherical wavefront that results in a point focus), the role of δ-kicking is to produce a wavefront in Fock space that has distortions that upon further propagation will generate caustics like those we have seen for the full Hamiltonian.

Since catastrophes are stable to perturbations the caustics we find in the kicked case will survive under more generic conditions.

In the examples that follow, the interaction term proportional to U will be flashed on instantaneously at $t = 0$ and the system will afterwards evolve purely under the hopping terms. In ultracold atom systems time-dependent manipulation of interactions can be achieved using a Feshbach resonance [86]. In general, when presented with Hamiltonians of the form,

$$\hat{H}_\delta(t) = \hat{H}_0 + \hat{H}_1 \delta(t) , \qquad (26)$$

time-evolution can be achieved via the Floquet operator,

$$\hat{\mathcal{F}} \equiv e^{-\frac{i}{\hbar}\hat{H}_0 t} e^{-\frac{i}{\hbar}\hat{H}_1} . \qquad (27)$$

In previous work [37], we demonstrated the presence of catastrophes of codimension 2 in (1+1)D kicked systems. Here, we employ and generalize this framework to higher-dimensional catastrophes in the triple-well system, in particular to the different available unfoldings of X_9. The δ-kick is sometimes, but not always, necessary to see caustics in each of the cases we study in this section, since Fock space trajectories can still be focused by the hopping terms, a fact which can be demonstrated by ignoring $\hat{H}_1$. We include the kick as part of the calculations since it is more general and it allows the $\hat{H}_1$ term to mimic a tuneable 'lens' as mentioned above.

We begin by considering the mean-field Hamiltonian,

$$H_{\delta \text{QPM}} = -\frac{2JN}{3} \cos(\phi_X - \phi_C) - \frac{2JN}{3} \cos(\phi_X + \phi_C)$$
$$- \frac{2K_X N}{3} \cos(2\phi_X) + \delta(t)\frac{\tilde{U}}{4} \left[3\delta n_2^2 + n_X^2 \right] , \qquad (28)$$

which describes a kicked trimer within the quantum phase model and with a tuneable K_X hopping term. Note that the interaction strength in the kicked model has the units of $\hbar$ and is therefore given the symbol $\tilde{U}$ in Eq. (28) in order to distinguish it from the original interaction energy U in Eq. (8). We recall that the QPM is a valid approximation to the BH model when the mode occupation numbers are large, so that the square root factors can be neglected from H_{MF} in Eq. (12). In fact, we shall see that the QPM gives circularly symmetric caustics and will consider small corrections to the QPM later on in Section VII in order to unfold the X_9 catastrophe that is orchestrating the dynamics from the shadows. To quote Nye [208]: '...generic unfoldings may be best understood as perturbations of symmetrical ones'.

The integrability of the kicked model is evident from the fact that analytic solutions for the classical trajectories can be found and are given in Appendix A. To obtain quantum dynamics under the Floquet operator with $H_{\delta \text{QPM}}$ we re-promote the observables in Eq. (28) to operators such that they obey the Dirac number-phase commutators $[\hat{\phi}, \hat{n}] = i$.

A. Linear trimer

We will first consider the dynamics of the linear BH trimer which means we set $K_X = 0$ in Eq. (28), and further specialize to starting from an equal superposition of Fock states

$$|\Psi(0)\rangle = \sum_{\delta n_2', n_X'} |\delta n_2', n_X'\rangle \ . \tag{29}$$

This state is a plane wave in the number difference basis but corresponds to a single phase state, $|\phi_X = 0, \phi_C = 0\rangle$. Being more concrete than we have in the earlier parts of this paper, we define the phase states as eigenstates of the phase operators and are the three-mode generalization of phase difference Bargmann states studied in Ref. [163]. These phase states are overcomplete and thus not strictly orthogonal for finite N [161], but in what follows we operate on the assumption that $N \gg 1$ is large enough to approximate a complete set of states. Furthermore, in such a semiclassical regime we will take sums to be continuous integrals when convenient.

The time-dependent state after undergoing Floquet evolution is given by

$$|\Psi(t)\rangle = \sum_{\delta n_2', n_X'} e^{-\frac{i}{\hbar}\hat{\Phi}t} e^{-\frac{i}{\hbar}\frac{\tilde{U}}{4}(3\delta n_2'^2 + n_X'^2)} |\delta n_2', n_X'\rangle \ , \tag{30}$$

where $\hat{\Phi} = \Phi(\hat{\phi}_X, \hat{\phi}_C)$ is the part of the Hamiltonian containing all the phase operators. To obtain the wavefunction in Fock space we project $|\Psi(t)\rangle$ onto the Fock basis by applying $\langle \delta n_2, \delta n_X|$ and insert a resolution of identity $\mathbb{1} = \sum_{\phi_X, \phi_C} |\phi_X, \phi_C\rangle\langle\phi_X, \phi_C|$ between the exponential term and the ket $|\delta n_2', n_X'\rangle$. Making use of relations such as $\langle \phi_X, \phi_C | \delta n_2', n_X'\rangle = \exp[-i(n_X'\phi_X + \delta n_2'\phi_C)]$ and evaluating Gaussian integrals over the variables n_X' and $\delta n_2'$ which appear at most quadratically, we arrive at Eq. (31). Next, since the phase variables $\{\phi_X, \phi_C\}$ are localized around zero, at least for short times, we expand the cosine terms to fourth order. Finally, under a change of variables, $\phi_C \to 18^{1/4}\phi_C$ and $\phi_X \to 18^{1/4}\phi_X$, we obtain Eq. (32) which is in a form recognizable as the diffraction integral of X_9, although the symmetry of the QPM Hamiltonian and the initial state we have chosen restricts the unfolding so that the terms C_3, C_6, and C_7 do not yet appear (the remaining symmetries will be broken in Section VII). Note that both Eqns. (31) and (32) have been written in a slightly more general form than necessary for the linear trimer by including the K_X term so that they also apply to the triangular case discussed in Section VI B.

$$\Psi(\delta n_2, n_X, t) = \frac{4\pi\hbar}{i\sqrt{3}\tilde{U}} \sum_{\phi_X, \phi_C} \exp\left[i\frac{2NJt}{3\hbar}\left(\cos(\phi_X - \phi_C) + \cos(\phi_X + \phi_C) + \frac{K_X}{J}\cos(2\phi_X)\right)\right.$$
$$\left. + n_X\phi_X + \delta n_2\phi_C + \frac{\hbar}{3\tilde{U}}(\phi_C^2 + 3\phi_X^2)\right] \tag{31}$$

$$\psi(\delta n_2, n_X, t) = A(t) \int\int d\phi_X d\phi_C \, \exp\left[i\frac{NJt}{\hbar}\left(\phi_X^4 + K\phi_X^2\phi_C^2 + \phi_C^4 + \alpha\phi_X^2 + \beta\phi_C^2 + \zeta\phi_X + \eta\phi_C\right)\right] \tag{32}$$

For the linear trimer, the modulus in Eq. (32) comes out to be $K = 6$, and the control parameters are given by

$$\alpha = \frac{3\sqrt{2}\hbar^2}{NJt\tilde{U}} - 2\sqrt{2} \tag{33}$$

$$\beta = \frac{\sqrt{2}\hbar^2}{NJt\tilde{U}} - 2\sqrt{2} \tag{34}$$

$$\zeta = \frac{2^{1/4}\sqrt{3}\hbar}{NJt}n_X \tag{35}$$

$$\eta = \frac{2^{1/4}\sqrt{3}\hbar}{NJt}\delta n_2 \tag{36}$$

with,

$$A(t) = \frac{4\sqrt{6}\pi\hbar}{U}e^{-i\frac{\pi}{2}}e^{i\frac{4NJt}{3\hbar}} \ . \tag{37}$$

The wave catastrophe described by Eq. (32) might appear four dimensional, with coordinates $\{\alpha, \beta, \zeta, \eta\}$, but examination of Eqns. (33) and (34) reveals that α and β are not independent: $\alpha = 3\beta + 4\sqrt{2}$, and therefore it is really three dimensional. Let us consider the particular case $\alpha = -\beta$ which occurs naturally at the time $t = \hbar^2/(JN\tilde{U})$. This gives a three-dimensional section of X_9 that is hyperbolic and described by the generating function

$$\Phi_{X_9}^H = s_2^4 + 6s_1^2s_2^2 + s_1^4 + C_4(s_2^2 - s_1^2) + C_2s_2 + C_1s_1 \ , \tag{38}$$

which has previously been studied by Berry and Howls and is relevant to liquid-droplet lenses [207]. The corresponding theoretical caustic surface is plotted in panel (a) of Fig. 10 where a two-dimensional section at $\alpha = C_4 = \sqrt{2}$ is highlighted in red. If we move slightly away from $t = \hbar^2/(JN\tilde{U})$, then $\alpha \neq -\beta$ leading to the introduction of a C_5 term.
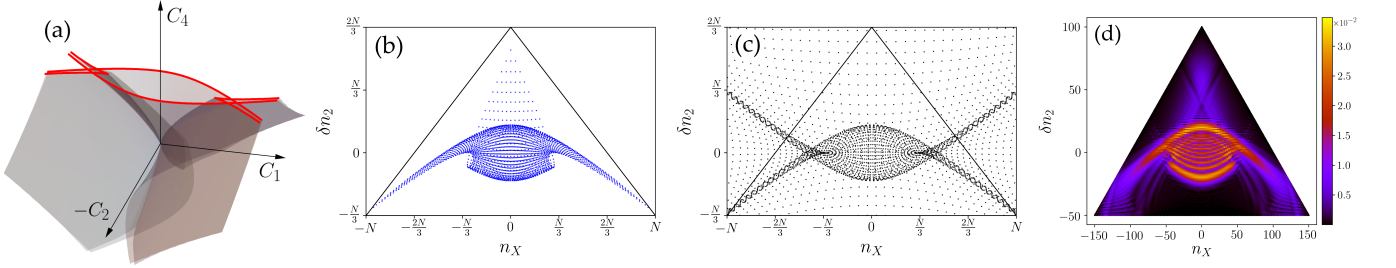
FIG. 10. Hyperbolic sections of X_9 in the classical and quantum BH trimer. **Panel (a):** Caustic surface for $\Phi^H_{X_9}$, as given in Eq. (38). The red highlights mark the intersection with the plane $C_4 = \sqrt{2}$. **Panel (b):** Distribution of points arising from classical trajectories of the δQPM Hamiltonian Eq. (28) (see Appendix A for solutions of Hamilton's equations) for the linear trimer ($K_X = 0$) at $t = \hbar^2/(JN\tilde{U})$ and $\alpha = C_4 = \sqrt{2}$, starting in an equal spread of number differences, and with phase differences $\phi_C(0) = \phi_X(0) = 0$. The resulting caustic is a partial section through the hyperbolic unfolding of X_9, restricted by the triangular Fock space (black solid lines) of physical classical paths. **Panel (c):** Same snapshot as in panel (b), now including some unphysical paths (such as those which have started or ended with $n_X > N$), to demonstrate how the caustic is restricted by the shape of Fock space (number conservation). **Panel (d):** Wavefunction amplitude at the same moment as panels (b) and (c), starting from an equal superposition of Fock states (29) and evolved using the RN equations corresponding to the δQPM model (square root factors set to unity). Here, $N = 150$, and $\tilde{U}/\hbar = 0.02$.

The actual caustic formed by the classical dynamics [with Hamiltonian Eq. (28)] is plotted in Fig. 10(b). This clearly resembles the analytical prediction but only half of it is present. This is because of the restriction of physical paths to always lie within the triangular Fock space $-\frac{N}{3} \leq \delta n_2 \leq \frac{2N}{3}$ and $-N \leq n_X \leq N$. If unphysical paths are allowed (i.e. non-number conserving paths such as those with $|n_X| > N$ or $n_2 > N$), the full caustic is captured, as shown in Fig. 10(c). Panel (d) shows the resulting quantum amplitudes in Fock space after time evolution under the corresponding RN equations. The quantum-classical correspondence is clear in this semiclassical regime and we can identify the hyperbolic X_9 boundary, which is now dressed with characteristic interference fringes across the fold lines.

B. Triangular trimer

Let us now consider the δQPM Hamiltonian Eq. (28) with $K_X = J$, corresponding to a system of three sites arranged in an equilateral triangle such that all three hopping amplitudes are equal. We follow the same procedure as the linear case, except that in order to bring the wavefunction to the canonical form given in Eq. (32) the two phase variables must be scaled differently: $\phi_C \to 2^{1/4}\phi_C$ and $\phi_X \to 18^{1/4}\phi_X$. We thereby obtain a modulus $K = 2$ and find the following mapping between physical quantities and abstract control parameters,

$$\alpha = \beta = \frac{\sqrt{2}\hbar^2}{\tilde{U}JNt} - 2\sqrt{2} \tag{39}$$

$$\zeta = \frac{2^{1/4}\hbar}{NJt}n_X \tag{40}$$

$$\eta = \frac{2^{1/4}\sqrt{3}\hbar}{NJt}\delta n_2 \tag{41}$$

and,

$$A(t) = \frac{4\sqrt{2}\pi\hbar}{\tilde{U}}e^{-i\frac{\pi}{2}}e^{i\frac{2NJt}{\hbar}} . \tag{42}$$

Once again we find that α and β are not independent which this time leads to a spun cusp surrounding an axial caustic line described by the generating function

$$\Phi^{\text{circ}}_{X_9} = s_2^4 + 2s_1^2 s_2^2 + s_1^4 + C_5(s_2^2 + s_1^2) + C_2 s_2 + C_1 s_1 \tag{43}$$

and pictured in Fig. 11. The axial caustic line is not generic and is in fact unstable. It arises from the rotational symmetry we have assumed in the δQPM with $K_X = J$. Physically speaking, the combination of isometric hopping along with the simplified quantum phase Hamiltonian causes the system to not 'feel' the triangular symmetry, and results in a perfectly circularly symmetric structure in Fock space. From the parameters (39), we can read off that the time at which the cusp point occurs is $t_{\text{cusp}} = \hbar^2/(2\tilde{U}JN)$.

Fig. 11 shows the dynamics of the wavefunction (32) with control parameters given in Eqs. (39)-(41) at $t = \hbar^2/(\tilde{U}JN)$, twice the cusp time. Panel (a) shows the circular caustic formed by the classical trajectories by mimicking the initial state Eq. (29) with an even spread of initial points in Fock space. Panel (b) shows the wavefunction amplitude under the same conditions as (a), with clearly visible interference effects and a bright central Fock state amplitude $|\langle 0, 0|\psi(t)\rangle|$ corresponding to the axial caustic. The canonical spun cusp caustic surface is shown in panel (c), with a two-dimensional circular caustic outlined in red. In Appendix B we give the control parameters for the X_9 wavefunction [Eq. (32)] for any intermediate value of K_X between the linear and triangular trimer cases.
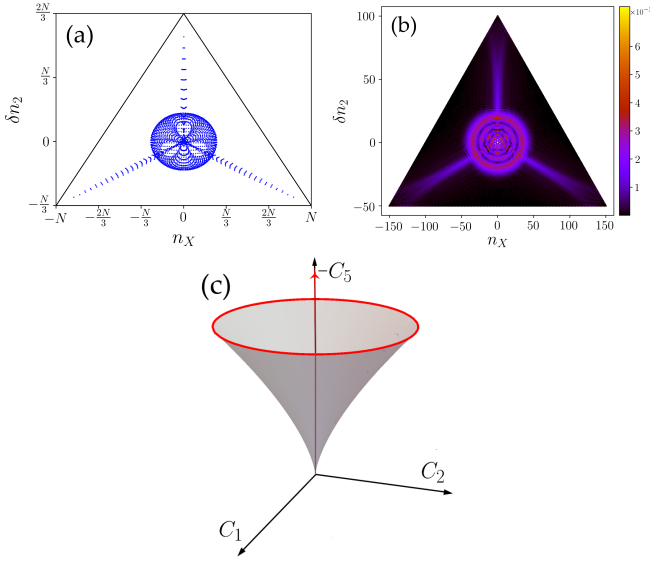
FIG. 12. A Gaussian initial state gives the same caustic as a 'plane wave'. **Panel (a):** The amplitude of the ground state of the noninteracting trimer model for $K_L = K_X = K_R \equiv J$ and $N = 120$ has a Gaussian form. **Panel (b):** Time evolution of the ground state using the kicked Hamiltonian with $\tilde{U}/\hbar = 0.08$, at time $t = 2\hbar^2/(JN\tilde{U})$. Comparing with Fig. 11 we see a strong resemblance indicating that initial states which differ significantly but have the same general form (flat near the center of Fock space) will give rise to qualitatively similar caustics.

After changing variables,

$$|\psi_G\rangle \approx \frac{3^{\frac{3}{4}}}{\sqrt{2\pi N}} \sum_{\delta n_2,\, n_X} e^{-\frac{3\ln 3}{8N}(3\delta n_2^2 + n_X^2)} |\delta n_2, n_X\rangle \ . \quad (45)$$

Note that the coefficients of δn_2^2 and n_X^2 are not the same since n_X ranges from $-N$ to N and δn_2 ranges from $-N/3$ to $2N/3$. The assumption of localized phase-state contributions around $\phi = 0$ still applies, since,

$$\langle \phi_X, \phi_C, \Theta | \psi_G \rangle \approx \frac{4\sqrt{2\pi N}}{3^{\frac{3}{4}} \ln 3} e^{i\Theta N/3} e^{-\frac{2N}{9\ln 3}(\phi_C^2 + 3\phi_X^2)} \ , \quad (46)$$

which for large N becomes narrowly peaked around $\phi_X = \phi_C = 0$, while widely spread in the number difference values. Starting from this initial state, we use the Floquet operator to propagate and the results are shown in Fig. 12 where we see that despite the fact that the Gaussian differs significantly from a plane wave we still obtain qualitatively the same caustic as in Fig. 11. Note that the result of applying the Floquet operator is to take $U \to U - i\frac{3\ln 3}{2N}$, implying that for finite N there is no longer a well-defined cusp point since the solution $\alpha = \beta = 0$ cannot occur for a real value of t. The outer circular caustic surface does, however, remain and we see a diffraction pattern reminiscent of the $K = 2$ spun cusp. Furthermore, in the semiclassical regime $N \gg 1$ we can closely approximate a cusp point.

FIG. 11. The spun cusp caustic generated by the triangular BH trimer ($K_X = J$) within the δQPM. **Panel (a):** Distribution of points arising from classical trajectories of the δQPM Hamiltonian Eq. (28) (see Appendix A for solutions of Hamilton's equations) at time $t = \hbar^2/(JN\tilde{U})$ (twice t_{cusp}), starting from an equal spread of number differences, and with phase differences $\phi_C(0) = \phi_X(0) = 0$. The circular caustic from the $K = 2$ section of X_9 is clearly visible. **Panel (b):** Quantum wavefunction amplitude at the same time as panel (a), starting from an equal superposition of Fock states (29) and evolved using linearized RN equations. $N = 150$, and $\tilde{U}/\hbar = 0.02$. **Panel (c):** Caustic surface for the spun cusp, for negative C_5. The 2D circular caustic and the axial caustic are highlighted in red.

C. Gaussian Initial states

Using the same system parameters, let us revisit our earlier choice of initial state as an equal superposition of Fock states [Eq. (29)] which is the Fock space analogue of a plane wave. The primary goal of this choice is to demonstrate the natural focusing effect of the BH dynamics. We claim that any sufficiently wide spread of initial Fock states will yield qualitatively similar results with only slightly altered coefficients. As an example, consider the ground state of the trimer model (8) for $U = 0$,

$$|\psi_G\rangle = \sum_{n_1+n_2+n_3=N} \sqrt{\frac{N!}{3^N n_1! n_2! n_3!}} |n_1, n_2, n_3\rangle \quad (44)$$

where the sum is over all Fock space occupation numbers such that $n_1 + n_2 + n_3 = N$. For more detail on the diagonalization of this model, see, e.g., Ref. [214] and references therein. In the limit of large N, this coherent state closely resembles a Gaussian centered at $\delta n_2 = n_X = 0$.
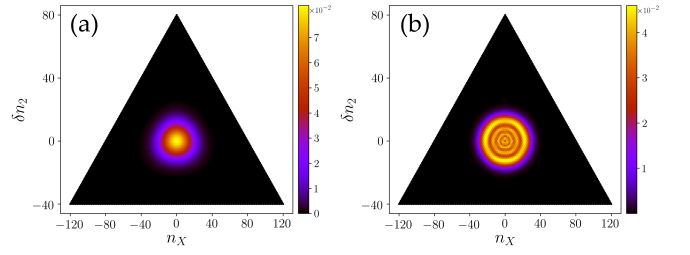
VII. BEYOND THE QUANTUM PHASE MODEL

In the QPM the effects of depletion of the modes [accounted for by the square root factors in the RN equations Eq. (11)] are ignored. This is often a good approximation in experimentally realizable superfluids, including arrays of Josephson junctions [170, 171] and also some
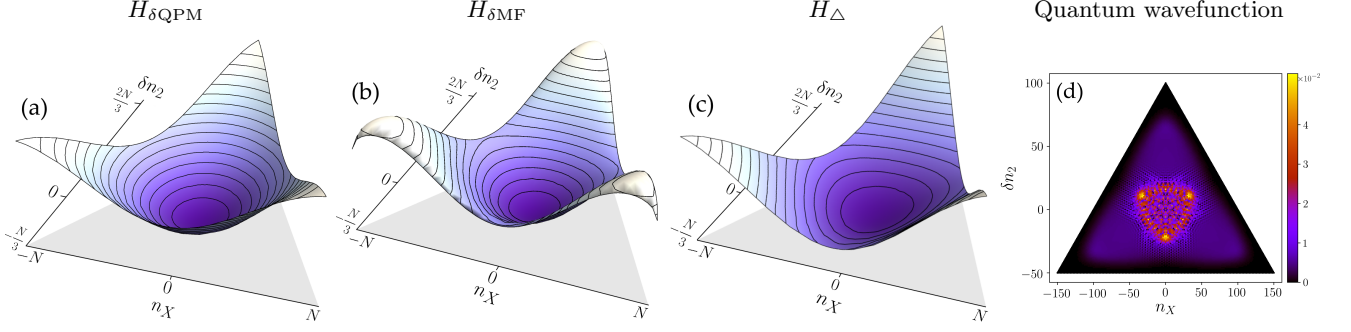
FIG. 13. Breaking circular symmetry by going beyond the QPM. **Panel (a):** The energy surface determining classical trajectories as provided by $H_{\delta\mathrm{QPM}}$ in Eq. (28) immediately following the δ-kick at $t = 0$. The initial values of the dynamical variables that generate this surface are $\phi_X = \phi_C = 0$ and an equal superposition of all number differences; the phase trajectories are bent by the δ-kick as explained in Appendix A. The overall scale is arbitrary and lighter colours represent higher energy. Note the circular symmetry as seen from the contour lines. **Panel (b):** Same as panel (a) but now with the δ-kicked mean-field Hamiltonian $H_{\delta\mathrm{MF}}$ given in Eq. (47) with all hopping amplitudes equal. The circular symmetry is broken by the square root factors and the resulting three-fold symmetric 'valleys' will act to pinch the caustic away from the corners of Fock space. **Panel (c):** Same as panel (a) but now with $H_{\triangle}$ as given in Eq. (48). In this Hamiltonian the square root factors have been expanded to first order and this is enough break the circular symmetry and replace it with a three-fold symmetric energy surface. **Panel (d):** Quantum wavefunction obtained using the full RN equations with δ-kicked interactions (quantum equivalent of $H_{\delta\mathrm{MF}}$) and the same parameters as used in Fig. 11 (b). The chosen time is $t = \hbar^2/(JN\tilde{U})$ which is twice that of where the cusp point appears.

regimes of atomic BECs in optical lattices [164–169]. However, in terms of caustics it can lead to some special situations such as the appearance of a $K = 2$ spun-cusp caustic for the triangular trimer with $K_X = J$, as discussed in the previous section. This has circular symmetry which is of course non-generic and, indeed, the modulus $K = 2$ is excluded from the X_9 catastrophe. The symmetry is broken by any perturbation which is noncircular, such as choosing $K_X \neq J$. Counter-intuitively, another way to break the symmetry is to go beyond the QPM by including the effects of the square root factors. For our purposes of illustrating generic many-body caustics, it suffices to expand the square roots and keep just the first order corrections because this is enough to generate the X_9 catastrophe (even when all the hopping amplitudes are equal), thereby providing an instructive example of structural stability, or lack thereof, for caustics that do not correspond to catastrophes.

A. Triangular deformations: a path integral formulation

The mean-field Hamiltonian that retains the square root factors, has δ-kicked interactions and all-equal hopping is given by

$$H_{\delta\mathrm{MF}} = -J\sqrt{2(\delta n_2 + \tfrac{N}{3})(n_X - \delta n_2 + \tfrac{2N}{3})}\cos(\phi_X - \phi_C)$$
$$-J\sqrt{2(\delta n_2 + \tfrac{N}{3})(-n_X - \delta n_2 + \tfrac{2N}{3})}\cos(\phi_X + \phi_C)$$
$$-J\sqrt{(\delta n_2 - \tfrac{2N}{3})^2 - n_X^2}\cos(2\phi_X) + \delta(t)\frac{\tilde{U}}{4}\left[3\delta n_2^2 + n_X^2\right].$$
$$(47)$$

In Fig. 13(a) and (b) we compare the energy surfaces produced by $H_{\delta\mathrm{QPM}}$ and $H_{\delta\mathrm{MF}}$. It is evident from the contour lines that $H_{\delta\mathrm{MF}}$ breaks the circular symmetry and replaces it with a triangular one. However, as explained above, our interest is more in generic many-body caustics rather than specific models, so all we really need to do is perturb away from the QPM and hence we expand the square roots in $H_{\delta\mathrm{MF}}$ and keep only the first order corrections:

$$H_{\triangle} = -\frac{J}{2}\left(n_X + \delta n_2 + \frac{2N}{3}\right)\cos(\phi_X - \phi_C)$$
$$-\frac{J}{2}\left(-n_X + \delta n_2 + \frac{2N}{3}\right)\cos(\phi_X + \phi_C)$$
$$-J\left(\frac{2N}{3} - \delta n_2\right)\cos(2\phi_X) + \delta(t)\frac{\tilde{U}}{4}\left[3\delta n_2^2 + n_X^2\right]$$
$$\equiv NJ\Phi_{\triangle} + \delta(t)\frac{\tilde{U}}{4}\left[3\delta n_2^2 + n_X^2\right] . \qquad (48)$$

As can be seen from the energy surface in Fig. 13(c), this 'triangular' Hamiltonian retains the basic triangular symmetry possessed by the full mean-field model. The cone shape of the energy surface present in all three models has an overall focusing effect on trajectories, but the triangular shape of the latter two models channels the trajectories away from the three corners of Fock space and effectively pinches the outer part of the caustic in three spots. This can be seen in the quantum version shown in panel (d) created using the RN equations under no approximations at $t = 2t_{\mathrm{cusp}} = \hbar^2/(JN\tilde{U})$. The caustic evolves at roughly the same speed in both the classical and quantum cases, and three bright spots appear both before and after the cusp point and correspond to the
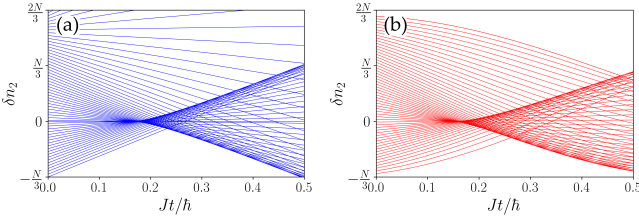
FIG. 14. Stability of cusp formation in the $n_X = 0$ plane against inclusion of beyond QPM effects. **Panel (a):** Set of classical trajectories for the δQPM when $n_X = 0$ starting from a range of δn_2 values and kicked with $\tilde{U}/\hbar = 0.02$. The cusp point here is $Jt/\hbar \approx 0.167$. **Panel (b):** Exact trajectories (without approximation to the square root factors) for the triangular trimer with a kicked interaction term as given by $H_{\delta\text{MF}}$. The cusp structure remains intact and is only curved near the edge of Fock space, showing that the δQPM is a good approximation for this sub-catastrophe and that caustics have structural stability against perturbations.

three valleys on the triangular energy surfaces. Another crucial feature is that there is no bright patch at the center of Fock space, due to the destruction of the axial caustic which is a feature peculiar to circular symmetry.

In order to treat this problem analytically we need to reconsider our approach, since calculating an analytic form for the wavefunction as a single diffraction integral in the same manner as we did for the δQPM is not possible for the full Hamiltonian. More precisely, in the δQPM there is a separation between the phase and number difference variables, like in a standard $H = p^2/2m + V(x)$ type Hamiltonian, allowing us to integrate out the number (momentum) variable using gaussian integrals leaving a diffraction integral purely in terms of the phase (position) variables. The presence of the square root factors

effectively gives us a potential $V(x,p)$ which depends on both position and momentum variables. This difficulty is not reduced by expanding out the square root factors and we instead resort to a phase space path integral-style formulation for the wavefunction:

$$\psi(n_X, \delta n_2, t) = \langle n_X, \delta n_2 | \hat{\mathcal{F}} | \psi(0) \rangle \qquad (49)$$

$$\propto \int \mathcal{D}\phi \mathcal{D}n \ e^{i\mathcal{S}[\boldsymbol{n}(\tau), \boldsymbol{\phi}(\tau)]} \qquad (50)$$

where we have introduced the bold vector notation $\boldsymbol{\phi} = (\Theta, \phi_X, \phi_C)$ and $\boldsymbol{n} = (\frac{N}{3}, n_X, \delta n_2)$. In the semiclassical regime the dominant contributions to the path integral come from the evaluation of the action $\mathcal{S}$ along *classical paths* which we denote by $\{\bar{\boldsymbol{n}}, \bar{\boldsymbol{\phi}}\}$. However, the standard WKB approximation blows up precisely at caustics because these are places where saddles of $\mathcal{S}$ coalesce. Following Schulman [215] and Dangelmayr and Veit [216], a proper treatment of the problem shows that the leading contribution to the path integral close to caustics can be factorized into a part involving the phase along the classical path and part which is a diffraction integral

$$\psi(\boldsymbol{n}, t) \propto e^{i\mathcal{S}(\bar{\boldsymbol{n}}, \bar{\boldsymbol{\phi}}, t)} \int \int ds_1 ds_2 \ e^{i\lambda \Phi_Q(\boldsymbol{s}; \boldsymbol{C})} , \qquad (51)$$

(in the above cited papers the diffraction integral is sometimes referred to as a 'generalized Airy function'). For the BH trimer model, $\boldsymbol{s}$ is two-dimensional and dependent on $\boldsymbol{\phi}$, and the control parameters $\boldsymbol{C}$ depend on the remaining parameters of the system, including $\boldsymbol{n}$.

The action that appears in Eq. 49 can be derived by breaking up the time evolution operator into infinitesimal steps, i.e. applying the Trotter prescription to the operator $\hat{\mathcal{F}}$ with $H_\triangle$. The details of this calculation are presented in Appendix C where we find

$$\mathcal{S}[\boldsymbol{n}(\tau), \boldsymbol{\phi}(\tau)] = \int_0^{\frac{NJt}{\hbar}} d\tau \left[\boldsymbol{n} \cdot \dot{\boldsymbol{\phi}} - \Phi_\triangle \right] + \frac{\hbar}{3\tilde{U}} \left[\phi_C^2(0) + 3\phi_X^2(0) \right] \qquad (52)$$

$$= \int_0^{NJt/\hbar} d\tau \left[\left(\frac{1}{2} - \frac{5}{8N}\delta n_2 \right) \phi_X^4 + \left(\frac{1}{18} + \frac{1}{24N}\delta n_2 \right) \phi_C^4 + \left(\frac{1}{3} + \frac{1}{4N}\delta n_2 \right) \phi_X^2\phi_C^2 - \frac{1}{6N}n_X \left(\phi_X^3\phi_C + \phi_X\phi_C^3 \right) \right.$$

$$\left. - \left(2 - \frac{3}{2N}\delta n_2 \right) \phi_X^2 - \left(\frac{2}{3} + \frac{1}{2N}\delta n_2 \right) \phi_C^2 + \frac{n_X}{N}\phi_X\phi_C + \boldsymbol{n} \cdot \dot{\boldsymbol{\phi}} \right] + \frac{\hbar}{3\tilde{U}} \left[\phi_C^2(0) + 3\phi_X^2(0) \right] .$$

Comparing to the standard relation $L = p\dot{x} - H$, we see that the generating function Φ plays the role of a Lagrangian.

The action given in Eq. (52) is not in a canonical form for any unfolding of X_9, since the coefficients of the fourth order phase variables have not been appropriately scaled away yet, and the terms $\phi_X^3\phi_C$ and $\phi_X\phi_C^3$ are still present. It is possible to remove these terms by an appropriate change of variables, resulting in the introduction

of the cubic unfolding terms ϕ_X^3 and $\phi_X\phi_C^2$, which lead to triangular symmetry and a stable caustic. However we shall not attempt this here since it involves the simultaneous solution of five equations of quartic and cubic order. We shall instead proceed by restricting ourselves to the projection $n_X = 0$. In Fig. 14 we plot the classical trajectories in the $n_X = 0$ plane and compare between the $H_{\delta\text{QPM}}$ and the $H_{\delta\text{MF}}$ cases. As expected, in (1+1)D the stable caustics are cusps and indeed the cusp point
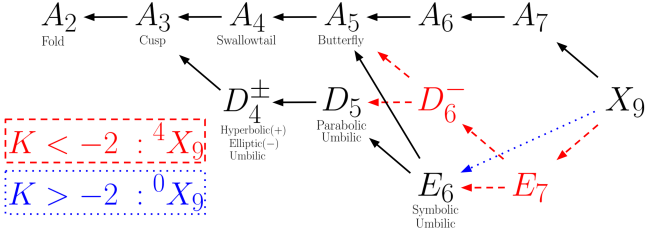
FIG. 15. Bordering (or abutment) diagram for the catastrophe X_9, adapted from Nye [49] and obtained using theorems of catastrophe projection. Each catastrophe of higher order contains (many, not necessarily all) catastrophes of lower order, shown by the direction of arrows. The subfamilies of X_9 lead to two different sub-catastrophe sets. $^4X_9$ contains the singularities E_7 and D_6, shown by the red dashed arrows. $^0X_9$ does not contain E_7 and will only contain E_6, shown by the blue dotted arrow.

occurs nearly simultaneously for $H_{\delta\mathrm{QPM}}$ and the $H_{\delta\mathrm{MF}}$. This is because the square roots multiplying the cosines do not drastically affect the shape of the focusing surface near the centre of Fock space. Rather, the effects of the square roots only become significant near the edges of Fock space, a region in which the QPM approximation becomes inaccurate. Indeed, we see from Fig. 14 that the effect of the square root factors is to make fold lines of the full model, shown in panel (b), become curved near the boundaries. Thus, although the rotational symmetry of the caustic is removed by beyond QPM effects, other features of the caustic are robust against such changes, a result that follows from structural stability.

Nevertheless, the $n_X = 0$ projection does allow us to account for some beyond-QPM effects and even obtain qualitative features such as the subfamily of X_9 that results from the breaking of the circular symmetry in $H_\triangle$ and $H_{\delta\mathrm{MF}}$. In particular, after scaling phase variables to put X_9 in its canonical form, the modulus for the restricted problem for $H_\triangle$ becomes,

$$K_{n_X=0}(\delta n_2) = (8N + 6\delta n_2)\sqrt{\frac{1}{3\delta n_2 + 4N}}\sqrt{\frac{1}{4N - 5\delta n_2}} \, . \tag{53}$$

This result warrants some explanation because the wavefunction contains a range of the Fock space variables $(\delta n_2, n_X)$, and hence there is no single well defined value of the modulus. However, because all physical paths must lie in the interval $-\frac{N}{3} \leq \delta n_2 \leq \frac{2N}{3}$, we have to first order, $\frac{6}{\sqrt{17}} \leq K \leq 6$ with $K = 2$ occurring only at $\delta n_2 = 0$. This range of values for K indicates that the system symmetry selects the $^0X_9$ subfamily of X_9, and specifically its $^0X_9^+$ variant, called *compact* by Callahan [212]. A schematic plot, known as an 'abutment' or 'bordering' diagram is given in Fig. 15 which summarizes the relationships between the sub-catastrophes which can appear within X_9 [49]. We see that the $^0X_9$ subfamily does not contain the umbilic catastrophes E_7 or D_6 given in Table II, both of which are instead members of the $^4X_9$ sub-
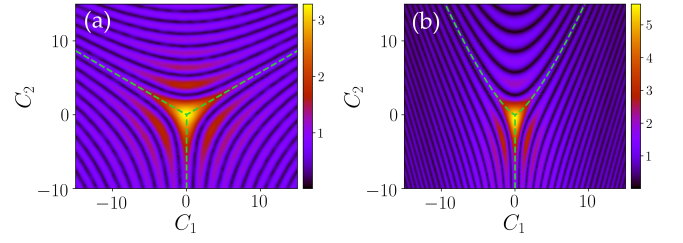

FIG. 16. Most singular sections of the diffraction patterns for D_4^- and D_6^- showing how the foci of the two sub-families of X_9 differ. **Panel (a)** The focal plane of D_4^- revealing an elliptic umbilic focus. **Panel (b)** The focal plane of D_6^- revealing another, but subtly different type of elliptic umbilic-like structure. In the case of D_4^- the caustic in its canonical form is threefold symmetric with the brightest ribs (traced with green dashed lines) meeting in straight lines at angles of $2\pi/3$. For D_6^- the bright central ribs meet along *curved* lines obeying $27C_2^4 = 64C_1^3$. The presence of a D_6^- focus can in principle be a diagnostic tool for determining the presence of $^4X_9$.

family. Diagnosing the family of X_9 experimentally via the sub-catastrophes is in principle possible via a careful analysis of elliptic umbilic foci [Fig. 1(c), the last time slice in Fig. 3(b), and Figs. 7(a) and (b) all show elliptic umbilic foci]. As illustrated in Fig. 16, elliptic umbilic foci are three-fold symmetric about straight axes of symmetry meeting at the origin, while for D_6^- two of these lines become curved and the pattern is only two-fold symmetric (see Nye [217] for more details).

There is an important lesson to be learned from Eq. (53) and the fact there is no single value of the modulus (except locally, at the origin of Fock space). Catastrophes have their origin in topology, and as such there is considerable flexibility as to their precise shape. In fact each catastrophe forms an equivalence class, where different specific realizations within each class are related by smooth transformations (diffeomorphisms) of state variables and control parameters (there is no smooth mapping between different classes). The dynamics of a nonlinear system such as the BH model results in a caustic of the X_9 class which slowly varies in space-time but which is not destroyed by nonlinearities.

B. Unequal hopping amplitudes

So far our consideration of beyond-QPM dynamics has centered on the effect of mode depletion accounted for by the square root factors. However, one can also consider the situation where we have already included the effects of the mode depletion but then additionally break the symmetry further by making the hopping amplitudes unequal (a similar effect could be had by including a bias, $\epsilon_i \neq 0$). In Fig. 17 we see the effects of changing the hoppings so that they are slightly detuned from one another ($K_R \neq K_L \neq K_X$). The elliptic umbilic caustic
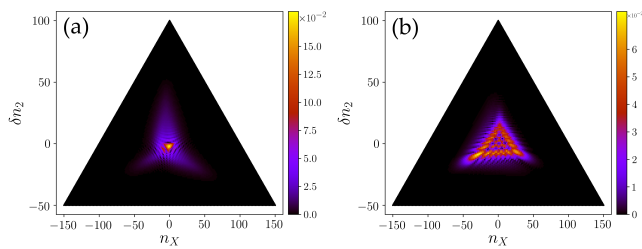
FIG. 17. Distorted elliptic umbilic due to unequal hopping strengths using the full trimer Hamiltonian. $K_R = 1.1K_L$, $K_X = 1.2K_L$, $U/K_L = 0.01$ and $N = 150$, starting from an equal superposition of Fock states. **Panel (a):** Distorted focus at $K_L t/\hbar = 0.431$. **Panel (b):** Unfolded at $K_L t/\hbar = 0.513$

becomes distorted and asymmetric, but due to the structural stability of the underlying catastrophe it remains intact and recognizable. In particular, panel (a) shows the effect on the focus, which can be shifted in space and time but clearly retains its form. Likewise for panel (b) which shows a time slice somewhat after the focus.

VIII. ROLE OF INTERACTIONS

In their original setting of natural optics (rainbows etc.), caustics occur in a linear and hence integrable system. Similarly, the BH dimer is an integrable, albeit nonlinear, system as long as energy is conserved. The trimer, by contrast, is not generally integrable. In our analytic calculations in this paper we used δ-kicked interactions such that the time evolution is integrable. While this made calculations possible, it does raise the question of the stability of caustics in the presence of constant interactions. It is therefore worth emphasizing again that all the (numerical) examples of caustics shown in Section V were obtained with the interactions switched on throughout the time evolution. Moreover, interactions can sometimes be *necessary* for catastrophes to fully manifest in both the dimer and trimer. This is best understood with an example, as given in Fig. 18. In panel (a) $U = 0$, $K_L = K_R = J$, and $K_X = 0$, for which the quantum revival time is $Jt_{rev}/\hbar = \pi/\sqrt{2}$ (the recurrence time is twice this time). Starting from an even spread of Fock states, we observe a set of classical trajectories in the $n_X = 0$ plane, similar to Fig. 6(a) except that here the trajectories form isolated focal points. According to catastrophe theory these are unstable in two dimensions and indeed, in panel (b) where interactions are present the focal points are unfolded to cusps. For variety we have chosen attractive interactions $U < 0$ here whereas Fig. 6 has repulsive interactions $U > 0$. The difference is that we find forward-opening cusps for $U > 0$ and backward-opening cusps for $U < 0$. The effect is similar when starting from a highly focused state, such as a Fock state, where a point focus will recur infinitely unless interactions are introduced and structurally stable caus-
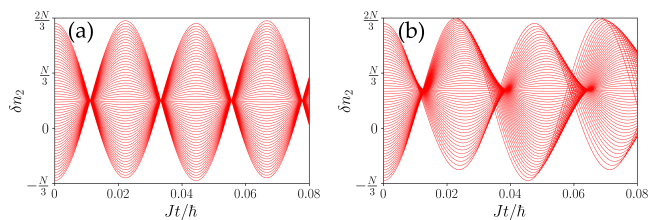

FIG. 18. Instability of perfect focusing events to the introduction of interactions. **Panel (a):** Set of classical trajectories starting from an equal spread of Fock states, with $K_L = K_R$, $U = K_X = 0$. Focusing events are isolated, meaning that all trajectories meet at a point. **Panel (b):** Same initial state as panel (a), but now with weakly attractive interactions, $K_L = K_R \equiv J$ and $U/J = -0.03$. A similar result was found for repulsive interactions in panel (a) of Fig. 6, except that the cusps open in the opposite direction for attractive interactions.

tics form. The nonlinearity introduced by interactions is therefore crucial to fully unfold the caustics (essentially by introducing different periods for different amplitudes of excitation).

Another example of dynamics with attractive interactions is shown in Fig. 19. The effect of negative U is to pull the caustic outwards towards the corners of Fock space in comparison to the case of the repulsive U shown in Fig. 8. This means that the elliptic umbilic emerges more clearly before the central focusing event, but also results in fold 'lips' around the edges of each cusp point.
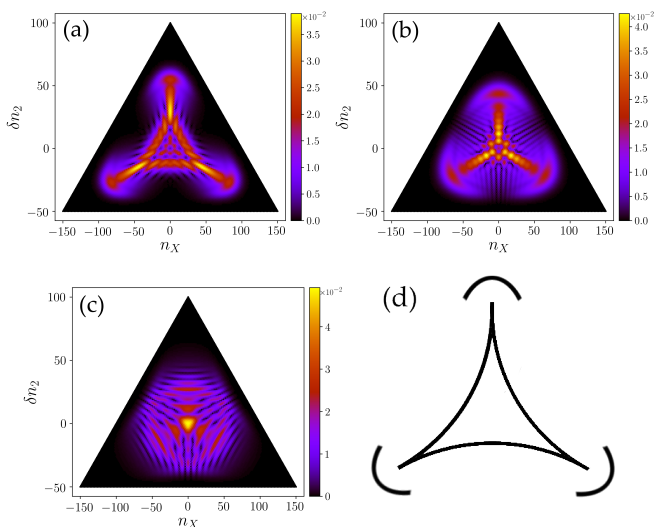
FIG. 19. Formation of fold lines around cusps due to attractive interactions. **Panel (a):** Same as panel (c) of Fig. 7, now with $U/J = -0.01$. The elliptic umbilic diffraction pattern is now surrounded by bright fringes, which consist of small fold lines. **Panels (b)-(c):** Same as panel (a) but at $Jt/\hbar = 0.641$ and $Jt/\hbar = 0.818$. As the elliptic umbilic focus is approached, the fold lines around each cusp extend and form a ring. **Panel (d):** Schematic of a section of the elliptic umbilic caustic, with 'lips' surrounding each cusp point.

The formation of lips around an elliptic umbilic caustic appears to be a threefold symmetric version of the fourfold unfolding of X_9 with a negative modulus studied in [208] (see also Fig. 9). These lips continue to extend into long fold lines as time progresses and ultimately intersect one another after the elliptic umbilic focus, reminiscent of the triple glass junction studied by Berry [209] and later elaborated on by Nye [49].

Finally, we note that our choice of parameters in this paper has been guided empirically so as to make the catastrophes as visible as possible. For example, the elliptic and hyperbolic umbilic unfoldings shown in Section V were made using relatively weak interactions in the range $U/J = 0.01J$ to $U/J = 0.25J$. This regime is called the strong-tunneling (or Josephson [179]) regime (see Refs. [149, 176, 182, 184, 185, 193]), and exhibits moderate quantum revivals, allowing the catastrophes to be clearly identified because a single caustic stretches across a good fraction of Fock space. Stronger interactions result in more powerful effective focusing potentials which, in the case of repulsive interactions, compress the wavefunction into a small region around the center of Fock space. In Fig. 20(a) we show that the canonical hyperbolic umbilic catastrophe is still visible even when $U = J$, although Fig. 20(b) indicates that at longer times this wavefunction evolves into a highly intricate structure (which will eventually reveal the discreteness of Fock space as the wavefunction fringes reach small scales). The highly distorted wavefronts that arise in this situation would probably be best described using the statistical version of catastrophe theory developed in the context of light passing through a turbulent atmosphere [46], where caustics manifest themselves as extreme amplitude events that occur more frequently than expected from random Gaussian fluctuations. This is the freak/rogue wave paradigm recently explored in microwave [55] and optical [59–67] experiments.

IX.   CONCLUSIONS AND EXPERIMENTAL PERSPECTIVES

Using a combination of exact numerical computations and analytic calculations (in the δ-kicked case), we have demonstrated the existence of simple and higher caustics in integrable and nonintegrable quantum many-body dynamics. More precisely, using a variety of initial states (broad and narrow in Fock space) we have shown that caustics occur generically following a quench in the BH dimer and trimer models even when the latter is in the chaotic regime (e.g. when $U \sim J$). In the semiclassical regime caustics dominate the many-body wavefunction which takes on characteristic patterns that are stable against perturbations to both the Hamiltonian and initial conditions. Catastrophe theory provides a mathematically rigorous tool for predicting and analyzing these universal wavefunctions. The universality of wave catastrophes is underlined by the fact that we find the same
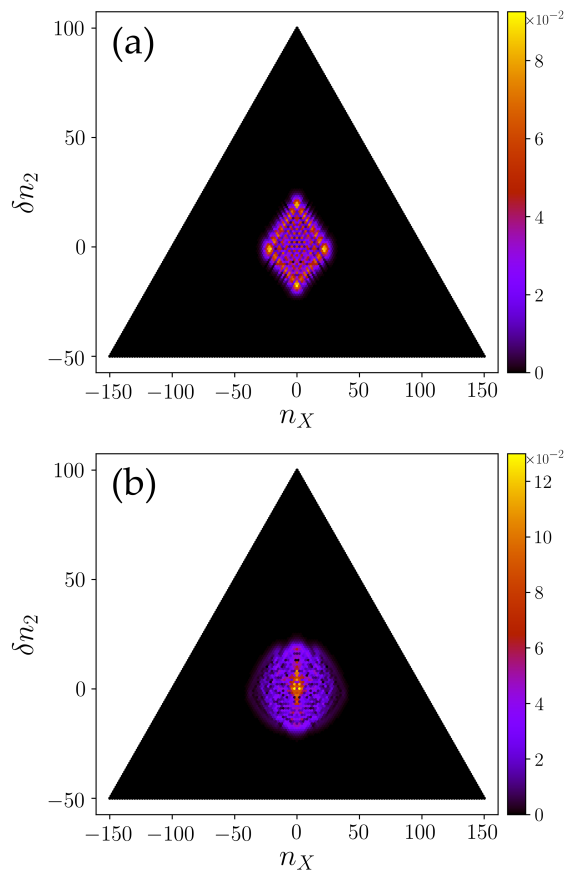

FIG. 20.   Catastrophe formation at high interaction strength. In this figure, we show exact (numerical) dynamics deep in the chaotic regime with $U = J$ in the linear BH trimer where $K_L = K_R \equiv J$, and $K_X = 0$. Caustic formation follows similarly to previously discussed cases with weaker interactions, however stronger interactions restrict the dynamics to a smaller region in Fock space. **Panel (a):** Formation of a fourfold diffraction pattern at $Jt/\hbar = 0.13$, similar to the one seen in Fig. 8(a), but its largest extent is smaller than the weaker interaction case. **Panel (b):** At $Jt/\hbar = 0.36$, the wavefront has become highly distorted, although strong focusing (fluctuations) remains.

basic caustic structures in the optics of liquid droplet lenses whose principal curvatures have been modified by a triangular perimeter, as shown in Fig. 1, as we do in the triangular Fock space of the BH trimer.

One may ask, if caustics are generic and striking why have they not been seen already? The answer is that they have been seen following quenches in experiments on ultracold atoms in optical lattices and trapped ions in the form of so-called light cones [1–5]. As shown in our previous paper on spin chains [40], and as we explain in Section III in this paper, light cones are caustics closely analogous to ship wakes. The ones seen experimentally so far are fold catastrophes (which have an Airy function profile [1]) and are the simplest in the hierarchy we discuss in Sec. III. Turning this around, the higher caustics

we predict can be viewed as *generalized light cones.*

Caustics will manifest themselves in experiments as *singularity dominated fluctuations* that are stronger than the random gaussian fluctuations one expects during generic chaotic dynamics [218]. For cold atoms in an optical lattice this means strong fluctuations (which form universal patterns) in the probability distribution for populations of different sites, see Figs. 3,5,6,7,8,9,10,11,12,13,14,17,18,19, and 20. In fact, thanks to advances in imaging such as the quantum gas microscope [219, 220], it is now possible to monitor the population of single sites *in situ* in optical lattices at the single atom level and thereby directly measure the Fock-space probability distribution, just as was done in the observation of light cones [1] and many-body localization [6, 7]. Alternatively, miscible spin-1 gases (as can be realized using ^{23}Na) where the atoms occupy the same spatial mode, also offer a highly controllable environment for exploring integrable and nonintegrable three-mode many-body dynamics where the populations of the three Zeeman sublevels can be obtained using Stern-Gerlach type measurements [41].

The above mentioned experimental examples suggest that it may soon be possible to map out wave catastrophe patterns in many-body wavefunctions in some detail. However, it should be borne in mind that there are fundamental differences between classical and quantum waves and this impacts the information we can extract in a single projective measurement. In classical waves, the wave catastrophe patterns can be captured in a single shot like in Fig. 1, whereas in the quantum case a measurement in the Fock basis will randomly collapse the wavefunction to give us a single Fock state. Thus, a single absorption image of the BH trimer case will yield just two numbers: the two relative population differences between the three wells (assuming total number conservation). The experiment must be repeated many times under the same conditions in order to build up a probability distribution for the population differences and thereby reveal the caustics in the probability distribution. The whole scheme should then be repeated for different evolution times if we wish to map out the full three dimensional dynamical caustic. This is a challenging task, and there is no getting around the fact that quantum many-body wavefunctions are high dimensional objects containing a huge amount of information, but it is important to note that measuring the probability distribution is a simpler task than full quantum tomography (see [39] for a discussion). It should also be pointed out that caustics equally occur in the phase-difference variables [37] conjugate to the number-difference variables and hence caustics can alternatively be seen by releasing the atoms from the wells and imaging after some time of flight to allow the atom clouds from each well to overlap and interfere [221].

In traditional measurements on condensed matter systems it is not the full wavefunction that is usually measured directly but one- and two-point correlation functions that are obtained. Although we have chosen to focus on the wavefunction in this paper, it is the key object needed to calculate correlation functions and we have seen here how it takes on universal forms. Furthermore, in our previous work on light-cones in integrable systems [40] we showed that due to the hierarchy of catastrophes and the projection identities they obey (such that the higher ones contain the lower ones), correlation functions also contain caustics. For example, the equal-time two-site correlation function on a spin chain can be expressed as the product of two single quasiparticle wavefunctions evaluated at different points (see Section VII of [40]) and gives codimension 3 catastrophes such as the hyperbolic umbilic. Based on the results of the present paper, we expect that following a quench correlation functions for nonintegrable systems will also display caustics.

Rather than a finished theory, the results presented in this paper are merely one step on the road to understanding caustics in quantum many-body systems. In going to systems with a larger number of wells we encounter higher dimensional Fock spaces and hence higher dimensional catastrophes. In these cases it is easier to proceed by going over to the statistical version of catastrophe theory mentioned in Section VIII and developed in the context of random focusing of light passing through a turbulent atmosphere [46], that has also been applied to freak waves in hydrodynamics and optics [59–67]. The statistical theory aims to predict the 'twinkling exponents' of fluctuations. Perhaps surprisingly, it is not the higher order (more singular) catastrophes that necessarily dominate these fluctuations due their relative rarity. Moreover, the existing theory for classical waves will need to be revised since in the quantum case there is a new scale provided by the discretization in Fock space that can alter the finest details and potentially change the exponents.

Appendix A: Classical Trajectories of the δQPM

Using Hamilton's equations of motion,

$$\dot{n}_2 = -\frac{1}{\hbar}\frac{\partial H}{\partial \phi_C} \tag{A1}$$

$$\dot{n}_X = -\frac{1}{\hbar}\frac{\partial H}{\partial \phi_X} \tag{A2}$$

$$\dot{\phi}_C = \frac{1}{\hbar}\frac{\partial H}{\partial n_2} \tag{A3}$$

$$\dot{\phi}_X = \frac{1}{\hbar}\frac{\partial H}{\partial n_X} \tag{A4}$$

The δ-kick allows classical trajectories to be calculated directly via integration,

$$\phi_C(t) = \phi_C(0) + \frac{3U}{2\hbar}\delta n_2(0)\Theta(t) \tag{A5}$$

$$\phi_X(t) = \phi_X(0) + \frac{U}{2\hbar}n_X(0)\Theta(t) \ , \tag{A6}$$

where we make use of the Heaviside function,

$$\Theta(t) = \begin{cases} 1 & t > 0 \\ 0 & t \leq 0 \end{cases} \tag{A7}$$

First, for the circular trimer, assuming a classical analogue of an equal superposition of Fock states corresponds to an ensemble of classical trajectories, each with different $\{\delta n_2(0), n_X(0)\}$, but all $\phi_C(0) = \phi_X(0) = 0$, then for $t > 0$,

$$\delta n_2(t) = \delta n_2(0) - \frac{4JNt}{3\hbar}\cos\left(\frac{U}{2\hbar}n_X(0)\right)\sin\left(\frac{3U}{2\hbar}\delta n_2(0)\right) \tag{A8}$$

$$n_X(t) = n_X(0) - \frac{4JNt}{3\hbar}\left[\cos\left(\frac{3U}{2\hbar}\delta n_2(0)\right)\sin\left(\frac{U}{2\hbar}n_X(0)\right) \right. \tag{A9}$$

$$\left. + 2\cos\left(\frac{U}{2\hbar}n_X(0)\right)\sin\left(\frac{U}{2\hbar}n_X(0)\right)\right]$$

Note that the trajectories $n_X(0) = \delta n_2(0) = 0$ have no time dependence and correspond exactly to the unstable axial caustic in the $K = 2$ excluded family of X_9.

In the case of the linear oligomer ($K_X = 0$), then $\delta n(t)$

remains the same, while,

$$n_X(t) = n_X(0) - \frac{4JNt}{3\hbar}\cos\left(\frac{3U}{2\hbar}\delta n_2(0)\right)\sin\left(\frac{U}{2\hbar}n_X(0)\right) \ . \tag{A10}$$

Appendix B: Dependence of δQPM wavefunction on K_X

For general K_X, the Hamiltonian (28) yields wavefunctions of the same form as in Eq. (32), but now with modulus,

$$K = \frac{6}{\sqrt{\frac{8K_X}{J} + 1}} \tag{B1}$$

and control parameters,

$$\alpha = \frac{\sqrt{2}\left(3\hbar^2 - 2NJtU - 4NtUK_X\right)}{NJtU\sqrt{\frac{8K_X}{J} + 1}} \tag{B2}$$

$$\beta = \frac{\sqrt{2}\left(\hbar^2 - 2JNtU\right)}{JNtU} \tag{B3}$$

$$\zeta = \frac{2^{1/4}\sqrt{3}\hbar}{NJt\left(\frac{8K_X}{J} + 1\right)^{1/4}}n_X \tag{B4}$$

$$\eta = \frac{2^{1/4}\sqrt{3}\hbar}{NJt}\delta n_2 \tag{B5}$$

and

$$A(t) = \left(\frac{324}{8K_X/J + 1}\right)^{1/4}\frac{4\pi\hbar}{\sqrt{3}U}e^{-i\frac{\pi}{2}}e^{i\frac{2NJt}{\hbar}} \ . \tag{B6}$$

Appendix C: Derivation of the Path Integral

Starting with the Hamiltonian given in Eq. (48) which goes beyond the QPM by including the square root factors to first order and hence includes effects due to the triangular boundaries of Fock space, we expand the cosine terms to fourth order in the phase difference coordinates to give

$$H_\triangle \approx -NJ\left[\left(\frac{1}{2} - \frac{5}{8N}\delta n_2\right)\phi_X^4 + \left(\frac{1}{18} + \frac{1}{24N}\delta n_2\right)\phi_C^4 + \left(\frac{1}{3} + \frac{1}{4N}\delta n_2\right)\phi_X^2\phi_C^2 - \frac{1}{6N}n_X\left(\phi_X^3\phi_C + \phi_X\phi_C^3\right) \right. \tag{C1}$$

$$\left. -\left(2 - \frac{3}{2N}\delta n_2\right)\phi_X^2 - \left(\frac{2}{3} + \frac{1}{2N}\delta n_2\right)\phi_C^2 + \frac{n_X}{N}\phi_X\phi_C\right] + \delta(t)\frac{\tilde{U}}{4}\left[3\delta n_2^2 + n_X^2\right]$$

$$\equiv NJ\Phi_\triangle + \delta(t)\frac{\tilde{U}}{4}\left[3\delta n_2^2 + n_X^2\right] \ . \tag{C2}$$

Notice that relative to the expansion of $H_{\delta\text{QPM}}$, all of the circularly symmetric terms get a perturbation proportional to δn_2 and we also pick up some non-circularly symmetric terms proportional to n_X. Applying the Floquet operator incorporating this Hamiltonian to an initial state comprising of an equal superposition of all Fock states, and projecting

onto the Fock basis, we obtain the wavefunction

$$\psi(n_X, \delta n_2, t) = \sum_{n'_X, \delta n'_2} e^{-i\frac{U}{4}\left[3\delta n'^2_2 + n'^2_X\right]} \langle n_X, \delta n_2| e^{i\frac{NJt}{\hbar}\Phi_\triangle(\hat{n}_X, \delta\hat{n}_2, \hat{\phi}_C, \hat{\phi}_X)} \underbrace{|n'_X, \delta n'_2\rangle}_{\mathbb{1} \approx \sum_{\Theta, \phi_X, \phi_C} |\Theta, \phi_X, \phi_C\rangle\langle\Theta, \phi_X, \phi_C|} \tag{C3}$$

$$= \int d\Theta d\phi_X d\phi_C \, \langle n_X, \delta n_2| e^{i\frac{NJt}{\hbar}\Phi_\triangle(\hat{n}_X, \delta\hat{n}_2, \hat{\phi}_C, \hat{\phi}_X)t} |\Theta, \phi_X, \phi_C\rangle e^{-i\frac{\Theta N}{3}} \underbrace{\sum_{n'_X, \delta n'_2} e^{-i\frac{U}{4\hbar}\left[3\delta n'^2_2 + n'^2_X\right]} e^{-i\left[n'_X\phi_X + \delta n'_2\phi_C\right]}}_{\approx \frac{4\pi\hbar}{i\sqrt{3}\tilde{U}} \exp\left[\frac{i\hbar}{3\tilde{U}}\left(\phi^2_C + 3\phi^2_X\right)\right]} \tag{C4}$$

where in the first line we have indicated where a resolution of the identity in terms of phase states should be inserted, and in second line we have turned the resulting double sums over phase variables into integrals as well as indicating that the double sum over the primed number variables can be approximated by gaussian integrals. Let us now focus on the matrix elements of $e^{i\frac{NJt}{\hbar}\hat{\Phi}_\triangle}$,

$$\langle n_X, \delta n_2| e^{i\frac{NJt}{\hbar}\Phi_\triangle(\hat{n}_X, \delta\hat{n}_2, \hat{\phi}_C, \hat{\phi}_X)} |\Theta, \phi_X, \phi_C\rangle \approx \langle n_X, \delta n_2| \left(\mathbb{1} + i\frac{NJt}{M\hbar}\hat{\Phi}_\triangle\right)^M |\Theta, \phi_X, \phi_C\rangle \tag{C5}$$

$$= \langle n_X, \delta n_2| \underbrace{\left(\mathbb{1} + i\frac{NJt}{M\hbar}\hat{\Phi}_\triangle\right)\left(\mathbb{1} + i\frac{NJt}{M\hbar}\hat{\Phi}_\triangle\right)...\left(\mathbb{1} + i\frac{NJt}{M\hbar}\hat{\Phi}_\triangle\right)}_{M\text{times}} |\Theta, \phi_X, \phi_C\rangle \, , \tag{C6}$$

where M is an integer giving the number of infinitesimal time steps t/M into which the propagation is decomposed. We shall assume that $M \gg N \gg 1$. Switching to the bold vector notation $\boldsymbol{\phi} = (\Theta, \phi_X, \phi_C)$ and $\boldsymbol{n} = (\frac{N}{3}, n_X, \delta n_2)$ for brevity, we insert resolutions of the identity

$$\mathbb{1} = \int d\boldsymbol{\phi} \, |\boldsymbol{\phi}\rangle \langle\boldsymbol{\phi}| \tag{C7}$$

between each set of parentheses

$$\langle n_X, \delta n_2| e^{i\frac{NJt}{\hbar}\Phi_\triangle(\hat{n}_X, \delta\hat{n}_2, \hat{\phi}_C, \hat{\phi}_X)} |\Theta, \phi_X, \phi_C\rangle \approx \int d\boldsymbol{\phi}_{M-1}...d\boldsymbol{\phi}_1 \left\{ \langle n_X, \delta n_2| \left(\mathbb{1} + i\frac{NJt}{M\hbar}\hat{\Phi}_\triangle\right) |\boldsymbol{\phi}_{M-1}\rangle \right.$$

$$\left. \times \langle\boldsymbol{\phi}_{M-1}| \left(\mathbb{1} + i\frac{NJt}{M\hbar}\hat{\Phi}_\triangle\right) |\boldsymbol{\phi}_{M-2}\rangle \times ... \times \langle\boldsymbol{\phi}_1| \left(\mathbb{1} + i\frac{NJt}{M\hbar}\hat{\Phi}_\triangle\right) |\boldsymbol{\phi}_0\rangle \right\} , \tag{C8}$$

where we have used $|\boldsymbol{\phi}_0\rangle$ to denote $|\Theta, \phi_X, \phi_C\rangle$. In order to evaluate each matrix element in this product, we note that $\hat{\Phi}_\triangle$ has the form

$$\hat{\Phi}_\triangle = \left(\frac{1}{2} - \frac{5}{8N}\delta\hat{n}_2\right) \hat{\phi}^4_X + \left(\frac{1}{18} + \frac{1}{24N}\delta\hat{n}_2\right) \hat{\phi}^4_C + \left(\frac{1}{3} + \frac{1}{4N}\delta\hat{n}_2\right) \hat{\phi}^2_X \hat{\phi}^2_C - \frac{1}{6N}\hat{n}_X \left(\hat{\phi}^3_X\hat{\phi}_C + \hat{\phi}_X\hat{\phi}^3_C\right) + ... \tag{C9}$$

where the operator ordering is assumed to be the same as the classical expression given in Eq. (C1) such that all the number operators lie to the left of the phase operators. We therefore insert resolutions of the identity over the number states $\mathbb{1} = \int d\boldsymbol{n} \, |\boldsymbol{n}\rangle \langle\boldsymbol{n}|$ inside the matrix elements so that the number operators can act to the left and the phase operators to the right

$$\langle\boldsymbol{\phi}_{j+1}| \left(\mathbb{1} + i\frac{NJt}{M\hbar}\hat{\Phi}_\triangle\right) |\boldsymbol{\phi}_j\rangle \longrightarrow \langle\boldsymbol{\phi}_{j+1}| \int d\boldsymbol{n}_j \, |\boldsymbol{n}_j\rangle \langle\boldsymbol{n}_j| \, \left(\mathbb{1} + i\frac{NJt}{M\hbar}\hat{\Phi}_\triangle\right) |\boldsymbol{\phi}_j\rangle \tag{C10}$$

$$\approx \int d\boldsymbol{n}_j \, \exp\left[i\boldsymbol{n}_j \cdot (\boldsymbol{\phi}_{j+1} - \boldsymbol{\phi}_j)\right] \, \exp\left[i\frac{NJt}{M\hbar}\Phi_\triangle(\boldsymbol{n}_j, \boldsymbol{\phi}_j)\right] \tag{C11}$$

where to obtain the second line we have used the relation $\langle\boldsymbol{\phi}|\boldsymbol{n}\rangle = \exp[i\boldsymbol{n}\cdot\boldsymbol{\phi}]$ twice and $\Phi_\triangle(\boldsymbol{n}_j, \boldsymbol{\phi}_j)$ is now a function of ordinary variables rather than operators. Thus, all the matrix elements apart from the most lefthand one in Eq. (C8) contribute a phase factor $\exp\left[i\frac{NJt}{M\hbar}\Phi_\triangle(\boldsymbol{n}_j, \boldsymbol{\phi}_j) + i\boldsymbol{n}_j \cdot (\boldsymbol{\phi}_{j+1} - \boldsymbol{\phi}_j)\right]$, and the wavefunction becomes

$$\psi(n_X, \delta n_2, t) = \int d\boldsymbol{\phi}_{M-1} \int \prod_{j=0}^{M-2} d\boldsymbol{\phi}_j d\boldsymbol{n}_j \, \underbrace{B(n_X, \delta n_2, \boldsymbol{\phi}_{M-1})}_{\text{boundary term}} \exp\left[i \sum_{j=0}^{M-2} \left\{\frac{NJt}{M\hbar}\Phi_\triangle(\boldsymbol{n}_j, \boldsymbol{\phi}_j) + \boldsymbol{n}_j \cdot (\boldsymbol{\phi}_{j+1} - \boldsymbol{\phi}_j)\right\}\right]$$

$$\times \left(\frac{4\pi\hbar}{i\sqrt{3}\tilde{U}} \exp\left[\frac{i\hbar}{3\tilde{U}}\left(\{\phi_C\}^2_0 + 3\{\phi_X\}^2_0\right)\right]\right) . \tag{C12}$$

The boundary term comes from the most lefthand matrix element in Eq. (C8) and is also a pure phase factor

$$B(n_X, \delta n_2, \boldsymbol{\phi}_{M-1}) = \exp\left[\mathrm{i}\frac{NJt}{M\hbar}\Phi_\triangle[n_X, \delta n_2, \boldsymbol{\phi}_{M-1}] - n_X\,\{\phi_X\}_{M-1} - \delta n_2\,\{\phi_C\}_{M-1}\right] \ . \qquad (C13)$$

in which the notation $\{\phi_X\}_{M-1}$ and $\{\phi_C\}_{M-1}$ is used for the individual components of $\boldsymbol{\phi}_{M-1}$ and likewise $\{\phi_X\}_0$ and $\{\phi_C\}_0$ is used for the individual components of $\boldsymbol{\phi}_0$.

A condition that the above expansion of the propagator into M terms is an accurate approximation is that $NJt/(\hbar M) \equiv \varepsilon$ is a small quantity. Assuming this to be the case we can write

$$B(n_X, \delta n_2, \boldsymbol{\phi}_{M-1}) + \varepsilon \sum_{j=0}^{M-2}\left\{\Phi_\triangle[\boldsymbol{n}_j, \boldsymbol{\phi}_j] + \boldsymbol{n}_j \cdot \frac{\boldsymbol{\phi}_{j+1} - \boldsymbol{\phi}_j}{\varepsilon}\right\} \sim \int_0^{NJt/\hbar} \mathrm{d}\tau \left\{\Phi_\triangle[\boldsymbol{n}(\tau), \boldsymbol{\phi}(\tau)] + \boldsymbol{n}(\tau) \cdot \dot{\boldsymbol{\phi}}(\tau)\right\} \ . \quad (C14)$$

This becomes exact when $\varepsilon \to 0$, or equivalently $M \to \infty$ so that we can express the wavefunction as a path integral

$$\psi(n_X, \delta n_2, t) = \frac{4\pi\hbar}{\mathrm{i}\sqrt{3\tilde{U}}}\int \mathcal{D}\boldsymbol{\phi}\mathcal{D}\boldsymbol{n}\ \exp\left[\mathrm{i}\int_0^{NJt/\hbar}\mathrm{d}\tau\{\Phi_\triangle[\boldsymbol{n}(\tau), \boldsymbol{\phi}(\tau)] + \boldsymbol{n}(\tau) \cdot \dot{\boldsymbol{\phi}}(\tau)\}\right]\exp\left[\frac{\mathrm{i}\hbar}{3\tilde{U}}\left\{\phi_C^2(0) + 3\phi_X^2(0)\right\}\right]$$
$$(C15)$$

where

$$\mathcal{D}\boldsymbol{\phi}\mathcal{D}\boldsymbol{n} = \lim_{M\to\infty}\mathrm{d}\boldsymbol{\phi}_{M-1}\prod_{j=0}^{M-2}\mathrm{d}\boldsymbol{\phi}_j\mathrm{d}\boldsymbol{n}_j = \lim_{M\to\infty}\prod_{j=0}^{M-1}\mathrm{d}\boldsymbol{\phi}_j\mathrm{d}\boldsymbol{n}_j\ \delta[\boldsymbol{n}_{M-1} - (n_X, \delta n_2)] \qquad (C16)$$

[1] M. Cheneau, P. Barmettler, D. Poletti, M. Endres, P. Schauß, T. Fukuhara, C. Gross, I. Bloch, C. Kollath, and S. Kuhr, Light-cone-like spreading of correlations in a quantum many-body system, Nature **481**, 484 (2012).

[2] T. Fukuhara, P. Schauß, M. Endres, S. Hild, M. Cheneau, I. Bloch and C. Gross, Microscopic observation of magnon bound states and their dynamics, Nature **502**, 76 (2013).

[3] T. Langen, R. Geiger, M. Kuhnert, B. Rauer, and J. Schmiedmayer, Local emergence of thermal correlations in an isolated quantum many-body system, Nat. Phys. **9**, 640 (2013).

[4] P. Richerme, Z.-X. Gong, A. Lee, C. Senko, J. Smith, M. Foss-Feig, S. Michalakis, A. V. Gorshkov, and C. Monroe, Non-local propagation of correlations in quantum systems with long-range interactions, Nature **511**, 198 (2014).

[5] P. Jurcevic, B. P. Lanyon, P. Hauke, C. Hempel, P. Zoller, R. Blatt, and C. F. Roos, Quasiparticle engineering and entanglement propagation in a quantum many-body system, Nature **511**, 202 (2014).

[6] M. Schreiber, S. S. Hodgman, P. Bordia, H. P. Lüschen, M. H. Fischer, R. Vosk, E. Altman, U. Schneider, and I. Bloch, Observation of many-body localization of interacting fermions in a quasirandom optical lattice, Science **349**, 842 (2015).

[7] J.-Y. Choi, S. Hild, J. Zeiher, P. Schauß, A. Rubio-Abadal, T. Yefsah, V. Khemani, D. A. Huse, I. Bloch, and C. Gross, Exploring the many-body localization transition in two dimensions, Science **352**, 1547 (2016).

[8] J. Smith, A. Lee, P. Richerme, B. Neyenhuis, P. W. Hess, P. Hauke, M. Heyl, D. A. Huse, and C. Monroe, Many-body localization in a quantum simulator with programmable random disorder, Nat. Phys. **12**, 907 (2016).

[9] A. Lukin, M. Rispoli, R. Schittko, M. E. Tai, A. M. Kaufman, S. Choi, V. Khemani, J. Léonard, and M. Greiner, Probing entanglement in a many-body-localized system, Science **364**, 256 (2019).

[10] R. Nandkishore and D. A. Huse, Many-body localization and thermalization in quantum statistical mechanics, Annu. Rev. Condens. Matter Phys. **6**, 15 (2015).

[11] D. A. Abanin, E. Altman, I. Bloch, and M. Serbyn, Many-body localization, thermalization, and entanglement, Rev. Mod. Phys. **91**, 021001 (2019).

[12] B. L. Altshuler, Y. Gefen, A. Kamenev, and L. S. Levitov, Quasiparticle lifetime in a finite system: A non- perturbative approach, Phys. Rev. Lett. **78**, 2803 (1997).

[13] P. Schauß, M. Cheneau, M. Endres, T. Fukuhara, S. Hild, A. Omran, T. Pohl, C. Gross, S. Kuhr, and I. Bloch, Observation of spatially ordered structures in a two-dimensional Rydberg gas, Nature (London) **491**, 87 (2012).

[14] H. Labuhn, D. Barredo, S. Ravets, S. de Lèsèleuc, T. Macrì, T. Lahaye, and A. Browaeys, Tunable two-dimensional arrays of single Rydberg atoms for realizing quantum Ising models, Nature (London) 534, 667 (2016).

[15] H. Bernien, S. Schwartz, A. Keesling, H. Levine, A. Omran, H. Pichler, S. Choi, A. S. Zibrov, M. Endres, M. Greiner, V. Vuletic, and M. D. Lukin, Probing many-body dynamics on a 51-atom quantum simulator, Nature (London) **551**, 579 (2017).

[16] C. J. Turner, A. A. Michailidis, D. A. Abanin, M. Serbyn and Z. Papić, Weak ergodicity breaking from quantum many-body scars, Nat. Phys. **14** 745, (2018).

[17] C. J. Turner, A. A. Michailidis, D. A. Abanin, M. Serbyn, and Z. Papić, Quantum scarred eigenstates in a rydberg atom chain: Entanglement, breakdown of thermalization, and stability to perturbations, Phys. Rev. B **98**, 155134 (2018).

[18] S. Moudgalya, N. Regnault, and B. A. Bernevig, Entanglement of exact excited states of AKLT models: Exact results, many-body scars and the violation of strong ETH, Phys. Rev. B **98**, 235156 (2018).

[19] V. Khemani, C. R. Laumann, and A. Chandran, Signatures of integrability in the dynamics of Rydberg-blockaded chains, Phys. Rev. B **99**, 161101(R) (2019).

[20] W. W. Ho, S. Choi, H. Pichler, and M. D. Lukin, Periodic Orbits, Entanglement, and Quantum Many-Body Scars in Constrained Models: Matrix Product State Approach, Phys. Rev. Lett. **122**, 040603 (2019).

[21] S. Choi, C. J. Turner, H. Pichler, W. W. Ho, A. A. Michailidis, Z. Papić, M. Serbyn, M. D. Lukin, and D. A. Abanin, Emergent SU(2) Dynamics and Perfect Quantum Many-Body Scars, Phys. Rev. Lett. **122**, 220603 (2019).

[22] J. M. Deutsch, Quantum statistical mechanics in a closed system, Phys. Rev. A. **43** 2046 (1991).

[23] M. Srednicki, Chaos and Quantum Thermalization, Phys. Rev. E **50** 888 (1994).

[24] M. Rigol, V. Dunjko, and M. Olshanii, Thermalization and its mechanism for generic isolated quantum systems, Nature **452**, 854 (2008).

[25] J. Eisert, M. Friesdorf, and C. Gogolin, Quantum many-body systems out of equilibrium, Nat. Phys. 11, 124 (2015).

[26] A. Polkovnikov, K. Sengupta, A. Silva, and M. Vengalattore, Nonequilibrium dynamics of closed interacting quantum systems, Rev. Mod. Phys. **83**, 863 (2011).

[27] E. Nicklas, M. Karl, M. Höfer, A. Johnson, W. Muessel, H. Strobel, J. Tomkovič, T. Gasenzer, and M. K. Oberthaler, Observation of Scaling in the Dynamics of a Strongly Quenched Quantum Gas, Phys. Rev. Lett. **115**, 245301 (2015).

[28] S. Erne, R. Bücker, T. Gasenzer, J. Berges, J. Schmiedmayer, Universal dynamics in an isolated one-dimensional Bose gas far from equilibrium, Nature **563**, 225 (2018).

[29] M. Heyl, Dynamical quantum phase transitions: a review, Rep. Prog. Phys. **81**, 054001 (2018).

[30] V. Link and W. T. Strunz, Dynamical phase transitions in dissipative quantum dynamics with quantum optical realization, Phys. Rev. Lett. **125**, 143602 (2020).

[31] A. Smith, M. S. Kim, F. Pollmann and J. Knolle, Simulating quantum many-body dynamics on a current digital quantum computer, npj Quantum Inf. **5**, 106 (2019).

[32] R. Thom, *Structural Stability and Morphogenesis* (Benjamin, Reading MA, 1975).

[33] V. I. Arnol'd, Critical points of smooth functions and their normal forms, Russ. Math. Survs. **30**, 1 (1975).

[34] E. C. Zeeman, Catastrophe Theory: Selected Papers 1972-1977 (Addison-Wesley, Reading, MA, 1977).

[35] M. Berry, *Singularities in Waves and Rays* in Les Houches, Session XXXV, 1980 *Physics of Defects*, edited by R. Balian et al. (North-Holland Publishing, Amsterdam, 1981).

[36] D. H. J. O'Dell, Quantum catastrophes and ergodicity in the dynamics of bosonic Josephson junctions, Phys. Rev. Lett. **109**, 150406 (2012).

[37] J. Mumford, W. Kirkby, and D. H. J. O'Dell, Catastrophes in non-equilibrium many-particle wave functions: universality and critical scaling, J. Phys. B: At. Mol. Opt. Phys. **50**, 044005 (2017).

[38] A. Z. Goldberg, A. Al-Qasimi, J. Mumford, and D. H. J. O'Dell, Emergence of singularities from decoherence: Quantum catastrophes, Phys. Rev. A **100**, 063628 (2019).

[39] J. Mumford, E. Turner, D. W. L. Sprung, and D. H. J. O'Dell, Quantum Spin Dynamics in Fock Space Following Quenches: Caustics and Vortices, Phys. Rev. Lett. **122**, 170402 (2019).

[40] W. Kirkby, J. Mumford, and D.H.J. O'Dell, Quantum caustics and the hierarchy of light cones in quenched spin chains, Phys. Rev. Research **1**, 033135 (2019).

[41] B. Evrard, A. Qu, J. Dalibard, and F. Gerbier, From Many-Body Oscillations to Thermalization in an Isolated Spinor Gas, Phys. Rev. Lett. **126**, 063401 (2021).

[42] M. V. Berry, J. F. Nye, and F. J. Wright, The elliptic umbilic diffraction catastrophe, Phil. Trans. R. Soc. A **291**, 453 (1979).

[43] M. V. Berry and C. Upstill, Catastrophe optics: morphologies of caustics and their diffraction patterns, Prog. Opt. **XVIII**, 257 (1980).

[44] T. Pearcey, The structure of an electromagnetic field in the neighborhood of a caustic. Phil. Mag. **37**, 311 (1946).

[45] *NIST Handbook of Mathematical Functions*, edited by Olver et al. (Cambridge University, New York, 2010), chapter 36. Available online at dlmf.nist.gov

[46] M. V. Berry, Focusing and twinkling: critical exponents from catastrophes in non-Gaussian random short waves. J. Phys. A: Math. Gen. **10**, 2061 (1977).

[47] V. L. Ginzburg, Radiation from uniformly moving sources (Vavilov-Cherenkov effect, transition radiation, and some other phenomena), Acoust. Phys. 51, 11 (2005).

[48] Y. G. Gladush, L. A. Smirnov, and A. M. Kamchatnov, Generation of Cherenkov waves in the flow of a Bose-Einstein condensate past an obstacle, J. Phys. B **41**, 165301 (2008).

[49] J. F. Nye, *Natural Focusing and Fine Structure of Light* (Institute of Physics, Philadelphia, 1999).

[50] Lord Kelvin, Deep water ship-waves, Phil. Mag. 9, 733 (1905).

[51] M. V. Berry, Tsunami asymptotics, New J. Phys. **7**, 129 (2005); Focused tsunami waves, Proc. R. Soc. London A **463**, 3055 (2007).

[52] H. Degueldre, J. J. Metzger, T. Geisel and R. Fleischmann, Random focusing of tsunami waves, Nat. Phys. **12**, 259 (2016).

[53] M. V. Berry, Minimal analytical model for undular tidal bore profile; quantum and Hawking effect analogies. New J. Phys. **20**, 053066 (2018).

[54] B. S. White and B. Fornberg, On the chance of freak waves at sea, J. Fluid Mechanics **355**, 113 (1998).

[55] R. Höhmann, U. Kuhl, H.-J. Stöckmann, L. Kaplan, and E. J. Heller, Freak waves in the linear regime: a microwave study. Phys. Rev. Lett. **104**, 093901 (2010).

[56] M. Onoratoab, S. Residoric, U. Bortolozzoc, A. Montinad, and F. T. Arecchi, Rogue waves and their gener-

ating mechanisms in different physical contexts, Phys. Rep. **528**, 47 (2013).

[57] T. A. A. Adcock and P. H. Taylor, The physics of anomalous ('rogue') ocean waves, Rep. Prog. Phys. **77**, 105901 (2014).

[58] E. J. Heller, R. Fleischmann, and T. Kramer, Branched flow, Physics Today **74**, 12, 44 (2021).

[59] D. R. Solli, C. Ropers, P. Koonath and B. Jalali, Optical Rogue Waves, Nature **450**, 1054 (2007).

[60] F. T. Arecchi, U. Bortolozzo, A. Montina, and S. Residori, Granularity and Inhomogeneity Are the Joint Generators of Optical Rogue Waves, Phys. Rev. Lett. **106**, 153901 (2011).

[61] N. Akhmediev, J. M. Dudley, D. R. Solli, and S. K. Turitsyn, Recent progress in investigating optical rogue waves, J. Opt. **15**, 060201 (2013).

[62] N. Marsal, V. Caullet, D. Wolfersberger, and M. Sciamanna, Spatial rogue waves in a photorefractive pattern-forming system, Opt. Lett. **39**, 3690 (2014).

[63] A. Mathis, L. Froehly, S. Toenger, F. Dias, G. Genty, and J. M. Dudley, Caustics and Rogue Waves in an Optical Sea, Sci. Rep. **5**, 12822 (2015).

[64] Spatial Rogue Waves in Photorefractive Ferroelectrics, D. Pierangeli, F. Di Mei, C. Conti, A. J. Agranat, and E. DelRe, Phys. Rev. Lett. **115**, 093901 (2015).

[65] M. Mattheakis, J. Pitsios, G.P. Tsironis, S. Tzortzakis, Extreme events in complex linear and nonlinear photonic media, Chaos, Solitons and Fractals **84**, 73 (2016).

[66] A. Safari, R. Fickler, M. J. Padgett, R. W. Boyd, Generation of Caustics and Spatial Rogue Waves from Nonlinear Instability, Phys. Rev. Lett. **119**, 203901 (2017).

[67] A. Zannotti, *Caustic Light in Nonlinear Photonic Media* (Springer, Cham, Switzerland, 2020).

[68] V. I. Arnold, S. F. Shandarin, and Ya. B. Zeldovich, The large scale structure of the Universe I. General properties. One- and two-dimensional models, Geophys. Astrophys. Fluid Dyn. **20**, 111 (1982).

[69] J. Feldbrugge, R. van de Weygaert, J. Hidding, and J. Feldbrugge, Caustic skeleton & cosmic web, J. Cosmol. Astropart. Phys. 05 (2018) 027.

[70] R. Da Silveira, Rainbow interference effects in heavy ion elastic scattering, Phys. Lett. B **45**, 211 (1973).

[71] T. C. Petersen, M. Weyland, D. M. Paganin, T. P. Simula, S. A. Eastwood, and M. J. Morgan, Electron Vortex Production and Control Using Aberration Induced Diffraction Catastrophes, Phys. Rev. Lett. **110**, 033901 (2013).

[72] W. Rooijakkers, S. Wu, P. Striehl, M. Vengalattore, and M. Prentiss, Observation of caustics in the trajectories of cold atoms in a linear magnetic potential, Phys. Rev. A **68**, 063412 (2003).

[73] T. P. Simula, T. C. Petersen and D. M. Paganin, Diffraction catastrophes threaded by quantized vortex skeletons caused by atom-optical aberrations induced in trapped Bose-Einstein condensates, Phys. Rev. A **88**, 043626 (2013).

[74] S. Rosenblum, O. Bechler, I. Shomroni, R. Kaner, T. Arusi-Parpar, O. Raz, and B. Dayan, Demonstration of Fold and Cusp Catastrophes in an Atomic Cloud Reflected from an Optical Barrier in the Presence of Gravity, Phys. Rev. Lett. **112**, 120403 (2014).

[75] M. E. Mossman, T. M. Bersano, M. McNeil Forbes, and P. Engels, Gravitational caustics in an atom laser, Nature Communications **12**, 7226 (2021).

[76] J. H. Huckans, I. B. Spielman, B. L. Tolra, W. D. Phillips, and J. V. Porto, Quantum and classical dynamics of a Bose-Einstein condensate in a large-period optical lattice, Phys. Rev. A **80**, 043609 (2009).

[77] R. Plestid, P. Mahon, and D. H. J. O'Dell, Violent relaxation in quantum fluids with long-range interactions, Phys. Rev. E **98**, 012112 (2018).

[78] U. Leonhardt, A laboratory analogue of the event horizon using slow light in an atomic medium, Nature (London) **415**, 406 (2002).

[79] M. V. Berry and M. R. Dennis, Quantum cores of optical phase singularities, J. Opt. A **6**, S178 (2004).

[80] L. S. Schulman, Tricritical Points and Type-Three Phase Transitions, Phys. Rev. B **7**, 1960 (1973).

[81] I. Stewart and T. Poston, *Catastrophe Theory and Its Applications* (Dover, New York, 2012).

[82] R. Gilmore, Structural Stability of the Phase Transition in Dicke-like Models, J. Math. Phys. **18**, 17 (1977).

[83] R. Gilmore and L. M. Narducci, Relation between the Equilibrium and Nonequilibrium Critical Properties of the Dicke Model, Phys. Rev. A **17**, 1747 (1978).

[84] R. Gilmore and L. M. Narducci, Laser as Catastrophe, in: Coherence and Quantum Optics (L. Mandel and E. Wolf, Eds.), (Plenum, New York, 1977).

[85] R. Gilmore, *Catastrophe Theory for Scientists and Engineers*, (Wiley, New York, 1981).

[86] F. A. van Abeelen and B. J. Verhaar, Time-dependent Feshbach resonance scattering and anomalous decay of a Na Bose-Einstein condensate, Phys. Rev. Lett. **83**, 1550 (1999).

[87] M. P. A. Fisher, P. B. Weichman, G. Grinstein, D. S. Fisher, Boson localization and the superfluid-insulator transition, Phys. Rev. B **40** 546 (1989).

[88] S. Sachev, Quantum Phase Transitions (Cambridge University Press, New York, 2001).

[89] D. Jaksch, C. Bruder, J. I. Cirac, C. W. Gardiner, and P. Zoller, Cold Bosonic Atoms in Optical Lattices, Phys. Rev. Lett. **81**, 3108 (1998).

[90] M. Greiner, O. Mandel, T. Esslinger, T. W. Hänsch, and I. Bloch, Quantum phase transition from a superfluid to a Mott insulator in a gas of ultracold atoms, Nature **415**, 39 (2002).

[91] E. Altman and A. Auerbach, Oscillating Superfluidity of Bosons in Optical Lattices, Phys. Rev. Lett. **89**, 250404 (2002).

[92] L. Isella and J. Ruostekoski, Nonadiabatic dynamics of a Bose-Einstein condensate in an optical lattice, Phys. Rev. A **72**, 011601(R) (2005).

[93] R. Schützhold, M. Uhlmann, Y. Xu, and U. R. Fischer, Sweeping from the Superfluid to the Mott Phase in the Bose-Hubbard Model, Phys. Rev. Lett. **97**, 200601 (2006).

[94] C. Kollath, A. M. Läuchli, and E. Altman, Quench Dynamics and Nonequilibrium Phase Diagram of the Bose-Hubbard Model, Phys. Rev. Lett. 98, 180601 (2007)

[95] M. Rigol, V. Dunjko, V. Yurovsky, and M. Olshanii, Relaxation in a completely integrable many-body quantum system: An ab initio study of the dynamics of the highly excited states of 1d lattice hard-core bosons, Phys. Rev. Lett. **98**, 050405 (2007).

[96] J. Dziarmaga, M. Tylutki, and W. H. Zurek, Quench from Mott insulator to superfluid, Phys. Rev. B **86**, 144521 (2012).

[97] P. Barmettler, D. Poletti, M. Cheneau, and C. Kollath,

Propagation front of correlations in an interacting Bose gas, Phys. Rev. A **85**, 053625 (2012).

[98] A. J. Daley, H. Pichler, J. Schachenmayer, and P. Zoller, Measuring Entanglement Growth in Quench Dynamics of Bosons in an Optical Lattice, Phys. Rev. Lett. **109**, 020505 (2012)

[99] M. Łacki and J. Zakrzewski, Fast Dynamics for Atoms in Optical Lattices, Phys. Rev. Lett. **110**, 065301 (2013).

[100] G. Kordas, D. Witthaut, and S. Wimberger, Non-equilibrium dynamics in dissipative Bose-Hubbard chains, Ann. Phys. (Berlin) **527**, 619 (2015).

[101] F. Vicentini, F. Minganti, R. Rota, G. Orso, and C. Ciuti, Critical slowing down in driven-dissipative Bose-Hubbard lattices, Phys. Rev. A **97**, 013853 (2018).

[102] J. G. Cosme, Hierarchical relaxation dynamics in a tilted two-band Bose-Hubbard model, Phys. Rev. A 97, 043610 (2018).

[103] M. R. C. Fitzpatrick and M. P. Kennett, Light-cone-like spreading of single-particle correlations in the Bose-Hubbard model after a quantum quench in the strong-coupling regime, Phys. Rev. A **98**, 053618 (2018).

[104] K. Nagao, M. Kunimi, Y. Takasu, Y. Takahashi, and I. Danshita, Semiclassical quench dynamics of Bose gases in optical lattices, Phys. Rev. A **99**, 023622, (2019).

[105] A. Mokhtari-Jazi , M. R. C. Fitzpatrick, and M. P. Kennett, Phase and group velocities for correlation spreading in the Mott phase of the Bose-Hubbard model in dimensions greater than one, Phys. Rev. A **103**, 023334 (2021).

[106] L. Fallani, L. De Sarlo, J. E. Lye, M. Modugno, R. Saers, C. Fort, and M. Inguscio, Observation of dynamical instability for a Bose-Einstein condensate in a moving 1D optical lattice, Phys. Rev. Lett. **93**, 140406 (2004).

[107] A. K. Tuchman, C. Orzel, A. Polkovnikov, and M. A. Kasevich, Nonequilibrium coherence dynamics of a soft boson lattice, Phys. Rev. A **74**, 051601(R) (2006).

[108] S. Will, T. Best, U. Schneider, L. Hackermüller, D.-S. Lühmann and I. Bloch, Time-resolved observation of coherent multi-body interactions in quantum phase revivals, Nature **465**, 197 (2010).

[109] S. Trotzky, Y-A. Chen, A. Flesch, I. P. McCulloch, U. Schollwöck, J. Eisert and I. Bloch, Probing the relaxation towards equilibrium in an isolated strongly correlated one-dimensional Bose gas, Nature Physics **8**, 325 (2012).

[110] F. Meinert, M. J. Mark, E. Kirilov, K. Lauber, P. Weinmann, A. J. Daley, and H.-C. Nägerl, Quantum Quench in an Atomic One-Dimensional Ising Chain, Phys. Rev. Lett. **111**, 053003 (2013).

[111] S. Braun, M. Friesdorf, S. S. Hodgman, M. Schreiber, J. P. Ronzheimer, A. Riera, M. del Rey, I. Bloch, J. Eisert, and U. Schneider, Emergence of coherence and the dynamics of quantum phase transitions, PNAS **112**, 3641 (2015).

[112] J. G. Cosme, C. Georges, A. Hemmerich, and L. Mathey, Dynamical control of order in a cavity-BEC system, Phys. Rev. Lett. **121**, 153001 (2018).

[113] T. Boulier, J. Maslek, M. Bukov, C. Bracamontes, E. Magnan, S. Lellouch, E. Demler, N. Goldman, and J. V. Porto, Parametric Heating in a 2D Periodically Driven Bosonic System: Beyond the Weakly Interacting Regime, Phys. Rev. X **9**, 011047 (2019).

[114] G. J. Milburn, J. Corney, E. M. Wright, and D. F. Walls, Quantum dynamics of an atomic Bose-Einstein conden-sate in a double-well potential. Phys. Rev. A **55**, 4318 (1997).

[115] A. Smerzi, S. Fantoni, S. Giovanazzi, and S. R. Shenoy, Quantum coherent atomic tunneling between two trapped Bose-Einstein condensates. Phys. Rev. Lett. **79**, 4950 (1997).

[116] A. Vardi and J. R. Anglin, Bose-Einstein Condensates beyond Mean Field Theory: Quantum Backreaction as Decoherence, Phys. Rev. Lett. **86**, 568 (2001).

[117] G.-S. Paraoanu, S. Kohler, F. Sols, and A. J. Leggett, The Josephson plasmon as a Bogoliubov quasiparticle, J. Phys. B: At. Mol. Opt. Phys. **34** 4689 (2001).

[118] L. Pitaevskii, and S. Stringari, Thermal vs Quantum Decoherence in Double Well Trapped Bose-Einstein Condensates, Phys. Rev. Lett. **87**, 180402 (2001).

[119] E. M. Graefe and H. J. Korsch, Semiclassical quantization of an N-particle Bose-Hubbard model, Phys. Rev. A **76**, 032116 (2007).

[120] M. Chuchem, K. Smith-Mannschott, M. Hiller, T. Kottos, A. Vardi, and D. Cohen, Quantum dynamics in the bosonic Josephson junction, Phys. Rev. A **82**, 053617 (2010).

[121] H. Veksler and S. Fishman, Semiclassical analysis of Bose-Hubbard dynamics, New J. Phys. **17**, 053030 (2015).

[122] M. Albiez, R. Gati, J. Fölling, S. Hunsmann, M. Cristiani, and M. K. Oberthaler, Direct observation of tunneling and nonlinear self-trapping in a single bosonic Josephson junction, Phys. Rev. Lett. **95**, 010402 (2005).

[123] S. Levy, E. Lahoud, I. Shomroni, and J. Steinhauer, The a.c. and d.c. Josephson effects in a Bose-Einstein condensate, Nature **449**, 579 (2007).

[124] L. J. LeBlanc, A. Bardon, J. McKeever, M. Extavour, D. Jervis, J. Thywissen, F. Piazza, and A. Smerzi, Dynamics of a Tunable Superfluid Junction, Phys. Rev. Lett. 106, 025302 (2011).

[125] S. Fölling, S. Trotzky, P. Cheinet, M. Feld, R. Saers, A. Widera, T. Müller, and I. Bloch, Direct observation of second-order atom tunnelling, Nature **448**, 1029 (2007).

[126] C. Ryu, P. W. Blackburn, A. A. Blinova, and M. G. Boshier, Experimental realization of Josephson junctions for an atom SQUID, Phys. Rev. Lett. **111**, 205301 (2013).

[127] A. Trenkwalder, G. Spagnolli, G. Semeghini, S. Coop, M. Landini, P. Castilho, L. Pezzè, G. Modugno, M. Inguscio, A. Smerzi, and M. Fattori, Quantum phase transitions with parity-symmetry breaking and hysteresis. Nat. Phys. **12**, 826 (2016).

[128] T. Zibold, E. Nicklas, C. Gross, and M. K. Oberthaler, Classical bifurcation at the Transition from Rabi to Josephson dynamics. Phys. Rev. Lett. **105**, 204101 (2010).

[129] A. Das, K. Sengupta, D. Sen, and B. K. Chakrabarti, Infinite-range Ising ferromagnet in a time-dependent transverse magnetic field: quench and ac dynamics near the quantum critical point. Phys. Rev. B **74**, 144423 (2006).

[130] J. W. Britton, B. C. Sawyer, A. C. Keith, C.-C. J. Wang, J. K. Freericks, H. Uys, M. J. Biercuk, and J. J. Bollinger, Engineered two-dimensional Ising interactions in a trapped-ion quantum simulator with hundreds of spins, Nature **484**, 489 (2012).

[131] C. K. Law, H. Pu, and N. P. Bigelow, Quantum Spins Mixing in Spinor Bose-Einstein Condensates, Phys.

Rev. Lett. **81**, 5257 (1998).

[132] W. Zhang, D. L. Zhou, M.-S. Chang, M. S. Chapman, and L. You, Coherent spin mixing dynamics in a spin-1 atomic condensate, Phys. Rev. A **72**, 013602 (2005).

[133] D. M. Stamper-Kurn and M. Ueda, Spinor Bose gases: Symmetries, magnetism, and quantum dynamics, Rev. Mod. Phys. **85**, 1191 (2013).

[134] J. Stenger, S. Inouye, D. M. Stamper-Kurn, H.-J. Miesner, A. P. Chikkatur and W. Ketterle, Spin domains in ground-state Bose-Einstein condensates, Nature **396**, 345 (1998).

[135] A. T. Black, E. Gomez, L. D. Turner, S. Jung, and P. D. Lett, Spinor dynamics in an antiferromagnetic spin-1 condensate, Phys. Rev. Lett. **99**, 070403 (2007).

[136] A. Farolfi, D. Trypogeorgos, G. Colzi, E. Fava, G. Lamporesi, and G. Ferrari, Rev. Sci. Instrum. **90**, 115114 (2019).

[137] L. Sadler, J. Higbie, S. Leslie, M. Vengalattore, and D. Stamper-Kurn, Spontaneous symmetry breaking in a quenched ferromagnetic spinor Bose-Einstein condensate, Nature (London) **443**, 312 (2006).

[138] C. S. Gerving, T. M. Hoang, B. J. Land, M. Anquez, C. D. Hamley, and M. S. Chapman, Non-equilibrium dynamics of an unstable quantum pendulum explored in a spin-1 Bose-Einstein condensate, Nature Commun. **3**, 1169 (2012).

[139] D. Linnemann, H. Strobel, W. Muessel, J. Schulz, R. J. Lewis-Swan, K. V. Kheruntsyan, and M. K. Oberthaler, Quantum-Enhanced Sensing Based on Time Reversal of Nonlinear Dynamics, Phys. Rev. Lett. **117**, 013001 (2016).

[140] K. Lange, J. Peise, B. Lücke, I. Kruse, G. Vitagliano, I. Apellaniz, M. Kleinmann, G. Tóth, and C. Klempt, Entanglement between two spatially separated atomic modes, Science **360**, 416 (2018).

[141] P. Kunkel, M. Prüfer, H. Strobel, D. Linnemann, A. Frölian, T. Gasenzer, M. Gärttner, and M. K. Oberthaler, Spatially distributed multipartite entanglement enables EPR steering of atomic clouds, Science **360**, 413 (2018).

[142] P. Kunkel, M. Prüfer, S. Lannig, R. Rosa-Medina, A. Bonnin, M. Gärttner, H. Strobel, and M. K. Oberthaler, Simultaneous Readout of Noncommuting Collective Spin Observables beyond the Standard Quantum Limit, Phys. Rev. Lett. **123**, 063603 (2019).

[143] M. Rautenberg and Martin Gärttner, Classical and quantum chaos in a three-mode bosonic system, Phys. Rev. A **101**, 053604 (2020).

[144] R. Franzosi and V. Penna, Chaotic behavior, collective modes, and self-trapping in the dynamics of three coupled Bose-Einstein condensates, Phys. Rev. E **67**, 046227 (2003).

[145] B. Liu, L.-B. Fu, S.-P. Yang, and J. Liu, Josephson oscillation and transition to self-trapping for Bose-Einstein condensates in a triple-well trap, Phys. Rev. A **75**, 033601 (2007).

[146] P. Buonsante, V. Penna, and A. Vezzani, Quantum signatures of the self-trapping transition in attractive lattice bosons, Phys. Rev. A 82, 043615 (2010).

[147] M. A. Garcia-March, S. van Frank, M. Bonneau, J. Schmiedmayer, M. Lewenstein, and L. F. Santos, Relaxation, chaos, and thermalization in a three-mode model of a Bose-Einstein condensate, New J. Phys. **20**, 113039 (2018).

[148] Q. Thommen, J. C. Garreau, and V. Zehnlé, Classical chaos with Bose-Einstein condensates in tilted optical lattices, Phys. Rev. Lett. **91**, 210405 (2003).

[149] A. R. Kolovsky, Semiclassical quantization of the Bogoliubov spectrum, Phys. Rev. Lett. **99**, 020401 (2007).

[150] M. Hiller, T. Kottos, and T. Geisel, Wave-packet dynamics in energy space of a chaotic trimeric Bose-Hubbard system, Phys. Rev. A **79**, 023621 (2009).

[151] T. F. Viscondi and K. Furuya, Dynamics of a Bose-Einstein condensate in a symmetric triple-well trap, J. Phys. A: Math. Theor. **44** 175301 (2011).

[152] S. Müller, J. Billy, E. A. L. Henn, H. Kadau, A. Griesmaier, M. Jona-Lasinio, L. Santos, and T. Pfau, Stability of a dipolar Bose-Einstein condensate in a one-dimensional lattice, Phys. Rev. A **84**, 053601 (2011).

[153] D. Peter, K. Pawlowski, T. Pfau, and K. Rzążewski, Mean-field description of dipolar bosons in triple-well potentials, J. Phys. B: At. Mol. Opt. Phys. **45** (2012).

[154] L. Dell'Anna, G. Mazzarella, V. Penna, and L. Salasnich, Entanglement entropy and macroscopic quantum states with dipolar bosons in a triple-well potential, Phys. Rev. A **87**, 053620 (2013).

[155] S. Baier, M. J. Mark, D. Petter, K. Aikawa, L. Chomaz, Z. Cai, M. Baranov, P. Zoller, and F. Ferlaino, Extended Bose-Hubbard models with ultracold magnetic atoms, Science **352**, 201 (2016).

[156] A. J. Leggett, Bose-Einstein condensation in the alkali gases: Some fundamental concepts, Rev. Mod. Phys. **73**, 307 (2001).

[157] R. Gati and M. K. Oberthaler, A bosonic Josephson junction, J. Phys. B: At. Mol. Opt. Phys. **40** R61 (2007).

[158] C. V. Raman and N. S. N. Nath, The diffraction of light by high frequency sound waves: part IV. Proc. Indian Acad. Sci. **2**, 119 (1936).

[159] M. V. Berry, *The Diffraction of Light by Ultrasound* (Academic, New York, 1966).

[160] D. H. J. O'Dell, Dynamical diffraction in sinusoidal potentials: uniform approximations for Mathieu functions, J. Phys. A: Math. Gen. **34**, 3897 (2001).

[161] S. Mossmann and C. Jung, Semiclassical approach to Bose-Einstein condensates in a triple well potential, Phys. Rev. A. **74**, 033601 (2006).

[162] S. Raghavan, A. Smerzi, S. Fantoni, and S. R. Shenoy, Coherent oscillations between two weakly coupled Bose-Einstein condensates: Josephson effects, π-oscillations, and macroscopic quantum self-trapping, Phys. Rev. A **59**, 620 (1999).

[163] J. R. Anglin, P. Drummond, and A. Smerzi, Exact quantum phase model for mesoscopic Josephson junctions, Phys. Rev. A **64**, 063605 (2001).

[164] F. S. Cataliotti, S. Burger, C. Fort, P. Maddaloni, F. Minardi, A. Trombettoni, A. Smerzi, and M. Inguscio, Josephson Junction Arrays with Bose-Einstein Condensates, Science **293**, 843 (2001).

[165] C. Orzel, A. K. Tuchman, M. L. Fenselau, M. Yasuda, and M. A. Kasevich, Squeezed States in a Bose-Einstein Condensate, Science **291**, 2386 (2001).

[166] Z. Hadzibabic, S. Stock, B. Battelier, V. Bretin, and J. Dalibard, Interference of an Array of Independent Bose-Einstein Condensates, Phys. Rev. Lett. **93**, 180403 (2004).

[167] C. Schori, T. Stöferle, H. Moritz, M. Köhl, and T. Esslinger, Excitations of a Superfluid in a Three-Dimensional Optical Lattice, Phys. Rev. Lett. 93,

240402 (2004).

[168] K. Xu, Y. Liu, D. E. Miller, J. K. Chin, W. Setiawan, and W. Ketterle, Observation of Strong Quantum Depletion in a Gaseous Bose-Einstein Condensate, Phys. Rev. Lett. **96**, 180405 (2006).

[169] Schweikhard, V., S. Tung, and E. A. Cornell, Vortex proliferation in the Berezinskii-Kosterlitz-Thouless regime on a two-dimensional lattice of Bose-Einstein condensates, Phys. Rev. Lett. **99**, 030401 (2007).

[170] A. van Otterlo, K. H. Wagenblast, R. Baltin, C. Bruder, R. Fazio, and G. Schön, Quantum-Phase Transitions of Interacting Bosons and the Supersolid Phase, Phys. Rev. B **52**, 16176 (1995).

[171] R. Fazio, H. van der Zant, Quantum phase transitions and vortex dynamics in superconducting networks, Phys. Rep. **355**, 235 (2001).

[172] A. D. Greentree, J. H. Cole, A. R. Hamilton, and L. C. L. Hollenberg, Coherent electronic transfer in quantum dot systems using adiabatic passage, Phys. Rev. B **70**, 235317 (2004).

[173] J. H. Cole, A. D. Greentree, L. C. L. Hollenberg, and S. Das Sarma, Spatial adiabatic passage in a realistic triple well structure, Phys. Rev. B **77**, 235418 (2008).

[174] M. Rab, J. H. Cole, N. G. Parker, A. D. Greentree, L. C. L. Hollenberg, and A. M. Martin, Spatial coherent transport of interacting dilute Bose gases, Phys. Rev. A **77**, 061602(R) (2008).

[175] T. Opatrný and K. K. Das, Conditions for vanishing central-well population in triple-well adiabatic transport, Phys Rev. A. **79**, 012113 (2009).

[176] C. J. Bradly, M. Rab, A. D. Greentree, and A. M. Martin, Coherent tunneling via adiabatic passage in a three-well Bose-Hubbard system, Phys. Rev. A **85**, 053609 (2012).

[177] M. K. Olsen, Quantum dynamics and entanglement in coherent transport of atomic population, J. Phys. B: At. Mol. Opt. Phys. **47** (2014) 095301.

[178] J. A. Stickney, D. Z. Anderson, and A. A. Zozulya, Transistorlike behavior of a Bose-Einstein condensate in a triple-well potential, Phys. Rev. A **75**, 013608 (2007).

[179] K. W. Wilsmann, L. H. Ymai, A. P. Tonel, J. Links, and A. Foerster, Control of tunneling in an atomtronic switching device, Commun. Phys. **1**, 91 (2018).

[180] Z. Zhang, V. Dunjko, and M. Olshanii, Atom transistor from the point of view of nonequilibrium dynamics, New J. Phys. **17** 125008 (2015).

[181] S. C. Caliga, C. J. E. Straatsma, and D. Z. Anderson, Transport dynamics of ultracold atoms in a triple-well transistor-like potential, New J. Phys. **18**, 025010 (2016).

[182] G. Arwas, A. Vardi, and D. Cohen, Triangular Bose-Hubbard trimer as a minimal model for a superfluid circuit, Phys Rev A **89**, 013601 (2014).

[183] G. Arwas, A. Vardi, and D. Cohen, Superfluidity and Chaos in low dimensional circuits, Sci. Rep. **5**, 13433 (2015).

[184] A. Gallemí, M. Guilleumas, J. Martorell, R. Mayol, A. Polls, and B. Juliá-Díaz, Fragmented condensation in Bose-Hubbard trimers with tunable tunnelling, New J. Phys. **17**, 073014 (2015).

[185] C. Lee, T. J. Alexander, and Y. S. Kivshar, Melting of discrete vortices via quantum fluctuations, Phys. Rev. Lett. **97**, 180408 (2006)

[186] Q. Guo, X. Chen, and B. Wu, Tunneling dynamics and band structures of three weakly coupled Bose-Einstein condensates, Opt. Express **22**, 19219 (2014).

[187] S. Dutta, M. C. Tsatsos, S. Basu, and A. U. J. Lode, Management of the correlations of ultracold bosons in triple wells, New J. Phys. **21** 053044 (2019).

[188] M. K. Olsen, Spreading of entanglement and steering along small Bose-Hubbard chains, Phys. Rev. A **92**, 033627 (2015).

[189] M. K. Olsen, Asymmetric steering in coherent transport of atomic population with a three-well Bose-Hubbard model, J. Opt. Soc. Am. B **32**, A15 (2015).

[190] J. K. Kalaga, A. Kowalewska-Kudłaszyk, W. Leoński, and A. Barasiński, Quantum correlations and entanglement in a model comprised of a short chain of nonlinear oscillators, Phys. Rev. A **94**, 032304 (2016).

[191] J. K. Kalaga, W. Leoński, and R. Szczęśniak, Quantum steering and entanglement in three-mode triangle Bose-Hubbard system, Quantum Inf. Process. **16**, 265 (2017).

[192] M. K. Olsen, T. W. Neely, and A. S. Bradley, Mesoscopic dynamical differences from quantum state preparation in a Bose-Hubbard trimer, Phys. Rev. Lett. **120**, 230406 (2018).

[193] A. A. Bychek, P. S. Muraev, D. N. Maksimov, E. N. Bulgakov, and A. R. Kolovsky, Chaotic and regular dynamics in the three-site Bose-Hubbard model, AIP Conference Proceedings **2241**, 020007 (2020).

[194] M. V. Berry and M. Robnik, Semiclassical level spacings when regular and chaotic orbits coexist, J. Phys. A **17**, 2413 (1984).

[195] M. V. Berry, Semiclassical Mechanics of regular and irregular motion, p171 in Les Houches Lecture Series Session XXXVI, eds. G. Iooss, R. H. G. Helleman and R. Stora (North Holland, Amsterdam, 1983).

[196] V. I. Arnold, Mathematical Methods of Classical Mechanics, Second Edition (Springer, Berlin, 1989).

[197] J-M. Stéphan and J. Dubail, Local quantum quenches in critical one-dimensional systems: entanglement, the Loschmidt echo, and light-cone effects, J. Stat. Mech. (2011) P08019.

[198] P. Calabrese, F. H. L. Essler, and Maurizio Fagotti, Quantum quench in the transverse field Ising chain: I. Time evolution of order parameter correlators, J. Stat. Mech. P07016 (2012).

[199] J. F. Nye, Wave dislocations in the diffraction pattern of a higher-order optical catastrophe, J. Opt. **12** (2010) 015702.

[200] A. Sinatra, C. Lobo, and Y. Castin, Classical-Field Method for Time Dependent Bose-Einstein Condensed Gases, Phys. Rev. Lett. **87**, 210404 (2001).

[201] A. Sinatra, C. Lobo, and Y. Castin, The truncated Wigner method for Bose condensed gases: limits of validity and applications, J. Phys. B **35**, 3599 (2002).

[202] A. Polkovnikov, Phase space representation of quantum dynamics, Ann. Phys. (Amsterdam) **325**, 1790 (2010).

[203] J. Javanainen and J. Ruostekoski, Emergent classicality in continuous quantum measurements, New J. Phys. **15**, 013005 (2013).

[204] G. B. Airy, On the intensity of light in the neighbourhood of a caustic, Trans. Cambridge Philos. Soc. 6, 379 (1838).

[205] I. Zapata, F. Sols and A. J. Leggett, Phase dynamics after connection of two separate Bose-Einstein condensates, Phys. Rev. A **67**, 021603(R) (2003).

[206] R. Borghi, Numerical computation of diffraction catas-

trophes with codimension eight, Phys. Rev. E **85**, 046704 (2012).

[207] M. V. Berry and C. J. Howls, Axial and focal-plane diffraction catastrophe integrals, J. Phys. A **43**, 375206 (2010).

[208] J. F. Nye, The catastrophe optics of liquid drop lenses, Proc. R. Soc. Lond. A **403**, 1 (1986).

[209] M. V. Berry and J. F. Nye, Fine Structure in Caustic Junctions, Nature **267**, 34 (1977).

[210] C. Nicolis, Stochastic resonance in multistable systems: The role of dimensionality, Phys. Rev. E. **86**, 011133 (2012).

[211] J. Callahan, The double cusp has five minima, Proc. Cambridge Philos. Soc. **84**, 537 (1978).

[212] J. Callahan, Special bifurcations of the double cusp, Proc. London Math. Soc. **45**, 227 (1982).

[213] C. Upstill, F. J. Wright, J. V. Hajnal, and R. H. Templer, The double-cusp unfolding of the $^0X_9$ diffraction catastrophe, Optica Acta **29**, 1651 (1982).

[214] A. R. Kolovsky, Bose-Hubbard Hamiltonian: Quantum Chaos approach, A. R. Kolovsky, Int. J. Mod. Phys. B **30**, 1630009 (2016).

[215] L. S. Schulman, *Techniques and Applications of Path Integration*, (Wiley, New York, 1981). Caustics and multivaluedness: Two results of adding path amplitudes, in

[216] G. Dangelmayr and W. Veit, Semiclassical Approximation of Path Integrals on and near Caustics in Terms of Catastrophes, Ann. Phys. **118**, 108 (1979).

[217] J. F. Nye, D. R. Hawst, and R. A. Smith, Use of diffraction gratings with curved lines to study the optical catastrophes D_6^+ and D_6^-. J. Mod. Opt. **34**, 407 (1987).

[218] M.V. Berry, Regular and irregular semiclassical wavefunctions, J. Phys. A **10**, 2083 (1977).

[219] W. S. Bakr, J. Gillen, A. Peng, S. Fölling, and M. Greiner, A quantum gas microscope for detecting single atoms in a Hubbard-regime optical lattice, Nature **462**, 74 (2009).

[220] J. F. Sherson, C. Weitenberg, M. Endres, M. Cheneau, I. Bloch, and S. Kuhr, Single-atom-resolved fluorescence imaging of an atomic Mott insulator, Nature **467**, 68 (2010).

[221] M. R. Andrews, C. G. Townsend, H.-J. Miesner, D. S. Durfee, D. M. Kurn, and W. Ketterle, Observation of Interference Between Two Bose Condensates, Science **275**, 637 (1997).

[222] Karin Wittmann W., E. R. Castro, A. Foerster, and L. F. Santos, Interacting bosons in a triple well: Preface of many-body quantum chaos, arXiv:2111.13714

"Functional Integration and Its Applications" (A. M. Arthurs, Ed.), Oxford Univ. Press XXX(Clarendon), London, 1975.

SUMMARY, CONCLUSIONS, AND DISCUSSION OF FUTURE WORK

We have explored the dynamics of many-body quantum systems, while focusing on two types of emergent behaviour: caustics and chaos. Both of these constitute different kinds of apparently independent universality in quantum systems and while we have made attempts to connect both, there remain open questions. In Chapter 2, we demonstrate that caustics are a universal structure in the dynamics of quantum spin chains. By making use of different limits of the anisotropic XY model with a transverse field, we categorize the light cones using catastrophe theory. The connection between light cones and catastrophes is naturally visible by considering the Lieb-Robinson (LR) velocity defined in Eq. (1.120), which equivalent to the focusing condition for rays following an effective action Φ, i.e. $\partial\Phi = \partial^2\Phi = 0$. In the XY model, there are two local solutions to Eq. (1.120) which indicates that there are two 'maximal' group velocities, although only the largest of these is the true LR velocity. This means that there are both primary and secondary light cones, corresponding to, respectively, the two first members of René Thom's elementary catastrophe organization list: the fold and the cusp. In the many-body wavefunction, these become quantized versions of the Airy and Pearcey functions.

Chapter 2 represents a first in-depth study into higher-order caustics in the dynamics of many-body systems. We analyze quenches in both the two-and three-mode Bose-Hubbard models and demonstrate that the corank-2 hyperbolic and elliptic umbilic catastrophes decorate the dynamics. Furthermore, in an analogy with optical experiments, we find that there is a catastrophe beyond Thom's list, X_9, which acts

as an organizing centre for different diffraction patterns. One of the most significant results from this work is that the caustics and diffraction patterns are the result of true many-body interference, rather than one-body interference from a mean-field theory. Importantly, the three-mode model has signatures of chaos, which we show qualitatively destroys visible caustics.

A significant portion of this thesis is also spent studying signatures of chaos, with particular attention paid to the out-of-time-ordered correlator and related functions. In Chapter 3, we connect our discussion of light cones as caustics with signatures of chaos by considering a Gaussian approximation to the wavefront. By demonstrating that the light cone scales quantitatively differently in the integrable and chaotic regimes, we not only demonstrate that the wavefront spreading can be used to identify chaotic models, but also reinforce the notion that caustics are destroyed by chaos. By showing that in a free system the wavefront must be an Airy function, we also therefore restrict how the broadening coefficients $m(x)$ and $b(x)$ must scale given that the wavefront is a caustic.

Chapter 4 addresses signatures of chaos with a different perspective from Chapter 3, by considering two-time correlation functions which act as generalizations of the OTOC. We show that while the original system is integrable, the effective Floquet Hamiltonian describing the n-fold OTOC yields signatures of chaos typically associated with return probabilities of chaotic systems. This article connects the OTOC with other signatures of chaos, and demonstrates that care must be taken when considering chaos 'diagnostic' tools and standard signatures of chaos.

Outlook

A key result from this thesis is that caustics are universal structures in quantum dynamics, and while their organization (through catastrophe theory) is dependent on the underlying geometries and symmetries of the system, they are stable to perturbations and are thus generic. While we have presented a prescription for the formation of caustics in integrable and models with relatively weak chaos, an interesting question as to exactly how these concepts connect on a much deeper level. More precisely, the connection of the existence and destruction of caustics by chaos remains somewhat unclear. By the Kolmogorov-Arnold-Moser (KAM) theorem [119], certain action-angle invariant tori into a weak chaotic regime, and thus a finite fraction of phase space trajectories remain regular. This may underline the formation of caustics in the weakly-interacting three-mode model, however it leaves an open question as to the survival of catastrophe deeper into the chaotic regime. Furthermore, the ability

156

of the OTOC to detect the onset of chaos is related to a fundamental shift in how the broadening coefficients $m(x)$ and $b(x)$ scale in each regime via the destruction of the caustic.

SELECTED CALCULATIONS

A.1 One-body operators in second quantization

The derivation for (1.11) is slightly tedious and messy, however we present it here for completeness. This derivation is adapted from Cohen-Tannoudji, Ref. [185]. Consider an operator $\hat{O}_1$ which is a one-body operator such that,

$$\hat{O}_1 = \sum_i \hat{o}_i \tag{A.1}$$

that is, it consists of a sum of operators $\hat{o}_i$ which only act on particle i. In more rigorous notation, this operator can be written in the full many-body Hilbert space,

$$\hat{o}_i = \mathbb{1}_1 \otimes \mathbb{1}_2 \otimes ... \otimes \hat{o}_i \otimes ... \otimes \mathbb{1}_N \tag{A.2}$$

Making use of a complete basis for particle i, $\{|\psi_k\rangle_i\}$, we can write the operator $\hat{o}_i$ in this basis,

$$\hat{o}_i = \sum_{k,\ell} o_{k\ell} |\psi_k\rangle_{ii}\langle\psi_\ell| \tag{A.3}$$

with

$$o_{k\ell} = {}_i\langle\psi_k|\hat{o}_i|\psi_\ell\rangle_i \tag{A.4}$$

Thus, the expression for the single-body operator becomes,

$$\hat{O}_1 = \sum_i \sum_{k,\ell} o_{k\ell} |\psi_k\rangle_{ii}\langle\psi_\ell| \tag{A.5}$$

Now, let us consider an N-body Fock state, written in the basis $\{|\psi_k\rangle\}$,

$$|n_1, n_2, ...\rangle = \sqrt{\frac{N!}{n_1! n_2! ...}} \hat{S}_\pm |\psi_1\rangle_1 |\psi_1\rangle_2 |\psi_1\rangle_3 ... |\psi_1\rangle_{n_1} |\psi_2\rangle_{n_1+1} ... |\psi_2\rangle_{n_1+n_2} ... . \quad (A.6)$$

In the above we have simply written the state as an arbitary ordering of $|\psi_k\rangle$, such that the symmetrizer operator $\hat{S}_\pm$ constructs either a symmetric $(+)$ or an antisymmetric $(-)$ state out of the product. The prefactor accounts for the redundancy in the exchange of these particles under (anti)symmetrization. Acting on this state with the part of the one body operator which is summed over all particles, i.e.,

$$\sum_i |\psi_k\rangle_{ii}\langle\psi_\ell|n_1, n_2, ...\rangle = \sum_i |\psi_k\rangle_{ii}\langle\psi_\ell| \sqrt{\frac{N!}{n_1! n_2! ...}} \hat{S}_\pm |\psi_1\rangle_1 ... |\psi_1\rangle_{n_1} |\psi_2\rangle_{n_1+1} ... |\psi_2\rangle_{n_1+n_2} ...$$

$$(A.7)$$

Since $\sum_i |\psi_k\rangle_{ii}\langle\psi_\ell|$ is simply a sum over all particles, it thereby commutes with the symmetrizer $\hat{S}_\pm$. The ith term in the sum will contain the overlap $_i\langle\psi_\ell|\psi_j\rangle_i = \delta_{\ell j}$, which will pick out a total of n_ℓ nonzero terms such that $|\psi_\ell\rangle_i$ becomes replaced with $|\psi_k\rangle_i$ with all other members of the product state are left the same. Hence,

$$\sum_i |\psi_k\rangle_{ii}\langle\psi_\ell|n_1, n_2, ...\rangle = n_\ell \sqrt{\frac{N!}{n_1! n_2! ...}} \hat{S}_\pm |\psi_1\rangle_1 ... |\psi_1\rangle_{n_1} |\psi_2\rangle_{n_1+1} ... |\psi_k\rangle_m ... \quad (A.8)$$

where we have used the shorthand m to represent whichever particle got put into state $|\psi_k\rangle$. Let us now consider the relationship between the right hand side of Eq. (A.8) and Eq. (A.6). By changing some particle from state $|\psi_\ell\rangle$ to $|\psi_k\rangle$, we are still in a Fock state, just with new Fock indices $n_\ell \to n_\ell - 1$ and $n_k \to n_k + 1$. By Eq. (A.6), we can write,

$$|n_1, ..., n_\ell-1, ..., n_k+1, ...\rangle = \sqrt{\frac{N!}{n_1! ... (n_\ell - 1)! ... (n_k + 1)! ...}} \hat{S}_\pm |\psi_1\rangle_1 ... |\psi_1\rangle_{n_1} |\psi_2\rangle_{n_1+1} ... |\psi_k\rangle_m ... .$$

$$(A.9)$$

then we can take the prefactors to one side and therefore replace everything to the right of (and including) $\hat{S}_\pm$ in Eq. (A.8),

$$\sum_i |\psi_k\rangle_{ii}\langle\psi_\ell|n_1, n_2, ...\rangle = n_\ell \sqrt{\frac{N!}{n_1! n_2! ...}} \sqrt{\frac{n_1! ... (n_\ell - 1)! ... (n_k + 1)! ...}{N!}} |n_1, ..., n_\ell - 1, ..., n_k + 1, ...\rangle$$

$$(A.10)$$

$$= \sqrt{n_\ell(n_k + 1)} |n_1, ..., n_\ell - 1, ..., n_k + 1, ...\rangle \quad (A.11)$$

$$= \hat{a}_k^\dagger \hat{a}_\ell |n_1, n_2, ...\rangle \quad (A.12)$$

159

and hence, $\sum_i |\psi_k\rangle_{ii}\langle\psi_\ell| = \hat{a}_k^\dagger \hat{a}_\ell$. Thus the one-body operator can be written,

$$\hat{O}_1 = \sum_{k,\ell} o_{k\ell} \hat{a}_k^\dagger \hat{a}_\ell \tag{A.13}$$

where $o_{k\ell} = \langle\psi_k|\hat{o}|\psi_\ell\rangle$ (the index i removed since we are dealing with identical particles). For two-body operators, the principle is similar.

A.2 Wigner's Semicircle Law

Here, we will give a somewhat succinct proof of the Wigner semicircle law, following Livan *et al.* in Ref. [136]. The central quantity here is the *average spectral density*, $\rho_N(\lambda)$ which essentially corresponds to the probability to find an eigenvalue around the point λ. Since it is a probability density,

$$\int d\lambda \, \rho_N(\lambda) = 1 \tag{A.14}$$

The subscript N indicates that we are considering random matrices of size $N \times N$. The quantity $\rho_N(\lambda)$ is highly non-universal, if we change the probability distribution of the entries, it is not necessarily possible to calculate. In the case of Gaussian matrices which are rotationally invariant (GOE, GUE and GSE), it is possible, but rather difficult. We shall focus on the case where $N \to \infty$, which yields Wigner's semicircular law.

The average spectral density is defined as,

$$\rho_N(\lambda) = \left\langle \frac{1}{N} \sum_i^N \delta(\lambda - \lambda_i) \right\rangle \tag{A.15}$$

where $\langle .. \rangle$ is an ensemble average (over many matrices drawn from, for example, the GOE). Each matrix contributes a set of 'spikes' corresponding to all of its N eigenvalues λ_i. Each matrix drawn from the ensemble will have N spikes, but in different locations due to randomness. When taking the average over the ensemble $\langle ... \rangle$, the highly singular spikes result in a smooth function which is peaked where the density of spikes are higher. The number of matrices in the ensemble average therefore has to tend to infinity so that $\langle ... \rangle$ produces a smooth function.

The average spectral density in a Hamiltonian system is closely related to the local density of states (LDOS) or strength function [178],

$$\rho(E) = \sum_\alpha |C_\alpha|^2 \delta(E - E_\alpha) \tag{A.16}$$

where $C_\alpha = \langle \psi_\alpha | \Psi(0) \rangle$ for an inital state $|\Psi(0)\rangle$ and an energy eigenbasis $\hat{H}|\psi_\alpha\rangle = E_\alpha|\psi_\alpha\rangle$. For a sufficiently broad spread of initial eigenvalues (i.e. $C_\alpha \to$ const.), then we recover a semicircular LDOS. As mentioned in Sec. 1.3.3, this has immediate implications on the two-point correlation function, and the Thouless time of the system.

Resolvent Method

Let us define,

$$G_N(z) = \frac{1}{N}\text{Tr}\frac{1}{z\mathbb{1} - X} = \frac{1}{N}\sum_i \frac{1}{z - \lambda_i} \tag{A.17}$$

where X is any matrix (not necessarily random), and z is a complex variable that is not an eigenvalue of X. If, however, X is a random matrix, we can take the average of this object $\langle G_N(z)\rangle$ and take the limit of the sum to be the integral,

$$\mathcal{G}(z) = \lim_{N\to\infty}\langle G_N(z)\rangle = \int d\lambda \frac{\rho(\lambda)}{z - \lambda} \tag{A.18}$$

This object is the "resolvent" or Green's function. We have defined $\rho_{N\to\infty}(\lambda) = \rho(\lambda)$ for simplicity. The proof is rather simple,

$$\int d\lambda \frac{\rho_N(\lambda)}{z - \lambda} = \int d\lambda \frac{1}{z - \lambda}\left\langle \frac{1}{N}\sum_i^N \delta(\lambda - \lambda_i)\right\rangle = \left\langle \frac{1}{N}\sum_i^N \frac{1}{z - \lambda_i}\right\rangle = \langle G_N(z)\rangle \tag{A.19}$$

where in the first equality we simply inserted the definition of the spectral density from Eq. (A.15).

In order to invert the resolvent for the spectral density, we make use of the Sokhotski-Plemelj theorem along the real line,

$$\lim_{\varepsilon\to 0^+}\int_a^b dy\frac{f(y)}{y \pm i\varepsilon} = \text{Pr}\left[\int_a^b dy\frac{f(y)}{y}\right] \mp i\pi f(0) \tag{A.20}$$

where $a < 0 < b$ and $\text{Pr}[\cdot]$ is the Cauchy principle value of the integral. Taking $f(y) \to \delta(y)$, we have,

$$\lim_{\varepsilon\to 0^+}\frac{1}{y \pm i\varepsilon} = \text{Pr}\left[\frac{1}{y}\right] \mp i\pi\delta(y) \tag{A.21}$$

We can then augment z in the resolvent with a small complex number,

$$\mathcal{G}(x - i\varepsilon) = \int d\lambda \frac{\rho(\lambda)}{x - i\varepsilon - \lambda} \tag{A.22}$$

Now, apply the Sokhotski-Plemelj theorem and take the imaginary part,

$$\lim_{\varepsilon\to 0^+}\text{Im}\mathcal{G}(x - i\varepsilon) = \int d\lambda\, \rho(\lambda)\pi\delta(x - \lambda) \tag{A.23}$$

So,

$$\rho(x) = \frac{1}{\pi} \lim_{\varepsilon \to 0^+} \mathrm{Im} \mathcal{G}(x - i\varepsilon) \tag{A.24}$$

Meaning that if we know an equation for $\mathcal{G}(z)$, we can compute it in the complex plane and take the limit as $\varepsilon \to 0$ to solve for $\rho(\lambda)$.

Gaussian Ensembles: The Semicircle

Start from the joint PDF for Gaussian matrices,

$$P(\lambda_1, \lambda_2, ..., \lambda_N) = \frac{1}{\mathcal{Z}_N(\beta)} e^{-\frac{1}{2}\sum_i \lambda_i^2} \prod_{j<k} |\lambda_j - \lambda_k|^\beta \tag{A.25}$$

where $\mathcal{Z}_N(\beta)$ is a normalization factor,

$$\mathcal{Z}_N(\beta) = \int d\lambda_1 ... d\lambda_N \; e^{-\frac{1}{2}\sum_i \lambda_i^2} \prod_{j<k} |\lambda_j - \lambda_k|^\beta \tag{A.26}$$

Let us also scale our eigenvalues by $\lambda_i \to \sqrt{\beta N}\lambda_i$, so that we're considering all of the Gaussian ensembles as one,

$$= C_N(\beta) \int d\lambda_1 ... d\lambda_N \; e^{-\beta N \mathcal{H}[\lambda_1,...,\lambda_N]} \tag{A.27}$$

where

$$\mathcal{H} = \frac{1}{2}\sum_{i=1}^N \lambda_i^2 - \frac{1}{2N}\sum_{i \neq j} \ln|\lambda_i - \lambda_j| \tag{A.28}$$

This notation is purposefully suggestive of the Hamiltonian $\mathcal{H}$ and partition function $\mathcal{Z}_N(\beta)$ for a 2D Coulomb gas (since the Coulomb interaction is logarithmic in 2D). For $N \gg 1$ we make a 'stationary-phase'-type argument in order to find the most likely configuration of the 'particles' (eigenvalues) at equilibrium. This amounts to a minimization with respect to λ_i,

$$\frac{\partial \mathcal{H}}{\partial \lambda_i} = 0 \qquad \forall i = 1, ..., N \tag{A.29}$$

which gives,

$$\lambda_i = \frac{1}{N}\sum_{j \neq i} \frac{1}{\lambda_i - \lambda_j} \; . \tag{A.30}$$

Multiplying both sides by $\frac{1}{N(z-\lambda_i)}$, and summing over index i,

$$\sum_{i=1}^N \frac{\lambda_i}{N(z - \lambda_i)} = \frac{1}{N^2}\sum_{i=1}^N \sum_{j \neq i} \frac{1}{z - \lambda_i}\frac{1}{\lambda_i - \lambda_j} \; , \tag{A.31}$$

162

It is simple to see that on the LHS, we can add and subtract z so that it can be simplified to give $-1 + zG_N(z)$ using Eq. (A.17). Simplifying the RHS of Eq. (A.31) requires rewriting $\frac{1}{z-\lambda_i}\frac{1}{\lambda_i-\lambda_j} = \frac{1}{z-\lambda_j}\left[\frac{1}{z-\lambda_i} + \frac{1}{\lambda_i-\lambda_j}\right]$ where both terms can be analyzed independently. The result is that,

$$-1 + zG_N(z) = \frac{1}{2}\left(G_N^2(z) + \frac{1}{N}\frac{\partial}{\partial z}G_N(z)\right) \tag{A.32}$$

This differential equation is classified as a Riccati equation, but we don't need to bother with it being a differential equation since we're interested in the $N \to \infty$ limit, so we throw away the last term. Hence, we can rearrange to get,

$$\mathcal{G}(z) = z \pm \sqrt{z^2 - 2} \tag{A.33}$$

Moving off the real axis by replacing $z = x - i\varepsilon$,

$$\mathcal{G}(x - i\varepsilon) = x - i\varepsilon \pm \sqrt{(x^2 - \varepsilon^2 - 2) + i(-2x\varepsilon)} \tag{A.34}$$

we just separated real and imaginary parts in the radical. We now use the fact that the square root of a complex number can be rewritten ,

$$\sqrt{a + ib} = \frac{1}{\sqrt{2}}\sqrt{\sqrt{a^2 + b^2} + a} + i\frac{\text{sgn}(b)}{\sqrt{2}}\sqrt{\sqrt{a^2 + b^2} - a} \ . \tag{A.35}$$

And taking the limit $\varepsilon \to 0$ gives,

$$\lim_{\varepsilon \to 0^+}\mathcal{G}(x) = \pm\frac{\text{sgn}(x)}{\pi\sqrt{2}}\sqrt{|x^2 - 2| - x^2 + 2} \tag{A.36}$$

Thus,

$$\rho(x) = \begin{cases} 0 & |x| > \sqrt{2} \\ \frac{1}{\pi}\sqrt{2 - x^2} & |x| < \sqrt{2} \end{cases} \tag{A.37}$$

Hence the average spectral density takes this semi-circular law for any β in the large N limit. Recall that we rescaled our eigenvalues by $\sqrt{\beta N}$, and in the process we also rescaled our 'Hamiltonian', giving the factors and ellipsoidal shape of Eq. (1.194).

At finite size, the semicircle is no longer sharp, and we can describe the fluctuations of the largest eigenvalue $\lambda_{\max}$ around $\sqrt{2}$ (scaled) by considering a random variable χ_β for $\beta = 1, 2, 4$. The finite-size corrections are, without proof,

$$\lambda_{\max} = \sqrt{2} + \frac{1}{\sqrt{2}}N^{-2/3}\chi_\beta \tag{A.38}$$

In the limit $N \to \infty$, the probability that χ_β is smaller than or equal to s (i.e. the cumulative distribution function) is,

$$\lim_{N\to\infty} P[\chi_\beta \leq s] = \begin{cases} F_1(s) \\ F_2(s) \\ F_4(s) \end{cases} \tag{A.39}$$

The $F_\beta(s)$ are called Tracy-Widom distributions [147].

Bibliography

[1]   O. Morsch and M. Oberthaler, Dynamics of Bose-Einstein condensates in optical lattices, Rev. Mod. Phys. **78**, 179 (2006).

[2]   R. Blatt and C. F. Roos, Quantum simulations with trapped ions, Nature Physics **8**, 277 (2012)

[3]   M. Anderson, J. Ensher, M. Matthews, C. Wieman and E. Cornell, Observation of Bose-Einstein condensation in a dilute atomic vapor, Science **269**, 198 (1995).

[4]   K. Davis, M.-O. Mewes, M. Andrews, N. van Druten, D. Kurn and W. Ketterle, Bose-Einstein Condensation in a Gas of Sodium Atoms, Phys. Rev. Lett. **75**, 3969 (1995).

[5]   C. C. Bradley, C. A. Sackett, J. J. Tollett, and R. G. Hulet, Evidence of Bose-Einstein Condensation in an Atomic Gas with Attractive Interactions, Phys. Rev. Lett. 75, 1687 (1995).

[6]   Y. Kawaguchi and M. Ueda, Spinor Bose-Einstein Condensates, Phys. Rep. **520**, 253 (2012).

[7]   D. M. Stamper-Kurn and M. Ueda, Spinor Bose gases: Symmetries, magnetism, and quantum dynamics, Rev. Mod. Phys. 85, 1191 (2013).

[8]   I. Bloch, J. Dalibard, and W. Zwerger, Many-body physics with ultracold gases, Rev. Mod. Phys. 80, 885 (2008).

[9]   T. Schumm, S. Hofferberth, L. M. Andersson, S. Wildermuth, S. Groth, I. Bar-Joseph, J. Schmiedmayer, and P. Kruger, Matter-wave interferometry in a double well on an atom chip, Nat. Phys. **1**, 57 (2005).

[10]   M. Albiez, R. Gati, J. Folling, S. Hunsmann, M. Cristiani, and M. K. Oberthaler, Direct Observation of Tunneling and Nonlinear Self-Trapping in a Single Bosonic Josephson Junction, Phys. Rev. Lett. **95**, 010402 (2005).

[11] L. J. LeBlanc, A. B. Bardon, J. McKeever, M. H. T. Extavour, D. Jervis, J. H. Thywissen, F. Piazza, and A. Smerzi, Dynamics of a Tunable Superfluid Junction, Phys. Rev. Lett. **106**, 025302 (2011).

[12] M. Cheneau, P. Barmettler, D. Poletti, M. Endres, P. Schauß, T. Fukuhara, C. Gross, I. Bloch, Corinna Kollath, and S. Kuhr, Light-cone-like spreading of correlations in a quantum many-body system, Nature (London) **481**, 484 (2012)

[13] P. Jurcevic, B. P. Lanyon, P. Hauke, C. Hempel, P. Zoller, R. Blatt, and C. F. Roos, Quasiparticle engineering and entanglement propagation in a quantum many-body system, Nature (London) 511, 202 (2014).

[14] E. Schrödinger, Quantization as an eigenvalue problem I, Ann. Phys. **79**, 361 (1926).

[15] E. Schrödinger, Quantization as an eigenvalue problem IV, Ann. Phys. **81**, 109 (1926).

[16] P. Coleman, *Introduction to Many-Body Physics*, (Cambridge University Press, Cambridge, 2015).

[17] A. Altland and B. Simons, *Condensed Matter Field Theory* 2nd Ed., (Cambridge University Press, Cambridge, 2010).

[18] P. Jordan and E. Wigner, On the Pauli exclusion principle, Z. Phys. **47** 631, (1928).

[19] C. Pethick and H. Smith, *Bose-Einstein Condensation in Dilute Gases*, (Cambridge University Press, Cambridge, 2002)

[20] G. J. Milburn, J. Corney, E. M. Wright, and D. F. Walls, Quantum dynamics of an atomic Bose-Einstein condensate in a double-well potential, Phys. Rev. A 55, 4318 (1997).

[21] R. Gati, M. K. Oberthaler, A bosonic Josephson junction, J. Phys. B: At., Mol. Opt. Phys. 40, R61 (2007).

[22] L. C. Biedenharn and H. V. Dam, *Quantum Theory of Angular Momentum: A Collection of Reprints and Original Papers*, (Academic Press, New York, 1965).

[23] A. Auerbach, *Interacting Electrons and Quantum Magnetism*, (Springer-Verlag, New York, 1994).

[24] S. Levy, E. Lahoud, I. Shomroni, and J. Steinhauer, The a.c. and d.c. Josephson effects in a Bose-Einstein condensate, Nature (London) **449**, 579 (2007)

[25] M. Pigneur, T. Berrada, M. Bonneau, T. Schumm, E. Demler, and J. Schmiedmayer, Relaxation to a Phase-Locked Equilibrium State in a One-Dimensional Bosonic Josephson Junction, Phys. Rev. Lett. **120**, 173601 (2018).

[26] T. Zibold, E. Nicklas, C. Gross, and M. K. Oberthaler, Classical Bifurcation at the Transition from Rabi to Josephson Dynamics, Phys. Rev. Lett. **105**, 204101 (2010).

[27] G. Spagnolli, G. Semeghini, L. Masi, G. Ferioli, A. Trenkwalder, S. Coop, M. Landini, L. Pezzè, G. Modugno, M. Inguscio, A. Smerzi, and M. Fattori, Phys. Rev. Lett. **118**, 230403 (2017).

[28] A. Smerzi, S. Fantoni, S. Giovanazzi, and S. R. Shenoy, Quantum Coherent Atomic Tunneling between Two Trapped Bose-Einstein Condensates, Phys. Rev. Lett. 79, 4950 (1997).

[29] S. Raghavan, A. Smerzi, S. Fantoni, and S. R. Shenoy, Coherent oscillations between two weakly coupled Bose-Einstein condensates: Josephson effects, π oscillations, and macroscopic quantum self-trapping, Phys. Rev. A **59**, 620 (1999).

[30] A. J. Leggett, Bose-Einstein condensation in the alkali gases: Some fundamental concepts, Rev. Mod. Phys. **73**, 307 (2001).

[31] F. Mulansky, J. Mumford, and D. H. J. O'Dell, Impurity in a Bose-Einstein condensate in a double well, Phys. Rev. A **84**, 063602 (2011).

[32] J. Mumford, J. Larson, and D. H. J. O'Dell, Impurity in a bosonic Josephson junction: Swallowtail loops, chaos, self-trapping, and Dicke model, Phys. Rev. A **89**, 023620 (2014)

[33] J. Mumford and D. H. J. O'Dell, Critical exponents for an impurity in a bosonic Josephson junction: Position measurement as a phase transition, Phys. Rev. A **90**, 063617 (2014).

[34] J. Mumford, W. Kirkby, and D. H. J. O'Dell, Measuring out-of-time-ordered correlation functions with a single impurity qubit in a bosonic Josephson junction, J. Phys. B: At. Mol. Opt. Phys. **53**, 145301 (2020).

[35]   M. Rinck and C. Bruder, Effects of a single fermion in a Bose Josephson junction, Phys. Rev. A **83**, 023608 (2011).

[36]   R. Gerritsma, A. Negretti, H. Doerk, Z. Idziaszek, T. Calarco, and F. Schmidt-Kaler, Bosonic Josephson Junction Controlled by a Single Trapped Ion, Phys. Rev. Lett. **109**, 080402 (2012).

[37]   J. A. Stickney, D. Z. Anderson, and A. A. Zozulya, Transistorlike behavior of a Bose-Einstein condensate in a triple-well potential, Phys. Rev. A **75**, 013608 (2007)

[38]   C. J. Bradly, M. Rab, A. D. Greentree, and A. M. Martin, Coherent tunneling via adiabatic passage in a three well Bose-Hubbard system, Phys. Rev. A 85, 053609 (2012).

[39]   A. R. Kolovsky and A. Buchleitner, Quantum chaos in the Bose-Hubbard model, Europhys. Lett. **68**, 632 (2004).

[40]   A. R. Kolovsky, Bose-Hubbard Hamiltonian: Quantum chaos approach, Int. J. Mod. Phys. B 30, 1630009 (2016).

[41]   A. A. Bychek, P. S. Muraev, D. N. Maksimov, E. N. Bulgakov, and A. R. Kolovsky, Chaotic and regular dynamics in the three-site Bose-Hubbard model, AIP Conference Proceedings 2241, 020007 (2020)

[42]   M. Rautenberg and M. Gärttner, Classical and quantum chaos in a three-mode bosonic system, Phys. Rev. A **101**, 053604 (2020).

[43]   V. Penna, Dynamics of the central-depleted-well regime in the open Bose-Hubbard trimer, Phys. Rev. E **87**, 052909 (2013).

[44]   A. Gallemí, M. Guilleumas, J. Martorell, R. Mayol, A. Polls, and B. Julia-Díaz, Fragmented condensation in Bose‚ÄìHubbard trimers with tunable tunnelling, New J. Phys. **17** (2015) 073014.

[45]   A. Gallemí, G. Queraltó, M. Guilleumas, R. Mayol, and A. Sanpera, Quantum spin models with mesoscopic Bose-Einstein condensates, Phys. Rev. A 94, 063626 (2016).

[46]   T. F. Viscondi and K. Furuya, Dynamics of a Bose-Einstein condensate in a symmetric triple-well trap, J. Phys. A: Math. Theor. **44** (2011) 175301.

[47] T. F. Viscondi, K. Furuya, and M. C. de Oliveira, Phase transition, entanglement and squeezing in a triple-well condensate, Europhys. Lett. **90**, 10014 (2010).

[48] A. D. Greentree, J. H. Cole, A. R. Hamilton, and L. C. L. Hollenberg, Coherent electronic transfer in quantum dot systems using adiabatic passage, Phys. Rev. B **70**, 235317 (2004).

[49] K. Eckert, M. Lewenstein, R. Corbalán, G. Birkl, W. Ertmer, and J. Mompart, Three-level atom optics via the tunneling interaction, Phys. Rev. A **70**, 023606 (2004).

[50] E. M. Graefe, H. J. Korsch, and D. Witthaut, Mean-field dynamics of a Bose-Einstein condensate in a time-dependent triple-well trap: Nonlinear eigenstates, Landau-Zener models, and stimulated Raman adiabatic passage, Phys. Rev. A **73**, 013617 (2006).

[51] G. Arwas, A. Vardi, and D. Cohen, Triangular Bose Hubbard trimer as a minimal model for a superfluid circuit, Phys Rev A 89, 013601 (2014).

[52] G. Arwas, A. Vardi, and D. Cohen, Superfluidity and chaos in low dimensional circuits, Sci. Rep. **5**, 13433 (2015)

[53] Probabilistic Hysteresis in Integrable and Chaotic Isolated Hamiltonian Systems, R. B urkle, A. Vardi, D. Cohen, and J. R. Anglin, Phys. Rev. Lett. 123, 114101 (2019).

[54] M. A. Garcia-March, S. van Frank, M. Bonneau, J. Schmiedmayer, M. Lewenstein, and L. F. Santos, New J. Phys. **20**, 113039 (2018).

[55] C. V. Raman, N. S. N. Nath, The diffraction of light by high frequency sound waves: part IV. Proc. Indian Acad. Sci. **2**, 119 (1936).

[56] W. Kirkby, Y. Yee, K. Shi, and D. H. J. O'Dell, Caustics in quantum many-body dynamics, Submitted to Physical Review Research, arXiv:2102.00288 (2021).

[57] Q. Thommen, J. C. Garreau, and V. Zehnlé, Classical chaos with Bose-Einstein condensates in tilted optical lattices, Phys. Rev. Lett. **91**, 210405 (2003).

[58] J. R. Anglin, P. Drummond, and A. Smerzi, Exact quantum phase model for mesoscopic Josephson junctions, Phys. Rev. A **64**, 063605 (2001).

[59] L. Amico and V. Penna, Time-dependent mean-field theory of the superfluid-insulator phase transition, Phys. Rev. B **62**, 1224 (2000).

[60] S. Mossmann and C. Jung, Semiclassical approach to Bose-Einstein condensates in a triple well potential, Phys. Rev. A. **74**, 033601 (2006).

[61] M. Hiller, T. Kottos, and T. Geisel, Wave-packet dynamics in energy space of a chaotic trimeric Bose-Hubbard system, Phys. Rev. A **79**, 023621 (2009)

[62] Federico Finkel, Artemio González-Lóopez, and Miguel A. Rodríguez, On the families of orthogonal polynomials associated to the Razavy potential, 1999 J. Phys. A: Math. Gen. **32** 6821 (1999)

[63] *NIST Digital Library of Mathematical Functions*. http://dlmf.nist.gov/, Release 1.1.3 of 2021-09-15. F. W. J. Olver, A. B. Olde Daalhuis, D. W. Lozier, B. I. Schneider, R. F. Boisvert, C. W. Clark, B. R. Miller, B. V. Saunders, H. S. Cohl, and M. A. McClain, eds.

[64] E. L. Ince, A linear differential equation with periodic coefficients, Proc. Lond. Math. Soc. (2) **23**, 53 (1925); E. L. Ince, The real zeros of solutions of a linear differential equation with periodic coefficients, Proc. Lond. Math. Soc. (2) **25**, 56 (1926)

[65] R. Gutiérrez-Cuevas, D. H. J. O'Dell, M. R. Dennis, M. A. Alonso, Emulating a many-body topological transition with an aberrated optical cavity, arXiv:2106.02712.

[66] S. Sachdev, Quantum Phase Transitions, 2nd ed. (Cambridge University Press, Cambridge, England, 2011).

[67] E. Lieb, T. Schultz, and D. Mattis, Two soluble models of an antiferromagnetic chain, Ann. Phys. (N.Y.) **16**, 407 (1961).

[68] P. G. de Gennes, Collective motions of hydrogen bonds, Solid St. Commun. 1, 132 (1963).

[69] P. Pfeuty, The One-Dimensional Ising Model with a Transverse Field, Ann. Phys. (NY) **57**, 79 (1969)

[70] C. Kittel, *Quantum Theory of Solids*, (Wiley, New York, 1963).

[71] N. N. Bogoliubov, On the Theory of Superfluidity, J. Phys. USSR 11, 23 (1947).

[72] N. N. Bogoliubov, A new method in the theory of superconductivity, Nuovo Cimento (1955‚Äì1965) **7**, 794 (1958).

[73] H. Bethe, On the Theory of Metals I: Eigenvalues and eigenfunctions of a linear chain of atoms, Z. Phys. **71**, 931 (1931).

[74] C. N. Yang and C. P. Yang, One-Dimensional Chain of Anisotropic Spin-Spin Interactions I: Proof of Bethe's Hypothesis for Ground State in a Finite System, Phys. Rev. **150**, 321 (1966).

[75] H. Kim, T. N. Ikeda, and D. A. Huse, Testing whether all eigenstates obey the eigenstate thermalization hypothesis, Phys. Rev. E 90, 052105 (2014).

[76] M. B. Hastings, Locality in quantum systems, arXiv:1008.5137.

[77] E. H. Lieb and D. W. Robinson, The finite group velocity of quantum spin systems, Commun. Math. Phys. **28**, 251 (1972).

[78] J. Eisert, M. van den Worm, S. R. Manmana, and M. Kastner, Breakdown of quasilocality in long-range quantum lattice models, Phys. Rev. Lett. **111**, 260401 (2013).

[79] M. C. Tran, C.-F. Chen, A. Ehrenberg, A. Y. Guo, A. Deshpande, Y. Hong, Z.-X. Gong, A. V. Gorshkov, and A. Lucas, Hierarchy of Linear Light Cones with Long-Range Interactions, Phys. Rev. X **10**, 031009 (2020).

[80] T. Kuwahara and K. Saito, Strictly Linear Light Cones in Long-Range Interacting Systems of Arbitrary Dimensions, Phys. Rev. X **10**, 031010 (2020)

[81] L. Cevolani, G. Carleo, and L. Sanchez-Palencia, Protected quasilocality in quantum systems with long-range interactions, Phys. Rev. A **92**, 041603(R) (2015).

[82] M. Foss-Feig, Z.-X. Gong, C. W. Clark, and A. V. Gorshkov, Nearly Linear Light Cones in Long-Range Interacting Quantum Systems, Phys. Rev. Lett. 114, 157201 (2015).

[83] P. Calabrese, F. H. L. Essler, and M. Fagotti, Quantum quench in the transverse field Ising chain I, J. Stat. Mech. (2012) P07016.

[84] P. Richerme, Z.-X. Gong, A. Lee, C. Senko, J. Smith, M. Foss-Feig, S. Michalakis, A. V. Gorshkov, and C. R. Monroe, Non-local Propagation of Correlations

in Quantum Systems with Long-Range Interactions, Nature (London) 511, 198 (2014).

[85] J. F. Nye, *Natural Focusing and Fine Structure of Light* (CRC Press/Taylor and Francis group, London, 1999).

[86] L. da Vinci, Arundel 263 Folio 87-v (France Manuscript F); Manuscript F in Institut de France, Folio 28-v, (c. 1508). Accessible in the e-Leo digital archive of the Biblioteca Leonardiana of Vinci, https://www.leonardodigitale.com/en/

[87] M. Selmke and J. A. Lock, Bubble optics: Leonardo's cross revisited Part 1: numerical methods, Appl. Opt. **60**, 6213 (2021).

[88] Lord Kelvin, Deep water ship-waves, Phil. Mag. **9**, 733 (1905).

[89] T. Poston and I. Stewart, *Catastrophe Theory and its Applications*, (Dover Publications, New York, 1978).

[90] T. P. Simula, T. C. Petersen, and D. M. Paganin, Diffraction catastrophes threaded by quantized vortex skeletons caused by atom-optical aberrations induced in trapped Bose-Einstein condensates, Phys. Rev. A **88**, 043626 (2013)

[91] T. C. Petersen, M. Weyland, D. M. Paganin, T. P. Simula, S. A. Eastwood, and M. J. Morgan, Electron Vortex Production and Control Using Aberration Induced Diffraction Catastrophes, Phys. Rev. Lett. 110, 033901 (2013).

[92] W. Rooijakkers, S. Wu, P. Striehl, M. Vengalattore, and M. Prentiss, Observation of caustics in the trajectories of cold atoms in a linear magnetic potential, Phys. Rev. A 68, 063412 (2003).

[93] J. H. Huckans, I. B. Spielman, B. L. Tolra, W. D. Phillips, and J. V. Porto, Quantum and classical dynamics of a Bose-Einstein condensate in a large-period optical lattice. Phys. Rev. A 80, 043609 (2009).

[94] S. Rosenblum, O. Bechler, I. Shomroni, R. Kaner, T. Arusi-Parpar, O. Raz, and B. Dayan, Demonstration of Fold and Cusp Catastrophes in an Atomic Cloud Reflected from an Optical Barrier in the Presence of Gravity, Phys. Rev. Lett. 112, 120403 (2014).

[95] M. E. Mossman, T. M. Bersano, Michael McNeil Forbes, and P. Engels, Catastrophe Atom Optics: Fold and Cusp Caustics in an Atom Laser, arXiv:2104.13535

[96]   R. Gilmore, *Catastrophe Theory for Scientists and Engineers*, (John Wiley & Sons, New York, 1981)

[97]   R. Thom, Stabilité Structurelle et Morphogénèse, (Benjamin, New York, 1975).

[98]   V. I. Arnol'd, Funkcional. Anal. i Priložen **6**, 3 (1972); Functional Anal. Appl. **6** 254, (1972).

[99]   M. V. Berry, Waves and Thom's Theorem, Adv. Phys. **25**, 1 (1976).

[100] R. Borghi, Numerical computation of diffraction catastrophes with codimension eight, Phys. Rev. E 85, 046704 (2012).

[101] M. V. Berry and J. H. Hannay, Umbilic points on Gaussian random surfaces, J. Phys. A: Math. Gen. **10**, 1809 (1977).

[102] P. T. Saunders, *An Introduction to Catastrophe Theory* (Cambridge University Press, Cambridge, UK, 1986).

[103] M. V. Berry and C. J. Howls, Axial and focal-plane diffraction catastrophe integrals, J. Phys. A: Math. Theor. **43**, 375206 (2010).

[104] J. F. Nye, The catastrophe optics of liquid drop lenses, Proc. R. Soc. Lond. A **403**, 1 (1986).

[105] J. W. Milnor, *Morse Theory* (Princeton University Press, Princeton, 1963), Vol. 51.

[106] M. V. Berry and C. Upstill, *IV Catastrophe Optics: Morphologies of Caustics and Their Diffraction Patterns*, Prog. Opt. **XVIII**, 257 (1980).

[107] L. S. Schulman, *Techniques and Applications of Path Integration*, (Wiley, New York, 1981).

[108] G. B. Airy, On the intensity of light in the neighbourhood of a caustic, Trans. Camb. Phil. Soc. **6**, 379 (1838).

[109] T. Pearcey, The structure of an electromagnetic field in the neighbourhood of a cusp of a caustic, Phil. Mag. **37**, 311 (1946).

[110] G. J. Gbur, *Singular Optics* (CRC Press, Boca Raton, 2016).

[111] J. Proudman and A. T. Doodson, The principal constituent of the tides in the North Sea, Phil. Trans. of the Roy. Soc. A **244**, 185 (1924).

[112] M. V. Berry, J. F. Nye, and F. J. Wright, The elliptic umbilic diffraction catastrophe, Philos. Trans. R. Soc. London A **291**, 1382 (1979).

[113] J. F. Nye, From Airy rings to the elliptic umbilic diffraction catastrophe, J. Opt. A: Pure Appl. Opt. **5**, 503 (2003).

[114] J. F. Nye, Dislocation lines in the hyperbolic umbilic diffraction catastrophe, Proc. R. Soc. A **462**, 2299 (2006).

[115] J. F. Nye, Rainbow scattering from spheroidal drops,Äîan explanation of the hyperbolic umbilic foci, Nature (London) **312**, 531 (1984).

[116] P. L. Marston and E. H. Trinh, Hyperbolic umbilic diffraction catastrophe and rainbow scattering from spheroidal drops, Nature (London) 312, 529 (1984)

[117] G. Kaduchak, P. L. Marston, and H. J. Simpson, E6 diffraction catastrophe of the primary rainbow of oblate water drops: observations with white-light and laser illumination, Appl. Opt. **33**, 4691 (1994)

[118] J. A. Lock, J. D. Walker and J. H. Andrews, Using refraction caustics to monitor evaporation of liquid drop lenses, Appl. Opt. **29**, 4599 (1990).

[119] A. Lichtenberg and M. Lieberman, *Regular and Chaotic Dynamics*, Applied mathematical sciences (Springer-Verlag, Berlin, 1992)

[120] S. H. Strogatz, *Nonlinear Dynamics and Chaos: With Applications to Physics, Biology, Chemistry, and Engineering* (CRC Press, Boca Raton, FL, 2018).

[121] E. N. Lorenz, Deterministic nonperiodic flow, J. Atmos. Sci. **20**, 130 (1963).

[122] M. Berry, Quantum Chaology, Not Quantum Chaos, Phys. Scr. **40**, 335 (1989).

[123] E. J. Torres-Herrera and L. F. Santos, Local quenches with global effects in interacting quantum systems, Phys. Rev. E **89**, 062110 (2014).

[124] F. Borgonovi, F. M. Izrailev, L. F. Santos, and V. G. Zelevinsky, Quantum Chaos and Thermalization in Isolated Systems of Interacting Particles, Phys. Rep. 626, 1 (2016).

[125] M. V. Berry and M. Tabor, Level clustering in the regular spectrum, Proc. R. Soc. Lond. A **356**, 375 (1977).

[126] O. Bohigas, M. J. Giannoni, and C. Schmit, Characterization of Chaotic Quantum Spectra and Universality of Level Fluctuation Laws, Phys. Rev. Lett. 52, 1

[127] O. Bohigas, M. J. Giannoni, and C. Schmit, Characterization of Chaotic Quantum Spectra and Universality of Level Fluctuation Laws, Phys. Rev. Lett. 52, 1

[128] P. Sarnak, Values at integers of binary quadratic forms, *Harmonic Analysis and Number Theory* (Montreal, PQ, 1996), 181-203, CMS Conf. Proc. 21, Amer. Math. Soc., Providence, RI, 1997.

[129] A. V. Andreev, O. Agam, B. D. Simons, and B. L. Altshuler, Quantum Chaos, Irreversible Classical Dynamics, and Random Matrix Theory, Phys. Rev. Lett. 76, 3947 (1996).

[130] E. B. Rozenbaum, S. Ganeshan, and V. Galitski, Universal level statistics of the out-of-time-ordered operator, Phys. Rev. B **100**, 035112 (2019).

[131] T. Scaffidi and E. Altman, Chaos in a classical limit of the Sachdev-Ye-Kitaev model, Phys. Rev. B 100, 155128 (2019).

[132] S. Sachdev and J. Ye, Gapless spin-fluid ground state in a random quantum Heisenberg magnet, Phys. Rev. Lett. **70**, 3339 (1993).

[133] S. Sachdev, Bekenstein-Hawking Entropy and Strange Metals, Phys. Rev. X **5**, 041025

[134] A. Kitaev, A simple model of quantum holography, http://online.kitp.ucsb.edu/online/entangled15/kitaev/ (2015).

[135] M. L. Mehta, *Random Matrices* (Academic, Boston, MA, 1991)

[136] G. Livan, M. Novaes, and P. Vivo, *Introduction to Random Matrices – Theory and Practice*, Springer Briefs in Mathematical Physics (Springer, New York, 2018).

[137] M. V. Berry and M. Robnik, Semiclassical level spacings when regular and chaotic orbits coexist,M. V. Berry and M. Robnik, J. Phys. A: Math. Gen. **17**, 2413 (1984).

[138] B. Batistić and M. Robnik, Semiempirical theory of level spacing distribution beyond the Berry,ÄìRobnik regime: modeling the localization and the tunneling effects, J. Phys. A **43**, 215101 (2010).

[139] G. Vidmar, H. -J. Stöckmann, M. Robnik, U. Kuhl, R. Hohmann, and S. Grossmann, Beyond the Berry,ÄìRobnik regime: a random matrix study of tunneling effects, J. Phys. A: Math. Theor. **40** (2007) 13883,Äì13905

[140] B. Batistić, C. Lozej, and M. Robnik, The level repulsion exponent of localized chaotic eigenstates as a function of the classical transport time scales in the stadium billiard, arXiv:2104.08915

[141] T. A. Brody, A Statistical Measure for the Repulsion of Energy Levels, Lett. Nuovo Cimento **7**, 482 (1973).

[142] F. M. Izrailev, Simple models of quantum chaos: spectrum and eigenfunctions, Phys. Rep. **196** 299 (1990)

[143] A. Relaño, J. Dukelsky, J. M. G. Gómez, and J. Retamosa, Stringent numerical test of the Poisson distribution for finite quantum integrable Hamiltonians, Phys. Rev. E **70**, 026208 (2004).

[144] E. J Torres-Herrera, J. A. Méndez-Bermúdez, and Lea F. Santos Phys. Rev. E **100**, 022142 (2019).

[145] C.E. Porter and N. Rosenzweig, Ann. Acad. Sci. Fennicae, Serie A VI Physica **6**, 44 (1960).

[146] F. J. Dyson, A Brownian-Motion Model for the Eigenvalues of a Random Matrix, J. Math. Phys. **3**, 6, 1191 (1962).

[147] C. A. Tracy and H. Widom, Level-Spacing Distributions and the Airy Kernel, Commun. Math. Phys. **159**, 151 (1994).

[148] V. Oganesyan and D. A. Huse, Localization of interacting fermions at high temperature, Phys. Rev. B **75**, 155111 (2007).

[149] Y. Y. Atas, E. Bogomolny, O. Giraud, and G. Roux, Distribution of the Ratio of Consecutive Level Spacings in Random Matrix Ensembles, Phys. Rev. Lett. **110**, 084101 (2013).

[150] Y. Y. Atas, E. Bogomolny, O. Giraud, P. Vivo, and E. Vivo, Joint Probability Densities of Level Spacing Ratios in Random Matrices, J. Phys. A **46**, 355204 (2013).

[151] A. I. Larkin and Y. N. Ovchinnikov, Quasiclassical Method in the Theory of Superconductivity, Sov. J. Exp. Theor. Phys. **28**, 1200 (1969).

[152] S. H. Shenker and D. Stanford, Black holes and the butterfly effect, J. High Energy Phys. 2014, 67 (2014).

[153] A. Kitaev and S. J. Suh, The soft mode in the Sachdev-YeKitaev model and its gravity dual, J. High Energy Phys. 05 (2018) 183.

[154] J. Maldacena, S. H. Shenker, and D. Stanford, A Bound on Chaos, J. High Energy Phys. 08 (2016) 106.

[155] Daniel A. Roberts and Douglas Stanford, Diagnosing Chaos Using Four-Point Functions in Two-Dimensional Conformal Field Theory, Phys. Rev. Lett. **115**, 131603 (2015).

[156] E. B. Rozenbaum, S. Ganeshan, and V. Galitski, Lyapunov Exponent and Out-of-Time-Ordered Correlator‚Äôs Growth Rate in a Chaotic System, Phys. Rev. Lett. **118**, 086801 (2017).

[157] B. Swingle, Unscrambling the physics of out-of-time-order correlators, Nat. Phys. **14**, 988 (2018).

[158] P. A. M. Dirac, *The Principles of Quantum Mechanics* (Clarendon, Oxford, United Kingdom, 1958).

[159] D. Stanford, Many-body chaos at weak coupling, J. High Energy Phys. 10 (2016) 09

[160] J. Maldacena and D. Stanford. Remarks on the Sachdev-Ye-Kitaev model, Phys. Rev. D, **94** 106002, (2016).

[161] Y. Sekino and L. Susskind, Fast scramblers, J. High Energy Phys. 10 (2008) 065.

[162] K. Jensen, Chaos in AdS_2 Holography, Phys. Rev. Lett. 117, 111601 (2016).

[163] J. Maldacena, D. Stanford, and Z. Yang, Conformal symmetry and its breaking in two-dimensional nearly anti-de Sitter space, Prog. Theor. Exp. Phys. **2016**, 12C104 (2016).

[164] H. Shen, P. Zhang, R. Fan, and H. Zhai, Out-of-time-order correlation at a quantum phase transition, Phys. Rev. B **96**, 054503 (2017).

[165] H. Liu and J. Sonner, Quantum many-body physics from a gravitational lens, Nat. Rev. Phys. **2**, 615 (2020).

[166] S. Pilatowsky-Cameo, J. Chávez-Carlos, M. A. Bastarrachea-Magnani, P. Stránský, S. Lerma-Hernández, L. F. Santos, and J. G. Hirsch, Positive quantum Lyapunov exponents in experimental systems with a regular classical limit, Phys. Rev. E **101**, 010202(R) (2020).

[167] T. Xu, T. Scaffidi, and X. Cao, Does Scrambling Equal Chaos?, Phys. Rev. Lett. **124**, 140602 (2020).

[168] K. Hashimoto, K.-B. Huh, K.-Y. Kim, and R. Watanabe, Exponential growth of out-of-time-order correlator without chaos: inverted harmonic oscillator, J. High Energy Phys. **2020**, 68 (2020).

[169] Q. Hummel, B. Geiger, J. D. Urbina, and K. Richter, Reversible Quantum Information Spreading in Many-Body Systems near Criticality, Phys. Rev. Lett. 123, 160401 (2019).

[170] C.-J. Lin and O. I. Motrunich. Out-of-time-ordered correlators in a quantum Ising chain, Phys. Rev. B **97**, 144304 (2018).

[171] S. Xu and B. Swingle, Accessing scrambling using matrix product operators, Nat. Phys. **16**, 199 (2020).

[172] J. Riddell and E. S. Sørensen. Out-of-time ordered correlators and entanglement growth in the random-field XX spin chain. Phys. Rev. B **99**, 054205 (2019).

[173] B. Dóra and R. Moessner. Out-of-time-ordered density correlators in Luttinger liquids. Phys. Rev. Lett. **119**, 026802 (2017).

[174] J. Lee, D. Kim, and D.-H. Kim, Typical growth behavior of the out-of-time-ordered commutator in many-body localized systems, Phys. Rev. B **99**, 184202 (2019).

[175] V. Khemani, D. A. Huse, and A. Nahum, Velocity-dependent Lyapunov exponents in many-body quantum, semiclassical, and classical chaos, Phys. Rev. B **98**, 144304 (2018).

[176] Y. Alhassid and R. D. Levine Spectral autocorrelation function in the statistical theory of energy levels, Phys. Rev. A **46**, 4650 (1992).

[177] D.J. Thouless, Electrons in disordered systems and the theory of localization, Phys. Rep. **13**, 93 (1974).

[178] M. Schiulaz, E. J. Torres-Herrera, and L. F. Santos, Thouless and relaxation time scales in many-body quantum systems, Phys. Rev. B **99**, 174313 (2019).

[179] E. J. Torres-Herrera and L. F. Santos, Dynamical manifestations of quantum chaos: correlation hole and bulge, Phil. Trans. R. Soc. A **375**, 20160434 (2017).

[180] E. J. Torres-Herrera, A. M. García-García, and L. F. Santos, Generic dynamical features of quenched interacting quantum systems: Survival probability, density imbalance, and out-of-time-ordered correlator, Phys. Rev. B **97**, 060303(R) (2018)

[181] L. F. Santos and E. J. Torres-Herrera, Analytical expressions for the evolution of many-body quantum systems quenched far from equilibrium, AIP Conference Proceedings **1912**, 020015 (2017).

[182] L. Leviandier, M. Lombardi, R. Jost, and J. P. Pique Phys. Rev. Lett. **56**, 2449 (1986).

[183] C. B. Dağ, K. Sun, and L. -M. Duan, Detection of Quantum Phases via Out-of-Time-Order Correlators, Phys. Rev. Lett. **123**, 140602 (2019).

[184] L. M. Sieberer, T. Alsacher, A. Elben, M. Heyl, P. Hauke, F. Haake, and P. Zoller, Digital quantum simulation, Trotter errors, and quantum chaos of the kicked top. npj Quantum Inf **5**, 78 (2019).

[185] C. Cohen-Tannoudji, B. Diu, and F. Lal oe, *Quantum Mechanics, Volume 3: Fermions, Bosons, Photons, Correlations, and Entanglement* (Wiley, New York, 2019).